Laser and Micro-Plasma Arc Welding of Thin Sheet Inconel 718 and AISI 316L Stainless Steel at Similar and Dissimilar Combinations

Ajit Kumar Sahu

Department of Mechanical Engineering

Indian Institute of Technology Guwahati

2021

Laser and Micro-Plasma Arc Welding of Thin Sheet Inconel 718 and AISI 316L Stainless Steel at Similar and Dissimilar Combinations

A thesis submitted

in partial fulfillment of the requirements

for the award of

Doctor of Philosophy

by

Ajit Kumar Sahu

(156103006)

Under the supervision of

Dr. Swarup Bag

Department of Mechanical Engineering

Indian Institute of Technology Guwahati, India

July 2021

Dedicated to

"My parents and teachers"

Department of Mechanical Engineering
Indian Institute of Technology Guwahati
Guwahati-781039
INDIA

CERTIFICATE

It is certified that the work contained in the thesis entitled **"Laser and micro-plasma arc welding of thin sheet Inconel 718 and AISI 316L stainless steel at similar and dissimilar combinations"** submitted by **Mr. Ajit Kumar Sahu** to the Indian Institute of Technology Guwahati for the award of the degree of doctor of Philosophy has been carried out under my supervision in the Department of Mechanical Engineering, Indian Institute of Technology Guwahati. This work has not been submitted elsewhere for the award of any other degree or diploma.

The thesis, in my opinion, has reached the standard fulfilling the requirements for the award of degree of Doctor of Philosophy in accordance with the regulations of the Institute.

Date: 9th July, 2021

Dr. Swarup Bag

Department of Mechanical Engineering,
Indian Institute of Technology
Guwahati, Guwahati, Assam 781039,
India

Declaration

I declare that the present written submission is my thoughts in my own words. I have adequately been cited and referenced the original sources, where others' ideas have been involved. I also declare that I have followed to all principles of academic morality and honesty and have not neither fabricated nor falsified any idea/data in the present thesis. I realize that any defilement of the above will be cause for disciplinary action by the Institute and can also induce disciplinary action from the sources which have thus not been properly cited.

(Ajit Kumar Sahu)

Date: 9th July, 2021 Roll No: 156103006

Acknowledgement

Firstly, I would like to take this opportunity to express my earnest gratitude to my supervisors, ***Dr. Swarup Bag****, for accepting me as his Ph.D. student. His continuous motivation, support, and guidance throughout my Ph.D. work helped me to continuously grow as a researcher. With every research meeting with Dr. Bag, I felt motivated. His methodical way of guidance taught me how to develop an inquisitive mind and test every hypothesis from a scientific standpoint. I learned to struggle to get better and better every day by acquiring knowledge under his guidance.*

I am grateful to Dr. Huang for his generous help during the course of my Ph.D. Discussion with him helped me in gaining in-depth knowledge of the various microstructural characterization techniques. I would like to thank my doctoral committee members, Prof. R. Ganesh Narayanan, Dr. Manas Das, and Prof. S. K. Majumder, for their insightful comments and encouragement during evaluation of my research activity time to time. The constructive inputs received from Dr. Swarup Bag further helped me to grow intellectually. My sincere acknowledgment goes to Prof. S. K. Dwivedy and Prof. S. Senthilvelan, the former and present Head of the Mechanical Engineering department. I thank them for providing excellent facilities and environment to conduct research work from the initial to final stage of my Ph.D. work.

I would also like to thank my batchmates, especially Ballabi, Sarita, Bikash, Sudip, Avinish, Dutta and Vivek, for their constant technical and social support throughout the PhD duration. My Labmates Ankan, Swagat, Debtanay, Amritesh, Vaibhav, Daniel, and Vivekanand for their support in conducting experiments during the research work. Lastly, I am grateful to my father Sri Gouranga Sahu, my mother Smt. Shantilata Gountia, my brother Mr. Vidhan Chandra Sahu, my sisters Mrs. Pragyan Sahu and Mrs. Prachee Sahu, and my nephew Mr. Parth. All of whom were a constant source of support and motivation in this endeavor. Finally, I would like to express my deepest gratitude to the Almighty for showing His blessings on me.

Ajit Kumar Sahu

Indian Institute of Technology Guwahati

Abstract

Fusion welding of Inconel 718 and AISI 316L stainless steel at similar and dissimilar combinations are challenging due to the formation of micro fissure or solidification crack that often adversely affects the mechanical properties of the welded joint. In the present work, this takes as an opportunity to address all the issues aiming at a successful weld of 700 µm thick sheet using both micro-plasma and laser welding processes. High transients and gradients affects the solidification behavior of fusion-welded structure. The welding of highly alloyed material like Inconel 718 invites different microstructural complexity during the solidification and may end up with formation of solidification cracking. The improper solidification parameters can trigger solute redistribution in the fusion zone and may cause chemical inhomogeneity in the welded structure. It leads to precipitation of different intermetallic secondary phases in the fusion zone by consuming a significant amount of strengthening alloying elements from the metal matrix. In this context, micro-segregation of Nb leads to the formation of brittle intermetallic Laves phase in the solidified interdendritic region. The present thesis is primarily motivated in the direction that address the factors influencing the micro-segregation and intermetallic formation in similar and dissimilar configuration of welding Inconel 718.

At first, micro-plasma arc welding (µ-PAW) process in both continuous and pulse mode is employed to produce acceptable quality of autogenous butt-welding of Inconel 718. The effect of pulse parameters (i.e., peak current, duty cycle and pulse frequency) on microstructural morphology and mechanical properties are analyzed. The estimated solidification parameters from the 3D finite element-based heat transfer model is utilized to predict the solidification behavior of the weld zone. Secondly, the effect of post-weld solution and different double aging treatments on Inconel 718 weld is carried out to further improve the weld strength by dissolving the existing intermetallic phases and by precipitating various strengthening phases. The main objective was to reduce the holding time of post-weld treatments without compromising the mechanical properties of welded components. Thirdly, the weldability of Inconel 718 and AISI 316L dissimilar material using pulse µ-PAW technique is carried out without using any third material. The impact of pulse parameters and welding speed to minimize segregation, intermetallic phases and eventually the solidification cracks through improvement in solidification mode are undertaken. Finally, the high power density, CO_2 laser source is also employed to join this dissimilar combination of materials for a comparative analysis of the solidification behavior and weld joint quality. The validation of numerical model results with experimentally measured weld-beads are also demonstrated to confirm the robustness of the developed model. Finally, the creation of database for reliable joining of these materials using micro

plasma arc and laser welding processes is the sole contribution of this dissertation, hence, can be recommended.

Keywords: AISI 316L, dissimilar welding, finite numerical modelling, Inconel 718, intermetallics, laser welding, micro fissures, plasma arc welding, segregation, solidification parameters, solution and aging treatments.

CONTENTS

No.	Title	Page No.
	Abstract	**i-ii**
	Contents	**iii-vii**
	List of Figures	**ix-xv**
	List of Tables	**xv**
	Nomenclature	**xvii-xix**
1	**Introduction**	**1-10**
	1.1 General Background	1
	1.2 The problem statement	3
	1.3 Objectives and scope of thesis	5
	1.4 Motivation for research	6
	1.5 Significance of the study and hypothesis statement	7
	1.6 Layout of thesis	8
2	**Literature Review**	**11-34**
	2.1 Introduction	11
	2.2 General Background	12
	2.3 Weldability of Inconel 718	13
	2.4 Post-weld heat treatments of Inconel 718 weld	17

No.	Title	Page No.
2.5	Feasibility of dissimilar welding	19
2.6	Solidification kinetics and impact on weld microstructure	21
2.7	Heat transfer model	25
2.7.1	Heat source model	25
2.7.2	Conduction based heat transfer model	27
2.8	Summary	31
2.9	Scope of the present work	33
3	**Experimental Methods**	**35-56**
3.1	Introduction	35
3.2	Micro-plasm arc welding of thin sheets	36
3.2.1	Welding of Inconel 718	37
3.2.2	Dissimilar welding of Inconel 718 and AISI 316L	43
3.3	Heat treatment of welded joints	46
3.4	CO_2 laser welding of Inconel 718 and AISI 316L	47
3.5	Mechanical characterization of welded joints	49
3.6	Microstructural characterization of welded joints	51
3.7	Summary	55
4	**Theoretical Background**	**57-68**
4.1	Introduction	57
4.2	Governing equation and boundary conditions	58
4.3	Heat source model	60

No.	Title	Page No.
4.4	Model geometry and material properties	63
4.4.1	Model geometry for similar material welding	63
4.4.2	Model geometry for dissimilar materials	65
4.5	Evaluation of temperature gradient	67
4.6	Summary	68
5	**Results and Discussion**	**69-146**
5.1	Introduction	69
5.2	Micro-plasma arc welding of Inconel 718	70
5.2.1	Characteristics of temperature distribution	72
5.2.2	Cooling rate and microstructure	76
5.2.3	Influence on mechanical properties	85
5.2.4	Summary	88
5.3	Post weld heat treatment of micro-plasma arc welded Inconel 718	89
5.3.1	General background	90
5.3.2	Macro and micro structural characterization	91
5.3.3	Segregation analysis	95
5.3.4	Influence on mechanical properties	99
5.3.5	Mechanism of post weld heat treatment	100
5.3.6	Summary	102
5.4	Micro plasma arc welding of Inconel 718 and AISI 316L	103
5.4.1	General background	104

No.	Title	Page No.
5.4.2	Characteristics of temperature distribution	105
5.4.3	Solidification parameters and the microstructure	109
5.4.4	Characterization of intermetallics	114
5.4.5	Impact on mechanical properties	118
5.4.6	Summary	121
5.5	Micro-crack analysis in Inconel 718 and AISI 316L dissimilar weld	122
5.5.1	General background	123
5.5.2	Macro and micro structural characterization	125
5.5.3	XRD characterization	128
5.5.4	Influence on mechanical properties	131
5.5.5	Summary	132
5.6	Studies on microstructure of CO_2 laser welding of Inconel 718 and AISI 316L stainless steel	132
5.6.1	General background	133
5.6.2	Characteristics of temperature distribution	134
5.6.3	Impact of solidification parameters on microstructure	137
5.6.4	XRD characterization of the fusion zone	140
5.6.5	Mechanical analysis	142
5.6.6	Summary	146

No.	Title	Page No.
6	**Conclusions and Future Scope**	147-154
6.1	Introduction	147
6.2	Conclusions	149
6.3	Scope for future work	152
	References	155-162
	Bibliography	163-164
	List of Publications	165-166

List of Figures

Figure No.	Caption	Page no.
2.1	Showing HAZ micro fissures in laser welded Inconel 718 (Cao et al., 2009)	14
2.2	(a) SEM cross section image of the crack in the HAZ (b) EDX spectrum of the Laves phase (c) SEM image of the crack surface, and (d) EDX elemental content analysis of the crack surface (Ye et al., 2015)	16
2.3	SEM images showing precipitated carbides and platelet δ phase at the grain boundary after solution and aging treatment (C.-M. Kuo et al., 2009)	18
2.4	Micrograph of Inconel 718 and AISI 316L laser weld bead showing formation of liquation cracks (K. et al., 2019)	20
2.5	Solidification path of Inconel 718 (Knorovsky et al., 1989)	23
2.6	(a) Impact of temperature gradient and solidification growth rate on morphology and size of solidified structure, and (b, c, d, e) schematic of different solidification mode (Kou, 2003)	24
2.7	Validation of AISI 316L laser weld with numerical results (Jiang et al., 2016)	29
2.8	Validation of experimental and numerical dissimilar laser weld (a) Inconel 625 side and (b) AISI 316L side (Ebrahimi et al., 2016)	30
3.1	(a) Experimental set-up of micro plasma arc welding process (b) Pulse remote and (c) Copper fixture	37
3.2	(a) Microstructure and (b) EDX analysis of the base material Inconel 718	38
3.3	(a) Characteristics of the pulse heat source (b) experimental setup and (c) schematic of thermocouple location on the work piece surface	40
3.4	Process map for pulse micro plasma arc welding of Inconel 718	41
3.5	Top surface weld bead profile of (a) CC (b) PC1 (c) PC2 (d) PC3 (e) PC4 (f) PC5 (g) PC6 and (h) PC7 welding condition	43

Figure No.	Caption	Page no.
3.6	Optical and SEM micrographs of Inconel 718 (a, c) and AISI 316 (b, d) base material	44
3.7	Cross-sectional view of (a) PD0 (b) PD1 (c) PD5 and (d) PD6 dissimilar welded joint	46
3.8	The schematic of TTT diagram of Inconel 718 along with designed heat treatment phases	47
3.9	CO_2 laser experimental setup	48
3.10	(a) Transverse tensile specimen location in the welded specimen (b) Sub size tensile specimens before testing and (c) Showing location of failure in base material and fusion zone after testing	50
3.11	Schematic diagram of hardness testing measurement	51
3.12	Fusion zone microstructure near to fusion boundary for welds obtained at (a) 78 J/mm (b) 74 J/mm and (c) 71 J/mm	52
3.13	SEM microstructure of weld interior for (a) constant current mode and (b) pulsed-current mode micro-plasma weld	53
3.14	EDX analysis of the weld dendritic structure	54
3.15	XRD analysis of the weld zone produced at (a) constant current and (b) pulsed-current mode micro-plasma weld	55
4.1	Representation of solution domain along with applied boundary condition of the thermal model	60
4.2	(a) Schematic of double ellipsoidal heat source and (b) experimental mapping on weld bead	61
4.3	(a) Schematic of quadruple ellipsoidal heat source model and (b) experimental mapping on dissimilar weld bead	62
4.4	Solution domain of similar welding and boundary interaction	63

Figure No.	Caption	Page no.
4.5	Temperature dependent material properties for Inconel 718	64
4.6	Temperature dependent material properties for AISI 316L	65
4.7	Showing discretized weld plates with heat source moving direction	66
4.8	Solution domain of dissimilar welding and boundary interaction	66
4.9	Illustration of temperature distribution over the weld-pool surface in order to estimate the longitudinal temperature gradient	68
5.1	3D computed temperature distribution at: (a, f) pulse-on and (b-e) pulse-off time of PC1 condition; (g, h) at different time step of CC condition	73
5.2	2D cross sectional view of the weld bead showing FZ and HAZ in transverse direction for (a) CC (b) PC1 (pulse-on) (c) PC1 (pulse-off) conditions	74
5.3	Comparison of experimentally (left) and numerically (right) obtained weld profile for (a) CC (b) PC1 (c) PC5 (d) PC7 and (e) top weld width	75
5.4	Comparison of time-temperature profiles between computed and experimentally measured quantity for (a) continuous mode (CC) and (b) pulse mode (PC1)	76
5.5	Temperature gradient in transverse direction (a) and longitudinal direction (b) for CC welding condition	77
5.6	Temperature gradient and time temperature profile for PC1 (a, b), PC5 (c, d), PC6 (e, f) and PC7 (g, h) welding conditions	79-80
5.7	Microstructure of (a) pulse (PC1) and (b) continuous (CC) welding condition	81
5.8	SEM images of (a) CC (b) PC1 (c) PC5 and (d) PC7 weld center zone	82
5.9	SEM images showing fusion zone morphology for (a) CC (b) PC1 (c) PC2 (d) PC3 (e) PC4 (f) PC5 (g) PC6 and (h) PC7 welding conditions	83

Figure No.	Caption	Page no.
5.10	EDX analysis of Laves phase for PC5 welding condition	84
5.11	(a) Stress-strain curve of base material and welded joints; (b, c) showing fracture location of CC (b) and PC5 (c) welding condition	86
5.12	Tensile fracture surfaces in lower and higher magnification (a, d) base material, (b, e) CC welded sample and (c, f) PC1 welded sample	86
5.13	Hardness distribution at different welding conditions	88
5.14	Post weld heat treatments: (a) aged, (b) STA1 and (c) STA2 conditions	91
5.15	Morphological variation of fusion zone at different condition (a) solidified dendritic structure (as-welded), (b) partially dissolved dendritic structure (direct aged), (c) formation of equiaxed grains after solution treatment (ST), (d) grain coarsening due to aging (STA1) and (e) (STA2)	92
5.16	Higher magnification SEM micrographs of fusion zone showing: (a) intermetallic Laves phase in as-welded condition; (b) precipitation of γ', γ" and δ phase around the Laves particle in direct aged condition; and (c) micro-fissure sites in the grain boundary of ST condition	94
5.17	Fusion zone SEM micrographs showing precipitation of (a) platelet type δ particles in the grain boundary and, fine γ″ and γ′ strengthening phases within the grain for STA1; (b) needle shape δ particles in the boundary and, coarse γ″ and γ′ phases in STA2 condition	95
5.18	XRD pattern of base material (a) and different conditioned fusion zones (b-f)	98
5.19	(a) Tensile test results and (b) hardness distribution of the as-welded and treated samples	99
5.20	Microstructural evolution from as-welded condition to various post weld solution and/or aging treatments	102
5.21	Simulated and experimental weld bead profile of the (a) PD1 and (b) PD5 welding conditions	106

Figure No.	Caption	Page no.
5.22	Weld bead temperature distribution for the (a) PD1 and (b) PD5 welding conditions	107
5.23	Transient temperature change during pulse on and off time	109
5.24	Weld interface and weld zone of (a, b, c) PD1 and (d, e) PD5 weld	110
5.25	Variation of temperature gradient at (a) PD1 and (b) PD5 welding conditions	111
5.26	Weld centre microstructure of (a) PD1 (b) PD2 (c) PD3 (d) PD4 and (e) PD5 welding conditions	113
5.27	Higher magnification microstructure of (a, c) columnar dendrites and (b, d) equiaxed dendrites	114
5.28	XRD pattern of (a) base material and (b) PD5 weld zone	115
5.29	Elemental line mapping across different zones for PD5 welding condition	116
5.30	EDX elemental mapping of the PD1 columnar structure	117
5.31	EDX analysis of (a) PD1 and (b) PD5 weld zone	118
5.32	Tensile fracture images of the (a) PD1 and (b) PD5 welding conditions	120
5.33	Tensile fractography of the (a) PD1, (b) PD2, (c) PD3, (d) PD4 and (e) PD5 welding conditions	120
5.34	Micro-hardness distribution across the weld joint	121
5.35	SEM micrographs of PD1 (a, b, c, d) and PD4 (e, f, g, h) weld zone	126
5.36	(a) EDS elemental mapping (b) area analysis and (c) line scanning across the crack surface	127

Figure No.	Caption	Page no.
5.37	XRD analysis of PD1 and PD4 weld	128
5.38	(a) Hardness distribution (b) tensile properties of the welds and (c, d) fractographs of tensile specimens	131
5.39	Comparison of experimental and numerically obtained weld bead	135
5.40	Showing (a) nodal time - temperature distribution and (b) weld temperature gradient variation during the welding	136
5.41	SEM micrographs of (a) LD1 (b) LD2 (c) LD3 (d) LD4 and (e) LD5 weld	138
5.42	(a) EDX elemental mapping and (b) EDX spot analysis on weld microstructure	139
5.43	X-ray diffraction analysis of (a) LD1 (b) LD3, and (c) LD5 weld	140
5.44	Tensile stress-strain curves along with fracture location for welded samples; (b) hardness distribution of welded samples (c) location of crack sites in final solidified structure and (d, e) tensile fracture surfaces of LD1 and LD5 weld respectively	145

List of Tables

Table No.	Title	Page no.
3.1	Chemical composition (wt. %) of Inconel 718	38
3.2	Welding parameters employed for Inconel 718 similar welding	42
3.3	Chemical composition (wt. %) of AISI 316L stainless steel	44
3.4	Selected process parameters of pulse welding process	45
3.5	Laser process parameters	48
3.6	Geometrical characteristics of the laser weld beads	49
5.1	Evaluation of solidification parameters	80
5.2	Tensile test and joint efficiency of welded samples	85
5.3	Average hardness value at different welding conditions	87
5.4	EDS elemental analysis of as-welded and heat treated samples at weld zone	96
5.5	Segregation co-efficient of principal alloying elements in the fusion zone	97
5.6	Tensile test results	99
5.7	Estimation of solidification parameters	111
5.8	Tensile test results of the welded samples	119
5.9	Selected process parameters for the welding process	124
5.10	Relative XRD phase intensities for PD1 and PD4 weld	129
5.11	Effect of welding conditions on dilution level of principal alloying elements	130
5.12	Thermal characteristics of the welding conditions	136
5.13	Relative XRD peak intensities for LD1, LD3 and LD5 weld	142
5.14	Tensile test results	143

Nomenclature

Symbol	Description	Unit
G	Temperature gradient	K mm^{-1}
R	Solidification growth rate	mm s^{-1}
G.R	Cooling rate	K s^{-1}
C	Specific heat of the material	J kg^{-1} K^{-1}
SOD	Stand-off distance	mm
I	Current	A
I_a	Average current	A
I_p	Peak current	A
I_b	Base current	A
t_{on}	Pulse on time	s
t_{off}	Pulse off time	s
V	Welding voltage	Volt
S	Welding speed	mm s^{-1}
F	Pulse frequency	Hz
MC	Metal carbide	-
H	Heat input	J mm^{-1}
$\dot{Q}$	Rate of internal heat generation per unit volume	W m^{-3}
ST	Solution treatment	-
L_P	Laser beam power	W
η	Arc efficiency	-
S_V	Laser scanning velocity	mm s^{-1}
Q	Heat input during laser welding	J mm^{-1}
UTS	Ultimate tensile strength	MPa
FZ	Fusion zone	-
HAZ	Heat affected zone	-
BCT	Body-centered tetragonal	-
T_0	Atmospheric temperature	K
v	Welding velocity	mm s^{-1}

Symbol	Description	Unit
EDX	Energy dispersive x-ray	-
XRD	X-ray diffraction	-
NIR	Normalized intensity ratio	-
T	Temperature of plate	K
δ	Thermal diffusivity	$m^2\ s^{-1}$
ρ	Density of the material	$kg\ mm^{-3}$
Ɛ	Emissivity of the surface	-
α	Absorption coefficient	-
h	Surface heat transfer coefficient	$W\ m^{-2}\ K^{-1}$
h_{eff}	Lumped heat transfer coefficient	$W\ m^{-2}$
k	Thermal conductivity	$W\ m^{-1}\ K^{-1}$
P	Laser beam power	W
x, y, z	Local coordinate system	-
t	time variable	s
σ	Stiffen-Boltzmann constant	$W\ m^{-2}\ K^{-4}$
a, b, c_f,c_r	Semi axes of the double ellipsoidal heat source	mm
f_f , f_r	Fractions of heat deposited in the front and rear quadrants	-
FE	Finite element	-
$\dot{\varepsilon}$	Cooling rate	$K\ s^{-1}$
PWHT	Post weld heat treatment	-
T_S	Solidus temperature	K
T_L	liquidus temperature	K
L	Latent heat of fusion	$J\ kg^{-1}$
SGB	Solidification grain boundaries	-
FCC	Face-centered cubic	-
C_{FZ}	Average fusion zone composition	wt.%
T_P	Peak temperature	K
SDA	Secondary dendritic arm	-
f_s	Solid fraction	-
C_{BM}	Elemental composition of base material	wt.%

Symbol	Description	Unit
D_E	Elemental dilution level	%
D	Dilution level	%

Chapter 1

Introduction

1.1 General background

The successful welding of Inconel 718 and Inconel 718-AISI 316L dissimilar combination is a challenging assignment as it susceptible to solidification cracking during the welding process. Hence, the micro plasma arc and CO_2 laser welding is chosen to produce sound quality welds. Solidification of the Inconel 718 superalloy is complex in nature and it governs the microstructural morphology and corresponding mechanical properties of the weld joint. In the current study, the focus is to find the critical parameters that are responsible for the solidification kinetics, solute redistribution, size and shape of the final solidified structure. Experimental measurement of the solidification parameters has its limitations because of the complexity of the process. Hence, the finite element model is developed to accurately predict the time-temperature profile of the weld pool and solidification process.

With growing interest of nickel based super alloys for the critical components of aerospace, automotive and power generation industries, present work is motivated to investigate the weldability of Inconel 718 alloy in similar and dissimilar mode. Inconel 718 belongs to the family of austenitic Ni-Fe based superalloys. It shows excellent oxidation and corrosion resistant, which is well suited for service in extreme environments when subjected to high pressure and temperature (Yuan and Liu, 2005). The superalloy retains its strength over a wide range of temperature (-250 ℃ to 650 ℃), hence it is mainly used for high temperature applications where aluminium and steel fail to creep. As a precipitation hardenable superalloy, it is widely used in rocket engines, specifically in the region of inlet to the combustion chamber, exhaust of preburner, and turbine exhaust (Manikandan et al., 2019). These entire region witnesses a temperature as high as 650°C with the gaseous hydrogen environment. Thin sheets

of Inconel 718 are used for fan containment applications around parts of the compressor and turbine region. The Inconel 718 fans in supersonic applications in the commercial turbine of jet engines is used because of its high ballistic impact strength (Pereira and Lerch, 2001).

Similarly, the austenitic steels are widely used in petrochemical, aerospace and power generating sectors in the form of plate, coil, sheet, bar and tubing for various applications. AISI 316L contain lower amount of carbon which makes this austenitic steel immune to the sensitization (precipitation of chromium carbides at grain boundaries) at elevated temperatures (Kar et al., 2017). AISI 316L exhibits higher creep and tensile strength as compared to other nickel-chromium austenitic steels over a wide temperature range. It also possesses excellent toughness even at the cryogenic temperature, which makes it distinct from other chromium-nickel austenitic stainless steels. The dissimilar combination of Inconel 718 and AISI 316L austenitic stainless steel are used in the aerospace, chemical processing and oil industries in addition to gas power stations for the fabrication of various hot section components. The Inconel 718 and AISI 316L material combination is widely used for making pressure tubes in nuclear reactors, that are implemented over a wide range of temperature, pressure and stress level (Hinojos et al., 2016). This combination of materials is also used for making multi stage compressor rotor where high pressure stages are made by Inconel 718 and low pressure stages are made of AISI 316L austenitic stainless steel (Henderson et al., 2004). This bimetallic welds are also implemented for construction of hoses (AISI 316L) and quick disconnects coupling (Inconel 718) for carrying ammonia in the international space station (Devendranath Ramkumar et al., 2014).

Fusion welding is one of the most preferred metal joining techniques in most of the industries, which is achieved by melting the base materials with an intense heat source followed by solidification. One important parameter that distinguishes all fusion-welding processes from each other is the intensity of the heat source used to melt the parent material to make the joint. The surface temperature of the base material during welding is a function of the surface power density and the time. As the power density of the heat source increases, the heat input to the workpiece that is required for welding decreases. At relatively low heat input during the welding process leads to less metallurgical and structural inhomogeneity in the welded components, which further help to enhance the weld quality. However, an excessive heating has detrimental effect on structural integrity as it can damage, weaken and distort the

final component due to high transients and gradients. On the other hand, if the same material exposed to a sharply focused plasma or laser beam, it can melt or even vaporize to form a deep keyhole instantaneously, and before much heat is conducted away into the workpiece, welding gets completed.

Joining of thin sheets especially by conventional arc welding processes is a major challenge due to the generation of larger weld beads, which induce undesirable microstructural inhomogeneity over a larger area in the welded component and may cause failure of the component. Hence, highly concentrated heat flux like micro plasma arc welding and laser beam welding techniques are extensively used for joining thin sheets. Micro plasma arc welding (μ-PAW) is a variant of conventional plasma arc welding that uses current lower than 15 A and is usually used for welding of thin sheets (upto 0.5 mm thickness). μ-PAW also possesses excellent arc stability at very low current range as compared to GTAW process along with economical operating cost (Baruah and Bag, 2016). Hence, μ-PAW in continuous and pulse mode is selected for the current investigation to weld thin sheet of Inconel 718 in similar and dissimilar configuration with AISI 316L. Laser welding is one of the most preferred joining techniques used by various industries for welding a wide range of material due to its very small, highly focused and precisely controlled intense heat source. CO_2 laser welding process is currently used for the fabrication of Inconel 718 and AISI 316L dissimilar weld. The process involves several controlled parameters like beam power, traverse speed, beam diameter and standoff distance, which can influence the weld joint quality.

1.2 The problem statement

Inconel 718 possesses considerably good weldability compared to other nickel-based superalloys because of its resistance to strain age cracking, due to sluggish precipitation of γ" (Ni_3Nb) during the welding process. However, fusion welding of Inconel 718 in similar and dissimilar combination is not utterly free from welding defects. The solidification cracking and micro fissuring in the fusion zone (FZ) and heat-affected zone (HAZ) are major problem associated with the Inconel 718. But these can be minimized by taking necessary precautions during and after the welding process. The formation of these deleterious defects are mainly due to the micro segregation of Nb, Mo and Ti in interdendritic boundaries, resulting in formation of Nb-rich brittle intermetallic NbC and Laves phase with $(Fe, Ni, Cr)_2(Mo, Nb, Ti)$

stoichiometry. These brittle intermetallic phases produce intergranular liquid films, which eventually produces sites for micro-crack initiation during the course of solidification. The distribution and volume fraction of NbC and Laves phases not only have detrimental effect on the mechanical properties of the weld joint but also consumes a significant amount of useful strengthening alloying elements from the matrix. The volume fraction of intermetallic phases and the segregational behaviour are found to be a function of the welding process parameter and solidification parameters. Hence, the major goal of the current work is to investigate the influence of different process parameters for micro-plasma arc and CO_2 laser welding technique with the solidification mode and its implication on the joint properties.

In the welding of Inconel 718, the intermetallic phases can be dissolved back to the bulk solution through proper design of the post-weld heat treatments. The dissolution of intermetallic phases at proper heat treatment temperature makes an extensive volume of principal elements available in the matrix for precipitation of various strengthening phases. Niobium is the major element of the Laves phase, and by dissolution, it precipitates into γ' (i.e., Ni_3 (Al, Ti) with FCC structure), γ'' (i.e., DO_{22} ordered- Ni_3Nb with BCT structure) strengthening phase and δ particles (DO_a ordered- Ni_3Nb with orthorhombic structure) during the aging treatment. As a result, the mechanical properties improve. However, a higher holding time at the peak temperature increases the operational cost by many folds. As a result, optimization of the post weld treatment need to be addressed. Hence, the current work attempts to reduce holding time of the post-weld treatment without compromising mechanical properties of the Inconel 718 welded components.

An accurate knowledge on weld pool peak temperature and time-temperature distribution at each location of the fusion zone is necessary requirement for accurate estimation of the solidification parameters and bead dimensions. However, the experimental determination of such parameters are extremely difficult owing to the small size of the weld pool and presence of high convection current within the weld pool. Theoretical investigation by implementing mathematical modelling of the process provides a better understanding of the fusion zone characteristics. Finite element based transient thermal model are helpful for obtaining these unknown parameters by considering the effect of conduction, convection and radiation phenomena during the welding process. These physical phenomena are expressed through mathematical form of governing equations with the corresponding boundary conditions.

Robustness of the model is validated by comparing numerical results with experimentally measured results. Conduction based heat transfer models are simpler and computationally economical and yet produce highly accurate results for smaller weld pool. Hence, the numerical models are need to be developed corresponding to the similar and dissimilar welds, produced through micro plasma arc and laser welding techniques.

1.3 Objectives and scope of the thesis

In the present work, major thrust is focused on to develop a micro-plasma arc welding process window for Inconel 718 in similar and dissimilar combination with AISI 316L steel through experiments. Both continuous and pulse mode of welding is followed to investigate solidification morphology, Laves formation and impact on the mechanical properties of the welded joint. Secondarily, the response of fusion zone intermetallic phases to various post weld heat treatment techniques and precipitation of various strengthening phases are envisaged. In addition, the feasible parameter domain is also established for CO_2 laser welding process for the dissimilar welding of Inconel 718 and AISI 316L sheets. To achieve the above research objectives, the following modules are accomplished sequentially and developed over whole duration of the research work.

- The optimization of welding process parameters to produce a sound quality weld for Inconel 718 sheets using pulse and constant current mode of micro plasma arc welding process. The establishment of feasible domain of parameters for successful weld joint is the main objective.
- To establish a correlation between the pulse process parameters with the solidification parameters (*G.R* and *G/R*) and the resulting impact on final microstructure, and mechanical properties of the welded joint.
- To develop a three-dimensional finite element based transient thermal model of the micro plasma arc welding process to predict the temperature distribution, weld pool dimensions and time-temperature history for pulse and continuous mode of welding.
- Optimization of the post weld solution and aging treatment to reduce the holding time of the post-weld treatment without compromising the mechanical properties of micro-plasma arc welded Inconel 718.

- Identification of feasible process parameter domain for producing defect free dissimilar welds of Inconel 718 and AISI 316L thin sheets using pulse mode of micro plasma arc welding (μ-PAW) process.
- To investigate the effect of pulse current and weld velocity on microstructural and mechanical properties of the dissimilar welded joints. To address the possible intermetallic formation in the fusion zone of dissimilar welding and its impact on formation of solidification crack.
- Investigation of CO_2 laser process parameters to produce successful weld between Inconel 718 and AISI 316L stainless steel. The influence of laser beam power on weld solidification mode and segregational tendency is needed to be analysed.
- To develop a three-dimensional transient heat transfer model using finite element method for the CO_2 laser welding processes in dissimilar welding of Inconel 718 and AISI 316L stainless steel.

1.4 Motivation for research

With growing interest of nickel based super alloys for the critical components of aero engines and gas turbines in power plant, motivated the present work to investigate the weldability of Inconel 718 alloy either in similar or dissimilar mode. It shows excellent oxidation and corrosion resistant which is well suited for service in extreme environments when subjected to high pressure and temperature, where aluminium and steel fail to creep, as a result of thermally induced crystal vacancies. Inconel 718 is one of the most successful high temperature application alloy, which has considerably good weldability as compared to other nickel-based superalloys because of its resistance to strain age cracking. Inconel 718 comprises 51% of the total weight of the space shuttle main engine and accounts for approximately 1,500 engine components, of various thickness and dimensions. It can be employed in the liquid and gaseous hydrogen, liquid oxygen, and hydrogen rich steam environments at a temperature ranging from -253°C to 760°C. The use of Inconel 718 as turbine wheels and disc material in gas turbine engines has increased significantly in recent years because of its high strength and corrosion resistance at both room temperature and high temperature condition. Thin sheets of Inconel 718 are also used for fan containment applications around parts of the compressor and the turbine region, or for fans in supersonic applications in the commercial turbine jet engines

because of its high ballistic impact strength. It is competitively low priced as the alloy contains negligible amount of cobalt and has a relatively high iron content (~18 wt.%).

AISI 316L grade is an austenitic variety of stainless steel which exhibit superior corrosion resistance as compared to ferritic and martensitic stainless steels. It also offers higher creep, stress-to-rupture, and tensile strength at elevated temperature. The austenitic structure gives these grades steels excellent toughness, even down to cryogenic temperatures. AISI 316L has a wide range of applications in aerospace industry, nuclear power plants, marine industry and in gas turbine engines as disc material for low pressure compressor rotor due to its superior corrosion resistance to most chemicals, salts, and acids. With the improvement in micro joining technology, now a days AISI 316L thin foils are even welded on various industrial parts and components as a protective cover to protect from corrosive environments and chemical attacks.

The needs of the dissimilar weld joint between nickel based superalloy and stainless steel is increasing in many industries. In view of the fact that, bimetallic joints not only satisfy the service conditions but also results in large cost reduction by minimizing the volume of expensive material. Combination of Inconel 718 and AISI 316L austenitic stainless steel finds their applications in aerospace industries and gas power plants. In multi stage compressor, generally the high-pressure stage rotor discs are made from Inconel 718 and the lower pressure stages are made of austenitic stainless steel. These bimetallic combinations of welds are also use for the construction of hoses (AISI 316L) and the quick disconnects (Inconel 718). Further the hoses and quick disconnects are welded using orbital Tungsten Inert Gas (TIG) welding process and employed in the international space station for carrying ammonia. Fusion welding is one of the most preferred joining techniques for Inconel 718 and AISI 316L to establish a good metallurgical bond between the mating surfaces. Hence, the present study is mainly motivated to mitigate the welding problems associated with Inconel 718 in similar configuration and during the joining of nickel based superalloy and austenitic stainless steels in dissimilar combination.

1.5 Significance of the study and hypothesis statement

In the present work, major thrust is focused on to develop a micro-plasma arc welding process window for Inconel 718 in similar and dissimilar combination with stainless steel. Both continuous and pulse mode of welding is followed to investigate solidification

morphology, Laves formation and impact on the mechanical properties of the welded joint. Secondarily, the response of fusion zone intermetallic phases to various post weld heat treatment techniques and precipitation of various strengthening phases is envisaged. The current work attempts to reduce holding time of the post-weld treatment by more than 50% without compromising the mechanical properties of Inconel 718 joint. Thirdly, the process window of CO_2 laser is also developed for the dissimilar welding of Inconel 718 and AISI 316L sheets.

The successful development of autogenous welding between Inconel 718 and AISI 316L stainless steel can significantly reduce the production cost through automation of the production line for various aerospace and automotive industries. The cost of AISI 316L austenitic stainless steel is of a fraction to that of Inconel 718. The welding compatibility between these material is exceptionally good, as a result aerospace and power generation industries can implement this material combination instead of only Inconel 718 components, where operating temperature is below 600°C. By implementing cost efficient plasma welding technique this material can even be welded with more than 100% (w.r.t. AISI 316L) joint efficiency. The replacement of Inconel 718 with AISI 316L will reduce the component cost significantly without affecting the operating condition.

1.6 Layout of the thesis

The thesis is organised into 10 chapters to elaborate all the aspects aimed at the research objectives. The **Chapter 1** provides a general background to the materials, problem statement, objectives and scope of the thesis, motivation for research, Significance of the study and the overall layout of the thesis.

Chapter 2 includes an extensive literature review on the work of previous researchers, which is focused on fusion welding of Inconel 718 in similar and dissimilar configuration (with AISI 316L) using arc and laser welding techniques in the perspective of practical applications. First, experimental investigation on process conditions, materials, and feasibility of fusion welding processes is reviewed. The impact of welding process parameters and solidification parameters on weld microstructure formation and segregation of different alloying elements is discussed extensively for similar and dissimilar welding. Subsequently, different post weld heat treatment processes are also discussed to improves the Inconel 718 weld mechanical properties. An extensive part of the chapter is devoted to review different finite element based

conduction heat transfer models implemented to predict the time-temperature history. Different issues related to numerical modelling of similar and dissimilar combination of materials is also addressed in the chapter. Finally, the research gaps and aim of the present thesis work are outlined based on the literature survey.

Chapter 3 describes the detailed experimental procedures followed during the thesis work. The feasible range of process parameters corresponding to micro-plasma arc welding and CO_2 laser welding to produce defect-free weld in butt joint configuration is outlined in this chapter. The impact of different process parameters on weld geometry, solidification behaviour and microstructural morphology are analysed systematically. In addition to that, different post weld heat treatments for Inconel 718 welds are developed to improve the mechanical and microstructural properties. The detailed microstructural characterization of the weld zone through optical microscope (OM), scanning electron microscope (SEM), energy dispersive X-ray (EDX) analysis, and X-Ray diffraction (XRD) technique are described in this chapter. The microstructural impact on mechanical properties are analysed through the tensile and Vickers micro-hardness testing.

The mathematical formulation employed to develop the finite element (FE) based heat transfer model for the similar and dissimilar welding is described in **Chapter 4**. The effect of current pulsation is incorporated with the model through DFLUX subroutine for better understanding of the cyclic variation of temperature during the pulse welding condition. The use of Gaussian distributed volumetric heat source to compensate the convective heat transport within the weld pool is explained. The model validation with the experimentally measured weld bead geometries and the time temperature history of heat-affected zone recorded during the welding process is described.

Chapter 5 outlines the computed results and the validation of these results with the corresponding experimental data. The effect of peak current, duty cycle and pulse frequency on cooling rate, weld morphology and mechanical properties are reported herein. The calculated solidification parameters from the 3D finite element-based heat transfer model is used to predict the solidification behaviour of the weld zone. The weld mechanical properties are found inferior to the base material, due to the presence of intermetallic phases. Current pulsation with optimum heat input in µ-PAW shows the improvement in the weld mechanical properties. The effect of post-weld solution and different double aging treatments on

precipitation of various strengthening phases in micro-plasma arc welded Inconel 718 is presented. The high-temperature solution treatment has dissolved the intermetallic phases and makes a suitable quantity of alloying elements accessible for precipitation of the strengthening phases. To analyse the impact of aging temperature and holding time on δ, γ' and γ'' phase precipitation, four different heat treatment paths are designed. The heat treatment holding time is reduced by 53% on the welded component by applying a higher aging temperature compared to the conventional aging temperatures. The weldability of Inconel 718 with AISI 316L stainless steel using micro-plasma arc welding technique through metallurgical and mechanical characterization addressed. The intermetallic formation due to solute segregation during dissimilar welding of Inconel 718 and stainless steel poses a serious challenge as it promotes solidification cracking in the fusion zone. So minimization of these intermetallic phases and eventually the solidification cracks through variation in pulse current and welding speed is also undertaken in this chapters. The high power CO_2 laser dissimilar welding of Inconel 718 and AISI 316L stainless steel is undertaken. The microstructural characterization along with mechanical properties are evaluated in the light of various intermetallic formation. The micro-segregation and intermetallic formation during the solidification are correlated with solidification parameters.

Finally, **Chapter 6** outlines the summary and conclusions drawn from the preceding chapters as a part of the present thesis work. Further scope of future works in the context of the theme of the present thesis are also highlighted in this chapter. The list of references is presented at the end.

Chapter 2

Literature Review

2.1 Introduction

In this chapter, an extensive literature review on fusion welding of Inconel 718 in similar and dissimilar configuration (with AISI 316L) using different conventional and advanced welding techniques are discussed. The metallurgical incompatibility in Inconel 718 weld is a major issue even after five decades of its invention. The effect of welding process parameters on microstructural morphology and formation of various intermetallic phases are the main concern. With proper selection of welding technique and its parameters, these defects can be minimized up to a larger extent. The impact of solidification parameters on weld microstructure formation and segregation of different alloying elements is discussed extensively. The welding process parameters mainly governs the solidification behavior. Therefore, proper selection of process parameter will result in reduction of secondary phases and improvement in weld mechanical properties. Different post weld heat treatment processes are also another alternative to dissolve these secondary phases in to the metal-matrix. Experimental measurement of intricate details within small weld-pool is not feasible due to the complexity of the process. The finite element based conduction model is an effective tool to predict the time-temperature data. Therefore, literature review relevant to different issues in numerical model of similar and dissimilar combination of materials is also addressed. Finally, the research gaps and aim of the present thesis work are outlined based on the literature survey.

2.2 General background

Welding is the process of joining two similar or dissimilar material with or without the application of heat and pressure or both to produce a permanent joint. Welding is widely divided into two categories, pressure welding and fusion welding. Pressure welding is also known as solid state welding process, where the weld is produced by applying mechanical pressure by mean of friction or explosion to the joining surfaces to produce the weld joint. The major drawback of solid state welding process is mainly limited to softer material like Aluminum and Copper. The operating cost increases manifold, because of the tool wear when high strength material like steel and Inconel are weld using solid state welding process. Hence, fusion welding technique is widely accepted by the fabrication industries to weld a wide range of similar and dissimilar combination of materials because of high production rate and cost effectiveness. In fusion welding process, the joining surfaces are heated above the melting point temperature by applying an intense heat source to create coalescence between the base materials, so that joint can be produced between them upon solidification.

The evolution in technology lead to the development of various advanced welding processes to minimize various welding defects in order to produce a sound quality weldment. The literature review is mainly concerned with different issues related to the joining of Ni-based superalloy (Inconel 718) and austenitic stainless steel (AISI 316L) by various welding techniques. Fusion welding involves various complex thermo-physical phenomenon such as localized heating, melting, cooling and solidification, which are responsible for producing a good quality weld. The interaction of high temperature heat source with the substrate material causes significant metallurgical changes around the weld area and affects the weld integrity. Similarly, fusion welding of Inconel 718 is not utterly free from defects, but it can be minimized by taking required precautions during solidification and post weld heat treatment processes. The segregation of Nb, Mo and Ti from the matrix and formation of different metal carbides and intermetallic phases (i.e., Laves phase) in the fusion zone upon solidification are the major challenges of welding Inconel 718 even after many decades of its invention. Formation of these secondary phases results in defects like solidification cracking and micro fissuring in the fusion zone (FZ) and heat affected zone (HAZ). Hence, the formation of secondary phases during welding affects the component performance when subjected to different loading conditions and may cause earlier breakdown of the entire system. This has a

larger impact especially in the critical applications like rocket propulsion system in aerospace industries and may lead to failure of the mission it is assigned.

Experimental investigations are necessary for optimizing the welding process parameters to obtain a defect free weld with superior mechanical properties. One important parameter that distinguishes all fusion-welding processes from each other is the intensity of the heat source used to melt the parent material to make the joint. The surface temperature of the base material during welding is a function of the surface power density and the time. As the power density of the heat source increases, the heat input to the workpiece that is required for welding decreases. Less heat input during the welding process leads to less metallurgical and structural inhomogeneity in the welded components. When the joining surfaces are exposed to a low intensity heat source, before the melting can occurs a large amount of heat is conducted away into the bulk of the workpiece. Thus, an excessive heating of the workpiece is required to create the molten pool. Excessive heating has detrimental effect as it can damage, weaken and distort the final component due to non-uniform cooling cycles. Hence, the overall aim behind the literature review is to gain an understanding of the effect of various welding techniques and its influence on weld solidification morphology and mechanical properties for similar and dissimilar combination of materials.

2.3 Weldability of Inconel 718

Inconel 718 is one of the widely used Ni-Fe based superalloy in aerospace and power generation industries, due to its exceptional mechanical properties and oxidation resistance at elevated temperature (up to 650 °C) and corrosive environment respectively (Ram et al., 2005). The composition of Inconel 718 is balanced with more than twenty major and minor alloying elements. The major alloying elements like Cr, Mo, Fe and Co are added in the superalloy for solid solution strengthening due to similar atomic radii to that of Nickel. The complex composition of Inconel 718 with high alloying elements results in formation of various secondary intermetallic phases during welding and casting processes. Due to the mismatch in atomic radii and solubility, segregation of heavy elements towards interdendritic region during solidification process is a well-known phenomenon especially for the superalloys. In Inconel 718 certain alloying elements like Nb, Ti, Mo and Al in the matrix leads to formation various carbide/carbonitrides and intermetallic phases. Hence, controlling the segregation level in

boundary region during melting and solidification is critically significant for the overall strength of welded component, specifically for the material to be used in aerospace and defense applications (Manikandan et al., 2015).

The advanced welding techniques are known for their high power density heat source that are capable of achieving a deeper weld penetration in a single pass without causing much geometrical distortion compared to conventional arc welding techniques. Inconel 718 possess good weldability as compared to other nickel-iron based superalloys (Hong et al., 2008). This is mainly due to sluggish precipitation kinetics of γ" (b.c.t. Ni_3Nb) strengthening phase which provides resistance to strain-age cracking (Kuo et al., 2009; Vincent, 1985; Zhao et al., 2008). The main challenge during fabrication of Inconel 718 is its vulnerability to solidification cracking and microfissuring (liquation crack) in the fusion zone (FZ) and heat affected zone (HAZ) during the welding process as shown in Fig. 2.1 (Cao et al., 2009; Zhang et al., 2013). The cause of these defects are mainly due to the micro segregation of important alloying elements to the interdendritic boundaries that leads to formation of different metal carbides (NbC and TiC) and brittle intermetallic Laves phase. The metal carbides produces intergranular liquid film when subjected to thermal cycles and may cause grain boundary embrittlement at elevated temperature (Tucho et al., 2017; Nastac and Stefanescu, 1996; Chen et al., 2001; Mei et al., 2016).

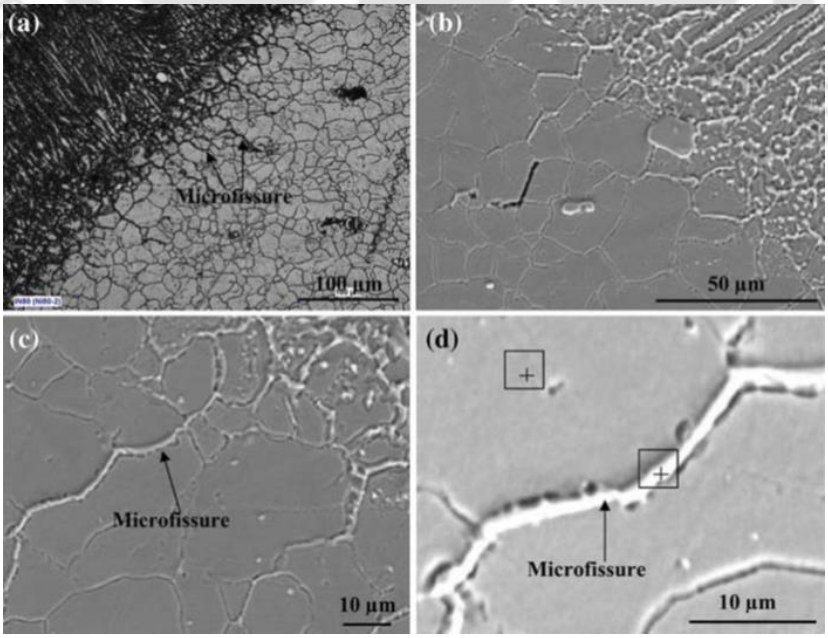

Fig. 2.1 Showing HAZ micro fissures in laser welded Inconel 718 (Cao et al., 2009)

The Laves phase basically forms during the terminal stage of solidification with a hexagonal close-packed (HCP) structure. It has a stoichiometry of A_2B with Ni, Cr, Fe in the place of A and Nb, Mo, Ti in the place of B. It is a brittle intermetallic phase and primarily formed due to strong segregation of Nb during the solidification process (Mei et al., 2016). It has been confirmed that continuous chain of these secondary phases have detrimental effect on ductility and rupture life, as it produces sites for micro crack initiation. Fig. 2.2 showing the Laves phase along with the crack generated near to it, and the corresponding EDX analysis proved enrichment of Nb, Al and Ti in the Laves phase and crack surface (Ye et al., 2015). Hence, distribution and volume fraction of these phases highly affect the mechanical properties of the joint as it consumes a significant amount of useful strengthening alloying elements from the metal matrix, and cause early failure of the component during service (Janaki Ram et al., 2005). Thus, many comparative studies were mainly performed between various advanced welding techniques like gas tungsten arc welding (GTAW), electron beam welding (EBW) and laser beam welding (LBW) to produce sound quality weld by minimizing the Nb segregation and Laves phase formation in the interdendritic regions (Gobbi et al., 1996; Janaki Ram et al., 2004; Manikandan et al., 2014; Radhakrishna and Rao, 1997; Thavamani et al. 2018).

The volume fraction of these deleterious phases and the segregational behavior in the FZ and HAZ were found to be a function of heat input and cooling rate followed during the welding process. Advanced welding techniques like LBW and EBW were found to have beneficial effects on Laves phase formation and mechanical properties of the welded joint as compared to the conventional welding techniques due to controlled and regulated low heat input and subsequent high cooling rate by these welding processes. Radhakrishna and Rao (1997), studied the segregational behavior of Inconel 718 produced by gas tungsten arc welding (GTAW) and electron beam welding (EBW) processes where a wide variety of thermal characteristics exist. The tendency of Laves phase formation was found to be greater in GTAW process as compare to low and concentrated heat input/high cooling rate EBW process. The weldment produced by gas GTAW have witnessed a continuous chain of Laves particles as compared to discrete morphology in the electron beam weld. The lower amount of Laves phase in EBW produces relatively better creep properties as compared to the GTAW weld. The liquid film at the grain boundaries promotes cracking during weld thermal cycle because of constitutional liquation of either Nb-rich carbides or Laves phase in GTA welded

structure (Thavamani et al., 2018). Gobbi et al., (1996), compared the microstructural characteristics between Nd-YAG pulsed laser and CO_2 laser welding process on the basis of heat input and cooling rate. With higher cooling rate, the secondary dendritic arm spacing decreases and produce a finer structure, and in effect, it hinders heavy segregation and formation of deleterious phases in the interdendritic areas. Janaki Ram et al., (2004), showed by using pulse GTAW process, the heat input can be minimized and the solidification rate can be further improved to obtain the refined grain morphology and lower Laves phase formation. Lower segregation and refined microstructure not only improves mechanical properties of the welded joint but also improves the post weld heat treatment (PWHT) response for Inconel 718. Thavamani et al., (2018), applied ultrasonic vibration during GTAW process of Inconel 718 and indicated that a significant reduction in crack sensitivity along with the dendritic arm spacing was possible.

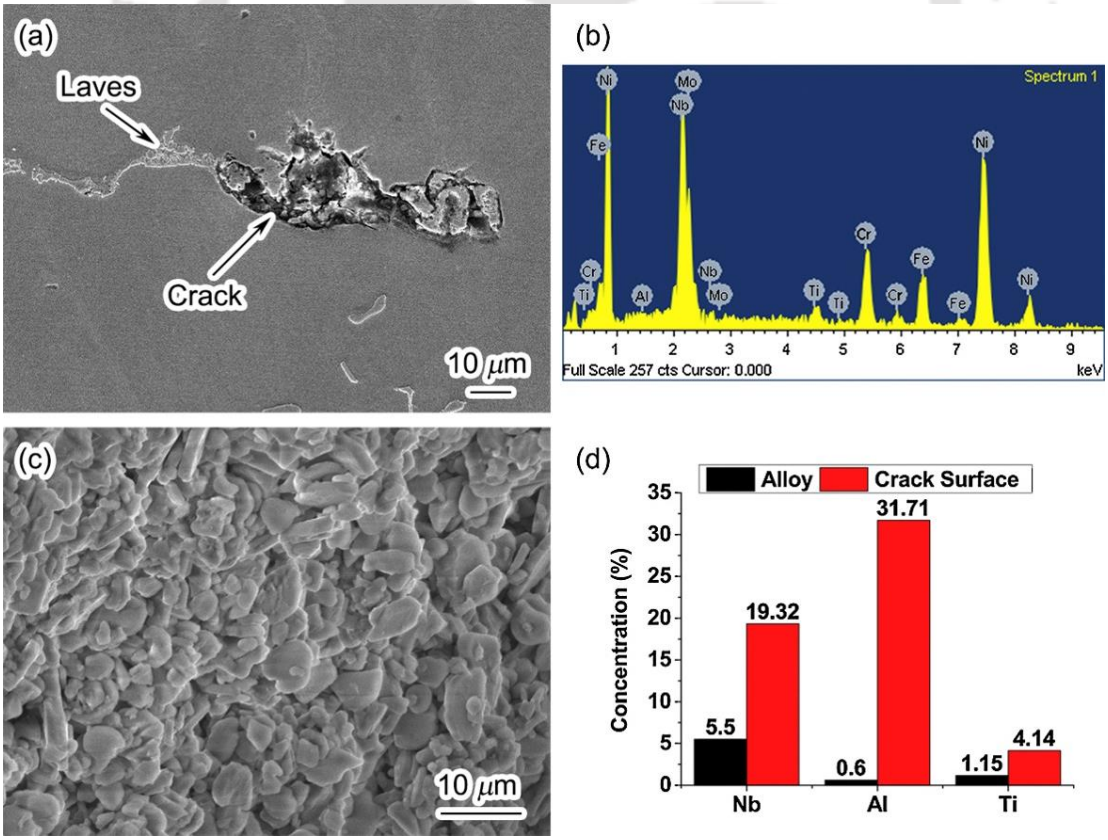

Fig. 2.2 (a) SEM cross section image of the crack in the HAZ (b) EDX spectrum of the Laves phase (c) SEM image of the crack surface, and (d) EDX elemental content analysis of the crack surface (Ye et al., 2015)

2.4 Post-weld treatments of Inconel 718

Fusion welding is one of the crucial fabrication process adopted by aerospace industries to produce complicated structures without altering the material property. But the involvement of high temperature heat source during welding induces microstructural heterogeneity in the fusion area. As a result, it is essential to eliminate the inhomogeneity across the welded component through suitable design of post weld heat treatments. Inconel 718 solidifies in dendritic mode over a wide solidification range of 164°C during the fusion welding process. Hence, the segregation of useful alloying elements like Nb, Mo, and Ti happens in the weld zone and results in the enrichment of these elements in the interdendritic region at the time of solidification. The presence of brittle intermetallic phases like Laves in the weld zone microstructure has a detrimental effect on mechanical properties (tensile and rupture strength) (Mei et al., 2016). As the formation of these phases depletes a significant quantity of useful strengthening elements (i.e., Nb, Mo, and Al) from the metal matrix, it hinders the precipitation of principal strengthening phase γ" (i.e., DO_{22} ordered- Ni_3Nb with BCT structure) and γ' (i.e., Ni_3 (Al, Ti) with FCC structure) in the matrix (McAllister et al., 2016; Phillips et al., 2012). As a result, the mechanical strength of the component deteriorates (Qi et al., 2009). Apart from the strengthening phases, intergranular δ particle (DO_a ordered- Ni_3Nb with orthorhombic structure) also plays a pivotal role in obstructing the sliding of grains during loading. Hence it contributes to enhance the strength of the component (Kuo et al., 2009). The low melting point intermetallic phases in the fusion zone also provide favorable sites for micro-crack initiation, which further in-service condition propagates and cause early failure of the components (Prabaharan et al., 2014).

It is observed that the Laves phase can be dissolved back to the bulk solution by proper design of post-weld heat treatments of the welded component. Nevertheless, quite restricted work has been perceived on the post-weld solution, and double aging treatment of Inconel 718 weld to reduce the effect of Nb enriched intermetallic phases. Ram et al., (2005) observed limited dissolution of Laves phase and Nb segregation in the fusion zone with solution treatment (ST) at 980ºC for 20 min. Then the solution treated samples were followed by double aging treatment (AT) at 720 ºC/8 h and 620ºC/8 h for precipitation of primary (γ") and secondary (γ') strengthening phases, respectively. The post-weld treatments result in the enhancement of the mechanical properties of the welded joint. Gobbi et al., (1996) found that

at a temperature above 1038ºC, the Laves phases were completely dissolved into the solution leaving only NbC in the fusion zone. The thorough dissolution of the Laves phase was witnessed at a solution treatment temperature of 1080 ºC for 1 h (Madhusudhana Reddy et al., 2009). In contrast, the complete dissolution of intermetallic phases was reported at 1165 ºC for a range of 5 min to 24 h depending on grain size (Thompson et al., 1986). It is obvious that the complete dissolution of intermetallic phases makes an extensive volume of principal elements available in the matrix for the precipitation of various crucial strengthening phases. Niobium is the major element of the Laves phase, and by dissolution, it precipitates into γ', γ'' strengthening phase and δ particles during the aging treatment (Shi et al., 2019). Fig. 2.3 showing precipitation of δ phase (Ni_3Nb) in the grain boundary of Inconel 718 material after solution treatment at 1095 ºC followed by aging at 955 ºC for 3.5 h (Kuo et al., 2009). Theska et al., (2018) reported an improvement in the yield strength (of 10%) of Inconel 718 by implementing direct aging (DA) treatment contrary to standard solution annealing and aging treatments. Hence, the improvement in mechanical properties can be tailored through metallurgical properties by suitable post-weld treatments. In most of the reported works, post-weld treatment holding time varies between 16 h to 100 h depending upon the holding temperatures (Banerjee et al., 2005; Qian and Lippold, 2003). However, a higher holding time at the peak temperature increases the operational cost by many folds, as a result optimization of the post weld treatment need to be addressed. Further, the effect of different aging temperatures on precipitation morphology and its impact on weld tensile properties and hardness distribution is to be investigated.

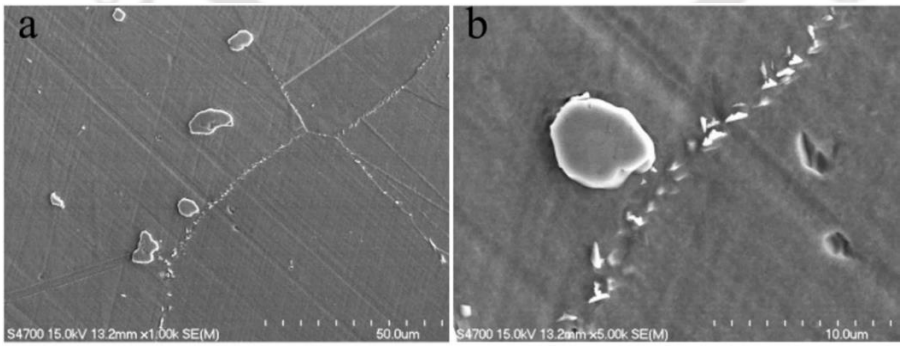

Fig. 2.3 SEM images showing precipitated carbides and platelet δ phase at the grain boundary after solution and aging treatment (Kuo et al., 2009)

2.5 Feasibility of dissimilar welding

Welding and joining of dissimilar combination of materials significantly reduces the component cost by reducing the volume of expensive material without sacrificing their service condition. The bimetallic combination of Inconel 718 and AISI 316L extensively find their applications in aerospace industries, chemical processing industries, oil industries, nuclear and gas power stations for making various hot section components (Bansal et al., 2016). Specifically, in compressor rotor, the high pressure and low pressure stages are made of Inconel 718 and austenitic stainless steel, respectively (Henderson et al., 2004). Dissimilar welding is always a challenging task due to the variation of composition and thermo-physical properties, which may result in metallurgical incompatibility between the metals to be joined. This issue is also associated with the Inconel 718 and AISI 316L bimetallic combination. The incompatibility between these materials is reflected by the formation of various intermetallic phases during fusion welding process which leads to the formation of micro fissuring and cracks in heat affected zone (HAZ) and fusion zone (FZ) (Lippold and Savage, 1982; Radhakrishnan and Thompson, 1992). Fig. 2.4 showing the formation of such micro-fissures or liquation cracks in Inconel 718 side HAZ during the laser welding with AISI 416 martensitic steel (Ramkumar. et al., 2019). The time–temperature profile of the welding technique influences the formation of various Nb based brittle intermetallic phases such as NbC and Laves in the inter-dendritic regions of Inconel 718 weld. In AISI 316L, formation of δ ferrite in a range of 3% to 9% reduces the tendency of hot cracking, but higher percentage of δ ferrite reduces the creep life along with corrosion resistance (Kar et al., 2017). These intermetallic phases are mainly responsible for the hot cracking of the weld during solidification. These defects are not entirely avoidable irrespective of the welding techniques but can be reduced significantly. Welding of Inconel 718 at a high cooling rate and low molten volume reduces deleterious intermetallic phases, which form readily when laser or electron beam welding processes are used (Radhakrishna and Rao, 1997). However, conventional arc welding processes are proven to produce sound joint properties for these bimetallic combinations. Ramkumar et al. (Ramkumar et al., 2014; Ramkumar et al., 2017) have reported successful welding of this bimetallic combination by using gas tungsten arc welding (GTAW) process with different filler materials. The mechanical properties achieved from pulse current welding processes were better than those from constant current welding processes due to well-

controlled grain growth and grain refinement from the pulse current. Kumar et al., (2015) demonstrated that the GTAW in a pulse mode reduced the formation of different intermetallic phases during the welding of Inconel 625 and AISI 316L stainless steel materials. Bansal et al., (2016) welded Inconel 718 and AISI 316L with Inconel 718 powder as filler material between the faying surfaces using micro wave hybrid heating process and reported good joint strength of the weld component. Apart from welding techniques, by using filler materials of suitable composition (i.e. with less Nb content) may also help to reduce the formation of solidification cracks by reducing the formation of intermetallic phases (Prabaharan et al., 2014). Hinojos et al., (2016) have used electron beam based additive technique to avoid the use of filler material for joining Inconel 718 and AISI 316L. It is reported that good metallurgical bonding with less thermal distortion in the base material is achieved. Although, the application of this bimetallic combination at high temperature is obvious, the selection of welding technique and proper filler composition for producing a defect-free dissimilar weld structure is a challenging task.

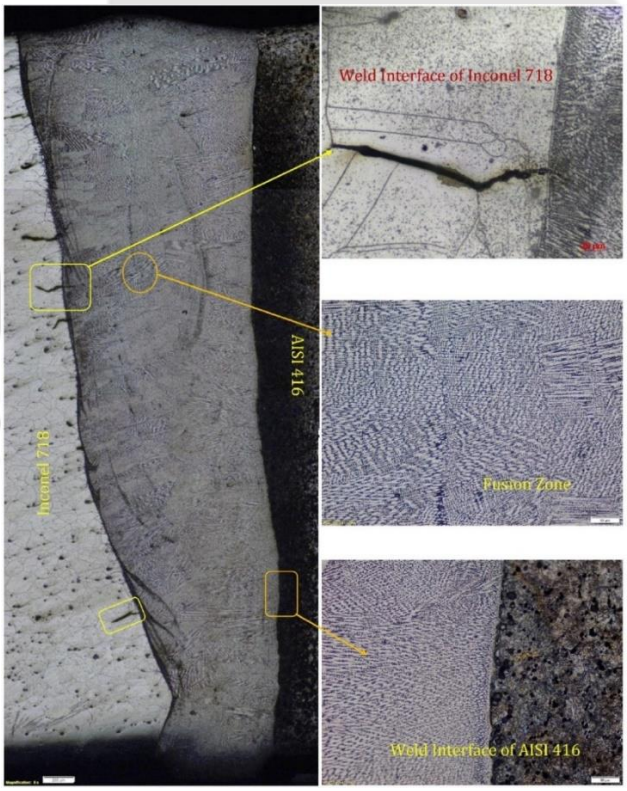

Fig. 2.4 Micrograph of Inconel 718 and AISI 316L laser weld bead showing formation of liquation cracks (Ramkumar et al., 2019)

The welding of this bimetallic combination is mainly performed by using GTAW process with a filler material of intermediate composition. If the composition of filler wire is not properly chosen, then it may trigger segregation of various useful elements from the metal matrix and can increase the intermetallic formation in the FZ and can severely affect the mechanical properties of the component. Ramkumar et al., (2014) revealed remarkable improvement in tensile strength and ductility when filler material with higher Ni, Ti and Cu content is used. Hence, selection of proper filler material is another challenging task that needs special attention for producing a sound quality weld. Prabaharan et al., (2014) used three different filler wires with a negligible Nb content to weld Inconel 718 and AISI 316L bimetallic combination using GTAW process. The presence of NbC phase in the HAZ of Inconel 718 side, (Nb, Ti) C in weld interface and Nb and Mo rich phases in the core and dendrites are witnessed. Bansal et al., (2016) demonstrated the presence of Laves, δ (Ni_3Nb) and various other carbides like NbC, TiC, Cr_3C_2 and $Cr_{23}C_6$ when welding was performed using Inconel 718 powder as interfacing layer. These intermetallic are mainly responsible for producing micro-fishers in the FZ and cause early failure of the weld when subjected to tensile loading. When filler material is used to produce weld, the composition and deposition technique becomes mainly responsible for the micro-structural morphology, intermetallic formation and corresponding effect on the mechanical properties. As a result, selection of proper filler material with a compatible welding technique to weld this material combination is a challenging task. Hence, the primary aim of the current study is to avoid the complexity of the welding processes, which is accomplished by avoiding the use of filler material during the welding. So it's become necessary to understand the micro-structural evolution and mechanical strength of the welded components, when joints are produced without using any filler material (i.e., autogenous welding).

2.6 Solidification kinetics and impact on weld microstructure

The defects during fusion welding are encouraged by the formation of intermetallic phases, that leads to solidification cracking and/or liquation crack during the course of joining process (Cao et al., 2009). These welding defects are not entirely avoidable irrespective of the welding techniques but can be reduced significantly. Solidification cracks generally occur during the terminal stage of solidification (i.e., solid fraction (f_s) close to 1), when the thin film of liquid

between two coherent solid-phases ruptures due to tensile stresses caused by thermal contraction (Davies and Garland, 1975). The range of solidification temperature along with the volume of solute concentration in the liquid phase mainly affects weld cracking susceptibility (Kou, 2003). This can be reduced significantly by controlling the micro-segregation of useful alloying elements that trigger the formation of low melting point secondary phases during solidification (DuPont et al., 1999). Many researchers have reported the formation of Laves phase and metal carbides (MC- type) as minor microstructural constituents in the Inconel 718 fusion zone (DuPont et al., 1998; Wang et al., 2009). The solidification path corresponding to Inconel 718 is developed, based on thermal studies and compositional measurements. The solidification reaction temperatures measured by differential thermal analysis and the sequence for Inconel 718 is shown in Fig. 2.5 (Cieslak et al., 1990; Knorovsky et al., 1989). The microscopic analysis of Inconel 718 fusion zone reveals the presence of two phase structure consisting of FCC γ- matrix with HCP Laves phase (a = 0.467 nm, c = 0.771 nm) in lamellar configuration or with blocky shape FCC metal carbides (i.e., NbC or TiC) (a = 0.443 nm). The solidification begins with transformation of liquidus surface into the γ + liquid region. The liquid near to S/L interface is enriched with the segregation of Nb and C as the solidification proceeds. With increase in the Nb concentration in liquid, the transformation finished up with γ-NbC eutectic reaction near 1525 K. With the γ-NbC eutectic reaction, the liquid phase gets depleted with C and enriched with Nb. As a result, the local liquid concentration shifts back towards the γ phase, hence re-entering the Liquid + γ region. Further, the enrichment of Nb would continue in the remaining liquid and finally terminate the solidification process with non-invariant γ + Laves eutectic reaction at around 1471 K. Hence, the solidification sequence of Inconel 718 is (1) proeutectic γ, (2) eutectic γ-NbC, (3) γ solidification continued, and (4) solidification terminates with γ-Laves reaction at 1471 K (with nearly 19 wt.% Nb). The solidification would have completed with γ-NbC eutectic reaction, if the C content is higher and lower Nb content in the alloy. Various researchers concluded from the solidification analysis, the elements Fe, Cr, Ni, Al and Ti strongly partitioned towards the γ matrix. Whereas Al and Ti segregates towards the liquid as the solidification progress, which is mainly due to the lower partition coefficient ($k < 1$) of these elements. Similarly, the Nb partitioned strongly to the Laves phase. The volume of γ + Laves eutectic constituent can be influenced by the Nb

segregation in the bulk and segregation of Nb can be influenced by the solidification rate and eventually can affect the solidification sequence.

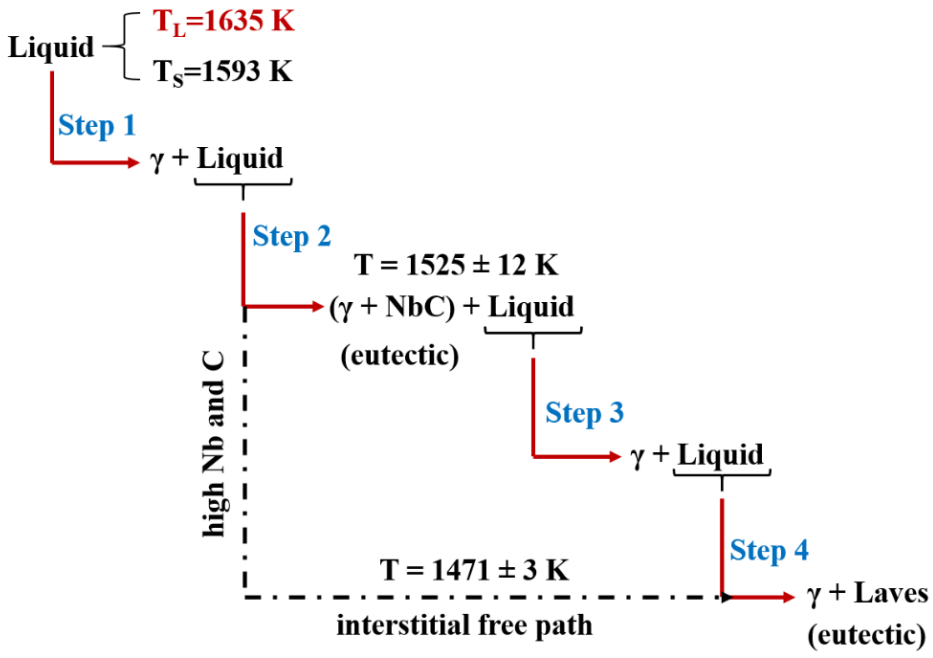

Fig. 2.5 Solidification path of Inconel 718 (Knorovsky et al., 1989)

The size, shape and distribution of the secondary phases (i.e., Laves and carbides particles) are highly influenced by the solidification mode of the fusion zone. The mechanical properties of the welds are contributed by these characteristics of the secondary phases. The melting point of intermetallic Laves phase is lower than the γ-matrix as a result it produces a microstructural weakness in the weld when subjected to elevated temperature (Radhakrishna et al., 1995). The Laves phase also act as favorable sites for micro-crack initiation and propagation and affects the tensile, rupture, fracture toughness and rupture properties along with fatigue life of the welded components (Mills, 1984; Reddy et al., 2009; Sivaprasad and Raman, 2007). In addition, it also depletes the precipitation potential of γ" phase by consuming the principal alloying elements from the bulk. This results in weak tensile strength of the component. Hence, initial size and dispersion of the Laves particles need be regulated by the solidification parameters (temperature gradient and solidification velocity), and in turn the mechanical properties of the welded component can be improved (Antonsson and Fredriksson, 2005). The impact of solidification variables *G* (temperature gradient) and *R* (solidification

growth rate) on weld microstructure is shown in Fig. 2.6 (Kou, 2003). The whole process of solidification is governed by the solidification parameters (*G.R* and *G/R*). The product of *G* and *R* mainly regulates the scale of solidified structure (i.e., coarser or finer), whereas ratio between them (*G/R*) decides the mode of solidification of the produced weld bead. A higher (*G/R*) produce a planar mode of solidification, whereas lower magnitude leads to equiaxed dendrites. With increase in *(G.R),* which is also known as the cooling rate, the solidification time reduces and results in finer weld microstructure (Rocha et al., 2003; Whitesell et al., 2000).

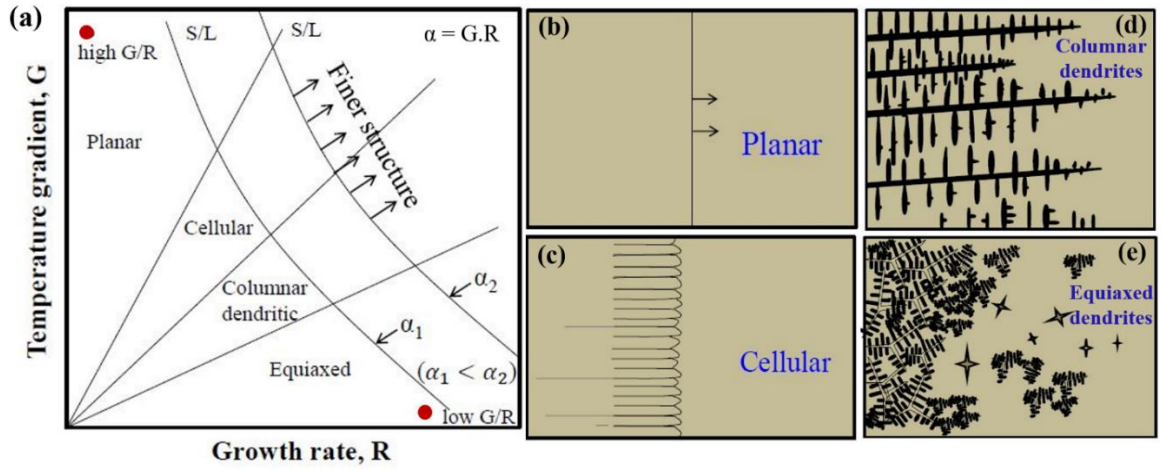

Fig. 2.6 (a) Impact of temperature gradient and solidification growth rate on morphology and size of solidified structure, and (b, c, d, e) schematic of different solidification mode (Kou, 2003)

Inconel 718 is a highly alloyed superalloy as a result it solidifies over a wide range of temperature; thus, dendritic mode of solidification dominates in Inconel 718 fusion zone (Manikandan et al., 2019). The solute redistribution during solidification triggers micro-segregation across the interdendritic region and around the dendritic arms hence produces a chemical inhomogeneity in the weld. It has been reported that the fine discrete and equiaxed microstructure are less susceptible to micro fissuring and micro-cracking as compared to the columnar structure (Janaki Ram et al., 2004). The advantage of equiaxed microstructure is mainly attributed to better adaptation of strain, liquid feeding, filling up of inceptive micro-cracks, and low segregation of impurity elements (Manikandan et al., 2019). A continuous chain of Laves network significantly reduces the tensile strength and ductility (Schirra et al.,

1991). Hence, the continuity need to be broken by optimizing the process parameters during the welding process. Refinement is achieved by implementing various conventional techniques like current pulsation, providing vibration and by electromagnetic stirring of the weld pool (Clark et al., 2010; Dvornak et al., 1991; Liao et al., 2007; Watanabe et al., 1990). Apart from that, the heat input (J/mm) and speed (m/s) during welding process affects the solidification mode. For a constant heat input, the solidification parameter *(G/R)* decreases with increasing the welding speed and vice versa (Savage et al., 1968). In addition, for a constant solidification growth rate the cooling rate *(G.R)* increases with decrease in the heat input.

2.7 Heat transfer model

Direct experimental investigation during fusion welding is extremely expensive and often impossible because of the complexity of the process, size of the weld pool and presence of high convention current within small weld pool. The recent advantages in computational efficiency boosts the development of numerical model using finite element (FE) method to solve the thermal problem. The heat transfer model predicts the temperature distribution and cooling rate during the fusion welding process. With the development of an accurate model, experimentally immeasurable parameters with respect to the fusion zone can be estimated easily. In fusion welding process, the important parameters that need to be estimated are (a) peak temperature achieved at weld pool, (b) thermal history at each location in the fusion zone and heat affected zone (HAZ), and (c) solidification parameters corresponding to different welding conditions. In the conduction mode heat transfer model, there are many factors that affects the shape and size of weld pool, in which the heat source model is commonly thought to be the most important one. Hence, the selection of proper heat source model in conduction mode heat transfer analysis plays a vital role in accurately predicting the weld shape and size, thermal cycles and cooling rates. In this section, different types of heat source models and their usability in different welding processes are explored.

2.7.1 Heat source model

The main idea of the heat source representation is to replace the physical process with an appropriate surface or volumetric heat flux for numerical computation to obtain an accurate

temperature profile during the welding process. In principle, the interaction of arc or laser with substrate materials is mathematically represented as a heat source. A volumetric heat source is often used in conduction based heat transfer model, to compensate the influence of convective heat transport in weld pool (Li et al., 2013). The precise description of the applied heat source and the appropriate selection of the relevant parameters are essential to the numerical simulation of thin-sheet welded structures (Sun et al., 2014). Rosenthal (Rosenthal, 1946) has applied Fourier heat conduction theory first time in 1940's to solve a moving heat source problem in fusion welding. It is the most popular analytical method to calculate the temperature field of the solution domain when subjected to a moving heat source. Rosenthal's model assumes a point and line source of heat, which fails to predict the temperature at the point or line of heat source. Even, the temperature distribution in fusion zone (FZ) and in the heat-affected zone (HAZ) lacks in accuracy because of its infinite temperature assumption at the heat source. To predict the temperature near the arc, Pavelic et al. (Pavelic, 1969) first time suggested distributed heat source (W/m^2) on the surface of the workpiece instead of a point or line heat source. The temperature fields for welding process became more accurate than Rosenthal's solution. Many researchers further combined the Pavelic's disc model with the Finite element analysis to obtain better temperature distributions in the FZ and HAZ. Friedman (Friedman, 1975), suggested a moving heat source for the Pavelic disc and incorporated with a moving coordinate system to integrate conventional arc welding techniques with the numerical model. Few authors have suggested distributing the heat flux throughout the molten pool to reflect more accurately the digging action of the arc, which transport the heat below the weld pool surface (i.e., thickness direction). In order to address all the issues and shortcomings, Gaussian distributed ellipsoidal heat source model was proposed by Goldak et.al (Goldak et al., 1984). It was observed that the temperature gradient in front of the ellipsoidal heat source was not as steep as expected and gradient at the trailing edge of the molten pool was steeper than the experimental value. Therefore, the application to semi-ellipsoidal heat source is limited to only stationary welding i.e. for spot welding processes. Goldak et al. (Goldak et al., 1984) further used a double ellipsoidal heat source model for a moving welding torch. It is a combination of the two ellipsoidal; one in the front quadrant of the heat source and the other in the rear quadrant that maintains C^1 continuity. Thus, double-ellipsoidal heat source model is suitable for both low penetration as well as deep penetration welding

processes. However, double-ellipsoidal heat source model is most popular because of the flexibility in formulation and adaptability in many arc and laser welding processes. It has been shown that a Gaussian distribution of power density of a double ellipsoid moving heat source along the weld path was convenient, accurate, and efficient for most realistic welds with simple shapes. Weld quality mainly depends upon the weld bead configuration and the final microstructure of the fusion zone, which can be explained based on thermal cycles during the welding process. Hence it is important during the numerical simulation to choose an appropriate heat source model for better result (Zacharia et al., 1989). Considerable accuracy can be obtained when the ellipsoidal parameters are equal to that of the weld pool size. If the fusion zone differs from an ellipsoidal shape, then other kind of heat source models are utilized to represent weld behavior correctly (Bag and Amin, 2020; Du et al., 2004; Yadaiah and Bag, 2014, 2012). Yadaiah and Bag (Yadaiah and Bag, 2012) studied an efficient estimation of the heat source model parameters, where the optimum ratio of front and rear length of the double ellipsoidal heat source is taken as a function of the welding velocity for a suitable range of welding current and velocity during the linear GTAW process. Du et al. (Du et al., 2004) used a combined heat source model compromising of a Gaussian plane heat source at the top surface and a cylindrical heat source along the thickness direction to simulate the geometry profile of weld pools during laser beam welding for titanium alloys. The results estimated from the model were found good agreement with the experimental results for the weld geometry profile. Yadaiah and Bag (Yadaiah and Bag, 2014) developed an egg shaped heat source model by modifying the ellipsoidal shape to minimize model input parameters compare to other heat source models for the simulation of linear fusion welding processes without violating the non-symmetry heat density distribution. The heat source model was implemented in finite element based heat transfer analysis to evaluate the effectiveness of the model for laser welding and conduction mode GTA welding process. In general, the heat source model accounts the geometric shape of fusion zone and the distribution of heat flux over the predefined geometric shape. Thus, a wide variety of heat source models have been developed to represent laser or arc interaction with the substrate materials.

2.7.2 Conduction based heat transfer model

The geometry of weld pool plays an important role in determining the mechanical properties of weld joints. Accurate information of temperature distribution in the fusion zone

(FZ) and heat affected zone (HAZ) is essential for the prediction of weld time- temperature history and bead dimensions (Jou, 2003). A finite element based transient thermal model can be helpful for obtaining these parameters by considering the effect of conduction, convection and radiation phenomena during the welding process. Robustness of the model can be validated by comparing numerically calculated results with experimental values. To estimate the thermal history during fusion welding process, energy conservation equation is need to be solved. The heat transfer during plasma and laser welding is estimated by the classical heat conduction theory. Conduction based heat transfer models are simpler and computationally economical and yet produce highly accurate results for simple welding techniques (De et al., 2003; Frewin and Scott, 1999; Trivedi et al., 2007). Thus, conduction based heat transfer models are often preferred as compared to the transport phenomena based heat transfer and fluid flow model for smaller weld pool involving rapid melting and solidification. Bag and De (Bag and De, 2010) found conduction based heat transfer models are important when weld geometry is small whereas transport phenomena based heat transfer and fluid flow analysis are more accurate for computed temperature field of comparatively bigger weld pool. De et al. (De et al., 2003) reported a two-dimensional axisymmetric finite element analysis of heat flow for laser spot welding. The analysis was based on conduction heat transfer alone, and applied a double ellipsoidal volumetric heat source to represent the laser beam. They reported good agreement of the predicted temperature isotherms and weld pool dimensions with the experimental results. Wu et al. (Wu et al., 2014) employed conduction based analysis for the keyhole PAW process by using Gaussian distributed heat source. The developed model predicted the weld geometry along with exact location of melt line in the PAW weld. Jiang et al. (Jiang et al., 2016) developed a conduction based heat transfer model for the laser welding of AISI 316L steel by implementing double ellipsoidal and conical heat source model together. The finite element model results of weld bead profile and temperature field have shown good agreement with a small relative error compared to the experimental results as shown in Fig. 2.7. Baruah and Bag (Baruah and Bag, 2017) developed a conduction based model with using an hourglass heat source model for the laser micro-welding of Ti-alloy and observed good agreement of temperature and weld bead profile with the experimentally measured value.

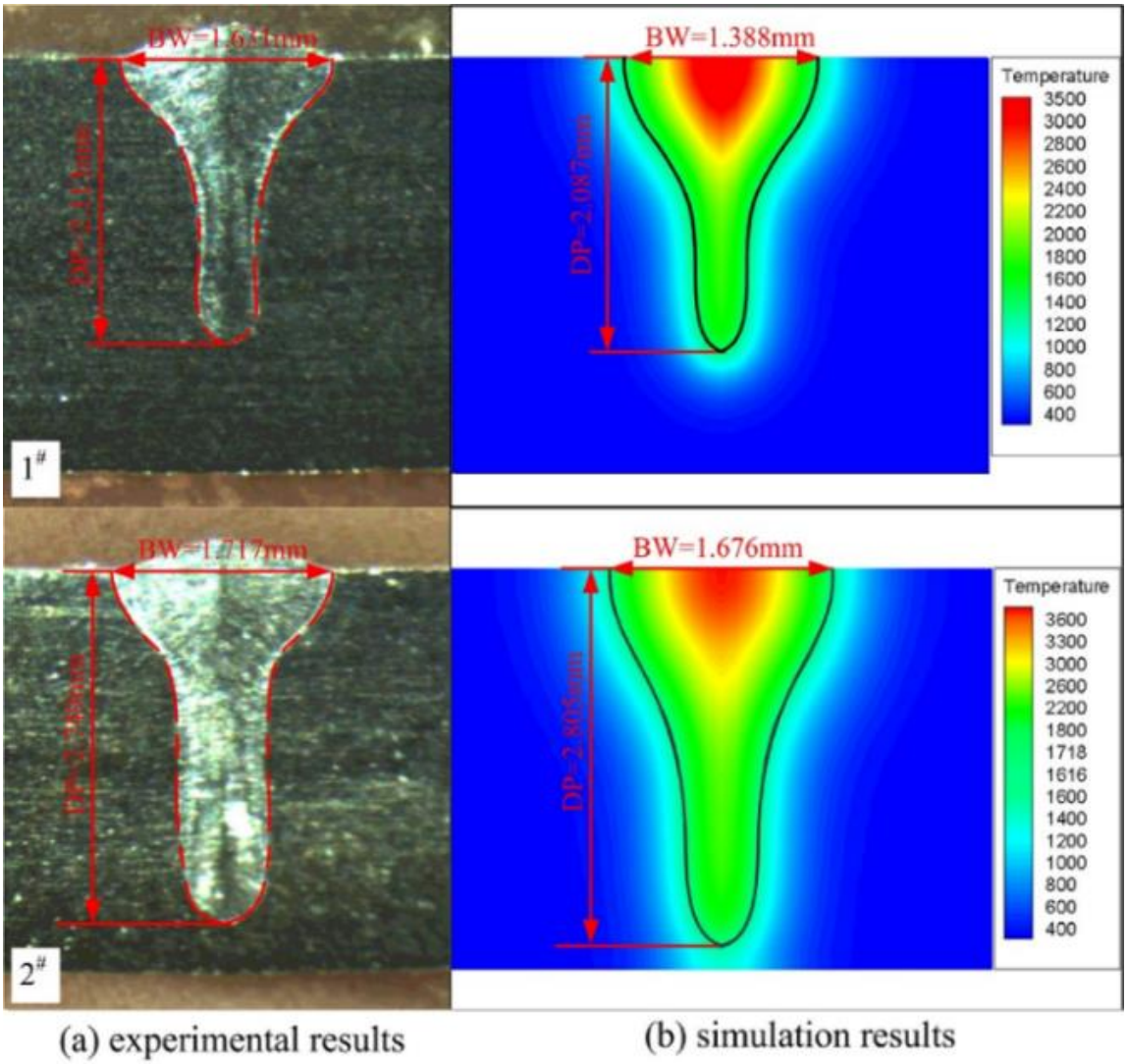

Fig. 2.7 Validation of AISI 316L laser weld with numerical results (Jiang et al., 2016)

Ebrahimi et.al.(Ebrahimi et al., 2016) applied a double ellipsoidal heat flux in a conduction based heat transfer model for the keyhole laser welding of Inconel 625 and AISI 316L dissimilar combinations with specific absorption coefficients for each material, and found the simulated results for the keyhole weld configurations were closer to the true state. The corresponding temperature isotherms are shown in Fig. 2.8. Ranjbarnodeh et al. (Ranjbarnodeh et al., 2012) developed a 3D model to predict the weld-pool geometry and temperature distribution for dissimilar welding (using TIG welding process) of low carbon and ferritic stainless steel using a Gaussian heat source. Due to variation in the thermo-physical properties asymmetry in the weld bead was witnessed in the experimental results and the corresponding consistency in temperature distribution was observed in the numerically

obtained results. For dissimilar welding (aluminum alloy and stainless steel), due to asymmetry in fusion zone, Bag and Amin (Bag and Amin, 2020) implemented a quadruple ellipsoidal heat source model in ultra-short pulse laser welding process to account the non-symmetry energy distribution and reported accurate prediction of weld-pool geometry. However, the explorations on the development of extended version of double ellipsoidal heat source model cratered for full penetration dissimilar welding of thin sheets between Inconel 718 and AISI 316L steel are limited and confined to primitive and in elemental stage.

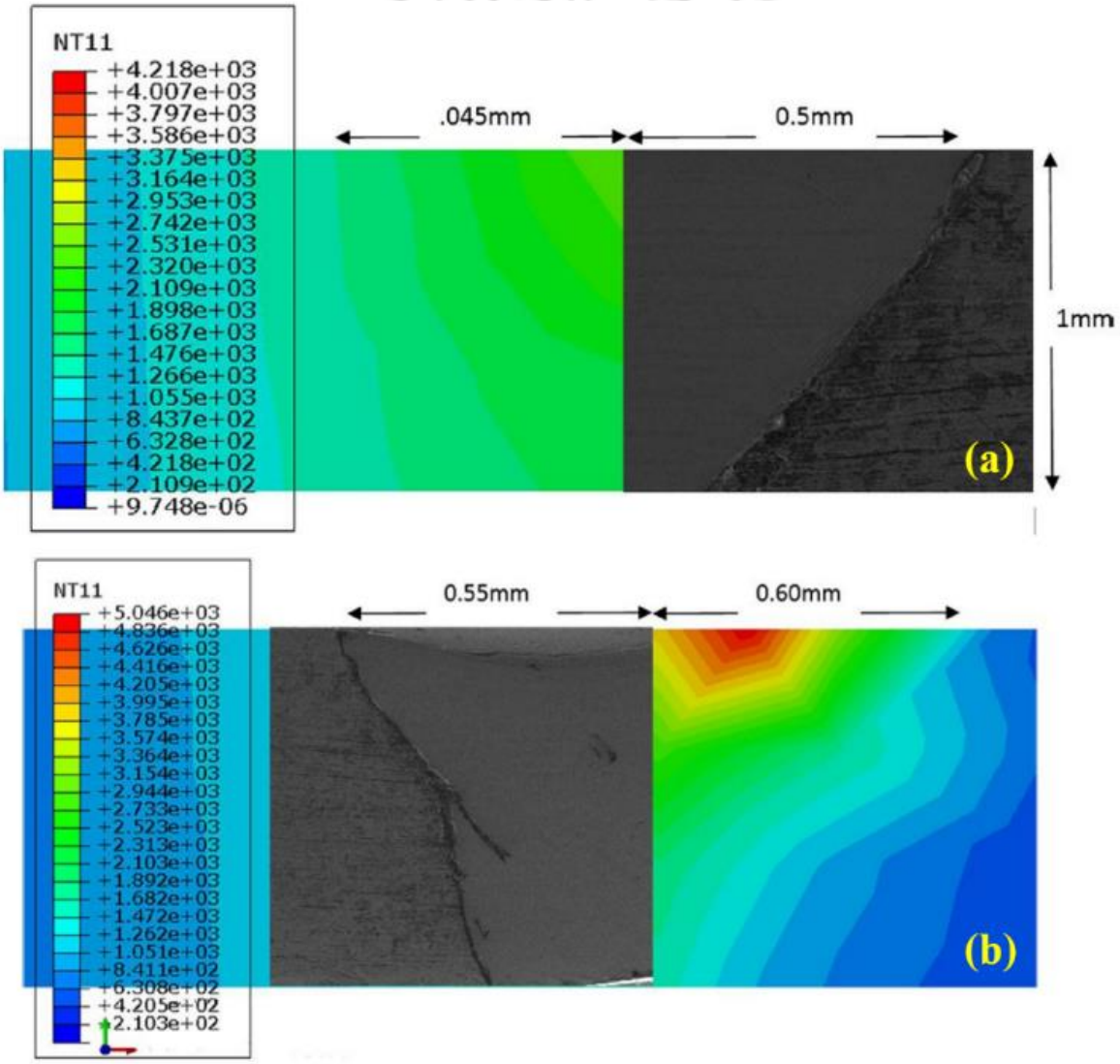

Fig. 2.8 Validation of experimental and numerical dissimilar laser weld (a) Inconel 625 side and (b) AISI 316L side (Ebrahimi et al., 2016)

2.8 Summary

The current chapter describes different challenges during the welding of Inconel 718 in similar and dissimilar configuration (with AISI 316L) from the practical aspects. First, the difficulties associated with similar welding of Inconel 718 is reviewed. A comprehensive part of the chapter is dedicated to address the impact of different welding techniques on metallurgical issues related to Inconel 718 weld. Secondly, the issues related with different post weld heat treatments of Inconel 718 are discussed. Thirdly, the difficulties during dissimilar welding of Inconel with austenitic stainless steel is outlined. Finally, the impact of solidification parameters on weld morphology is discussed and different finite element based numerical model employed to estimate these parameters are discussed. The selection of proper heat source model to represent the welding heat source is a challenging task and its effect on the accuracy of the model to predict the temperature profile during welding is illustrated. In brief, this chapter provides an overview on weldability of Inconel 718 by using different conventional and advanced welding techniques. The metallurgical issues related to morphology, segregation and its impact on joint mechanical properties are extracted from the existing literature and further improvement in the welding technique and weld mechanical properties need to be addressed. The key findings from this chapter are summarized as:

- Researchers have used different high-energy beam welding techniques like EBW and LBW that are advantageous to encounter the segregational problem in Inconel 718. However, these techniques have certain limitations in terms of delicate setup, difficulty in accessing particular area while joining complicated shapes, and high operating cost of these processes. Hence, μ-PAW is considered for the current study, which is known for higher power density due to the constricted arc as compared to other conventional arc welding processes. μ-PAW also possesses excellent arc stability at very low current range as compared to GTAW process. However, there is lack in esteemed literature on μ-PAW of Inconel 718 and the effectiveness of current pulsation on microstructural refinement and solidification behavior.
- It has been realized from the literature survey, by applying suitable volumetric heat source in the conduction mode heat transfer model, accurate temperature field of the FZ and HAZ

can be predicted. However, the issue related to transient thermal model of micro plasma arc welding of thin sheet Inconel 718 is not addressed.

- The literature survey indicates that the intermetallic phases in the welded components can be dissolved back to the bulk solution by proper design of post-weld heat treatments. In most of the reported works, post-weld treatment holding time varies between 16 h to 100 h depending upon the holding temperatures. However, a higher holding time at the peak temperature increases the operational cost by many folds. Therefore, design of suitable post weld heat treatment technique with an aim to optimize the holding time is needed to address. Nevertheless, quite restricted work has been perceived on the post-weld solution, and double aging treatment of Inconel 718 weld to reduce the effect of Nb enriched intermetallic phases.
- It is obvious that the welding between Inconel 718 and AISI 316L combinations are mainly performed by using GTAW process with a filler material of intermediate composition. Where, the selection of welding technique and proper filler composition for producing a defect-free dissimilar weld structure is a challenging task. If the composition of filler wire is not properly chosen, it may trigger segregation of various useful elements from the metal matrix and can increase the intermetallic formation in the fusion zone. It also adversely affects the mechanical properties of the component. Hence, it is important to understand the microstructural evolution and corresponding mechanical properties of welded components when the joints are made without using any filler material. The effect of welding process parameters like welding current and velocity on weld solidification mode and grain morphology are needed to be addressed.
- While many publications related to the study of microstructure and mechanical properties for dissimilar arc welding of Inconel 718 and AISI 316L are available, the implication of high-energy beam source for a thin sheet welding of these combinations of materials is not addressed so far. The solidification mechanism in laser welding for a thin sheet is completely different from the conventional arc welding techniques in terms of cooling rate. The rate of cooling is relatively high in case of laser welding and it depends on the thickness of the materials. Therefore, the variation in solidification mechanism of laser welding compared to arc welding and the corresponding impact on microstructure and mechanical strength is necessary to address.

- The literature indicates that the numerical simulation of the dissimilar material welding can be performed by using a volumetric heat source, which must be asymmetry in nature due to difference in thermo-physical properties. For thin sheets, conduction based heat transfer model is suitable to obtain the time-temperature history of the small fusion zone by neglecting convective flow. The establishment of 3D finite element based thermal model corresponding to similar and dissimilar plasma and laser welding is necessary to address. This will help to reduce the cost and cumbersome experimental effort to analyze the thermal history specifically for weld pool model.

2.9 Scope of the present work

Based on the detailed literature survey of existing work, the objectives of the present work have been summarized as follows.

- The primary objective of the present work is to optimize the welding process parameters out of several trials-and-errors to produce a sound quality weld for thin sheet Inconel 718. Both the variation of pulse parameters and continuous mode of micro plasma arc welding is taken into account. Identification of feasible domain of parameters in the form of process map for successful weld joint is the scope of work here. The effect of pulsation is often neglected by approximating the continuous average current, which is not trivial in small-scale welding process. There is a huge scope to analyze the effect of pulse parameters on solidification characteristics, grain morphology, Laves phase formation and corresponding impact on the mechanical properties of the weld joint.
- A 3D heat transfer model is always advantageous for better understanding of the effect of current pulsation on solidification parameters in micro-plasma arc welding of Inconel 718. The conduction mode heat transfer model with a volumetric heat source is sufficient to predict the temperature distribution, weld pool dimensions and time-temperature history both for pulse and constant current mode of welding.
- The secondary objective of the present work is to optimize the post weld heat treatment process for the Inconel 718 expecting the improvement of the microstructural and mechanical properties of the weld joint. The aim is to reduce the holding time of the post-weld treatment without compromising the mechanical properties of micro-plasma arc welded components. Further, there is a scope of investigation on the effect of different

aging temperatures on precipitation morphology and its impact on strength properties and hardness distribution of a weld joint.

- The welding of dissimilar combinations of materials like Inconel 718 and AISI 316L stainless steel is often performed with a third material. In the present work, an attempt is made to weld Inconel 718 and AISI 316L stainless steel by using micro plasma and CO_2 laser welding processes in autogenous mode. There is a scope to investigate the feasible domain of parameters like welding current, speed and beam power through extensive experiments. The effect of pulse parameters on microstructural morphology through solidification parameters (i.e., *G.R* and *G/R*) and its corresponding effect for improvement of mechanical properties is need to be correlated.
- Dissimilar welding, specifically when Inconel is involved, is often associated with the formation micro crack. Therefore, an investigation is performed to understand the formation of any micro fissure or micro crack and corresponding influence of process parameters.
- The heat source model becomes more complicated in case of dissimilar welding due the difference in thermo-physical properties. Therefore, transient heat transfer model for the micro plasma and laser beam welding process using a suitable heat source representation has to be developed to predict the temperature distribution.

Chapter 3

Experimental Methods

3.1 Introduction

The experimental procedures followed during the thesis work are described in this chapter. Experimental investigation is necessary for optimizing a reliable database of welding process parameters to obtain defect free welds with superior mechanical properties. Fusion welding is one of the widely accepted joining techniques used by fabrication industries to weld a wide range of similar and dissimilar combination of material because of high production rate and cost effectiveness. It involves various complex thermo-physical phenomenon such as localized heating, melting, cooling and solidification that are responsible for producing a sound quality weld. One critical parameter that distinguishes all fusion welding techniques from each other is the intensity of the heat source used to melt the base material to produce the joint. The surface temperature of the base material during welding is a function of the surface power density and time. As the power density of the heat source increases, the heat input to the workpiece required for welding decreases. Less heat input during the welding process leads to less metallurgical and structural inhomogeneity in the welded components. When the joining surfaces are exposed to a low intensity heat source, before the melting can occurs a large amount of heat gets conducted away into the bulk of the workpiece. In the present work, micro-plasma arc welding technique is employed to autogenously weld the Inconel 718 sheets in similar and dissimilar (with AISI 316L) combinations of materials. High power density CO_2 laser source is also applied to weld this

material combination in butt joint configuration. The impact of different welding process parameters on weld geometry, solidification behavior and microstructural morphology are analyzed systematically. In addition to that, different post weld heat treatments for Inconel 718 welds are carried out to improve mechanical and microstructural properties. Fusion welding of Inconel 718 is not utterly free from welding defects, but it can be minimized by taking required precautions during and after the welding process. The interaction of a high temperatures heat source with the weld pool causes significant metallurgical changes around the weld area and affects the weld integrity. Microstructural characterization of the weld zone is performed through optical microscope (OM), scanning electron microscope (SEM), energy dispersive X-ray (EDX) analysis, and X-Ray diffraction (XRD) technique. Microstructural impact on weld mechanical properties are also analyzed through the tensile and Vickers micro-hardness testing for each welding condition. In this chapter different complication related to the welding of Ni-Fe based superalloy (Inconel 718) and austenitic stainless steel (AISI 316L) by micro-plasma or CO_2 laser beam welding techniques are reported.

3.2 Micro-plasm arc welding of thin sheets

In plasma arc welding (PAW) process the coalescence is produced by application of heat produced by a constricted plasma arc. The PAW process can be used in two different operating modes; one is the 'melt-in-mode' refers to low current mode (0.1 to 15 A) of welding which is also called as micro plasma welding. It produces a stable, concentrated arc at low current range, which gives high energy density and low heat input as a result the size of heat affected zone and distortion during welding reduces (Baruah and Bag, 2016). There are some principal welding parameters of PAW which are responsible for producing sound quality welds. These parameters include plasma current, arc voltage, welding speed, shielding gas and its flow rate. The main advantage of the PAW over the conventional welding techniques is the arc stability at low current range which gives it a high level of control on accuracy to produce small scale joining. The experimental setup of micro-plasma arc welding is shown in the Fig. 3.1. Experiments are conducted using 0.05–50 A plasma arc welding machine (MP – 50, EWM, Germany) with direct current electrode negative (DCEN) mode. The plasma torch is kept fixed whereas the base materials are moved with the help of a rail guided platform. Commercial pure argon (99%) gas is used as plasma gas as well as

shielding gas where the flow rate is maintained at 0.4 and 5 lit/min, respectively. A thoriated tungsten electrode of 1 mm diameter is used along with a nozzle standoff distance of 2 mm. The current pulsation during pulse welding is achieved with the help pulse remote as shown in Fig. 3.1(b). The workpieces are clamped in a restrained fixture which is made up of copper (Fig. 3.1c) to achieve high rate of cooling.

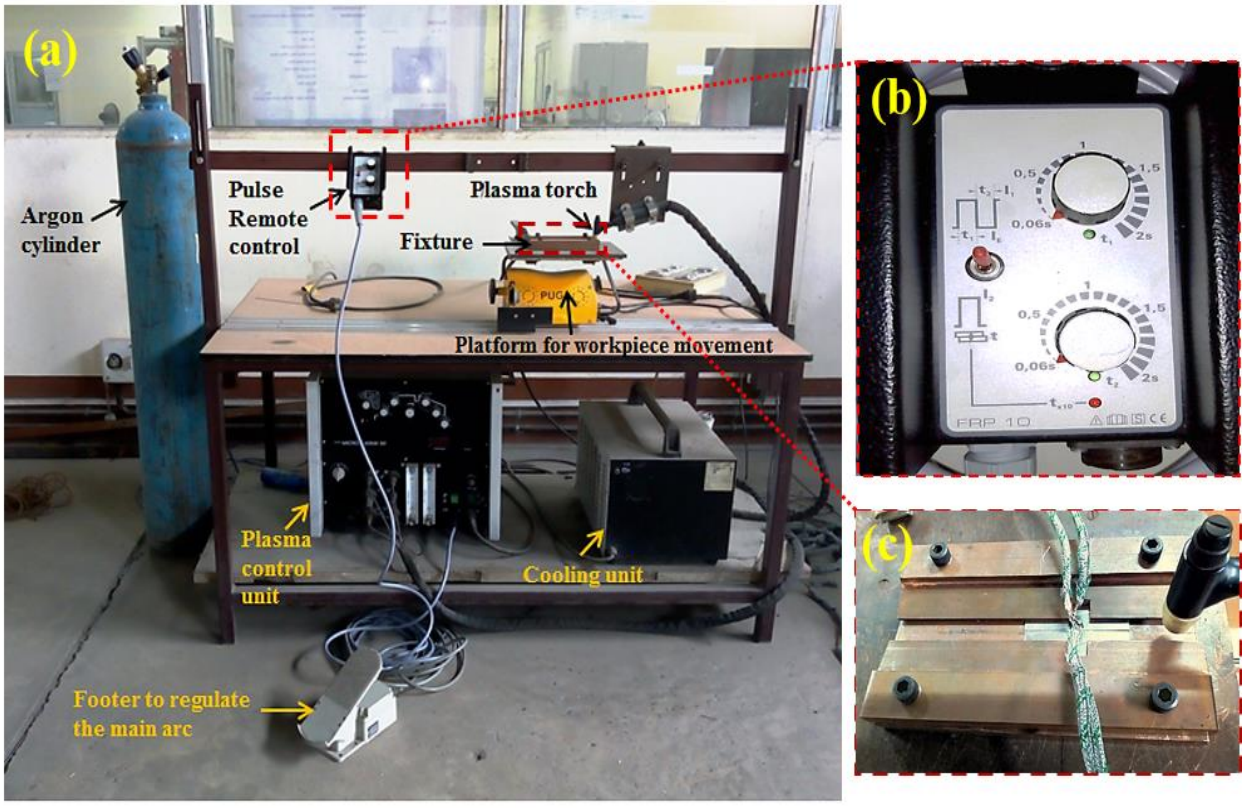

Fig. 3.1 (a) Experimental set-up of micro plasma arc welding process (b) Pulse remote and (c) Copper fixture

3.2.1 Welding of Inconel 718

Solution treated (at 980°C/ 1h) Inconel 718 sheets of thickness 0.7 mm are used to produce autogenous weld. Solution treatment at high temperature was done to obtain a homogeneous microstructure by putting age hardening and carbide constituents into the solid solution. The microstructure of base material is shown in Fig. 3.2(a) and is consists of equiaxed grains with an average diameter of 72 µm (ASTM 4-5). The chemical composition

(wt. %) is obtained by EDX analysis for Inconel 718 and is given in Table 3.1. Chromium, aluminum and silicon are essential for oxidation resistance in Inconel 718. Niobium plays a significant role for improving the strength of Inconel 718, it act as a grain boundary strengthening element by forming Ni_3N_b (γ'') intermetallic compound with the nickel which arrest the slip and creep effectively at elevated temperatures (Janaki Ram et al., 2005). It also contains carbide formers like C, Mo, Nb and Ti that tends to precipitate at grain boundaries and hence reduce the tendency for grain boundary sliding.

Table 3.1 Chemical composition (wt. %) of Inconel 718

Element	Ni	Cr	Nb	Mo	Ti	Al	Si	Cu	Co	Fe
wt. %	51.0	19.2	5.5	3.2	1.1	0.7	0.2	0.2	0.1	Bal.

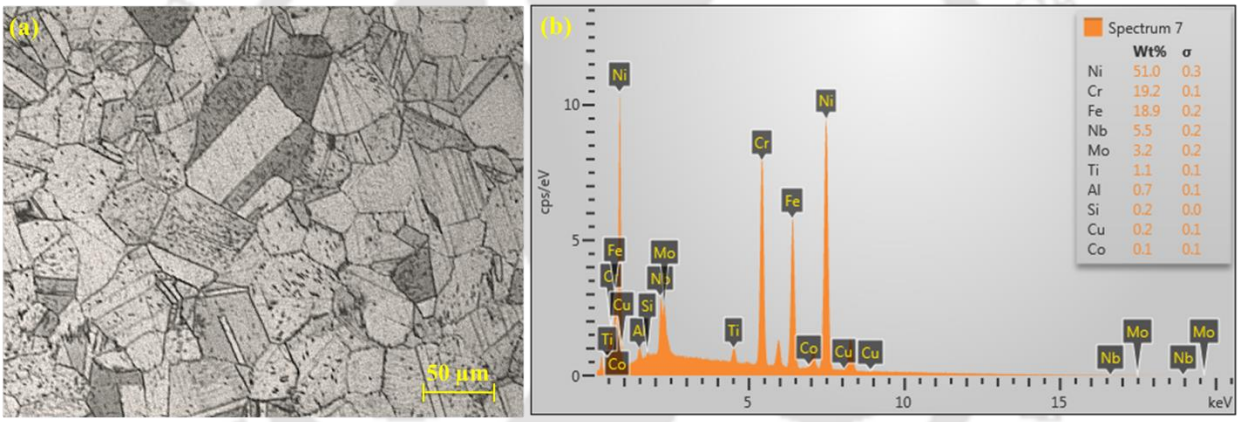

Fig. 3.2. (a) Microstructure and (b) EDX analysis of the base material Inconel 718

It is apparent that with decrease in welding sheet thickness the amount of precaution has to be taken for welding thin sheets increases. Hence, the welding of thin sheets is carried out under carefully selected parameters, as the stable welding conditions exist over a narrow region. Insufficient heat input can produce a partially penetrated weld bead where as excessive heat input may cause partial or full burnout of the base material. Therefore, precise control of the heat input is required during the welding process. Several bead-on-plate welding were also carried out in constant and pulsed current mode over a current range of 10 - 25 amperes by keeping standoff distance and plasma gas flow rate constant to evaluate the proper ranges of process parameters. The welding surfaces are cleaned with acetone to

remove the oxides and other foreign impurity prior to welding process. Autogenous butt configuration welds are produced by continuous and pulse current mode of micro-plasma arc welding technique. The nature of pulse used in µ-PAW process is shown in Fig. 3.3(a). The welding torch is kept fixed and the workpieces are allowed to move over a velocity range of 2.5 to 4 mm/s. Time- temperature cycle in the HAZ and BM is measure by using K- type thermocouples and data accusation system (34972A LXI Data Acquisition series) with a 0.1s sampling rate (Fig. 3.3b). The thermocouples are employed at a distance of 2.5 mm and 4 mm in both side of the weld centerline to measure temperature characteristics during the welding process. The locations of the thermocouple were selected in such a way that they experienced maximum temperature of the molten pool for measuring the time temperature profile along the transverse direction. The experimental set-up and the position of thermocouple-points are shown in Fig. 3.3(b, c). The heat of fusion is produced by the constricted plasma arc which is delivered by the plasma torch that melts and joins the metals. The heat input per unit length (H) is calculated as (Thavamani et al., 2018)

$$H = \frac{V \times I_a}{S} \quad (3.1)$$

where V, I_a and S represent welding voltage, current and speed respectively. The average current (I_a) in pulse welding is calculated as

$$I_a = \frac{(I_p \times t_{on}) + (I_b \times t_{off})}{(t_{on} + t_{off})} \quad (3.2)$$

where I_p and I_b are peak and base current, respectively, and t_{on} and t_{off} are pulse on and off-time in pulse welding process, respectively.

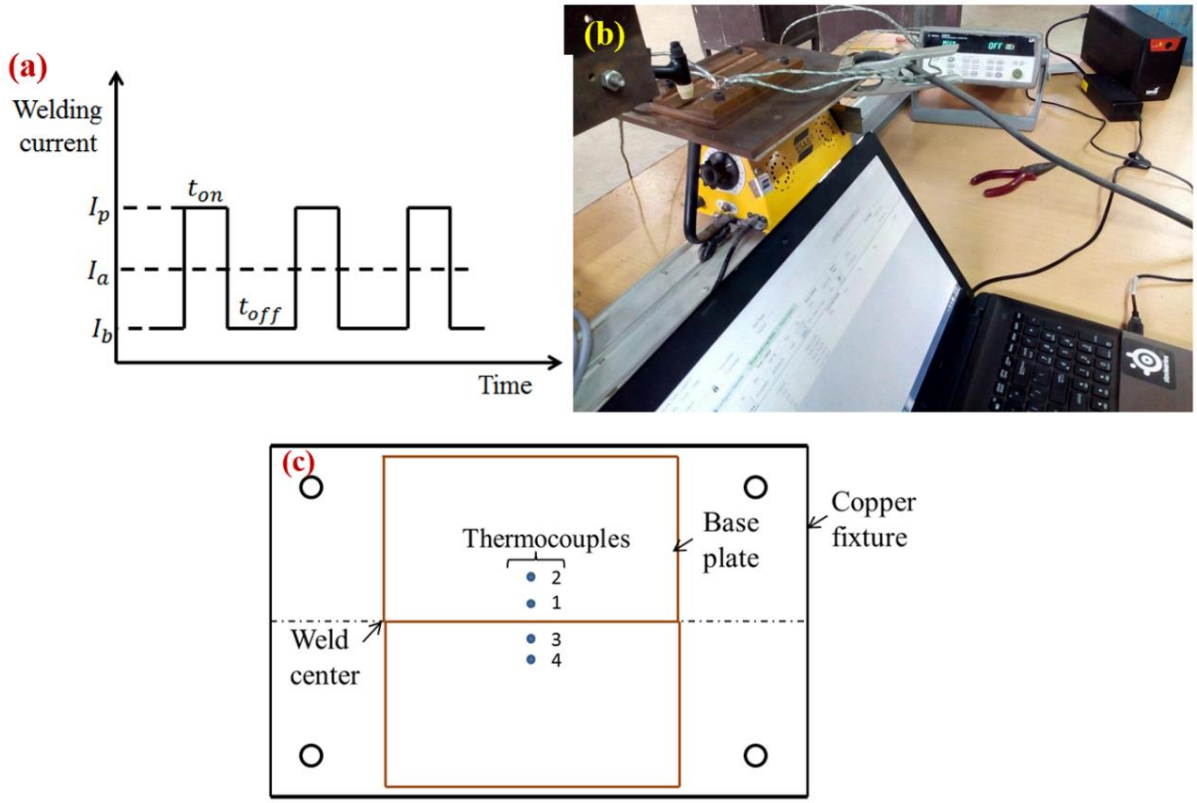

Fig. 3.3 (a) Characteristics of the pulse heat source (b) experimental setup and (c) schematic of thermocouple location on the work piece surface

Pulse welding involves cyclic heating and cooling of the weld pool by periodic variation of welding current between the peak and base value respectively. Hence selection of proper peak and base current is an important criterion in pulsed welding process to produce a sound weld, as it directly influences the heat input and peak temperature of the weld pool. Apart from current the weld quality also depends upon various other process parameters like pulse duration, frequency and welding speed. The ranges of welding parameters were evaluated by varying a single parameter while keeping all other parameter constant. Hence for selection of optimum welding parameters for a successful weld lot of trials were conducted. In the present work, heat input during welding is mainly controlled by varying the average current (I_a) and welding speed (S) to obtain full penetration welds as lower heat input will lead to a weld bead of partial penetration whereas higher heat input can cause burn out of the base material. Several partially and fully penetrated weld beads were obtained over a wide range of process parameter. Fig. 3.4 shows a feasible domain of average

welding current and speed for obtaining a successful joint. The cross sectional weld bead profiles of pulse welding condition at different process parameter are also depicted in Fig. 3.4. It is observed that full depth of penetration is achieved at a minimum average current of 8 A and welding speed of 2.7 mm/s with almost flat surface profile. The geometric defects like undercut along with the material vaporization are observed with further increment of average welding current beyond 10.6 A at the same welding speed of 2.7 mm/s. The other welding parameters employed for achieving full depth of penetration and a defect free weld are depicted in Table 3.2. The data points are chosen such that the variability in average current, welding speed, and pulse frequency is followed. The range of base current is considered as 20 – 25% of the peak current, fixed on-time of 0.06 s and off-time of 0.06 – 0.21 s to obtain different duty cycle and pulse frequency.

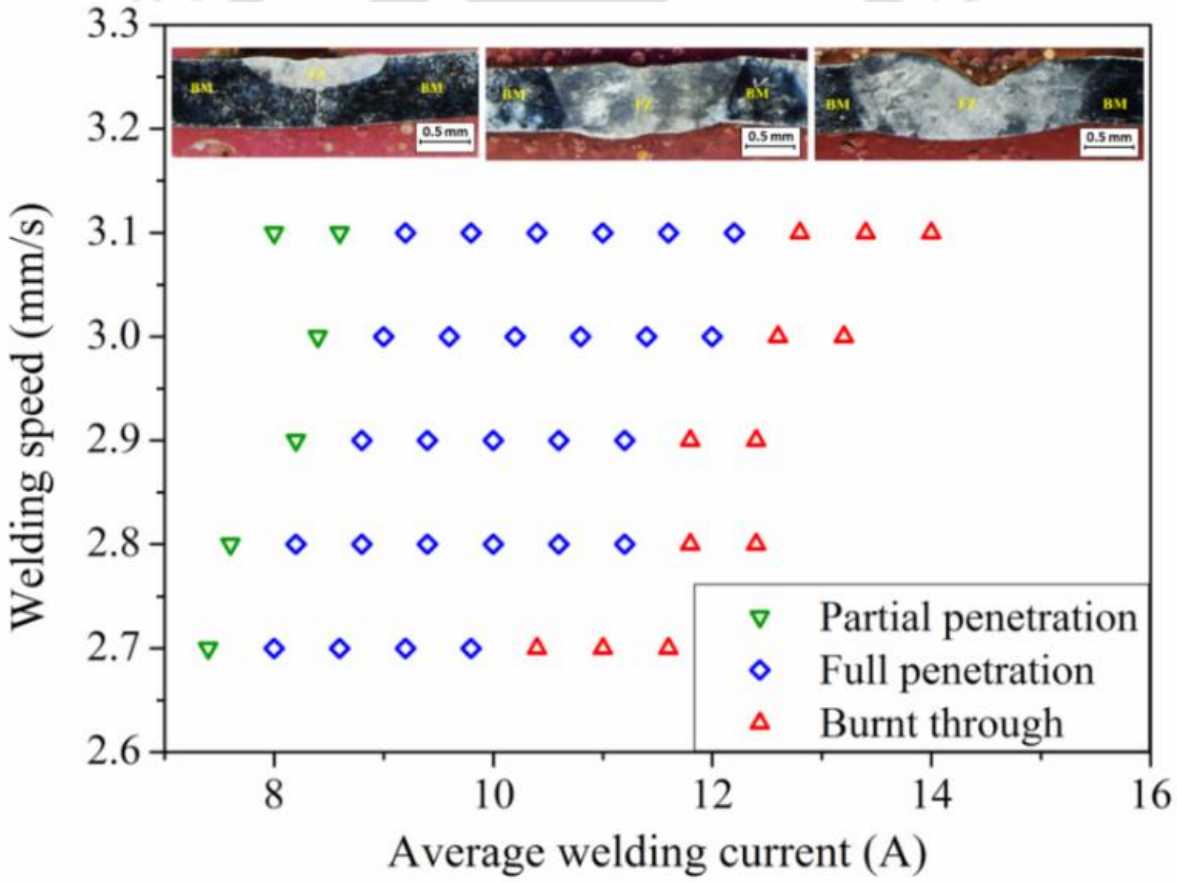

Fig. 3.4 Process map for pulse micro plasma arc welding of Inconel 718

Table 3.2 Welding parameters employed for Inconel 718 similar welding

Sample	Mode of Current	Peak current (A)	Welding speed (mm/s)	Average current (A)	Pulse frequency (Hz)	Heat Input (J/mm)
CC	Constant	-	3.6	12	-	52.8
PC1	Pulse	25	3.1	9.2	3.5	47
PC2	Pulse	25	2.8	9.2	3.5	52
PC3	Pulse	25	3.2	11.3	4.3	56
PC4	Pulse	24	2.8	10.6	4.3	60
PC5	Pulse	24	2.7	10.6	4.3	62.2
PC6	Pulse	21	2.9	10.6	5.8	58
PC7	Pulse	19	3.0	11.4	8.3	60.2

The top weld bead profile obtained at different mode of current and pulse parameters is shown in Fig. 3.5. With increase in peak current, the weld width increases and results in higher weld dimensions. Weld dimension affects the temperature gradient within the molten pool as well as cooling rate variation during solidification. Partially overlapped types of weld beads are obtained during the pulsed mode welding as compared to constant current mode due to the periodic repetition of pulses. The percentage of overlapping mainly depends on welding speed and pulse frequency. Since PC6 and PC7 welds are obtained at a higher frequency, the corresponding weld bead morphology is different as compared to other welding cases which are easily distinguishable in Fig. 3.5. In constant current mode, a smooth weld surface (Fig. 3.5a) is observed due to the application of a constant heat flux throughout the welding process. The melting, re-melting and solidification time is characterized by the pulse frequency and welding velocity. However, the weld morphology is different by combined effect of high pulse frequency and at high heat input (PC6 and PC7).

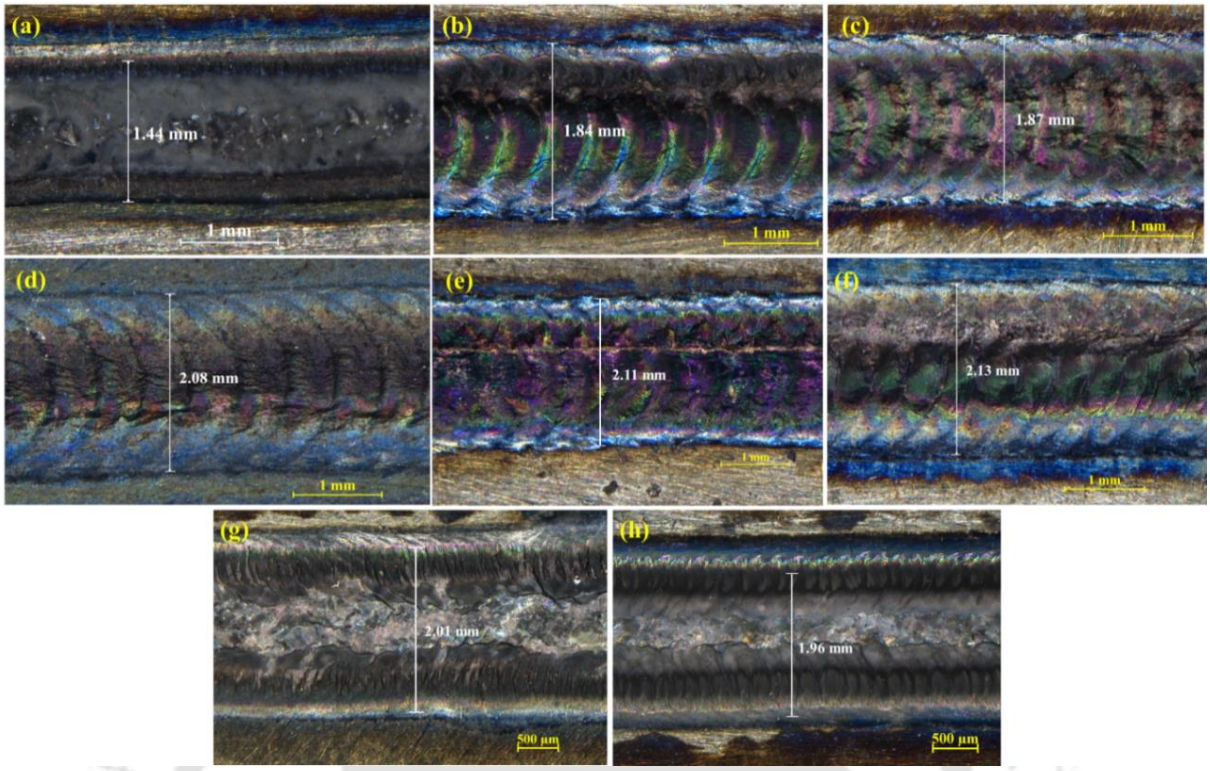

Fig. 3.5 Top surface weld bead profile of (a) CC (b) PC1 (c) PC2 (d) PC3 (e) PC4 (f) PC5 (g) PC6 and (h) PC7 welding condition

3.2.2 Dissimilar welding of Inconel 718 and AISI 316L

Welds with a butt joint configuration are produced herein by using the µ-PAW process with a pulse current mode for solution-treated Inconel 718 (1020°C for 1 hr.) and AISI 316L stainless steel. The samples are cut into 120 × 60 × 0.7 mm^3 coupons, where the cross-section is normal to the welding direction. The chemical composition of the AISI 316L base materials is evaluated using (EDX) analysis and given in Table 3.3 (Fig. 3.6a). The Inconel 718 and AISI 316L base materials consist of equiaxed grains with an average diameter of 78 µm (ASTM 4-5) and 25 µm (ASTM 7-8), respectively. The microstructure of the base materials is obtained from optical microscopy and SEM images (Fig. 3.6). The microstructure of the Inconel 718 shows the presence of various MC-type carbides distributed in the metal matrix (Fig. 3.6b). The grain boundaries of the Inconel 718 are decorated with a fine plate-like and needle-shaped δ phase (Fig. 3.6d).

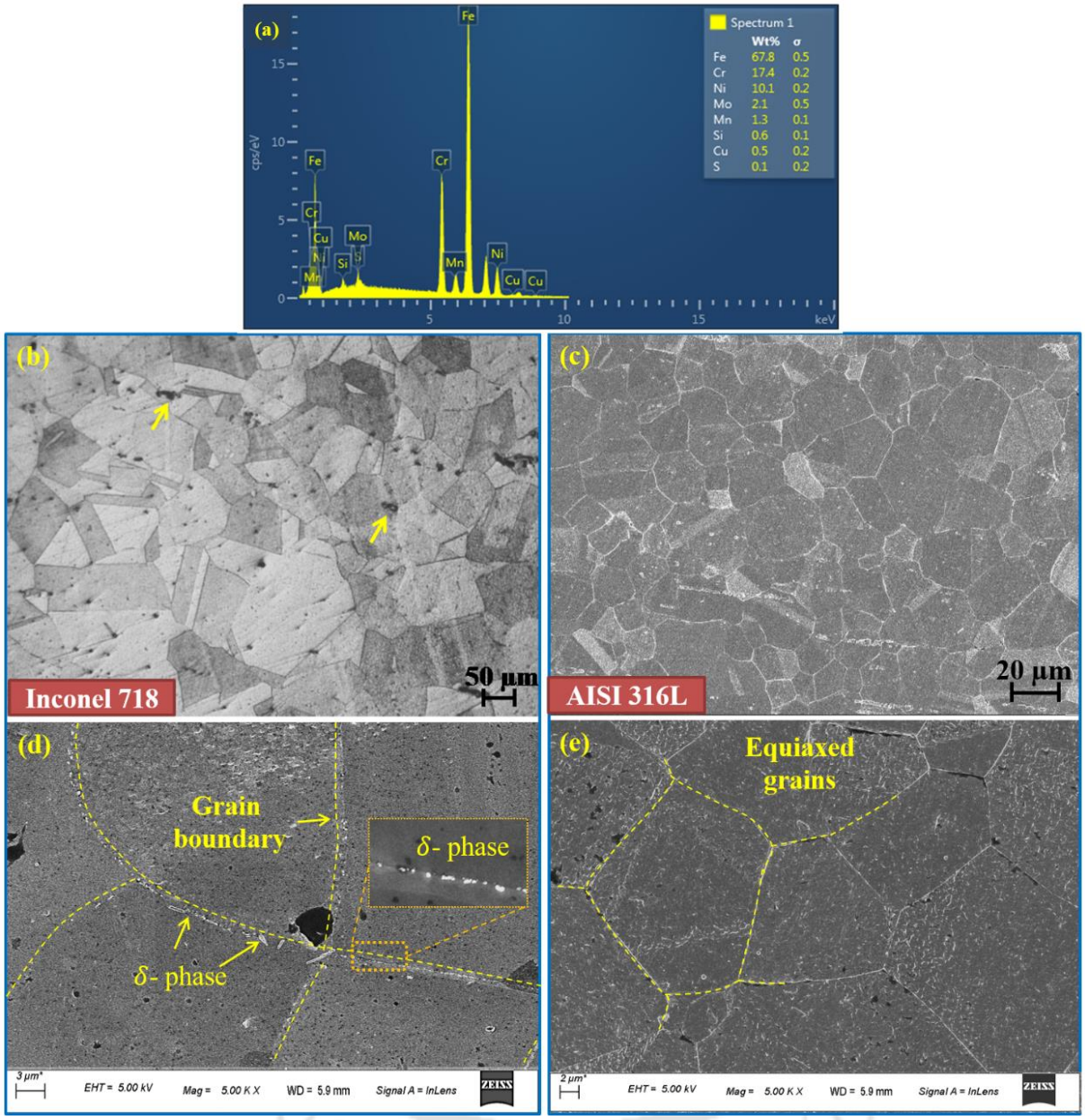

Fig. 3.6 Optical and SEM micrographs of Inconel 718 (a, c) and AISI 316 (b, d) base material

Table 3.3 Chemical composition (wt. %) of AISI 316L stainless steel

Element	**Ni**	**Cr**	**Mo**	**Mn**	**Si**	**Cu**	**S**	**Fe**
wt. %	10.1	17.4	2.1	1.3	0.6	0.5	0.1	Bal.

During welding the frequency of pulse current is maintained at 4.3 Hz. The other process parameters employed for the present experiment are shown in Table 3.4. The trials are performed by varying the pulse current over a certain range while keeping all other parameters constant. The peak current is varied between 17 A and 27 A with a base current that is 35% of that peak current, and the welding velocity is almost constant (~ 3.3 mm/s). A constant duty cycle of 26% is used for all welding conditions. In the present work, the parameters are chosen such that the heat input per unit length varies over a wide range of 42 J/mm to 72 J/mm.

Table 3.4 Selected process parameters of pulse welding process

Sample	Peak current (A)	Pulse energy (J)	Heat input (J/mm)
PD0	17.0	48.8	42
PD1	19.0	54.5	48
PD2	20.0	57.4	51
PD3	22.0	63.1	53
PD4	23.5	67.3	59
PD5	25.0	71.7	68
PD6	27.0	77.4	72

The transverse cross sections of the welded samples are shown in Fig. 3.7. Full penetration and defect-free welds (Fig. 3.7b) are achieved above a peak current of 19 A. In contrast, partial penetration (Fig. 3.7a) is obtained below a peak current of 17 A. Nonuniform weld beads due to under-filling and material vaporization are observed at a peak current of above 27 A. Fig. 3.7(b) and (c) shows that nearly flat weld beads are obtained between the peak current ranges of 19 A to 25 A without any under-fill and undercut. Hence, the above current ranges are considered to produce weld joints free from any type of visible defect. The fusion zone profile is asymmetric due to the different thermo-physical properties of the base materials. On the Inconel 718 side, the fusion zone is trapezoidal, whereas it resembles an hourglass shape on the AISI 316L stainless steel side.

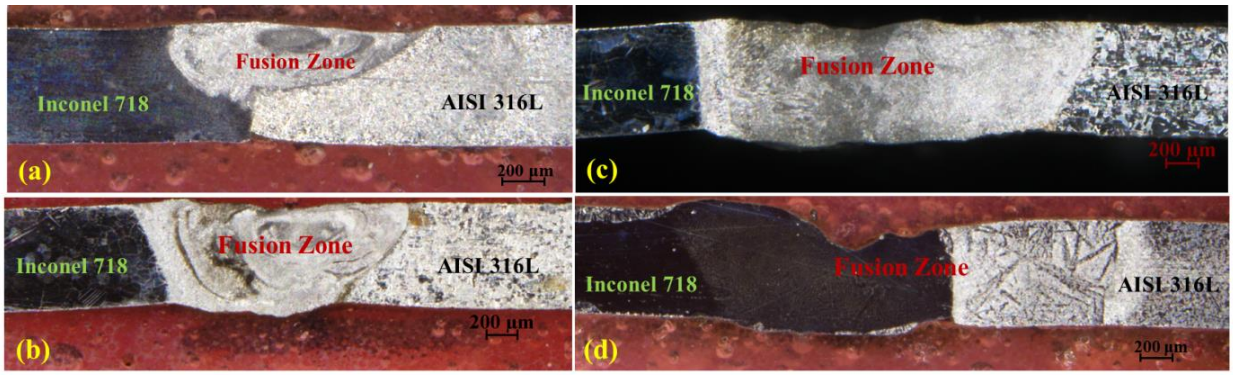

Fig. 3.7 Cross-sectional view of (a) PD0 (b) PD1 (c) PD5 and (d) PD6 dissimilar welded joint

3.3 Heat treatment of welded joints

The response of the Inconel 718 fusion zone intermetallic phases to different heat treatment techniques on reduction of Nb concentration and precipitation of various strengthening phases is investigated. To study the post weld heat treatment (PWHT) response on various intermetallic phases, PC4 welding condition (Table 3.2) is considered for the current analysis. The impact of holding time and temperature on microstructure and distribution of strengthening phases and δ particles are correlated. The holding time and temperatures are explicitly designed with reference to the time-temperature-transformation (TTT) diagram of Inconel 718 for precipitation of the required strengthening phases in the weld zone. The schematic of the TTT curve, along with the resulting strengthening phases corresponding to a particular holding time and temperature, are shown in Fig. 3.8 (Niang et al., 2010; Thompson et al., 1986). The welded samples are subjected to different post-weld treatments named as (a) aged (direct aging at 760ºC/8 h/Furnace cooling to 680ºC/6 h/Air cooling), (b) ST (only solution treatment at 1165 ºC/1 h/Air cooling) (c) STA1 (solution treatment at 1165 ºC/1 h/Air cooling followed by double aging at 960ºC/1 h/Furnace cooling plus 760ºC/5 h/Furnace cooling), (d) STA2 (solution treatment at 1165ºC/1 h/Air cooling and aging at 760 ºC/8 h/Furnace cooling plus 680ºC/6 h/Air cooling). The impact of post-weld treatments on strengthening phase precipitation and its influence on mechanical properties are correlated through tensile and micro-hardness testing of the welded samples.

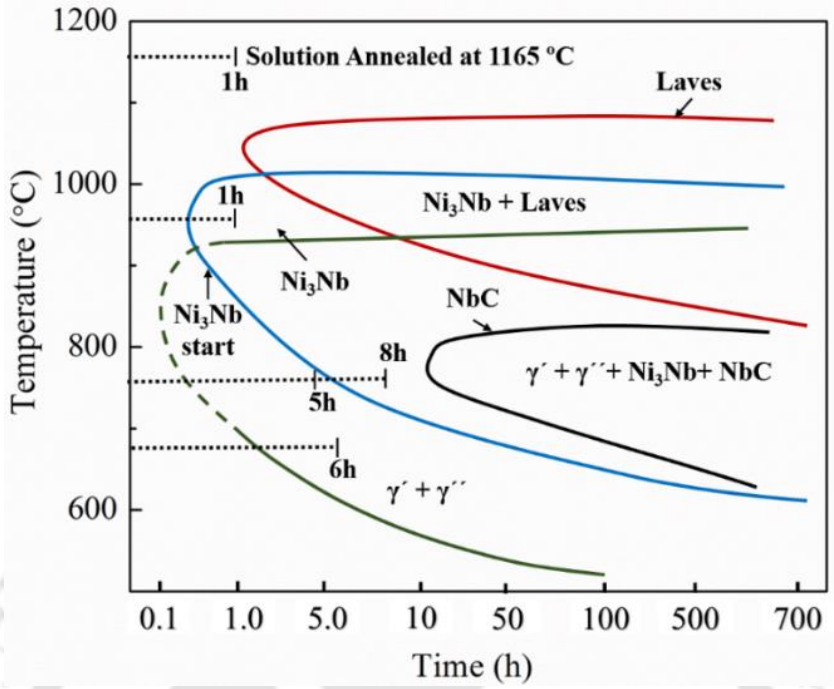

Fig. 3.8 The schematic of TTT diagram of Inconel 718 along with designed heat treatment phases

3.4 CO_2 laser welding of Inconel 718 and AISI 316L

The primary objective of this section is to generate a window of CO_2 laser process parameter to produce successful weld between Inconel 718 and AISI 316L material. The impact of laser process parameters on solidification behavior, microstructural morphology and joint mechanical properties are analyzed systematically. In the present analysis, butt configuration welding is carried out on a 2.5 kW continuous wave CO_2 laser setup (LVD, Orion 3015) and the experimental process is shown in Fig. 3.9. The as-received base materials of Inconel 718 and AISI 316L are sheared into coupons of dimension 70 × 60 × 0.7 mm^3. The welding process parameter varied over 500 W to 900 W the beam power while keeping the scanning speed constant. The acceptable range of laser parameters are optimized through number of trials and the successful welding parameter are listed in Table 3.5. The nozzle diameter and stand-off distance of 25 mm and 15 mm is maintained during the welding process respectively. The workpieces are tacked in both the edges by spot welding technique for better alignment then clamped in the fixture for welding. The heat input (J/mm) during laser welding is estimated by the relation

$$Q = (\eta . L_P / S_v) \quad (3.3)$$

where L_P is laser beam power (W), η is the process efficiency and S_V is the scanning velocity of CO_2 laser beam.

Table 3.5 Laser process parameters

Sample no.	Power (W)	Welding speed (mm/min)	Heat Input (Q) (J/mm)
LD1	500	400	22.5
LD2	600	400	27
LD3	700	400	31.5
LD4	800	400	36
LD5	900	400	40.5

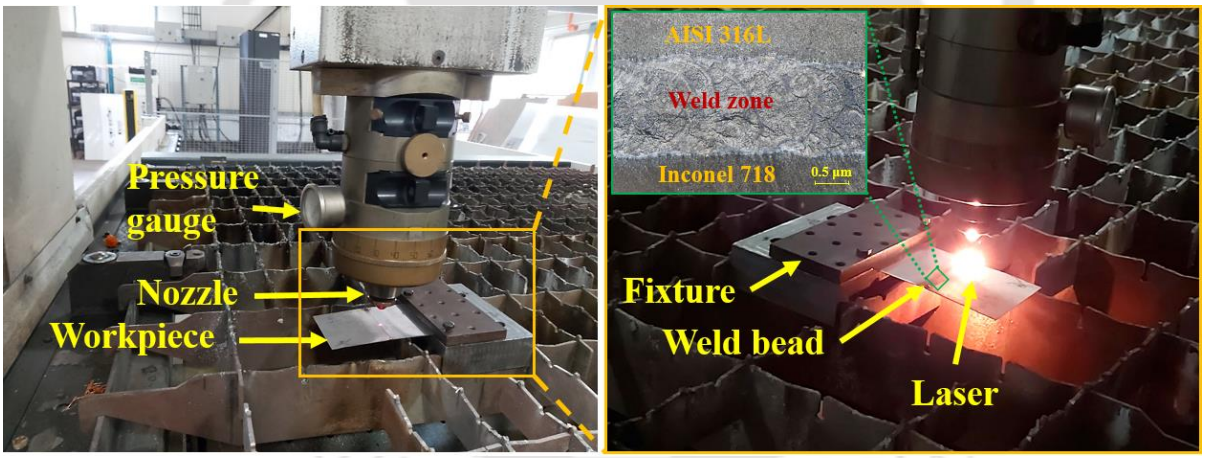

Fig. 3.9 CO_2 laser experimental setup

The transverse weld bead cross-section for each successful welding condition with bead dimension is given in the Table 3.6. The full penetration autogenous weld beads are produced by employing CO_2 laser heat source and observed to be free from any type of visual welding defects. The asymmetry in bead geometry is clearly evident from the macrophotographs due to different base material thermos-physical properties. The fusion zone in Inconel side is of trapezoidal shape whereas it is of hourglass shape in the stainless steel side. The weld aspect

ratio (w/d) is increasing from 3.01 (LD1) to 3.88 (LD5) with increase in the beam power. At constant scanning speed, increase in the beam power cause more melting action due to more heat input as a result the aspect ratio increases. Hence, the conduction mode of welding prevails over keyhole mode in the present analysis.

Table 3.6 Geometrical characteristics of the laser weld beads

Weld macrophotographs	Weld bead details
	Welding condition: LD1 Top width: 2.11 mm Bottom width: 1.71 mm
	Welding condition: LD2 Top width: 2.17 mm Bottom width: 1.92 mm
	Welding condition: LD3 Top width: 2.23 mm Bottom width: 1.85 mm
	Welding condition: LD4 Top width: 2.34 mm Bottom width: 1.98 mm
	Welding condition: LD5 Top width: 2.72 mm Bottom width: 2.36 mm

3.5 Mechanical characterization of welded joints

Mechanical properties were evaluated with cross weld tensile and micro-hardness test for all successful welding cases. The room temperature tensile test is carried to evaluate the

proof stress, tensile strength, and degree of elongation of the weldment. The ultimate tensile strength and percentage elongation which is a measure of ductility is evaluated. The joint efficiency is defined by the ultimate tensile strength (UTS) of a joint with respect to the ultimate tensile strength of the base material. For each condition three sub-size transverse specimens are prepared according to ASTM E8M standard with a gauge length of 25 mm as shown in Fig. 3.10 (ASTM Standard, 2008). The samples were sectioned using the wire-cut EDM machine. Then the tensile tests were conducted by a computer controlled servo-hydraulic universal tensile testing machine with extensometer attachment with a cross head speed of 1 mm/min. The analysis of fracture surface was carried out with the help of scanning electron microscope (SEM) to investigate the failure behavior of the weld joint. Fig. 3.10(c) showing the variation of failure location in dissimilar weld due to variation in the welding process parameter. Tensile failure in the fusion zone signifies formation of a relatively weak weld bead. Whereas failure in the base material indicates that the obtained weld bead is stronger than the parent material.

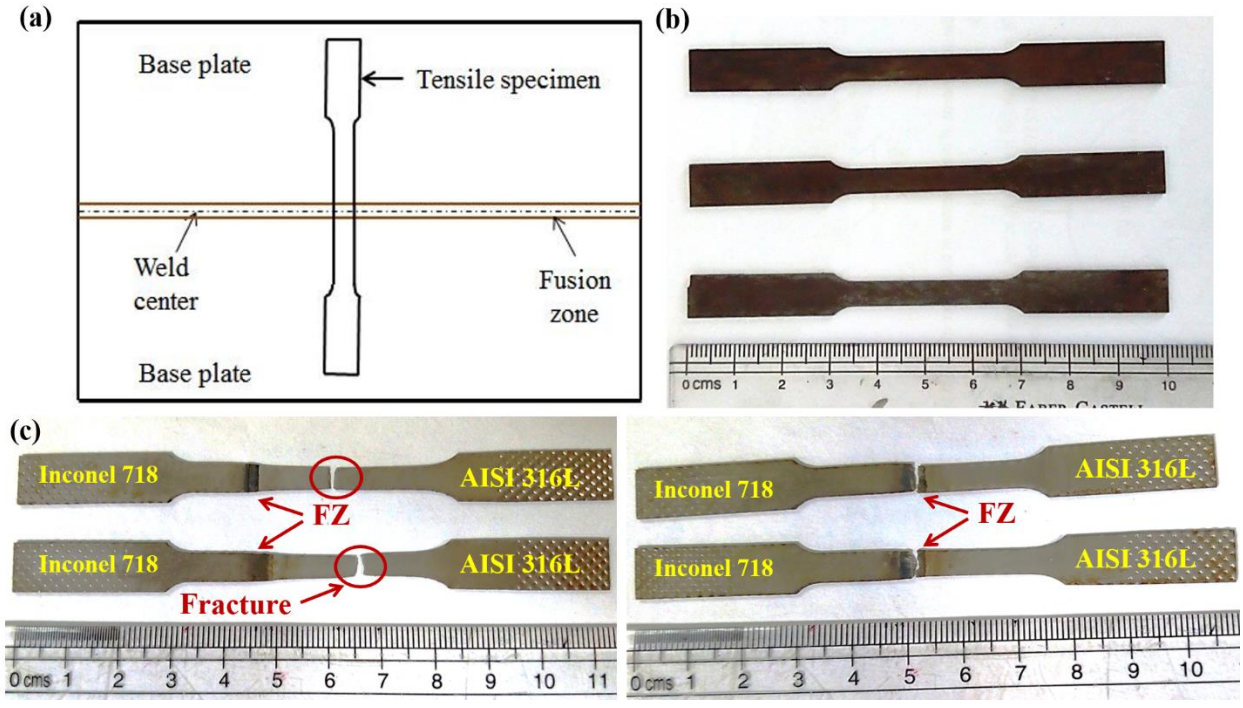

Fig. 3.10 (a) Transverse tensile specimen location in the welded specimen (b) Sub size tensile specimens before testing and (c) Showing location of failure in base material and fusion zone after testing

According to ASTM E384 standard, the micro-hardness tests were carried using Vickers micro-hardness testing machine to analyze the hardness behavior of the fusion zone with respect to different process parameters (ASTM int., 2012). Micro hardness measurements were conducted across the weld bead with an indentation spacing of 0.15 mm for each specimen at a load of 500 g and a dwell time of 15 s. The hardness was measured in the middle section of the welded joint as shown in the Fig. 3.11.

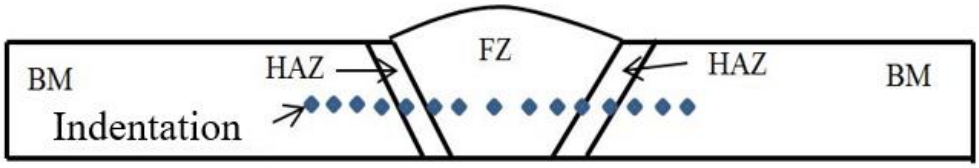

Fig. 3.11 Schematic diagram of hardness testing measurement

3.6 Microstructural characterization of welded joints

After successful welding, macro and microstructural analysis were carried out to characterize the weld pool shape and its microstructure by using optical and scanning electron microscope. The detailed microstructural analysis is conducted for each welded specimen to correlate the effect of solidification parameters on final solidified structure and segregation of various intermetallic phases. Welded samples were sectioned normal to the welding direction by using the wire cut EDM and polished with various grades (from 80 - 2000 grit size) of emery paper followed by velvet cloth polishing with the diamond paste to achieve mirror surface finish. The polished specimens were then etched according to ASTM E407 standard, for few seconds in a solution of HCl, HF, and HNO_3 in the ratio of 2:1:1 respectively for Inconel 718 similar welds (ASTM Standard, 1999). Whereas the dissimilar welds (i.e., Inconel 718 and AISI 316L) were etched in a solution of $CuCl_2$ (1gm), HCl (20 ml) and C_5H_5OH (20 ml). After etching the microstructural analysis is performed in the FZ and HAZ for each sample with the help of optical microscope and scanning electron microscope (SEM). Fig. 3.12 showing the optical micrographs of weld fusion zone along with fusion boundary (FB) and heat affected zone (HAZ) for different welded samples obtained at 78 J/mm, 74 J/mm and 71 J/mm respectively using micro-PAW technique. The dendritic structures are clearly evident in the weldment with the interdendritic regions etching dark as compared to the dendritic core. Coarser columnar dendrites grown from solid

liquid interface are seen in all welding conditions, which is mainly due to the higher temperature gradient in the fusion boundary (Janaki Ram et al., 2005). Whereas fine and equiaxed dendrites were observed in the weld interior.

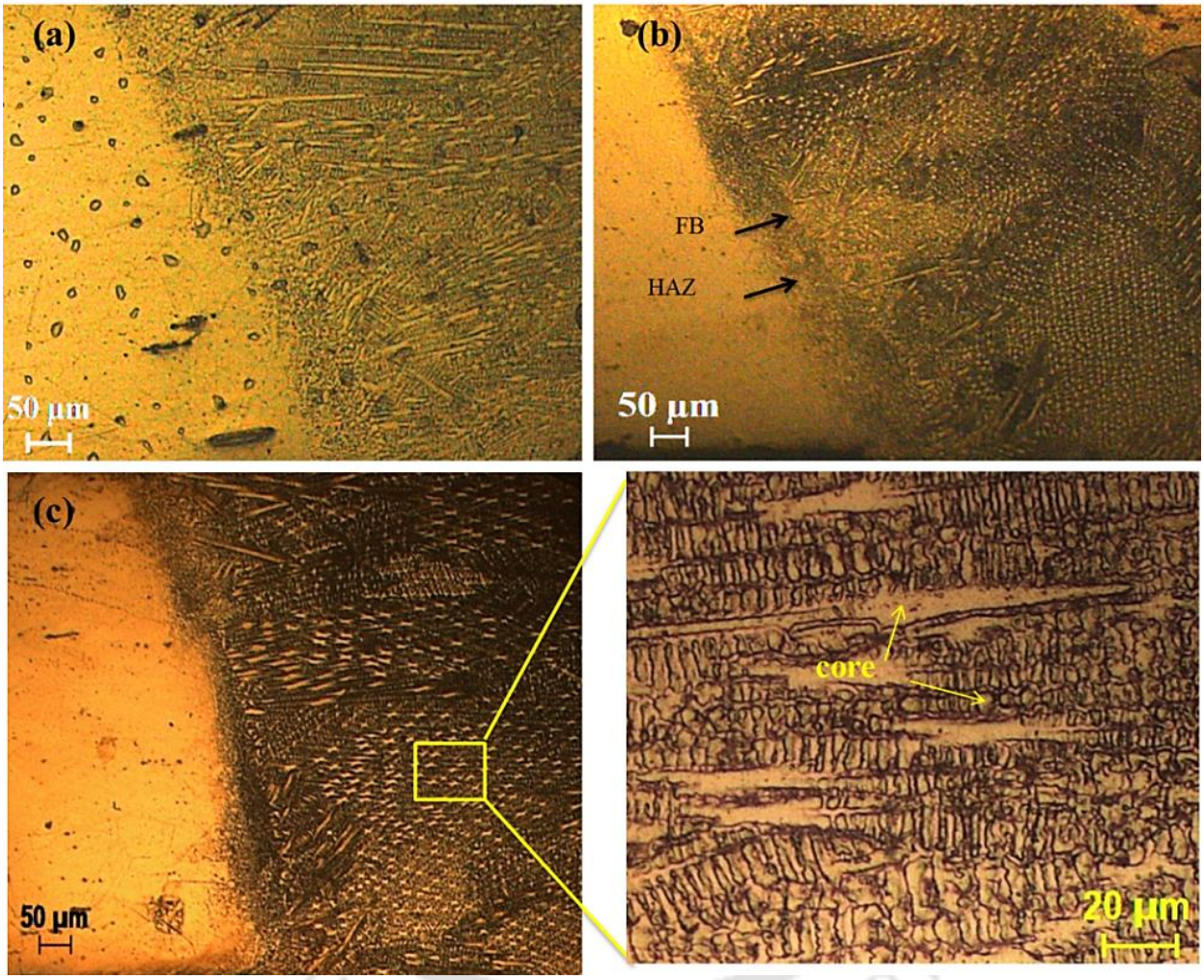

Fig. 3.12 Fusion zone microstructure near to fusion boundary for welds obtained at (a) 78 J/mm (b) 74 J/mm and (c) 71 J/mm

The higher magnification SEM analysis of the weld zone interior corresponding to constant current (CC) and pulsed current (PC) mode weld using micro-PAW is shown in Fig. 3.13. At the weld interior, numbers of bright irregular shaped Laves particles are observed in the interdendritic region. The Laves particles in CC weld are witnessed to be interconnect columnar type and moderately coarser against to the equiaxed dendrites of the PC weld. The current pulsation has refined the microstructure due to the temperature variation during the

welding process. The continuous temperature variation during pulsed welding, causes remelting and breaking off of the long continuous dendritic chain at the solidification front as a result reducing the segregation and volume percentage of intermetallic phase. Hence the amount (vol. %) of Laves phase is higher in the columnar dendritic regions of CC weld as compared to the equiaxed dendrites of the PC mode weld (Ram et al., 2004).

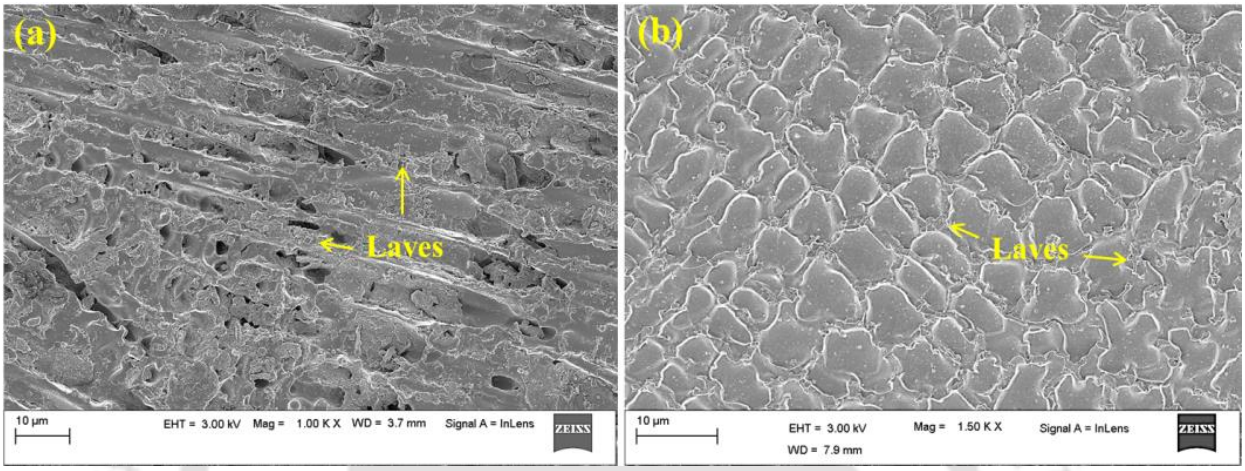

Fig. 3.13 SEM microstructure of weld interior for (a) constant current mode and (b) pulsed-current mode micro-plasma weld

The characterization of intermetallics in fusion zone is performed through energy dispersive x-ray technique (EDX) and x-ray diffraction (XRD) technique. Fig. 3.14 shows the elemental distribution of interdendritic and core region for the micro-plasma weld through EDX analysis. It can be seen from the spectrum 1 (Fig. 3.14b) interdendritic regions are enriched with Nb and Al as compared to the dendritic core (Fig. 3.14c). The weight percentage of Nb in the interdendritic region is almost 400% to that of the dendritic core region, signifying a higher segregation during the weld solidification. Due to higher segregation, it consumes a significant amount of favorable alloying elements and promotes formation of brittle intermetallics Laves phase. The Laves formation can be controlled by refining the solidified structure, which can be achieved by controlling the welding process parameters or weld solidification parameters.

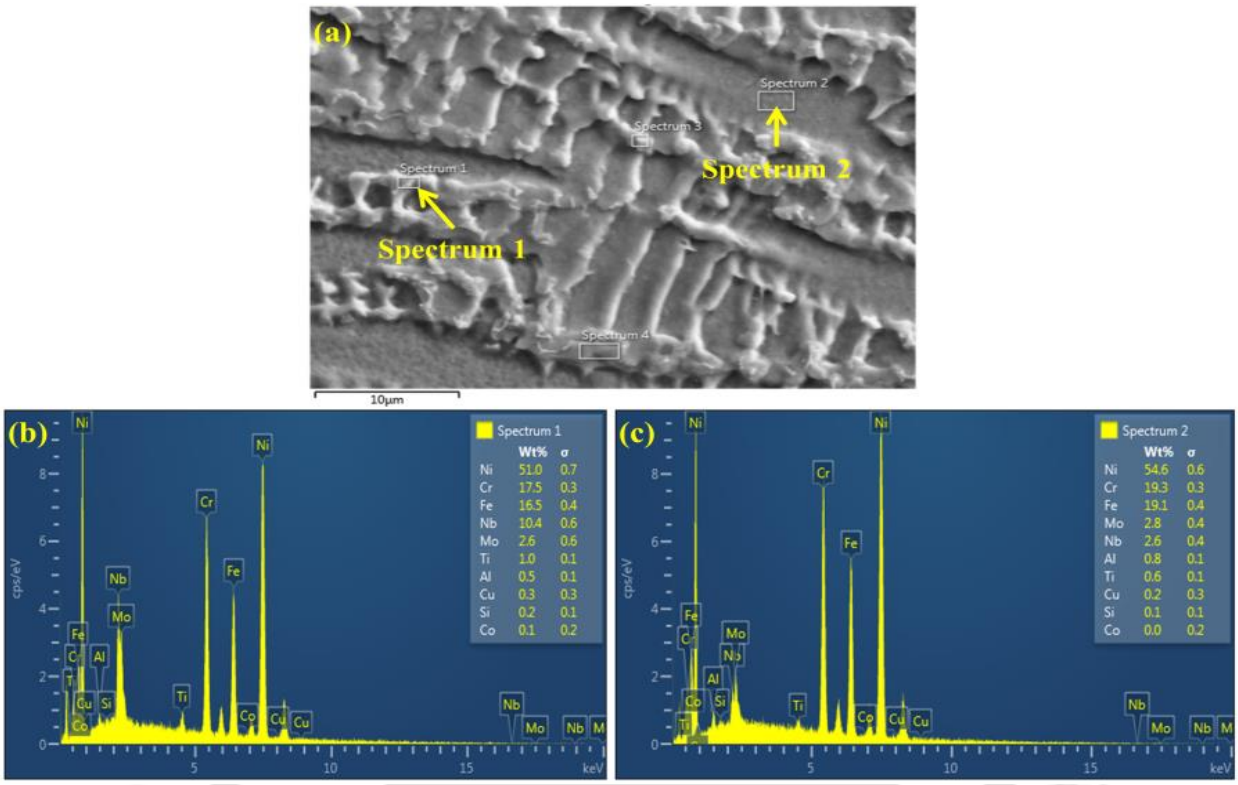

Fig. 3.14 EDX analysis of the weld dendritic structure

The fusion zone diffraction (XRD) peaks corresponding to the constant and pulse current mode Inconel 718 weld zones are depicted in Fig. 3.15. The main Fe-Ni austenite (γ) matrix dominating in (111) plane is witnessed from the sharp diffraction peak. Presence of diffraction peaks corresponding to various intermetallic phases such as Laves (Fe_2Nb), NbC and TiC dominating in the direction (110) (112), (111) (220) and (222) respectively are observed from the diffraction plot. The diffraction peaks corresponding to CC weld are found to be sharp and strong as compared to the peaks of PC weld. The small and weak peaks of PC weld will reduce the normalized intensity ratio (NIR) with respect to the CC weld, which signifies reduction in relative quantity of different intermetallic phases in the weld zone (Peelamedu et al., 2002). Hence, current pulsation during the welding hinders the precipitation of various secondary intermetallic phases in the final solidified weld zone.

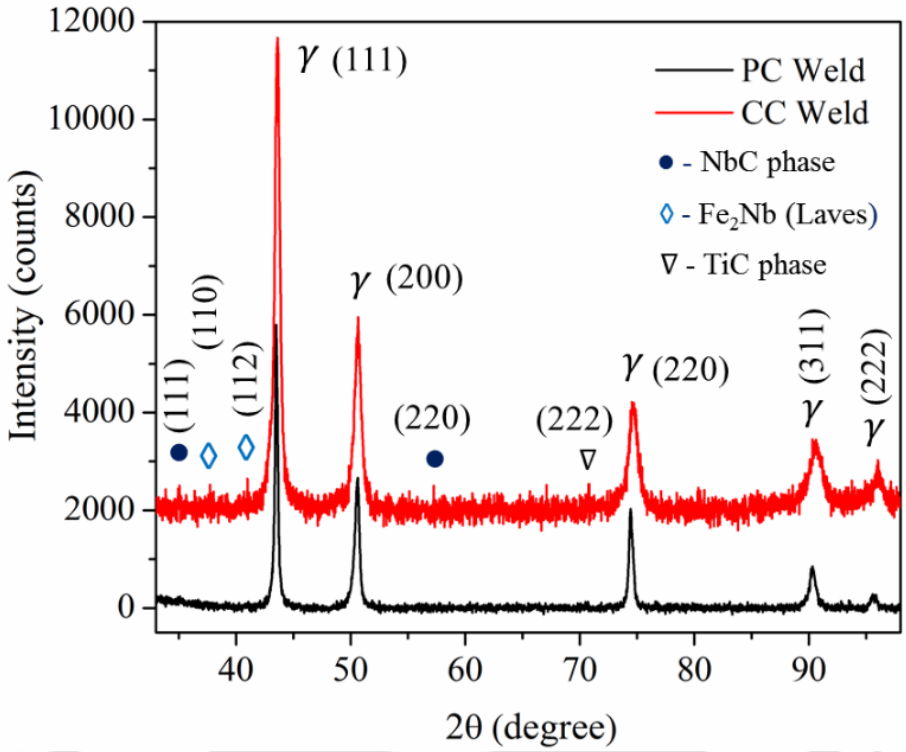

Fig. 3.15 XRD analysis of the weld zone produced at (a) constant current and (b) pulsed-current mode micro-plasma weld

3.7 Summary

A brief experimental methodology is explained in this chapter for welding Inconel 718 in similar and dissimilar combination (with AISI 316L) using micro-plasma arc welding and CO_2 laser welding process in butt joint configuration. The micro plasma welding is undertaken in constant and pulsed current mode of welding. Whereas CO_2 laser welding is performed in continuous wave mode. Post weld processing of welded joints like microstructural and mechanical property analysis has explained elaborately. The primary objective of experimental investigation is to generate a database of suitable process parameters required for producing a successful weldment of good strength and ductility. The experimental results suggested that the mode of current and solidification parameters has a larger impact on the welding of Inconel 718 with AISI 316L. The experimentally measured weld pool dimensions are further used for validating the calculated results of numerically obtained weld beads in successive chapters.

भारतीय प्रौद्योगिकी संस्थान गुवाहाटी
Indian Institute of Technology Guwahati

Chapter 4

Theoretical Model Development

4.1 Introduction

A comprehensive finite element (FE) based numerical model is developed and the detailed theoretical formulation employed in the heat transfer model is described in this chapter. In fusion welding process an intense heat source is applied to melt the localized regions of the metallic plates along the interface to produce the weld joint. Fusion welding involves various complex phenomena like heating, melting, cooling and solidification inside the weld pool. The theoretical development provides a better understanding of the physics that involved behind these phenomena by using mathematical modeling are illustrated in this chapter. Experimental investigations have certain limitations due the involvement of high temperature heat source and formation of a small scale weld pool during the fusion welding process. Hence a numerical heat transfer model is developed for similar and dissimilar fusion welding process based on finite element (FE) method by using a Gaussian distributed volumetric heat source. The moving heat source is incorporated in the thermal model by using a DFLUX subroutine for the constant and pulsed mode of welding process, for better understanding of the cyclic variation of temperature during the pulse welding condition. The FE based conduction heat transfer model is further employed to obtain time-temperature distribution with the final weld pool shape and size of the entire weldment corresponding to micro-plasma and CO_2 laser welding processes. Weld quality mainly depends upon the weld bead configuration and the final microstructure of the fusion zone, which can be explained on the basis of thermal cycles during the welding process; hence it is important during the

numerical simulation to choose an appropriate heat source model for better result (Goldak et al., 1984). The most popular model for the heat input is a double ellipsoidal, because in many welding technique, the double ellipsoid shape is a good approximation. Kumar et al., (Kumar and Bag, 2019) employed double ellipsoidal heat source for welding Ti-alloy using pulse laser welding process and predicted weld pool dimension with an maximum error of 12%. It has been shown that a Gaussian distribution of power density inside a double ellipsoid moving along the weld path was convenient, accurate, and efficient for most realistic welds with simple shapes (Goldak and Akhlaghi, 2005). Ebrahimi et.al. (Ebrahimi et al., 2016) applied double ellipsoidal heat flux model for laser welding of Inconel 625 and AISI 316L in dissimilar configuration and reported the simulated thermal results for the laser welding configurations were in good agreement to the experimentally obtained results. Baruah and Bag (Baruah and Bag, 2017) developed a conduction based heat transfer model for the laser micro-welding process and observed good agreement of temperature and weld bead profile with the experimental results. The heat transfer model starts with defining the governing equation and boundary conditions.

4.2 Governing equation and boundary conditions

The conduction based heat transfer model is often employed in macro welding process due to insignificant volume of molten zone that directly reduces the computational cost. To approximate the importance of convective heat transport in the weld pool a volumetric heat source is mostly used for the conduction heat transfer based numerical model. Heat transfer in macro scale welding provides a reliable solution domain by employing Gaussian distributed volumetric heat source that substitutes the actual plasma or laser heat source in the model. The thermal analysis is performed in two stages: in first stage, the volumetric heat source is applied to the joining surfaces in order to perform the welding operation, whereas the second stage allowed complete cooling down of welded surfaces to steady state condition after removal of the heat source. The second stage gets completed by providing a cooling time of twice to that of the welding time. If x-axis is considered as the moving coordinate axis of the laser beam or plasma arc with velocity ‘v’, the fundamental governing equation of heat transfer or conservation of energy in 3D Cartesian coordinate system is expressed as

$$\frac{\partial}{\partial x}\left(k\frac{\partial T}{\partial x}\right)+\frac{\partial}{\partial y}\left(k\frac{\partial T}{\partial y}\right)+\frac{\partial}{\partial z}\left(k\frac{\partial T}{\partial z}\right)+\dot{Q}=\rho C\left(\frac{\partial T}{\partial t}-v\frac{\partial T}{\partial x}\right) \quad (4.1)$$

where (x, y, z) is the local coordinate system with respect to the heat source, k, ρ and C refer to thermal conductivity (W/m . K), density (Kg/m^3) and specific heat (J/Kg. K) of the base material respectively. The T and t refer to temperature (K) and time (sec) variable respectively and $\dot{Q}$ is the internal heat generation per unit volume (W/m^3). The term on the left side of equation 4.1 indicates conductive heat transfer in the three directions and the term on right side infer to transient nature of the heat transfer process. The development of numerical model is based on the following assumptions:

- The welded sheets are considered as solid deformable bodies, geometrically ideal and totally stress free. The top surface of the weld pool is considered to be flat to avoid the computational complexity for free surface modeling.
- In similar welding condition, only half of the geometry is considered due to symmetry along the weld line. This effectively reduces the computational time and cost.
- The temperature dependent thermo-physical properties (i.e., thermal conductivity and specific heat) and constant emissivity is considered in the model.
- The initial temperature of the substrate material is considered as 293 K.
- The heat losses through convection and radiation from different substrate surfaces are incorporated through the lumped heat transfer coefficient.

Fig. 4.1 refers to the solution domain and boundary condition associated with the butt weld joint in transverse direction along with the applied heat source. Different zones of the weld beads are differentiated by the respective temperature isotherms. At the symmetric surface, temperature gradient is considered as zero. The top surface of the substrate is subjected to the heat flux as a welding arc and the remaining surfaces are subjected to convection and radiation heat losses. Mathematically heat interactions of all the surfaces can be expressed as (Baruah and Bag, 2017)

$$k\frac{\partial T}{\partial n}-q+h(T-T_0)+\sigma\varepsilon(T^4-T_0^4)=0 \quad (4.2)$$

where n denotes the direction normal to the surface; $\sigma, \varepsilon, q, k, h$ and T_0 refer to Stiffen-Boltzmann constant (W/m^2K^4), emissivity, imposed heat flux (W/m^2) onto the surface, thermal conductivity (W/m. K) normal to the surface, surface heat transfer coefficient (W/m^2. K) and initial temperature (K) of the work piece respectively. The first term denotes the heat conduction to the boundary surface, the second term represents the surface heat flux from the heat source on the top surface, and the third and second term represents the heat loss by convection and radiation respectively. The surfaces that are in direct contact with air are assigned coefficient of convective heat transfer of air. However, at the workpiece surfaces in tight contact with copper fixture and backing plate are assigned with a higher heat transfer coefficient.

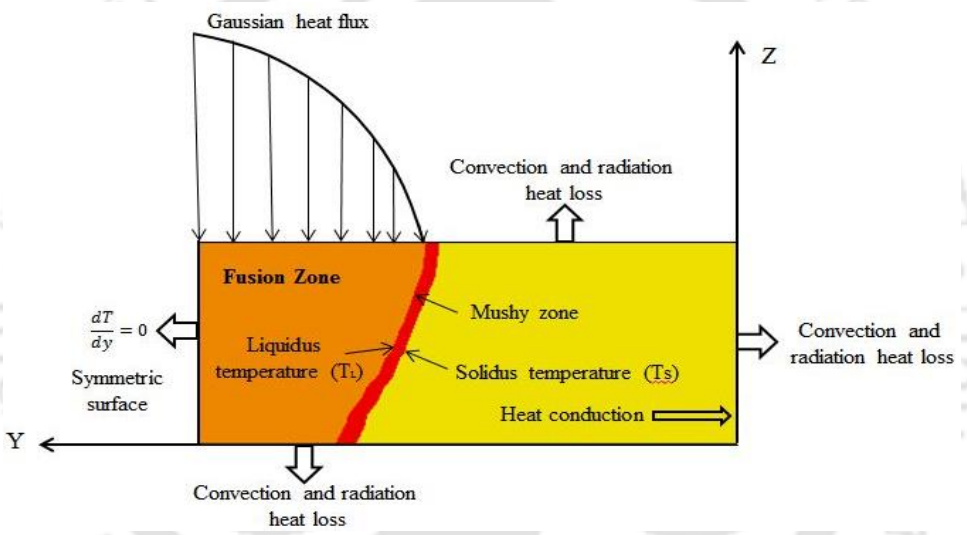

Fig. 4.1 Representation of solution domain along with applied boundary condition of the thermal model

4.3 Heat source model

The main idea of the heat source representation is to replace the physical process with an appropriate surface or volumetric heat flux in the numerical computation to obtain an accurate temperature profile during the welding process. To approximate the influence of convective transport of heat in the weld pool during conduction heat transfer based thermal analysis, a volumetric heat source term is often used. The Gaussian distribution of heat flux is found to be the best approximation for most of the fusion welding processes. So in this proposed work a Gaussian distributed double ellipsoidal volumetric heat source model used to

predict the thermal behavior of the fusion welding processes. According to the moving coordinate system the power density distribution inside the front quadrant (f) and rear quadrant (r) for moving heat source model in Cartesian coordinate system is given by following equations (Goldak et al., 1984)

$$q_f(x,y,z) = \frac{6\sqrt{3}\, f_f Q}{abc_f\, \pi\sqrt{\pi}} e^{-3x^2/c_f^2} e^{-3y^2/a^2} e^{-3z^2/b^2} \tag{4.3}$$

$$q_r(x,y,z) = \frac{6\sqrt{3} f_r Q}{abc_r\, \pi\sqrt{\pi}} e^{-3x^2/c_r^2} e^{-3y^2/a^2} e^{-3z^2/b^2} \tag{4.4}$$

where a, b, c_f and c_r are semi axes of the double ellipsoidal heat source and shown in Fig. 4.2(a). The selection of double ellipsoidal parameters is a challenging job, the width (b) and depth (c) of the double ellipsoidal is directly taken from the experimental results (Fig. 4.2b). The length of front (c_f) and rear (c_r) quadrant is taken by various heat and trial methods. The actual heat intensity that causing heating and melting of the workpiece is given by following equation

$$Q = \eta \times V \times I \quad \text{or} \quad Q = \eta \times P \tag{4.5}$$

where η, V, I and P depicts welding process efficiency, welding voltage, current and laser beam power respectively. The fractions of heat deposited in the front (f_f) and rear (f_r) quadrants are related by (Goldak and Akhlaghi, 2005)

$$f_f + f_r = 2 \tag{4.6}$$

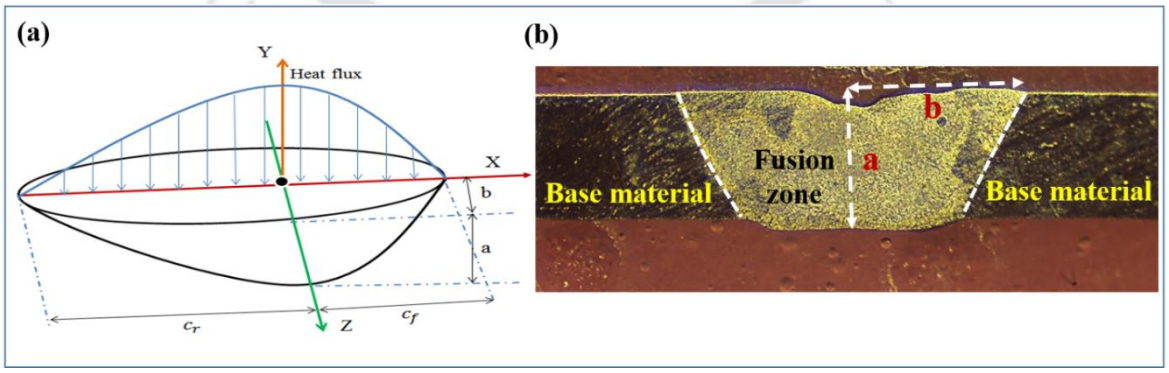

Fig. 4.2 (a) Schematic of double ellipsoidal heat source and (b) experimental mapping on weld bead

Due to cyclic variation of current between peak and base value, the temporal variation of flux will be witnessed. Hence, the current pulsation effect is incorporated with the model by the heat intensity parameter (Q) of equation 4.5. As a result, the equation becomes 4.5 becomes

$$Q(t) = \begin{cases} \eta \times V \times I_P, & \text{if} \quad t \leq t_{on} \\ . & \\ \eta \times V \times I_b, & \text{if} \quad t > t_{on} \end{cases} \tag{4.7}$$

where I_P and I_b are the peak current (applied during pulse **ON** period) and base current (applied during pulse **OFF** period) maintained during the welding process.

For dissimilar material welding, due to difference in thermo-physical properties, the produced weld bead would be asymmetrical as shown in Fig. 4.3(b). Hence, instead of a double ellipsoidal model, a quadruple ellipsoidal model is used to account the non-symmetry energy distribution (Bag and Amin, 2020). The schematic of quadruple ellipsoidal heat source is shown in Fig. 4.3(a), it consists of four ellipsoid parts (i.e., 1, 2, 3 and 4) that are accountable for different energy absorption in specified directions. The ellipsoid 1 and 2 corresponds to one base material and uses common geometric parameter b_1 and a. The energy distribution in front and rear quadrant are not equal due to the moving heat source, hence the ellipsoid 1 and 2 are associated with different geometric parameter i.e., c_f and c_r. Similarly, the second base material (ellipsoid 3 and 4) is associated with geometric parameter b_2, c_f and c_r. The experimental mapping for b1 and b2 corresponding to dissimilar material welding is shown in Fig. 4.3(b). The geometric parameter a is taken as constant for both the material as there is not much difference in thickness direction.

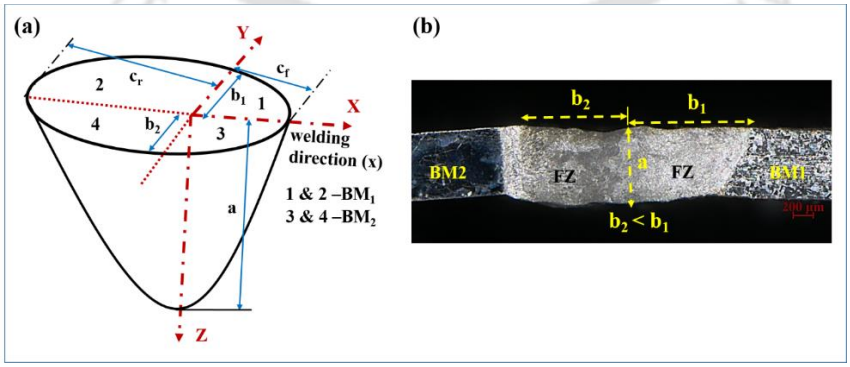

Fig. 4.3 (a) Schematic of quadruple ellipsoidal heat source model and (b) experimental mapping on dissimilar weld bead

4.4 Model geometry and material properties

4.4.1 Model geometry for similar material welding

The heat transfer model is calibrated with proper choice of solution geometry, optimum meshing, heat source parameters, time increments and assigning convective heat transfer coefficient. In similar welding condition due to symmetry in material and loading condition, only one-half plate of the joint is considered for the analysis. The interaction of the welding surfaces with the ambient is integrated in the numerical model to incorporate the heat losses during the welding process and shown in Fig. 4.4. The surfaces that are in direct contact with air are assigned coefficient of convective heat transfer (h) of 35 W/m^2 K (Dye et al., 2001). However, the surfaces which are in tight contact with the copper fixture and backing plate, which have high thermal conductivity, are assigned with a high heat transfer coefficient of 1000 W/m K (Baruah and Bag, 2016). The emissivity of Inconel 718 fusion zone is taken as 0.65 to incorporate the heat losses due to radiation.

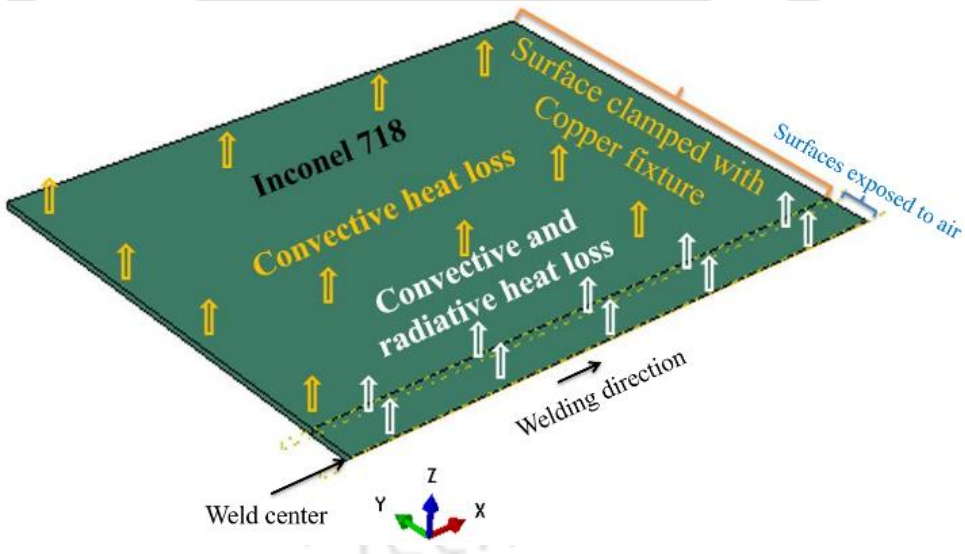

Fig. 4.4 Solution domain of similar welding and boundary interaction

The transient heat transfer model is dependent on specifying thermo-physical properties of the material. The parameters namely, specific heat, thermal conductivity and density, vary upon the temperature. Specific heat (C_p) is the most remarkable parameter among thermal properties required to predict the temperature field during welding simulation. The

magnitude of specific heat increases with increase in the temperature. Another important parameter is the thermal conductivity (k), which accounts for the ability of material to transfer the heat. Lower thermal conductivity signifies that material accumulates more heat than it transfers to the neighboring material, hence resulting in formation of a larger weld bead compared to a material with higher thermal conductivity (k). During dissimilar welding process, material with low thermal conductivity takes longer time to conduct the heat to the neighboring material. This parameter is highly temperature-dependent and increases upon increase in temperature. For welding problem physical properties of the material can be implemented as temperature independent. But temperature dependent thermal conductivity is provided as it falls linearly from room temperature towards the melting point of material. Temperature dependent thermos-physical properties of Inconel 718 are considered in the numerical model as shown in Fig. 4.5 (Dye et al., 2001).

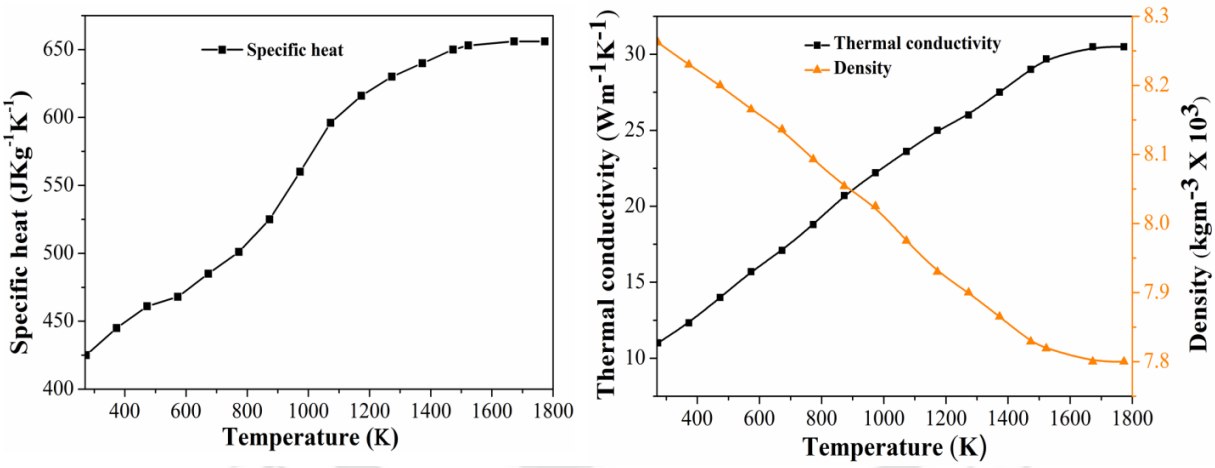

Fig. 4.5 Temperature dependent material properties for Inconel 718

Fig. 4.6 shows the mesh arrangement of the solution domain, as the fusion zone is exposed to a very concentric heat source; the temperature gradient becomes steep, hence very fine meshing is provided to capture the thermal history in these regions. While coarser meshing was created in the area, which are far from the heat flux to reduce computational time and cost. The optimization of mesh size and computational time is one of the most important factors that determines stability and efficiency of the numerical model. In order to achieve this, mesh sensitivity analysis is performed to find optimum mesh size (i.e., at 0.1 to 0.5 mm) and time-step without compromising the quality of the computed results. The optimize, elements size in

the fusion and heat-affected zone is found to be 0.2 mm×0.2 mm×0.07 mm, whereas it is 4.5 mm × 0.25 mm × 0.07 mm in the base material zone. The variation in peak temperature between 0.1 and 0.2 mm mesh size is observed to be very less, i.e., 33 K, but reduces 2.3hr of computational time, Hence, 0.2×0.2×0.07 mm^3 set of mesh size is considered as optimized size with optimum computational time. Continuum eight nodded brick solid elements (DC3D8 type) were selected for diffusive heat transfer in the thermal analysis. The space and time variation of the moving heat source is accommodated by different DFLUX subroutines for each constant and pulsed mode of operation.

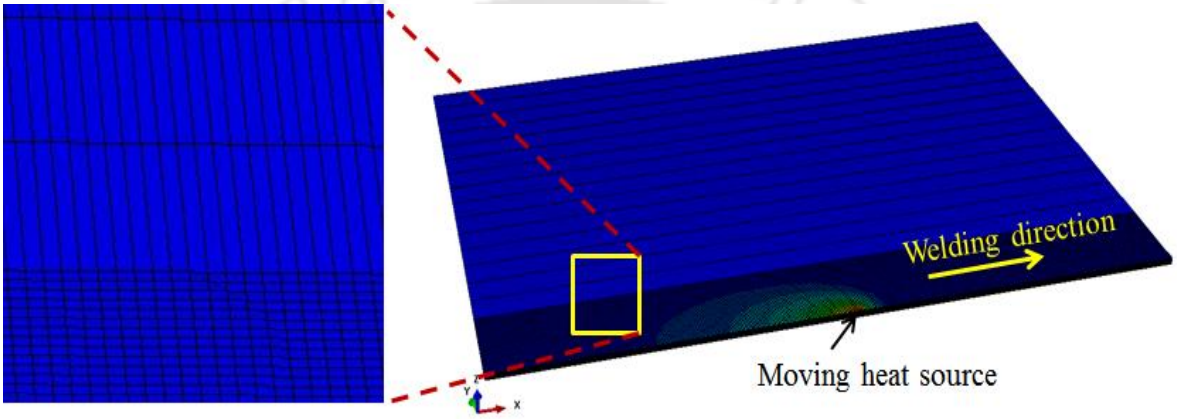

Fig. 4.6 Showing discretized weld plates with heat source moving direction

4.4.2 Model geometry for dissimilar material welding

All temperature dependent thermo-physical properties (i.e. different for solid and liquid phase) for Inconel 718 and AISI 316L material are considered in the thermal model and the material properties of AISI 316L is shown in Fig. 4.7 (Dye et al., 2001; Rahman Chukkan et al., 2015). The weld zone is assigned with the same temperature dependent properties (i.e. thermal conductivity, density and specific heat) corresponding to the base materials (Lee and Chang, 2012).

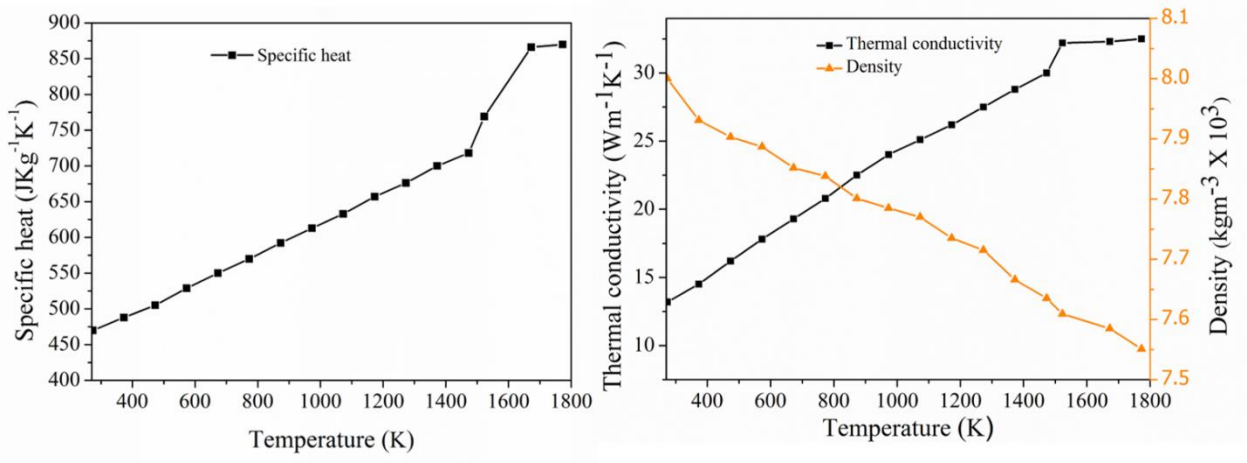

Fig. 4.7 Temperature dependent material properties for AISI 316L.

The solution domain of 70 mm×60 mm×0.7 mm for each material is modeled as compared to the actual experimental dimensions. Emissivity of AISI 316L and Inconel 718 is assumed to be 0.7 and 0.65, respectively. The average convective heat transfer coefficient (h) of the surface which is directly exposed to the air (Fig. 4.8) is taken as 30 W/m^2 K and 35 W/m^2 K for AISI 316L and Inconel 718 respectively (Dye et al., 2001; Jiang and Yahiaoui, 2010). The surfaces which are in direct contact with the copper backing and clamping pates as shown in Fig. 4.8 are assigned a heat transfer coefficient of 1000 W/m^2 K (Baruah and Bag, 2016).

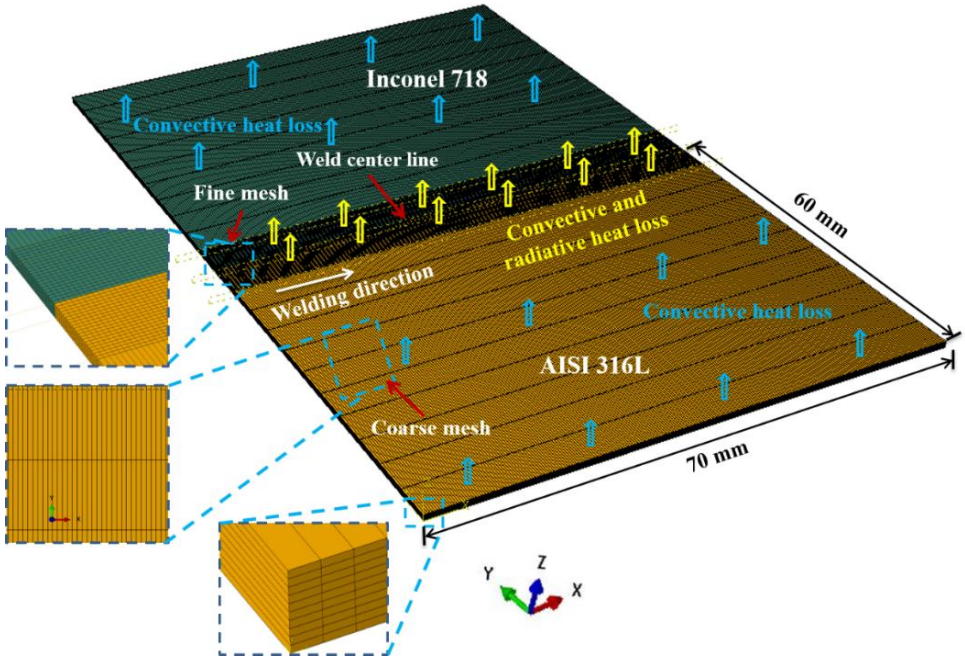

Fig. 4.8 Solution domain of dissimilar welding and boundary interaction

The computational time is reduced by assigning fine meshing near the fusion zone and heat affected zone to accommodate the high temperature gradient whereas coarse meshing is used far away from the weld pool as the temperature distribution in these region is much below the solid phase transformation temperature. Elements size in the fusion and heat-affected zone is 0.25 mm×0.25 mm×0.07 mm, whereas it is 5 mm × 0.25 mm × 0.07 mm in the unaffected zone. The three dimensional 8 nodded liner brick elements (DC3D8) for diffusive heat transfer are generated and employed in the thermal model. Total number of nodes and elements generated in the model are 161711 and 144000 respectively. Gaussian distributed double ellipsoidal heat source is incorporated in the model by using DFLUX user subroutine to represent the welding heat source. The fusion zone time-temperature distribution obtained from the model is then employed to estimate the solidification parameters of the weld pool corresponding to different welding conditions.

4.5 Evaluation of temperature gradient

The impact of temperature gradient (G) and solidification growth rate (R) on final weld microstructure is significant. The maximum variation of these parameters occurs along the weld velocity vector, i.e. in the longitudinal direction. Hence, to explain the microstructural morphology, longitudinal temperature gradient *(G)* along the velocity vector (K/mm) is used to calculate the solidification parameters. The temperature gradient is estimated for each welding condition by using the time-temperature history extracted from the numerical model. The longitudinal temperature gradient of the weld pool (Fig. 4.9) is estimated by the following equation

$$\boldsymbol{G = \frac{T_1 - T_2}{L_{long}}} \tag{4.8}$$

where T_1 and T_2 are the minimum and maximum temperature corresponding to the weld pool. As the heat source approaches to the solution domain between point 1 and 2 (Fig. 4.9), the temperature gradient increases (due to heating phase), and when it moves away the temperature gradient decreases and becomes negative (due as cooling phase).

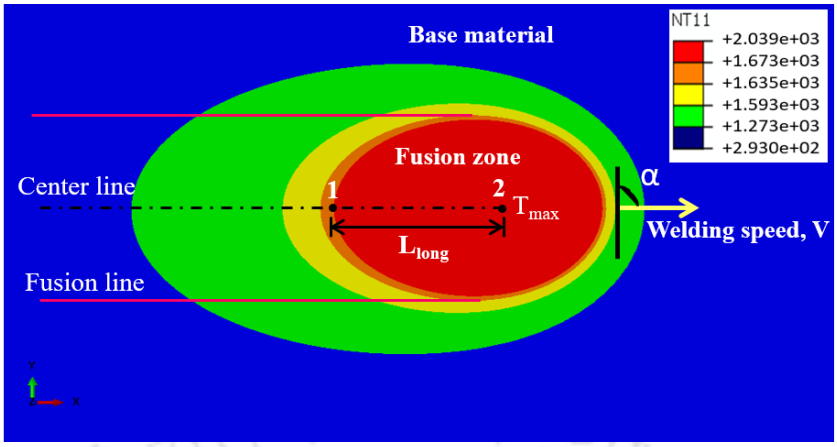

Fig. 4.9 Illustration of temperature distribution over the weld-pool surface in order to estimate the longitudinal temperature gradient

4.6 Summary

In the current chapter, the theoretical background of the conduction based heat transfer model corresponding to similar (Inconel 718) and dissimilar (Inconel 718 - AISI 316L) welding is outlined here. The intention is to develop a numerical model corresponding to the micro plasma arc welding and CO_2 laser welding processes, that is capable of predicting the significant effects of the process parameters on the weld pool characteristics. The developed numerical model is used to predict the weld pool geometry and temperature distribution during pulse and constant current mode of the welding. The current pulsation effect is incorporated by using DFLUX subroutine of commercial software ABAQUS. Double ellipsoidal volumetric heat source is used to approximate the convective heat transport inside the weld pool. After successful validation with the experimentally obtained results, thermal history of the weld pool during welding is extracted to estimate the solidification parameters. The magnitude of solidification parameters affects the final weld morphology and eventually the weld mechanical properties. A correct estimation of the solidification parameters helps to predict the final weld microstructure and corresponding impact on the weld mechanical properties. Hence, an attempt has been made to correlate the numerically obtained results with the experimentally obtained weld bead characteristics.

Chapter 5

Results and Discussion

5.1 Introduction

In the current chapter, results obtained through numerical modeling and experimental analysis for micro-plasma arc welding and CO_2 laser welding of Inconel 718 and AISI 316L stainless steel are presented. The computed results are validated with the experimentally obtained data, that includes thermal cycle, weld bead geometry and dimension of the fusion zone. Post validation, the time-temperature data is used to evaluate the solidification parameters for each welding process and correlated with the weld microstructural morphology. The influence of welding process parameters on weld microstructure and mechanical properties are further analyzed. The microstructural characterization involves SEM, EDX and XRD analysis of the fusion zone, heat affected zone and base material. The pulsation of current improves the solidification morphology as compared to continuous mode. The effect of peak current, duty cycle and pulse frequency on cooling rate, weld morphology and mechanical properties are reported herein. Current pulsation with optimum heat input in µ-PAW shows the improvement in the weld mechanical properties. The average heat input reduced by current pulsation, leads to a high cooling rate and results in fine microstructure and lower segregation of Nb in the interdendritic region. Lower segregation hinders the formation of deleterious Laves phase and improved the mechanical properties of the micro-plasma arc welded Inconel 718. The effect of post-weld solution and different double aging treatments on precipitation of various strengthening phases in micro-plasma arc welded Inconel 718 weld is also reported in the current chapter. The high-temperature solution treatment, dissolves the intermetallic phases formed during solidification and makes a suitable quantity of alloying elements available for precipitation of the strengthening phases. Finally, the weldability of Inconel 718 with AISI 316L stainless steel in autogenous mode is investigated by

employing μ-PAW and CO_2 laser welding technique and the influence of process parameters in mitigating solidification crack is illustrated.

5.2 Micro-plasma arc welding of Inconel 718

Inconel 718 is vulnerable to solidification cracking and microfissuring (liquation crack) in the fusion zone (FZ) and heat affected zone (HAZ) during the fusion welding process (Draxler et al., 2019). The formation of cracking defects are mainly due to micro segregation of Nb in the interdendritic boundaries, that results in formation of Nb-rich brittle intermetallic NbC and Laves phase [$(Fe, Ni, Cr)_2 (Mo, Nb, Ti)$] (Gobbi et al., 1996). The intermetallic phases produces intergranular liquid film which eventually produce sites for micro-crack initiation when subjected to thermal cycles (Mei et al., 2016). Hence, distribution and volume fraction of NbC and Laves phases not only have detrimental effect on the mechanical properties of the weld joint but also consumes a significant amount of useful strengthening alloying elements from the matrix (Gobbi et al., 1996). Several comparative studies are performed between conventional arc welding techniques and advanced welding techniques to minimize the Nb segregation and Laves phase formation (Hong et al., 2008; Huang et al., 2005; Ye et al., 2015). Radhakrishna and Rao (Radhakrishna and Rao, 1994) observed continuous chain of Laves particles in the weldment produced by gas tungsten arc welding (GTAW) process as compared to discrete morphology in the weld produced by electron beam welding (EBW) technique. The lower amount of Laves phase in EBW produces relatively better creep properties as compared to the GTAW weld. The formation of NbC and Laves phases in Inconel 718 weld produces intergranular liquid films when subjected to rapid thermal cycles (Thompson et al., 1991). The liquid film at the grain boundaries then promotes micro-cracks during weld thermal cycle because of constitutional liquation of either Nb-rich carbides or Laves phase (Knorovsky et al., 1989). Chen et al. (Chen et al., 2001) reported susceptibility to HAZ cracking depends on level of segregation of principal alloying elements at the grain boundaries and can be reduced significantly by selection of proper welding technique.

The volume fraction of intermetallic phases and segregational behavior in the weld zone is mainly a function of heat input and cooling rate. Advanced welding techniques, such as laser welding and EBW are beneficial to control the Laves phase formation and mechanical properties of the welded joint by regulating low heat input with a high rate of cooling as compared to the conventional arc welding processes (Odabaşı et al., 2010). The segregational

behavior of GTAW and EBW is entirely different because of wide variety of thermal cycle characteristics (Radhakrishna and Rao, 1997). The tendency of Laves phase formation is found to be greater in GTAW process as compared to concentrated heat/high cooling rate EBW process. When a pulse laser modulates high cooling rate, the secondary dendritic arm spacing reduces and typically produces a finer structure. In effect, substantial segregation of deleterious phases in the interdendritic regions are avoided (Gobbi et al., 1996). The pulsed Nd-YAG laser, characterized by the low heat input with a high cooling rate, improves the grain morphology and lowers Laves phase formation (Janaki Ram et al., 2005). The formation of equiaxed grain morphology results in reduction of segregation and volume of Laves phase formation by breaking the long columnar structure during pulsed welding process (Manikandan et al., 2014). Low segregation and refined microstructure improve the mechanical properties of the welded joint. Therefore, the impact of solidification morphology on the formation of an equiaxed dendritic structure at low heat input with a relatively high cooling rate may reduce the deleterious Laves phases.

High-energy beam welding techniques as EBW and LBW are always advantageous to encounter the segregational problem, but major restriction is the installation and operating cost of these processes. The application of ultrasonic vibration and current pulsation during GTA welding of Inconel 718 resulted in significant reduction of dendritic arm spacing as the cooling rate improves significantly compared to conventional GTAW process (Thavamani et al., 2018, Manikandan et al., 2014). However, there is lack of literature on plasma arc welding of Inconel 718 and the effectiveness of current pulsation of μ-PAW on microstructural refinement and Laves phase formation. Therefore, it is worthwhile to explore the possibility of enhancement of the weld quality by reducing the segregation of various deleterious intermetallic phases in the solidified structure. Hence, micro-plasma arc welding (μ-PAW) in constant and pulse mode is considered for the current study which is known for its constricted arc and higher power density compared to GTAW process. The effect of current pulsation is often neglected by approximating the continuous average current, which is not trivial in small-scale welding process. Hence, the primary objective of the present work is to investigate the effect of pulse parameters on heat input/cooling rate of the fusion zone and corresponding effect on grain morphology and Laves phase formation. A 3D finite element (FE) based thermal model is also developed to trace the thermal history of the welding process during constant and pulse mode

configuration. The simulation is performed by using a moving heat source, which accounted various complex physical phenomena like conduction, convection and radiation heat transfer to the faying surface. The heat source is modulated according to the actual pulse current in temporal frame. Thereafter, the time-temperature profile from the simulation of the inaccessible thermocouple points on the work piece is accounted for the estimation of solidification parameters. The cooling rate and temperature gradient at selective points indicate the solidification modes and typical nature of weld microstructure. Solution treated (at 980°C/ 1h) Inconel 718 sheets of thickness 0.7 mm are used to produce autogenous weld. Solution treatment at high temperature was done to obtain a homogeneous microstructure by putting age hardening and carbide constituents into the solid solution. Autogenous butt-welding was carried out by using μ-PAW machine both in continuous and pulse mode. The process map is indicated in Table 3.2 of Chapter 3.

5.2.1 Characteristics of temperature distribution

The experimental measurement of thermal cycles for inaccessible thermocouple points is extremely difficult because of the complexity of the process. Hence, the finite element-based heat transfer model is developed to predict time temperature history of the fusion zone during welding. Three-dimensional temperature distribution corresponding to CC and PC1 of Table 3.2 at pulse on and off condition is shown in Fig. 5.1. The peak temperature of 2039 K is achieved at the weld center during CC welding condition whereas a peak temperature of 2110 K is reached for PC1 welding because of high pulse current during pulse-on period (Fig. 5.1a). However, the temperature falls below 1396 K with increment of time step during the pulse off period for PC1 welding condition as shown in Fig. 5.1(d-e). The FZ is defined above the liquidus temperature of 1635 K whereas the HAZ is defined below solidus temperature of 1593 K (Thompson, 1988). The mushy zone where liquid and solid phase co-exist is defined between these two temperature isotherms. The temperature distribution of PC1 is shown in Fig. 5.1(a-f). Fig. 5.1(a) depicts the temperature contours at the end of the pulse-on period where Fig. 5.1(b) illustrates at the beginning of pulse-off period. The temperature falls below solidus temperature within 0.14 s (half of the cycle time) during the pulse-off period. Fig. 5.1(f) shows the temperature rise due to the beginning of the applied peak current for the next cycle. The temperature decrement of the entire fusion zone below the solidus temperature during the pulse-off period confirms the complete solidification of the weld pool (Fig. 5.1(c-e)).

Continuous re-melting and re-solidification of the weld pool with the application of pulse current indicates that the solidification behavior in pulse mode is different from the continuous mode. Fig. 5.1(g-h) depicts the temperature profile of CC weld at two different time instants, which are in a quasi-steady state. Fig. 5.2 shows the temperature distribution on transverse cross-section where FZ, mushy zone and HAZ are well defined. The width of FZ for PC1 is found more as compared to CC due to high input over short span of time. The FZ profile is more uniform in case of continuous welding as compared to pulse welding due to interrupted energy supply effectively at low heat input. However, this non-uniformity reduces with increase in heat input. At very high heat input there may be the formation of keyhole and leads to hour glass type of weld profile (Baruah and Bag, 2017).

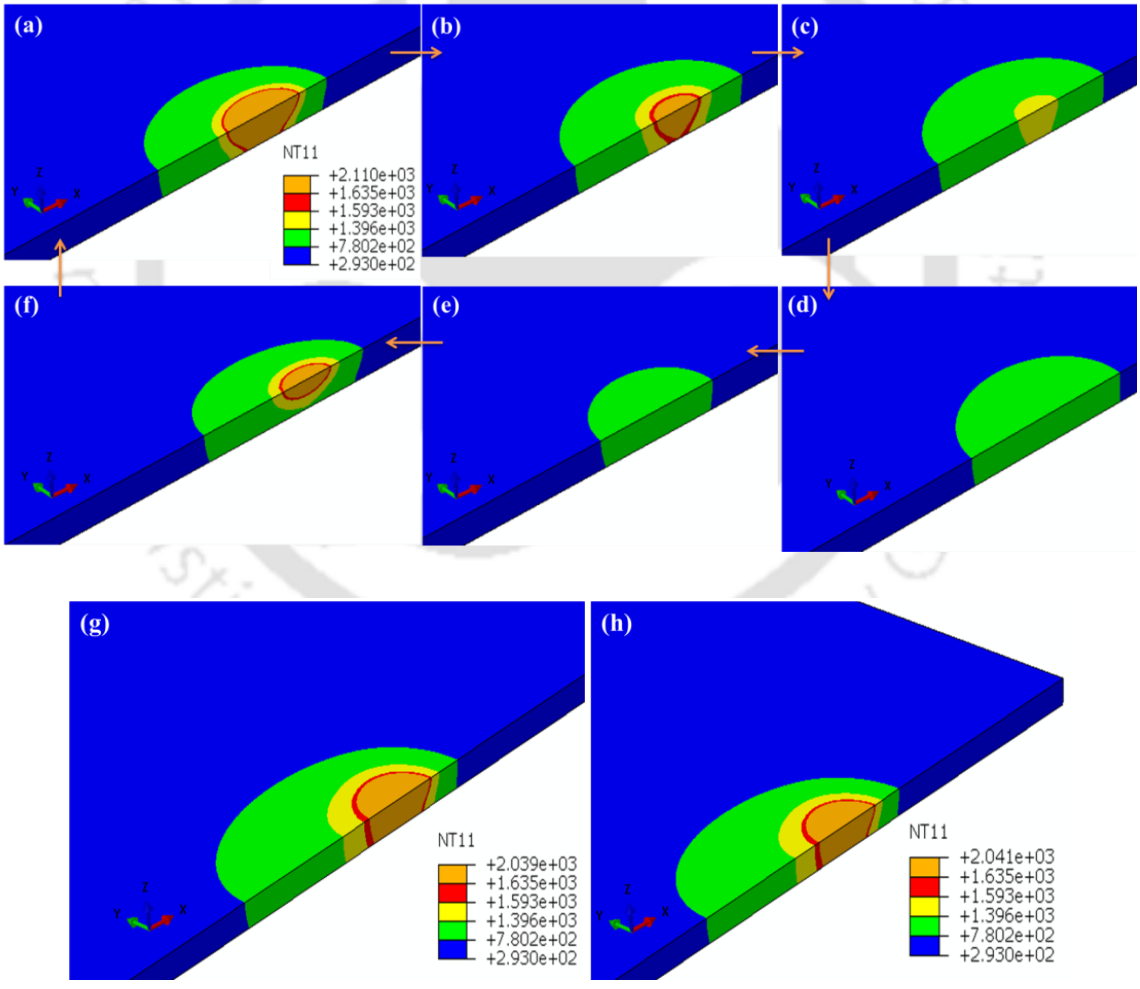

Fig. 5.1 3D computed temperature distribution at: (a, f) pulse-on and (b-e) pulse-off time of PC1 condition; (g, h) at different time step of CC condition

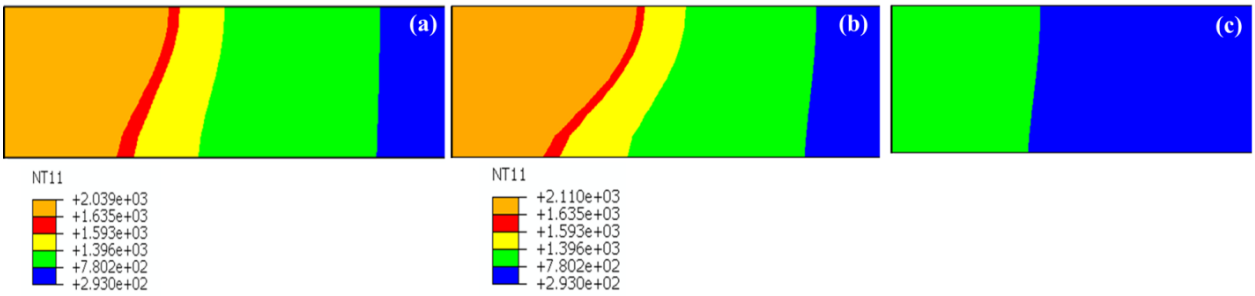

Fig. 5.2 2D cross sectional view of the weld bead showing FZ and HAZ in transverse direction for (a) CC (b) PC1 (pulse-on) (c) PC1 (pulse-off) conditions

The computed macrographs are compared with experimentally measured weld pool shape and size corresponding to different welding conditions. As shown in Fig. 5.3 due to variation in process parameters during CC (52.8 J/mm), PC1 (47 J/mm), PC5 (62.2 J/mm) and PC7 (60.2 J/mm) welding condition, the weld pool profile also varies. However, the shape and size of the simulated weld profile are found in good agreement with the experimentally measured macrographs. The peak temperature achieved is 2387 K for PC5 welding condition which is much below the boiling temperature (3190 K) of Inconel 718(Chen et al., 2011). Hence it can be concluded that the conduction mode heat transfer mainly prevails against keyhole formation within the investigated range of parameters. With increase in heat input, the weld dimension increases and the fusion zone becomes wider. Fig. 5.3(e) shows the comparison between the experimentally measured and computed weld width from the numerical model corresponding to the welding conditions depicted in Table 3.2. The maximum error is found as 7.3% for top weld bead profile at CC welding which defines robustness of the numerical model.

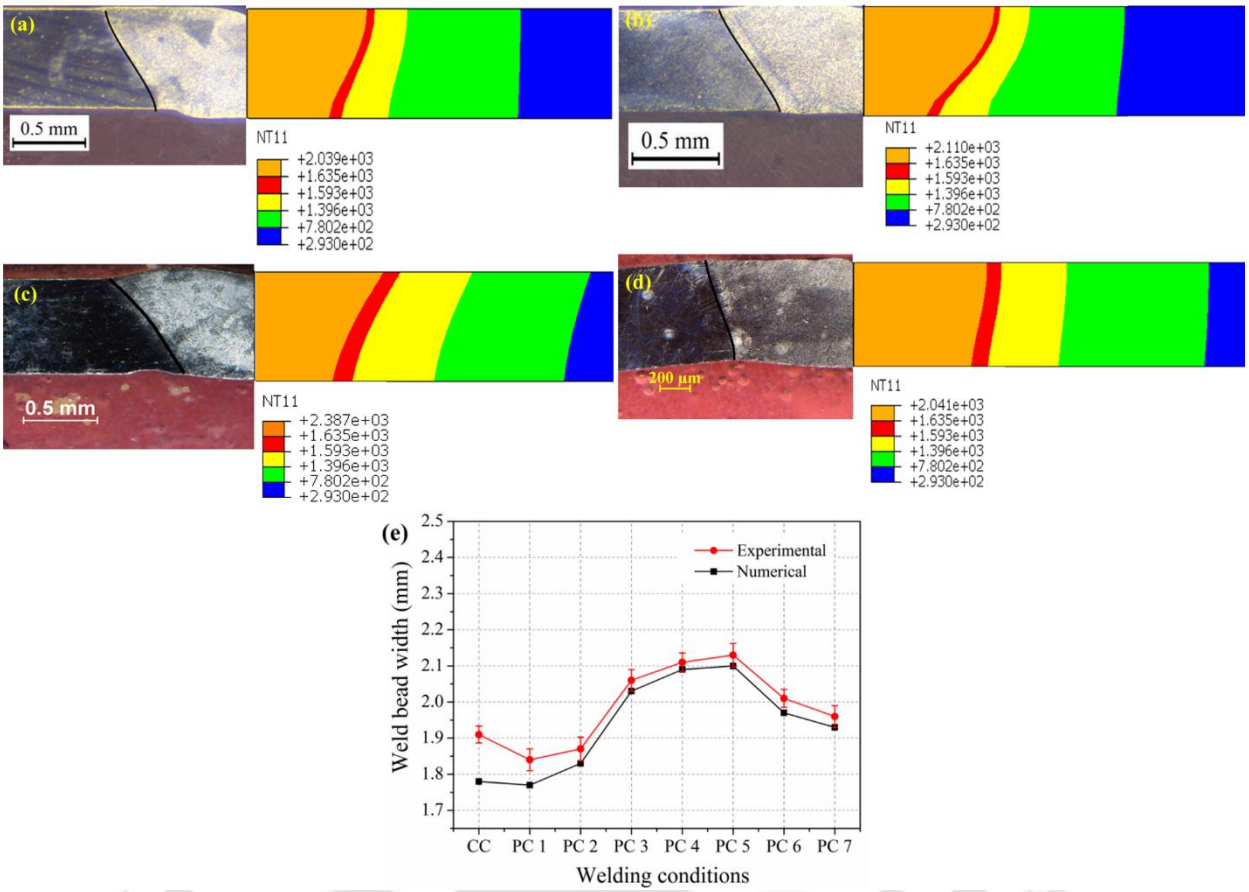

Fig. 5.3 Comparison of experimentally (left) and numerically (right) obtained weld profile for (a) CC (b) PC1 (c) PC5 (d) PC7 and (e) top weld width

Fig. 5.4 depicts the comparison of numerically and experimentally obtained time-temperature profiles at 2.5 mm from the weld centerline for CC and PC1 welding conditions. For continuous welding, the profile is characterized by a single peak as the heat source approaches to thermocouple point and gradually decreases when the arc moves away. The peak temperature of 599 K is achieved by the numerical model against 570 K by the experiment. Multiple peaks (each peak signifies one cycle time) characterize the PC1 welding due to the periodic variation of welding current over time. The maximum temperature of 620 K is obtained numerically against experimental value of 593 K for PC1. The accuracy of temperature measurements depends upon several factors like sensitivity of the thermocouple, peak temperature and distance between the heat source and thermocouple. The temperature difference between experimental and numerically predicted value is less than 5%, hence indicates the robustness of the numerical model. So, numerically predicted temperature data

are further used to investigate the solidification behavior, cooling rate and microstructural morphology of Inconel 718 weld.

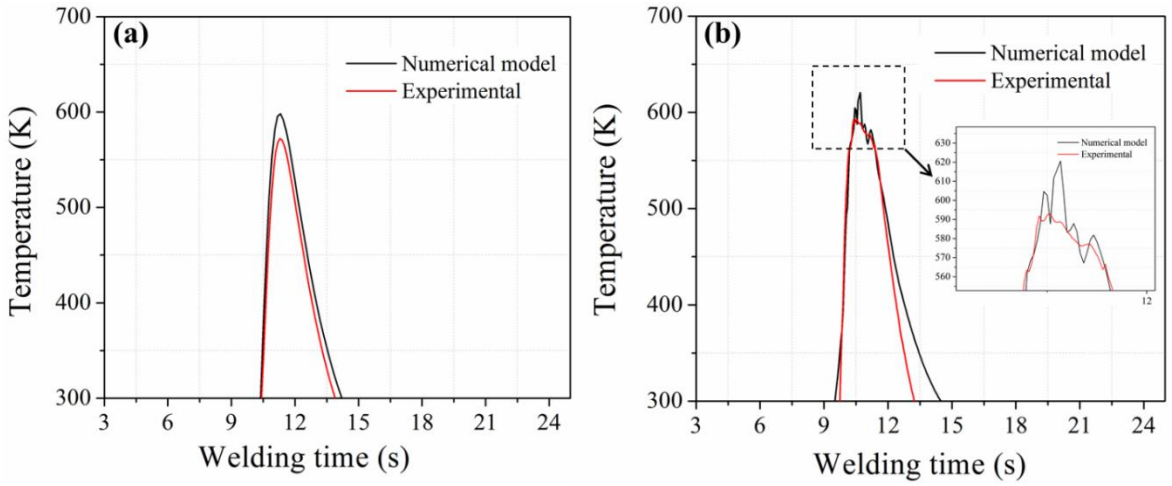

Fig. 5.4 Comparison of time-temperature profiles between computed and experimentally measured quantity for (a) continuous mode (CC) and (b) pulse mode (PC1)

5.2.2 Cooling rate and microstructure

The quality of the final weld joint greatly depends on the welding process, temperature history, and cooling rate. A quantitative knowledge of cooling rate in and around the weld zone is useful for understanding of the final microstructural morphology and its effect on mechanical properties of the welded joint. The time-temperature profile at various welding conditions is utilized to calculate the cooling rate of the weldment. From the earlier work of Arnberg et al. (Arnberg et al., 1993) on solidification under higher temperature gradient, the basic objective of study was to enhance the weld cooling rate, however, is limited by the welding process conditions and process itself. The cooling rate is calculated as

$$\dot{\varepsilon} = GR \tag{5.1}$$

where *G* and *R* represents temperature gradient (K/mm) and solidification growth rate (mm/s), respectively. The solidification growth rate in the weld center line is the maximum and is equal to the welding speed (Manikandan et al., 2014). Hence, the cooling rate can be enhanced by creating higher temperature gradient as the solidification growth rate varies over a small range. A steep temperature gradient in the weld zone often promotes increased instantaneous cooling

rate and results in fine weld morphology. Fig. 5.5(a) shows the estimation of temperature gradient at 2.5 mm from the weld center along transverse direction corresponding to CC mode of welding. Relatively good agreement of temperature gradient is observed between the experimental and numerical results. Fig. 5.5(b) depicts the transient temperature profile and corresponding temperature gradient along the longitudinal direction measured at the weld center line for CC weld. The maximum temperature gradient in this direction is found as 263 K/mm and 176 K/mm during heating and cooling cycle, respectively, with a peak temperature of 2039 K. However, the magnitude of temperature gradient in longitudinal direction is always less than that of the transverse direction due to the formation of elongated weld pool along the weld direction. Hence, to explain the microstructural morphology, longitudinal temperature gradient *(G)* is used in Eq. (5.1). It is obvious that *G* is changing from initial steeper positive value to a shallow negative value with respect to time. The fall in *G* over time corresponds to cooling phase of the weld pool. Hence the maximum cooling rate in the FZ is analogous to the highest negative value of the longitudinal temperature gradient.

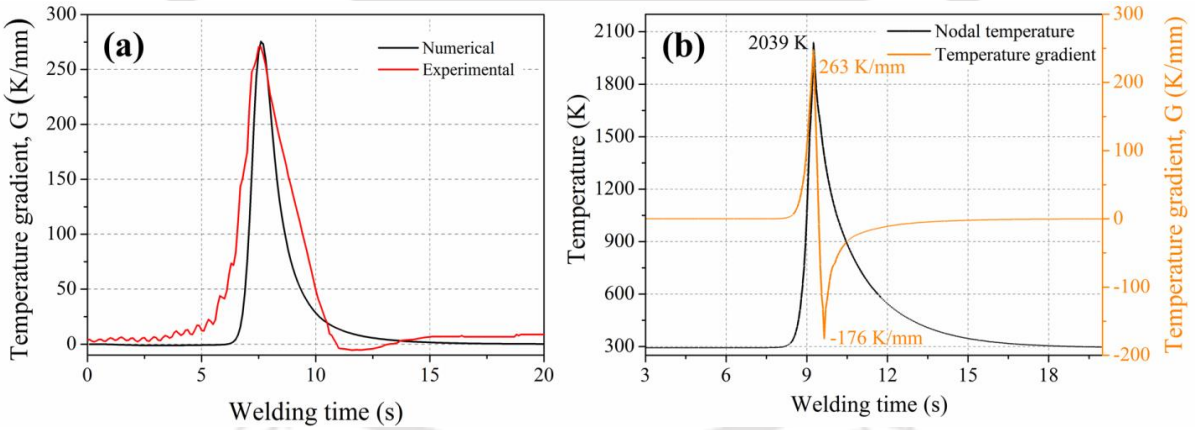

Fig. 5.5 Temperature gradient in transverse direction (a) and longitudinal direction (b) for CC welding condition

The peak temperature attained during welding process and the size of the weld pool has major impact on the magnitude of temperature gradient. The temperature profile depends on the combined effect of several process parameters like pulse peak current, base current, welding speed, duty cycle and the pulse frequency. All these process parameters control the average heat input per unit length. With increase in average heat input, the peak temperature in the weld pool raises that allow the molten pool to last for longer period and hence reduces

the average cooling rate and temperature gradient during cooling period (Janaki Ram et al., 2004). Fig. 5.6 shows the variation of nodal temperature and longitudinal temperature gradient with respect to time. In one cycle, the temperature rises to a maximum value and then drop to a minimum value due to cyclic variation of pulse current and base current, respectively. For PC1 condition, the maximum temperature of 2110 K is reached during pulse on-time and it falls to a minimum temperature of 838 K during the pulse-off period which is far less than the solid state phase transformation temperature (i.e. 1353 K) of Inconel 718 (Thavamani et al., 2018). In the next pulse, the temperature rises to 1848 K, causing re-melting followed by complete solidification. For PC5 condition, due to higher base current and pulse frequency, and lower welding velocity as compared to PC1, the maximum temperature rises to 2387 K and the minimum temperature reaches to 1183 K during pulse-off period. The complete solidification of PC5 takes place after several pulses and in the fourth pulse, the maximum temperature reaches to 1626 K which is above the solidus temperature. It leads to partial solidification of the weld pool. In effect, the allowable time for complete solidification is more and may promote micro segregation in the interdendritic region. For PC6 and PC7 conditions, with increase in duty cycle and pulse frequency, the temperature during pulse-off period increases further to 1272 K and 1597 K, respectively as compared to PC1 and PC5 (Fig. 5.6e and g). The maximum drop in temperature during pulse-off period leads to increase in undercooling for the growth of the solid phase in the fusion zone. Increase in undercooling at the dendrite tip due to curvature effect reduces the micro-segregation by solidifying at a composition close to that of alloy composition (Oreper et al., 1986). The maximum temperature drop between peak and base current is 1272 K for PC1 whereas it is 1204 K, 923 K, 444 K for PC5, PC6 and PC7, respectively. The maximum temperature drop for PC1 is mainly due to the choice of different pulse parameter as compared to PC5, PC6 and PC7 conditions. Periodic temperature variation in the weld pool creates a drastic change of G at the solidification front with respect to time (Manikandan et al., 2014). A transition from a positive to negative gradient enforce an additional amount of heat to flow towards the solid phase (i.e. S/L interface) which results in re-melting of the secondary dendrite arms from the root due to higher constitutional supercooling. It also affects the redistribution of principal alloying elements such as Nb and Mo, resulted in lower segregation at the interdendritic region. The maximum temperature gradient of 301 K/mm (i.e. during heating) is found for PC1 condition

and within two cycles of time span (~ 0.56 s) it changes to a negative gradient of 271 K/mm. Similar trend of thermal gradient is observed for all pulse conditions and is described in Fig. 5.6. With combined effect of base current, pulse frequency and welding speed for PC5, PC6 and PC7 conditions, the magnitude of temperature gradient during cooling (G_c) cycle decreases. The maximum magnitude of 'G_c' for PC1 is mainly due to high peak current with low base current and low pulse frequency. PC7 condition is found to have lower temperature gradient among all other welding conditions that promotes to have high heat input during the welding process. The value of longitudinal temperature gradient along the weld center line during heating and cooling cycle for all welding conditions is depicted in Table 5.1. Cooling rate of the weld pool is calculated by considering the negative temperature gradient magnitude whereas heating rate is calculated by the positive magnitude. Maximum heating and cooling rate of 998 K/s and 840 K/s is achieved, for PC3 and PC1 welding conditions, respectively. With increase in duty cycle and pulse frequency, the magnitude of negative temperature gradient is observed to be decreasing which could be mainly due to overlapping of pulse energy supply.

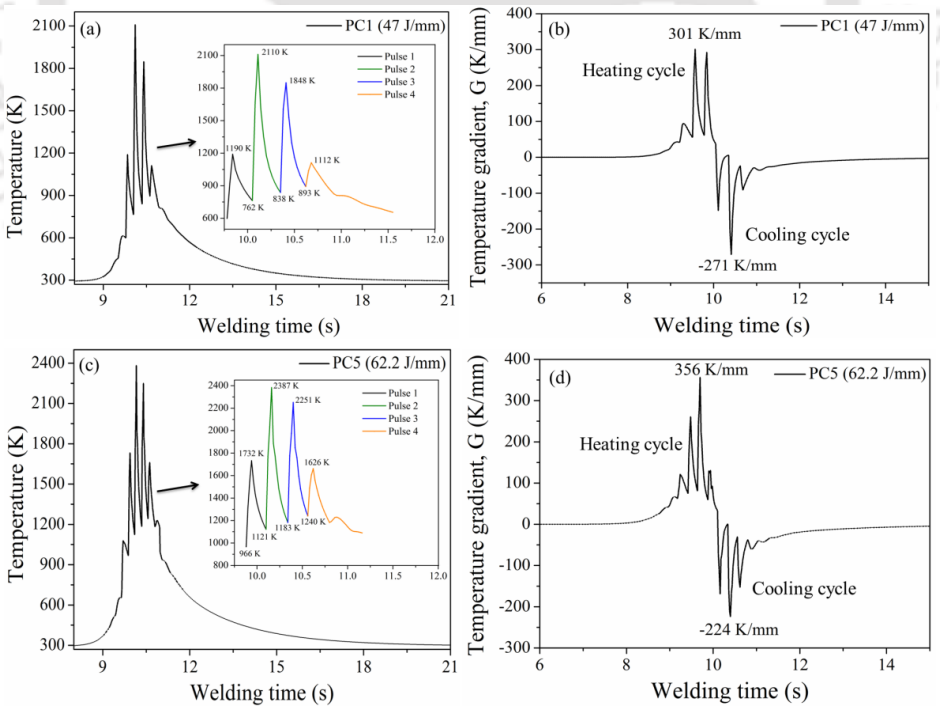

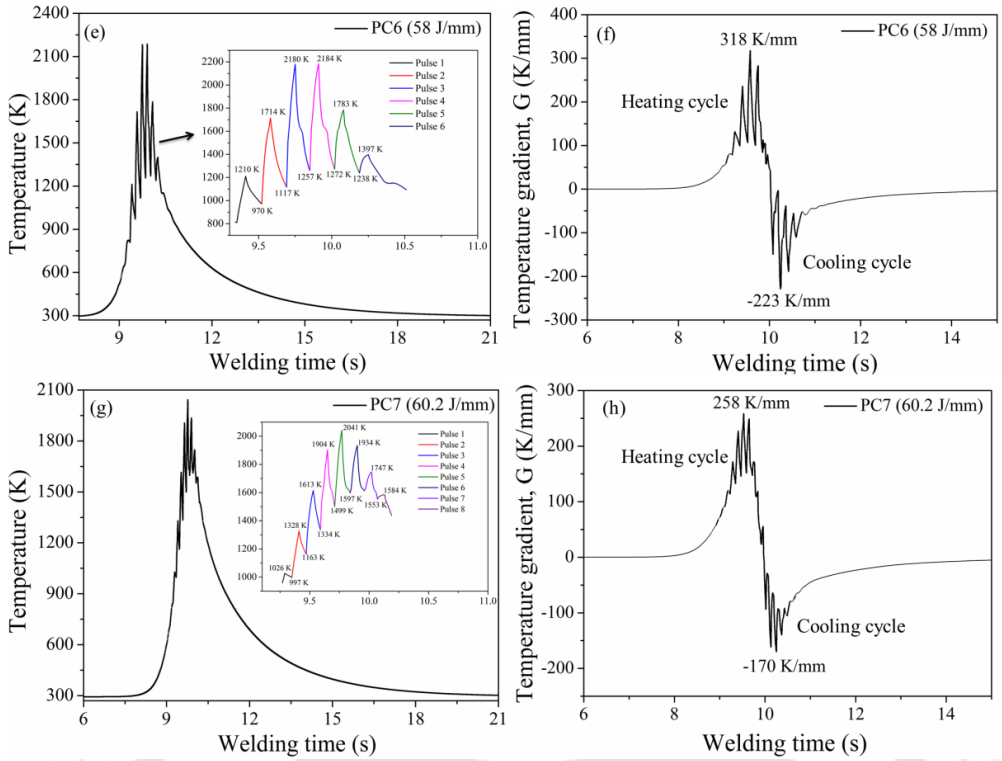

Fig. 5.6 Temperature gradient and time temperature profile for PC1 (a, b), PC5 (c, d), PC6 (e, f) and PC7 (g, h) welding conditions

Table 5.1 Evaluation of solidification parameters

Sample	$T_P(K)$	G_H $\left(\frac{K}{mm}\right)$	G_C $\left(\frac{K}{mm}\right)$	$G_H \cdot R$ (K/s)	$G_C \cdot R$ (K/s)	G_C/R
CC	2039	263	176	947	633	49
PC1	2110	301	271	933	840	87
PC2	2181	335	265	938	742	94
PC3	2140	312	229	998	733	72
PC4	2201	342	224	957	627	81
PC5	2387	356	224	961	605	82
PC6	2184	318	223	922	646	77
PC7	2041	258	170	774	510	56

The other important parameter which governs the mode of solidification is the ratio of *G* and *R*. Low *(G/R)* promotes equiaxed dendritic structure whereas high value promotes

columnar dendritic structure. However, the scale of solidification structure is dominantly controlled by the cooling rate *(G.R)*. Higher *(G.R)* value produces finer dendrites whereas lower value promotes coarse dendrites (Kou, 2003). Fig. 5.7 shows the microscopic view of fusion weld zone for PC1 and CC conditions. Columnar dendrites grown from S/L interface/fusion boundary (FB) is observed in both welding conditions. For PC1 weld, columnar dendritic growth near to FB results in finer and fewer that diminishes in the weld interior due to cyclic variation of temperature and enhanced cooling rate (Janaki Ram et al., 2004). Fragmentation of columnar dendrites occurs in the weld center due to current pulsation, results in lower interdendritic segregation. However, for CC weld, the continuous coarse columnar structure is seen near the fusion boundary and even at the weld interior (Fig. 5.7b).

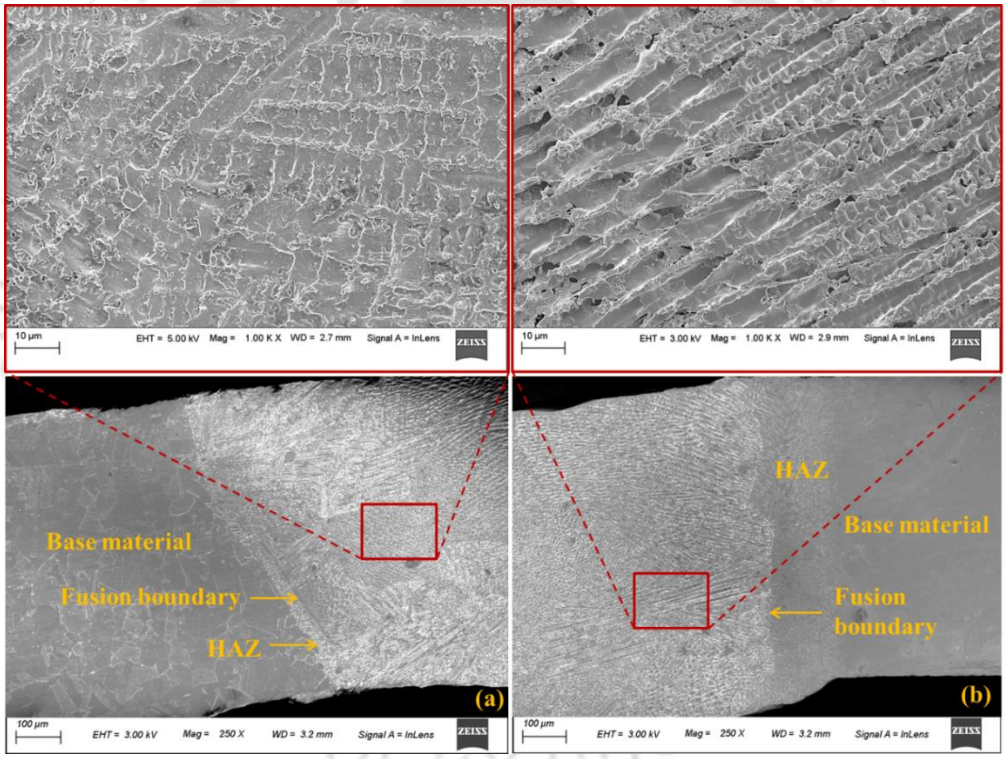

Fig. 5.7 Microstructure of (a) pulse (PC1) and (b) continuous (CC) welding condition

The major issue associated with the fusion welding of Inconel 718 is the segregation of Nb, Ti and Mo in the interdendritic region which leads to the formation of various deleterious intermetallic phases (i.e. NbC and Laves) during solidification. These secondary intermetallic phases promote microfissuring or liquation cracks in the HAZ, fusion boundary and FZ (Cieslak et al., 1990; Radhakrishnan and Thompson, 1992). Laves phase in Inconel

718 is one of the major unavoidable solidification phase and is always found to present in the interdendritic region of as-solidified microstructure. Fig. 5.8 shows higher magnification SEM images of various fusion zones with different welding conditions and cooling rates. Very fine and fragmented Laves particles are observed for PC1 weld (shown with arrow) whereas continuous coarse phases are observed for other condition. The average length/thickness of interdendritic Laves particles are found as 1.81 μm (CC), 1.12 μm (PC1), 2.3 μm (PC5), and 1.9 μm (PC7). Due to higher cooling rate of PC1, the volume of Laves phase reduces significantly as compared to the other welding conditions which is evident in Fig. 5.8(b). Whereas segregation increases remarkably due to lowest cooling rate in PC5 welding condition and results in relatively higher volume of Laves phase formation. The formation of Laves and other carbides consumes a significant amount of favorable alloying elements from the metal matrix which results in weld quality deterioration. Hence, control of Laves phase in the interdendritic regions improves the mechanical properties of the welded joint.

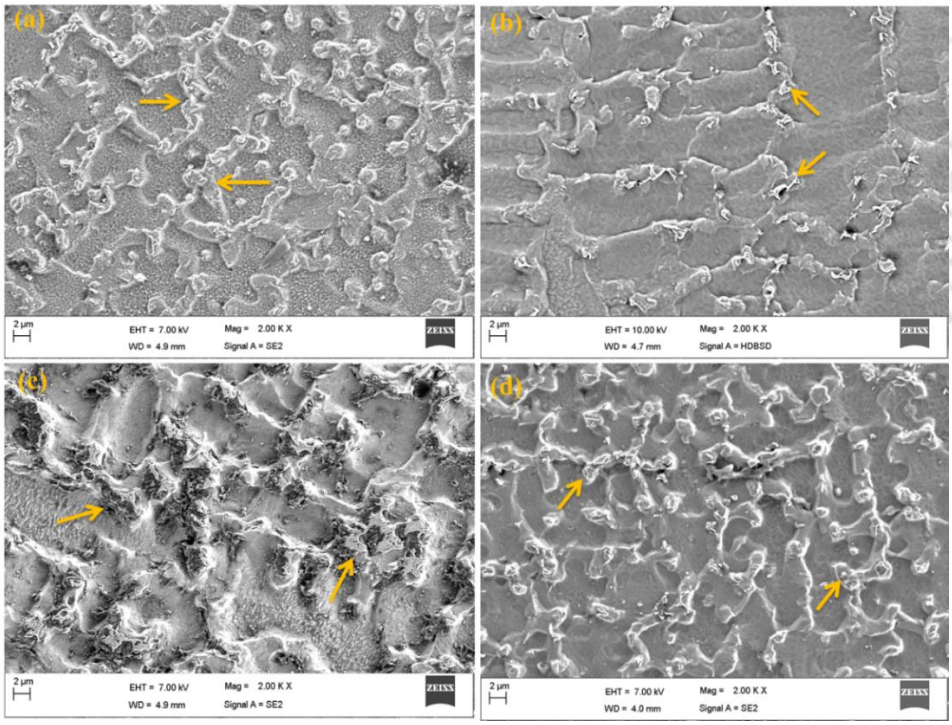

Fig. 5.8 SEM images of (a) CC (b) PC1 (c) PC5 and (d) PC7 weld center zone

Fig. 5.9 shows the lower magnification SEM images of FZ for welding conditions depicted in Table 3.2. The correlation of solidification parameters i.e. *(G.R)* and *(G/R)* with the morphology of SEM micrographs are possible outcome here. The maximum cooling rate of

840 K/s for PC1 weld results in very fine microstructure in the weld zone as well as lower segregation in the interdendritic region as compared to other conditions (Fig. 5.9b). The fusion zone microstructure is found to become coarser with decrease in cooling rate. The minimum cooling rate of 627 K/s, 605 K/s and 510 K/s are achieved for PC4, PC5 and PC7 welding conditions. As a result, the final microstructure becomes coarser and may lead to higher segregation of Nb in the interdendritic region (Fig. 5.9e, f, and h). The magnitude of *(G/R)* for PC1 to PC6 conditions is relatively higher than the other welding conditions. As a result, the final microstructure morphology becomes columnar dendritic type. The magnitude of *(G/R)* is lower in case of CC and PC7 as compared to other cases, which results in interconnected equiaxed type of microstructure at the weld center (Fig. 5.9a and h). The PC6 condition has higher cooling rate *(G.R)* as compared to PC4, PC5 and PC7 which results in finer microstructure (Fig. 5.9g). The secondary dendritic arm spacing of PC1 is found as 4.1 ± 0.9 µm, whereas it is 4.8 ± 1µm (PC2), 4.9 ± 1µm (PC3), 6.87 ± 1.4µm (PC4), 7.3 ± 1.3µm (PC5), 6.09 ± 1µm (PC6), and 7.1 ± 1.1µm (PC7) for other welding conditions.

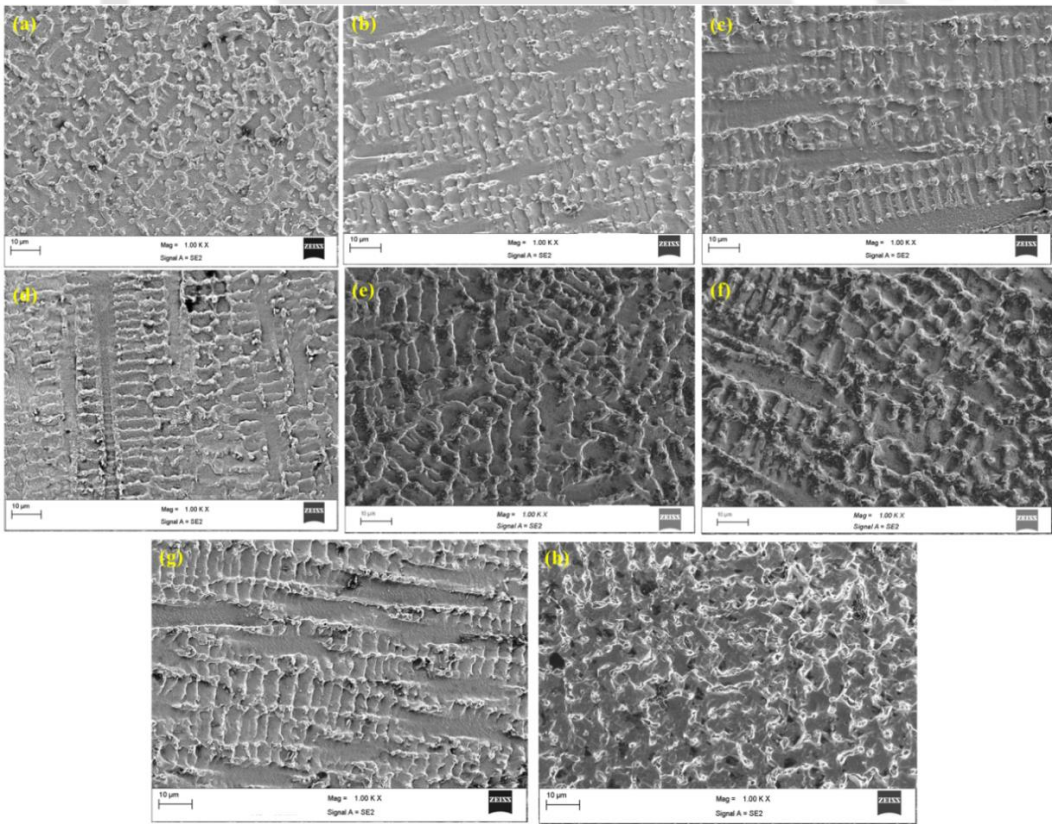

Fig. 5.9 SEM images showing fusion zone morphology for (a) CC (b) PC1 (c) PC2 (d) PC3 (e) PC4 (f) PC5 (g) PC6 and (h) PC7 welding conditions

The average Nb concentration (wt%) in Laves phase is estimated by EDX spot analysis. The concentration of Nb, Ti and Mo are considerably high in the dendritic boundaries as compared to the core. Fig. 5.10 shows that Nb concentration in the boundary is five times of the dendritic core region and two times of the base material composition. As Nb is the main compositional element of Laves phase, hence presence of the deleterious secondary Laves phase is obvious in the FZ. But, at high cooling rate, the final microstructure gets finer as seen in the case of PC1. Hence, by increasing the weld cooling rate, the Laves phase formation can be restricted up to a large extent.

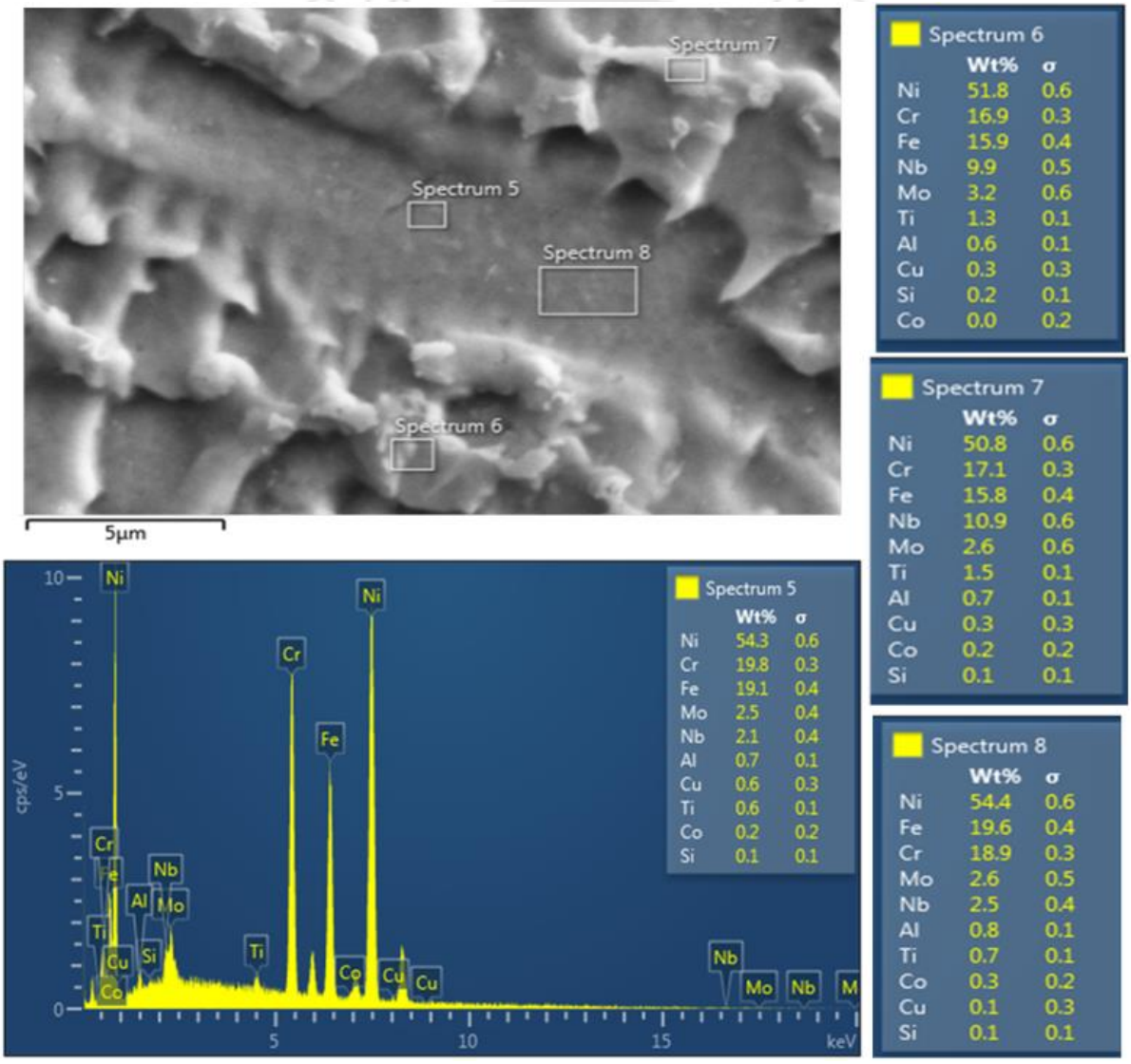

Fig. 5.10 EDX analysis of Laves phase for PC5 welding condition

5.2.3 Influence on mechanical properties

The stress-strain diagram for base material and all other welded joints are shown in Fig. 5.11(a) and the significant data are depicted in Table 5.2. All the welded samples are found to fail in the FZ as shown in Fig. 5.11(b) and (c). The tensile strength of the base material is found to superior as compared to the welded samples. The strength of PC1 and PC2 are found to be 96% and 95% of the base material whereas the strength of PC5 and PC7 are reduced to 72% and 74%. The properties of CC are found superior to high heat input cases (i.e., PC4, PC5, PC6, PC7). This is because of high cooling rate (Table 5.1), which probably reduces Laves segregation in the grain boundary and produces relatively fine equiaxed interconnected type microstructure. The heat input in PC3 weld is more than CC weld but current pulsation favors to achieve a steep temperature gradient. As a result, the cooling rate has increased and produced a fine microstructure along with superior tensile strength. It is obvious that rapid heat extraction with sudden change in temperature gradient at the S/L interface is observed in pulse welding condition. The secondary dendrite arms are normally shortened because of temperature gradient induced compression in the mushy zone (Ma, 2004). These factors are due to the periodic variation of the input energy to the molten pool that results in additional convective flow due to thermal fluctuations. In effect, high cooling rate promoted by current pulsation favors the reduction of columnar dendrite arm spacing and segregation of Laves phase in the dendritic boundary which further improves the tensile properties of the welded joint. The percentage elongation of PC1 welded sample is found as 96.4% as compared to BM which is superior to all other welding cases. Table 5.1 indicates that the minimum variation in cooling rate *(G.R)* as well as *(G/R)* ratio produces the highest quality welded joint. The weld joint properties of PC2 are nearer to PC1 and are characterized by the lower variation of solidification parameters. These welding conditions are corresponding to the lowest heat input and the highest cooling rate (Table 5.1).

Table 5.2 Tensile test and joint efficiency of welded samples

	BM	**CC**	**PC1**	**PC2**	**PC3**	**PC4**	**PC5**	**PC6**	**PC7**
0.2% Proof stress (MPa)	564	459	551	498	481	413	390	394	336
UTS (MPa)	935	764	898	887	847	705	675	702	685
Elongation (%)	19.7	14.5	19	18.6	16.6	11.4	11	13	12.5
Joint efficiency (%)	--	81.7	96	95	90	75	72	75	74

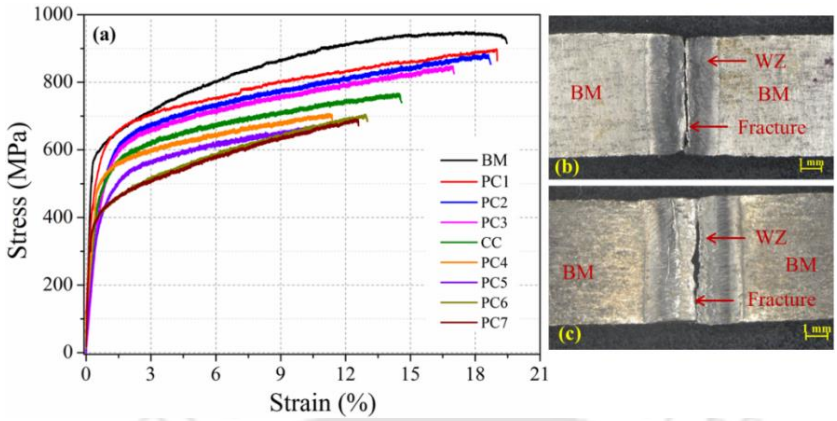

Fig. 5.11 (a) Stress-strain curve of base material and welded joints; (b, c) showing fracture location of CC (b) and PC5 (c) welding condition

The SEM images of the fracture surface of the base material and welded samples are shown in Fig. 5.12. The base material fracture surface exhibits a very fine dimple structure free from micro voids and cracks, resulting in a ductile mode of failure as compare to the welded samples. The fracture surfaces of CC and PC1 weld exhibit a shallow dimple feature along with various crack initiation sites as shown in Fig. 5.12(e) and (f). The presence of Laves particles in the interdendritic region is the main cause of early failure which creates favorable sites for micro crack initiation in the Laves-matrix interface. Hence it is evident that the fracture occurs preferentially along the interdendritic regions due to the presence of Laves phase and results in lower ductility of the joint. Fine and deeper dimples are observed in the fracture surface of PC1 (Fig. 5.12b) as compared to CC weld (Fig. 5.12c).

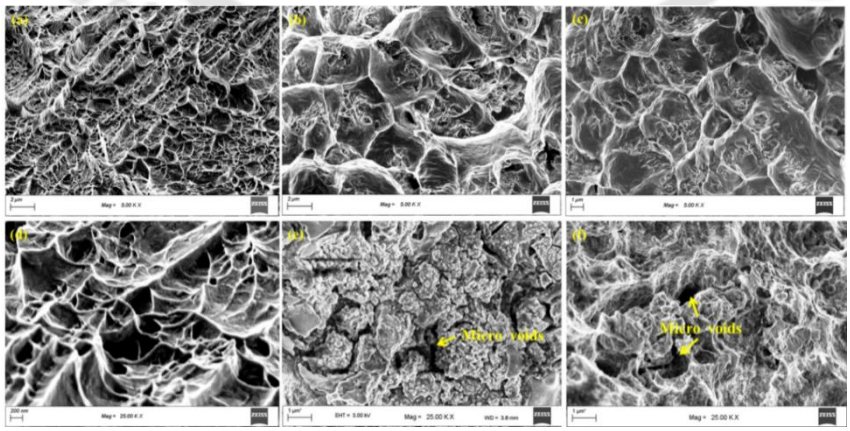

Fig. 5.12 Tensile fracture surfaces in lower and higher magnification (a, d) base material, (b, e) CC welded sample and (c, f) PC1 welded sample

The micro hardness profiles for all welding cases are depicted in Fig. 5.13 and the average hardness values of base material, FZ and HAZ is given in Table 5.3. Three measurements are taken at the same location and the average value is reported with a scatter of ±4 -7%. In solution treated condition, the average base material hardness is found to be 219 HV. The variation of hardness is clearly observed among the FZ for all welding conditions. The FZ hardness value has decreased with increase in heat input which could be mainly due to the higher segregation of Nb and Ti (Mei et al., 2016). A stronger micro-segregation will promote the formation of continuous thick Laves phase in the FZ and could be the main reason of lowering the FZ hardness value. For PC1 weld, the FZ micro hardness is found more than the base material and other samples. The higher hardness value in FZ of PC1 and PC2 weld is mainly due to the refined microstructure at relatively higher cooling rate which leads to the reduction of micro-segregation (Cao et al., 2009). In case of PC7, the FZ hardness is almost reduced to 24% to that of the base metal since it follows relatively lower cooling rate of 510 K/s. The drop of hardness value in HAZ is evident in all the welding cases, which is mainly due to higher attained temperature in this zone that leads to dissolution of precipitates above 900 °C and cause grain coarsening (Qian and Lippold, 2003). However, the exact reason for softening at HAZ needs further investigation.

Table 5.3 Average hardness value at different welding conditions

Sample name	Base material	Fusion zone	Heat affected zone
CC	219.5 ± 9.5	213.1 ± 5	197.4 ± 7
PC1		225.5 ± 6	209 ± 8
PC2		220.9 ± 5	202.5 ± 9
PC3		208 ± 4.5	199.5 ± 9
PC4		188.6 ± 4.5	189.2 ± 12
PC5		183.5 ± 4	187.5 ± 13
PC6		170.3 ± 10	167 ± 11
PC7		172.2 ± 9	170 ± 14

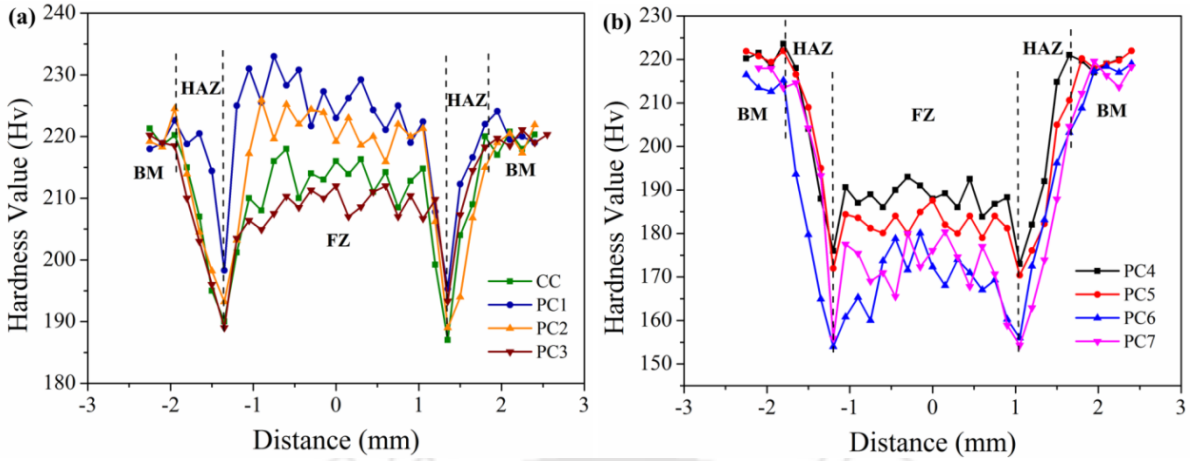

Fig. 5.13 Hardness distribution at different welding conditions

5.2.4 Summary

The outcome of the present work confirms the formation of deleterious Laves phases during fusion welding of Inconel 718. Segregation of various useful alloying elements in the interdendritic region from metal-matrix is confirmed by EDX and SEM analysis. Formation of these secondary phases deteriorates the tensile and hardness properties by providing preferable sites for crack initiation. Formation of these micro-voids during tensile test is evident from the fractograph analysis. The solidification parameters are found to have direct impact on weld microstructural morphology. The cooling rate is more deterministic parameter as compared to the solidification mode. Higher cooling rate refines the weld microstructure and as a result, the segregational effect reduces in the interdendritic region. By implementing current pulsation, it is possible to obtain the welded structure at a lower heat input with higher cooling rate as compared to constant current mode. Moreover, the variability in the solidification parameters i.e. *G.R* and *G/R* due to melting and re-melting (solidification or re-solidification) by the pulsation effect is also a deterministic factor to obtain a sound quality weld joint. The following conclusions are derived from the current study on micro plasma arc welding of Inconel 718.

- Full depth of penetration is achieved at a heat input of 52.8 J/mm for constant mode of current whereas it is 47 J/mm in case of pulse current. The maximum cooling rate of 840 K/s is attained at low average heat input (47 J/mm) by current pulsation effect. Laves phase in the interdendritic region reduces considerably at this cooling rate and achieves joint efficiency of 96% and ductility of 96.4%.

- Chain of columnar structure has seen to break into equiaxed structure below a *(G/R)* value of 56. The lowest variability in *G.R* and *G/R* between heating and cooling phase in pulse mode produces the highest quality weld joint.
- The secondary dendritic arm spacing is reduced by 44% and average Laves particle size by 51% with the lowest heat input welding (i.e., PC1) compared to high heat input welding process (PC5).
- Segregation of secondary phases enriched with Nb, Mo and Ti are observed in the interdendritic region of solidified zones and found increasing with reduction in cooling rate.
- Heat input above 60 J/mm, the average cooling rate at pulse current decreases as compared to constant current mode (52.8 J/mm) and leads to higher segregational effect and relatively inferior mechanical properties.
- High welding cycle time and pulse frequency (5.8 Hz and 8.3 Hz) have detrimental effect on the mechanical properties. Cooling rate above 733 K/s is found to have beneficial effect on welded component with a joint efficiency and ductility of more than 90% and 81%, respectively.
- With increase in heat input, the average hardness in the fusion zone decreases. Overall, current pulsation with low heat input (less than 52 J/mm) results in significant improvement of the weld microstructure.

5.3 Post weld heat treatment of micro-plasma arc welded Inconel 718

The effect of post-weld solution along with different double aging treatments on precipitation of various strengthening phases in micro-plasma arc welded Inconel 718 weld is carried out in the current section. The formation of intermetallic phases in the Inconel 718 weld deteriorates the mechanical properties and quality of the weld joint and explained in section 5.2. The high-temperature solution treatment at 1165ºC/1 h has dissolved these intermetallic phases and makes a suitable quantity of alloying elements accessible for precipitation of the strengthening phases. To analyze the impact of aging temperature and holding time on δ, γ' and γ" phase precipitation, four different heat treatment paths are designed. The heat treatment holding time is reduced by 53% on the welded component by applying a higher aging temperature compared to the conventional aging temperatures. The variation in aging temperature and holding time followed by solution treatment changes the platelet morphology

of the δ phase to needle shape in the grain boundary. Significant enhancement in the tensile strength and weld hardness is witnessed due to duplex aging treatment compared to as-welded condition. The XRD analysis confirms the precipitation of γ' and γ'' strengthening phases inside the grain and δ particles in the grain boundaries.

5.3.1 General background

Fusion welding is one of the crucial fabrication process adopted by aerospace industries to produce complicated structures without altering the material property. However, the involvement of high temperature heat source during welding induces microstructural heterogeneity in the fusion area. As a result, it is essential to eliminate the non-uniformity across the welded component through suitable design of post weld heat treatments. Thin sheets of Inconel 718 in annealed and aged conditions are suitable for making fan containment systems for supersonic application due to its excellent impact strength at elevated temperature (Pereira and Lerch, 2001). Inconel 718 solidifies in dendritic mode over a wide solidification range of 151°C during the fusion welding process; hence cause segregation of useful alloying elements and results in formation of intermetallic phases in the interdendritic region. The intermetallic phases could be dissolved back to the bulk solution by proper design of post-weld heat treatments. Hence, the purpose of present investigation is to analyze the response of intermetallic phases to various post weld heat treatment (PWHT) techniques and precipitation of various strengthening phases. The effect of holding time and aging temperatures on microstructural morphology, distribution of δ particles and strengthening phases are correlated and its impact on weld tensile properties and hardness distribution is investigated.

In the present investigation, the response of the fusion zone Laves phase to various heat treatment techniques on the reduction of Nb concentration and precipitation of various strengthening phases is envisaged. The effect of holding time and aging temperature on microstructural morphology, distribution of δ particles and strengthening phases are correlated. In most of the reported works, post-weld treatment holding time varies between 16 h to 100 h depending upon the holding temperatures (Banerjee et al., 2005; Qian and Lippold, 2003). However, a higher holding time at the peak temperature increases the operational cost by many folds, as a result optimization of the post weld treatment need to be addressed. Hence the current work attempts to reduce holding time of the post-weld treatment without compromising the mechanical properties of micro-plasma arc welded components. Further, the effect of

different aging temperatures on precipitation morphology and its impact on weld tensile properties and hardness distribution is investigated.

As reported in section 5.2.2, at lower cooling rate (*G.R*), the weld final microstructure becomes coarser and leads to a higher segregation of Nb in the interdendritic region. Hence, to study the PWHT response on various intermetallic phases, PC4 welding condition (with heat input: 60 J/mm) is considered for the current analysis. The welded samples are subjected to the various solution and aging treatments (in Fig. 5.14) to precipitate various strengthening phases at different temperatures. The different post-weld treatments are named as (a) aged (direct aging at 760ºC/8 h/Furnace cooling to 680ºC/6 h/Air cooling), (b) ST (only solution treatment at 1165 ºC/1 h/Air cooling) (c) STA1 (solution treatment at 1165 ºC/1 h/Air cooling followed by double aging at 960ºC/1 h/Furnace cooling plus 760ºC/5 h/Furnace cooling), (d) STA2 (solution treatment at 1165ºC/1 h/Air cooling and aging at 760 ºC/8 h/Furnace cooling plus 680ºC/6 h/Air cooling).

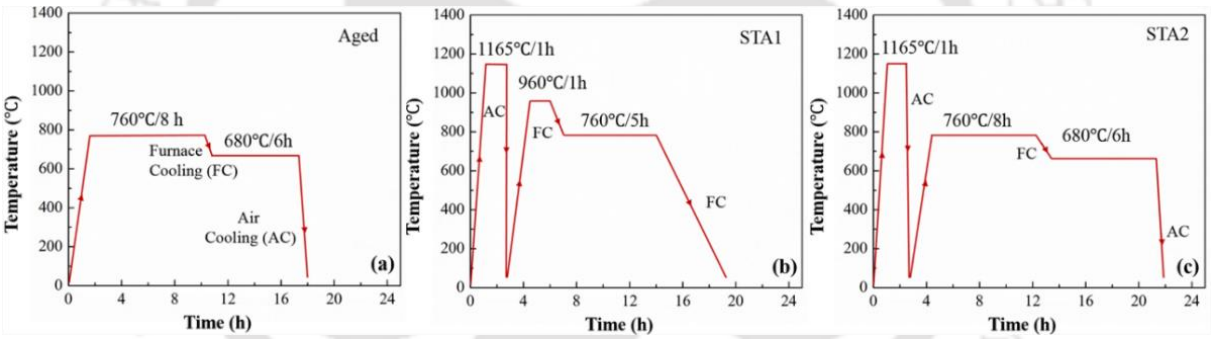

Fig. 5.14 Post weld heat treatments: (a) aged, (b) STA1 and (c) STA2 conditions

5.3.2 Macro and micro structural characterization

The cross sectional view of as welded and heat-treated samples are shown in Fig. 5.15. The dendritic solidified structures are witnessed in the fusion zone for as-welded and aged condition samples. The aged specimens do not show any apparent change in the fusion zone and the microstructure due to the involvement of very low aging temperatures (i.e., 760 ºC and 680 ºC). However, precipitation of δ, γ″, and γ′ strengthening phases takes place during the treatment. In ST, STA1, and STA2 conditions, due to the involvement of high-temperature solution treatment (i.e., 1165 ºC), the dendritic structure along with various secondary phases are dissolved back into the austenite (γ) matrix and forms a homogeneous microstructure (Fig. 5.15c-d). The average equiaxed grain size of 162 μm (ASTM 2-3) is observed in the FZ of ST

weld as compared to 252 μm (ASTM 0-1) and 183 μm (ASTM 1-2) for STA1 and STA2 weld, respectively. The development of fine grains in STA2 weld is mainly due to the higher aging time to that of the STA2 weld (Gobbi et al., 1996).

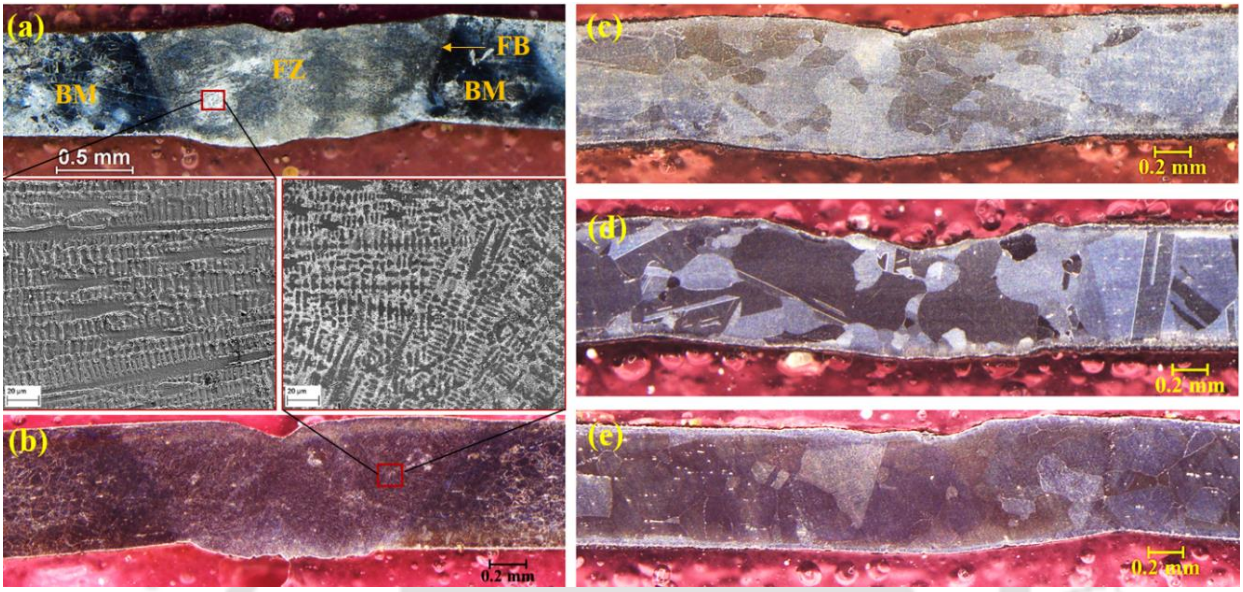

Fig. 5.15 Morphological variation of fusion zone at different condition (a) solidified dendritic structure (as-welded), (b) partially dissolved dendritic structure (direct aged), (c) formation of equiaxed grains after solution treatment (ST), (d) grain coarsening due to aging (STA1) and (e) (STA2)

The higher magnification SEM images of as-welded, aged, and ST samples are shown in Fig. 5.16. The as-welded fusion zone consists of a mixture of columnar (near fusion boundary) and equiaxed (weld interior) dendritic morphology (Fig. 5.16a). The variation in dendritic morphology is primarily due to the variation of the temperature gradient across the fusion zone. The intermetallic Laves phase is clearly witnessed in the interdendritic region and shown with the arrow marks. The length of discrete Laves particles in the weld interior are varying over a range of 1 μm – 5 μm, and the width is varying between 0.5 μm – 2 μm. In the aged condition, the microstructure has not changed significantly as compared to the as-welded condition, but precipitation of δ (Ni_3Nb) needles by limited dissolution of the Laves phase is witnessed and shown in Fig. 5.16(b). The δ phase is a stable precipitate with an orthorhombic structure and is formed mainly due to aging treatment at 760ºC/8h. Precipitation of principal (γ'') and secondary (γ') strengthening phases around the Laves phase is also witnessed and

shown in Fig. 5.16(b). Precipitation of these strengthening phases is mainly due to the aging treatment at 680ºC/6h. The temperature (760ºC) is not enough to dissolve the deleterious Laves particles and other intermetallic completely in the interdendritic region. Hence, solution treatment at 1165ºC is carried out to dissolve it back into the solid solution to produce a homogeneous microstructure. The fusion zone microstructure of the solution treated sample is shown in Fig. 5.16(c). The post-weld solution treatment has completely dissolved the existing dendritic structure and produced equiaxed grains throughout the fusion zone. The grain boundaries are found to be decorated with carbide particles, having a width of almost 150-200 nm. Micro-fissures sites of approximate length 500 nm are also observed near to the carbide particles and shown with the arrow mark. The dissolution of the Laves phase during the solution treatment enhances the availability of Nb for the formation of MC type of carbides (i.e., NbC and TiC). However, some of the micro segregates (enriched with Nb and Ti) are not even possible to dissolve at a high solution temperature of 1250ºC (Tucho et al., 2017). Hence the grain boundary micro-fissure is mainly due to the presence of Nb and Ti-rich constituents, responsible for the constitutional liquation when subjected to elevated temperature during the solution treatment (Cao et al., 2009).

The SEM images of STA1 and STA2 conditions are shown in Fig. 5.17. The grain boundaries are decorated with platelet type (STA1) and thin needle shape (STA2) δ phases, precipitated during the aging treatments. In STA1 condition, double aging at 960ºC/1h and 760ºC/5hr is followed by solution treatment at 1165ºC/1h. The TTT diagram indicates the possible strengthening phases in the grain boundary are δ phase (due to aging at 960ºC/1h) along with γ″ and γ′ phases (due to aging at 760ºC/5h) in the austenitic (γ) matrix. The energy-dispersive X-ray spectroscopy (EDS) investigation reaffirms the chemical composition as Ni_3Nb for the δ phase. In STA2 condition, the double aging is performed at 760ºC/8h and 680ºC/6h to precipitate δ phase (in the grain boundary) and γ″+ γ′ phases, respectively. Due to variation in the aging temperature and soaking time distribution, the shape and size of the δ phases are different for STA1 and STA2 conditions. The width of δ particles are observed to be larger in STA1 compared to STA2 conditions, probably due to high-temperature aging. In STA1, the length and width of precipitated δ particles are varying over a range of 300 nm – 600 nm and 100 nm – 200 nm, respectively. Whereas in the STA2 condition, the length and width are between 1000 nm – 1600 nm and 100 nm – 150 nm, respectively. A significant rise

in the length (~300%) of δ-particles in STA2 condition could be due to higher holding time at the aging temperature, whereas marginal variation in the width of δ-particles is witnessed.

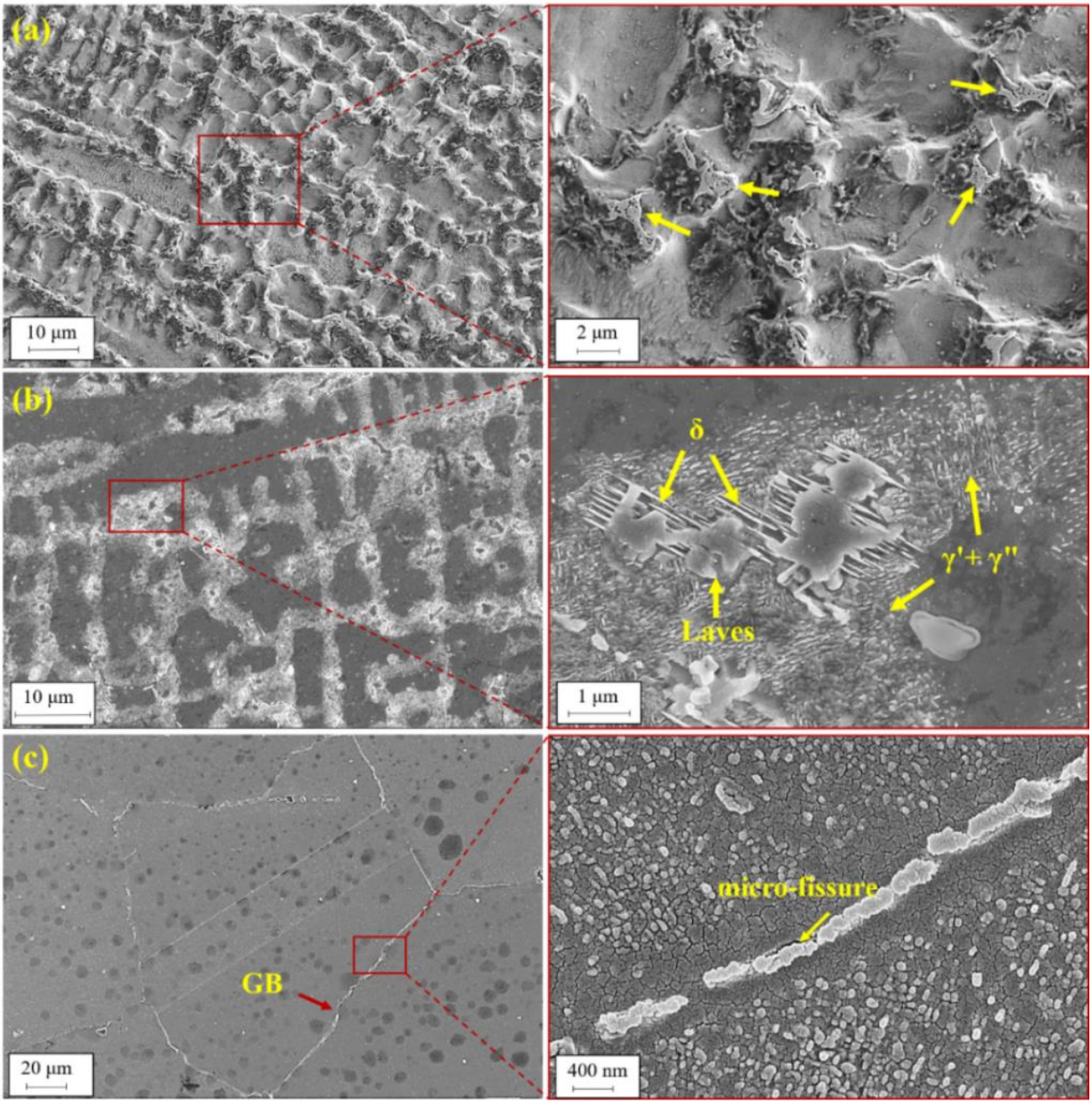

Fig. 5.16 Higher magnification SEM micrographs of fusion zone showing: (a) intermetallic Laves phase in as-welded condition; (b) precipitation of γ', γ" and δ phase around the Laves particle in direct aged condition; and (c) micro-fissure sites in the grain boundary of ST condition

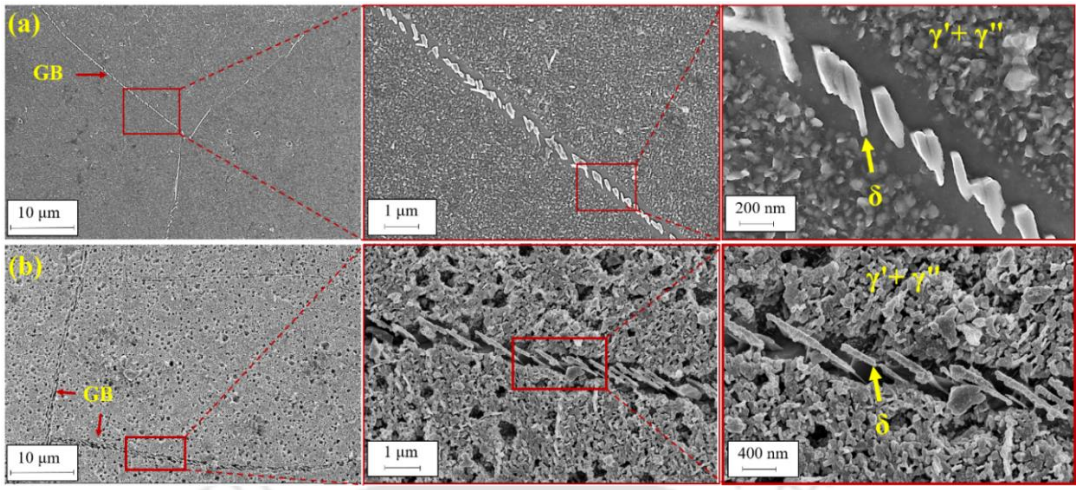

Fig. 5.17 Fusion zone SEM micrographs showing precipitation of (a) platelet type δ particles in the grain boundary and, fine γ″ and γ′ strengthening phases within the grain for STA1; (b) needle shape δ particles in the boundary and, coarse γ″ and γ′ phases in STA2 condition

5.3.3 Segregation analysis

The EDS elemental analysis of the weld bead for each condition is given in Table 5.4, and the calculated segregation coefficient of major alloying elements are presented in Table 5.5. The enrichment of Nb and Ti in the interdendritic regions and grain boundaries is evident from Table 5.5 for all treated conditions. In the as-welded condition, the wt. percentage of Nb in the interdendritic Laves phase is 14.8% (Spectrum 1) as compared to 4.4% of the dendritic core (Spectrum 2). Hence segregation of Nb in the inter-dendritic region during solidification is inevitable and is the main reason for Laves phase formation. Similarly, an increase in Ti weight percentage is observed in the interdendritic region, which is mainly responsible for the formation of MC type of carbides (i.e., TiC). The weight percentage of Nb has reduced by 20% in the aged condition (spectrum 3), due to the precipitation of δ and γ″+γ′ phases during the aging treatment as Nb is the main compositional element of these strengthening phases. The segregation coefficient of Nb, Mo, and Ti is found to be the highest for the solution treated sample. Hence the coarse MC carbides that are distributed in an irregular manner in the grain boundary are mainly enriched with these alloying elements. The higher weight percentage Nb (40.2%) and Ti (17.2%) confirms the presence of (Nb, Ti)C type carbides in the grain boundary (Richards et al., 1992). In STA1 and STA2 treatment, due to different aging time and temperature, the morphology of strengthening phases has changed, also affecting the Nb

weight percentage in the δ phase. Marginal improvement in Nb and Ti segregation coefficients is observed for STA1 compared to STA2, which could be mainly due to aging at 960ºC as compared to 760ºC. The presence of a higher Nb percentage in the grain boundary confirms the existence of Nb rich δ phase in the STA1 and STA2 fusion zones.

Table 5.4 EDS elemental analysis of as-welded and heat treated samples at weld zone

Weld bead condition		Elements								
		Ni	Nb	Cr	Fe	Ti	Mo	Al	Si	Mn
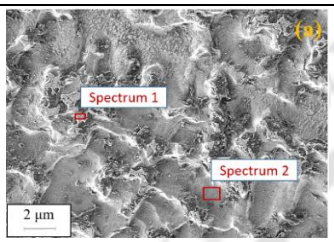	Sp.1	65.2	14.8	9.6	6.1	2.0	1.6	0.5	0.2	0.0
	Sp.2	53.9	4.4	20.8	16.5	0.9	2.6	0.5	0.0	0.0
	As received weld									
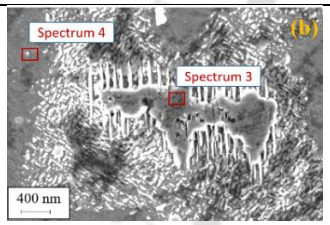	Sp.3	64.4	11.9	10.9	8.6	1.5	1.9	0.8	0.0	0.0
	Sp.4	55.9	4.6	19.3	16.2	0.7	2.3	0.7	0.1	0.1
	Aged condition weld									
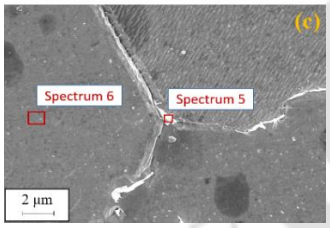	Sp.5	34.4	40.2	0.0	0.0	17.2	4.5	1.1	0.0	0.0
	Sp.6	52.7	2.7	20.8	19.6	0.7	2.0	0.0	0.1	1.0
	ST weld									
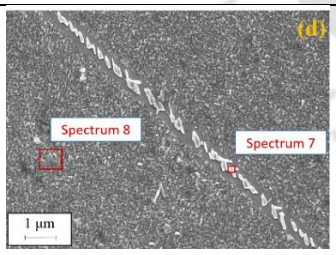	Sp.7	31.4	30.4	19.9	12.6	2.8	2.3	0.2	0.0	0.0
	Sp.8	51.3	5.2	21.6	16.7	0.8	2.7	0.4	0.1	1.1
	STA1 weld									
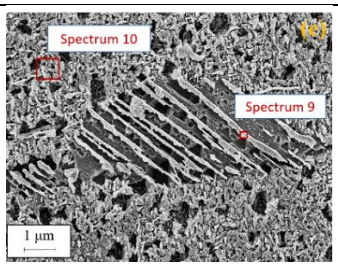	Sp.9	62.2	16.6	8.9	5.7	2.3	2.5	0.8	0.0	1.2
	Sp.10	55.0	3.5	19.6	18.2	0.7	2.3	0.6	0.1	0.0
	STA2 weld									

Table 5.5 Segregation co-efficient of principal alloying elements in the fusion zone

Weld Condition	**Segregation coefficients**			
	Nb	**Mo**	**Ti**	**Ni**
as-welded	3.36	0.61	2.22	1.2
aged	2.58	0.82	2.14	1.15
ST	14.8	2.25	24.5	0.65
STA1	5.8	0.85	3.5	0.61
STA2	4.74	1.08	3.28	1.13

The XRD analysis of base material and all heat-treated conditions in the weld zone area are shown in Fig. 5.18. In the base material, strong diffraction peaks of austenite (γ) matrix are observed (Fig. 5.18a), mainly dominating in (111) direction (2θ - 43.83). Multiple diffraction peaks along with the γ matrix are observed for the as-welded fusion zone, which indicates the precipitation of different intermetallic phases (Fig. 5.18b). The presence of NbC (2θ – 34.88, 58.47), Laves (Fe_2Nb) (2θ – 43.5), and TiC (2θ – 73.36) phases are identified from the respective diffraction peaks, and the corresponding plane are shown in Fig. 5.18b. Due to the partial dissolution of the intermetallic phases in the aged condition, the corresponding diffraction peaks are not observed to be that strong compared to the as-welded condition (Fig. 5.18c). The aging treatment at 760ºC (8h) and 680 ºC (6h) lead to precipitation of δ (2θ – 43.02), γ' and γ" strengthening phases, respectively, along with the austenite (γ) matrix. The corresponding diffraction peaks of γ' and γ" phases along with the γ-matrix are shown in Fig. 5.18c. Due to the incomplete dissolution of the Laves phase, a weak diffraction peak in (110) orientation is witnessed for the aged condition. The high temperature (at 1165 ºC) of solution treated sample facilitates in dissolving back the intermetallic phases to the solution matrix and hence, only the diffraction peaks corresponding to γ-matrix are observed in Fig. 5.18d. The peaks corresponding to MC carbides in ST weld are found to be very weak and small, which could be primarily due to the uneven distribution of carbides in the grain boundary (Sundararaman and Mukhopadhyay, 1993). In STA1 and STA2 conditions, the high temperature (1165ºC) solution treatment is followed by double aging treatments to precipitate δ, γ' and γ" strengthening phases in the grain boundary and austenite matrix, respectively. In STA1 weld, the peaks corresponding to the δ phase (2θ – 40.56, 59.5) and NbC phase (2θ –

35.05) are observed to be weak, as these phases are confined to the grain boundary only as compared to the bulk sample. Similar diffraction peaks for δ (2θ – 43.05, 59.5) and NbC phase (2θ – 35.05) are observed for the STA2 weld zone along with γ' and γ'' strengthening phases.

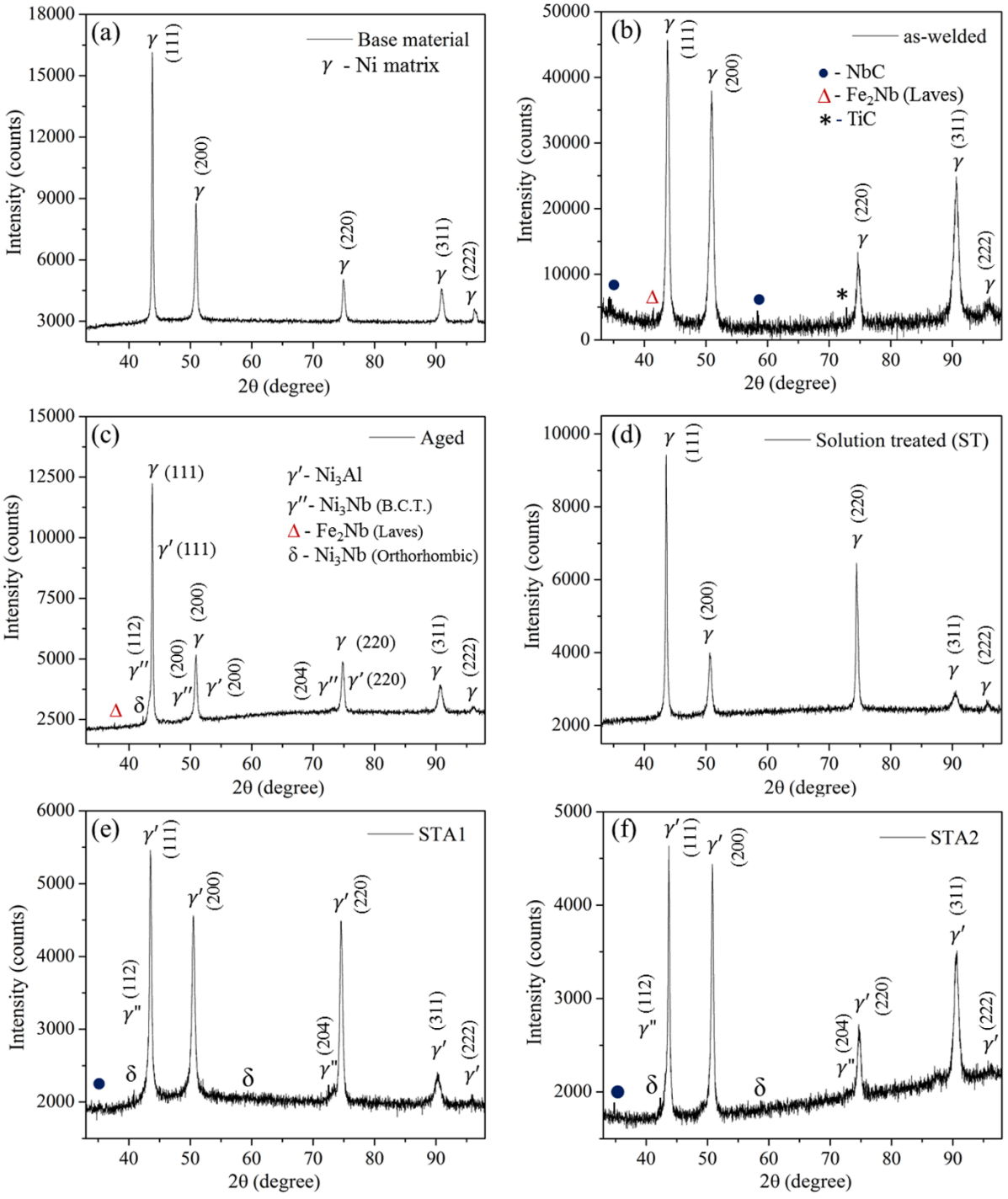

Fig. 5.18 XRD pattern of base material (a) and different conditioned fusion zones (b-f)

5.3.4 Influence on mechanical properties

The room temperature tensile and hardness test-results are plotted in Fig. 5.19 for each heat-treated condition. The corresponding tensile results along with the joint efficiency (w.r.t. to UTS) are given in Table 5.6. The tensile strength of the as-welded sample is witnessed to be inferior to that of the base material with a joint efficiency of 86.6%. Whereas the joint efficiency for STA1 and STA2 weld is found to be more than 100%. All the welded samples except STA1 and STA2 failed at the fusion zone during the testing and can be seen in Fig. 5.19(a). For STA1 and STA2 conditions, the failure zone is in the base material, which is much away from the weld zone. It signifies that the strength of the weld zone is surpassing the base material. The percentage elongation of the base material is found to be superior compared to all the welded samples.

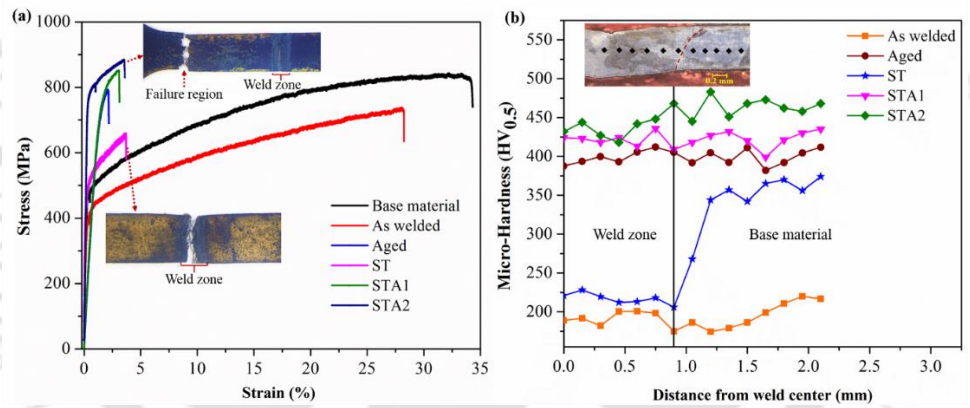

Fig. 5.19 (a) Tensile test results and (b) hardness distribution of the as-welded and treated samples

Table 5.6 Tensile test results

Condition	Yield stress (MPa)	UTS (MPa)	Elongation (%)	Joint efficiency (%)
Base material	462 ± 13	845 ± 12	34 ± 5.1	-
As welded	415 ± 14	732 ± 9	28 ± 3.2	86.6
Aged	573 ± 10	783 ± 16	2.1 ± 0.4	92.6
ST	347 ± 14	659 ± 15	3.7 ± 0.8	77.9
STA1	642 ± 15	852 ± 17	3.5 ± 1.1	103.4
STA2	722 ± 12	884 ± 20	3.7 ± 1.2	105.2

The micro-hardness distribution across the weld zone for each sample is depicted in Fig. 5.19(b). The solution treated base material has an average hardness value of 211 ± 10 HV. In the as weld condition, the maximum hardness attained in the fusion zone is 202.2 HV, which is almost near to the hardness distribution of base material. The ST condition witnesses a considerable difference in hardness value between the fusion zone and base material. The maximum fusion zone hardness has increased to 228 HV in contrast to the as-welded condition. In comparison, significant improvement in base material hardness is observed with the solution treatment at 1165 °C/1h against the base material solution treated at 980 °C/1h. In the aged condition, the maximum fusion zone hardness is found as 411.9 HV, which is almost twice that of the as-welded sample. Whereas in STA1 and STA2 double aging condition, the FZ hardness has further increased to 436 HV and 448 HV, respectively, with the increase in γ' and γ" precipitation. The heterogeneity in hardness distribution across the welded component has curtailed with the aging treatment and can be clearly evident from the Fig. 5.19(b).

5.3.5 Mechanism of post weld heat treatment

The present study reaffirms the reduction in aging time by more than 50% using the modified aging technique (i.e., STA2) without affecting the weld mechanical properties. The microstructural configuration corresponding to different solution and double aging treatments are shown in Fig. 5.20. The microstructural evolution in Inconel 718 weld is a complex phenomenon due to the coexistence of different phases (i.e., γ', γ", δ and MC) along with the γ matrix (Theska et al., 2020b). The γ" strengthening phase has similar composition to that of δ phase (i.e., Ni_3Nb). Hence, the δ phase precipitates in the grain boundary at the expense of γ" phase during the aging treatment (i.e., post STA1 and STA2 in Fig. 5.20) (Texier et al., 2016). Few literatures reported that the precipitation and growth of δ phase is detrimental to the mechanical properties. However, the limited quantity in the weld provides resistance to grain sliding under the loading and as a result the creep resistance improves (Ahmadi et al., 2017; Zhou et al., 2014). The δ phase aids in pinning the austenite (γ) grain boundaries and contributes to the grain strengthening by hindering the grain growth (Drexler et al., 2018).

In fusion welding, the formation of intermetallic Laves is the major challenge in Inconel 718 as it provides favorable spot for micro-crack initiation during the solidification and as a result, the strength of the welded component deteriorates. Hence, reduction in strength is mainly due to the formation of intermetallic phases that consumes a significant amount of

principal strengthening elements (i.e., Nb, Mo, Al, and Ti) from the matrix during the fabrication process. The interface between the intermetallic and matrix form a weaker zone that may act as a location for micro-crack initiation and causes early failure of the component. Hence, with an aim to dissolve the intermetallic phases and bringing back the strengthening elements, different heat treatments are designed. In the direct aged condition, the joint efficiency has increased marginally to 92.6% from 86.6%. This is mainly due to the partial dissolution of Laves and MC type carbides. Partial dissolution of these intermetallic makes a limited amount of Nb available for the precipitation of δ particles and γ'-γ" strengthening phases around it. The diffraction peaks in Fig. 5.18(c) and SEM images in Fig. 5.16(b) confirms the presence of these phases. The joint efficiency has reduced to 77.9 % for the solution treated (ST) sample. The absence of strengthening phases (i.e., γ' and γ") in the matrix and δ phase in the grain boundary is the main cause for the reduction of strength in only ST condition. However, the presence of MC type carbides along with micro-fissure in the grain boundary could also be responsible for the early failure of the ST components (Fig. 5.16c). The EDS analysis confirms that the intergranular carbide is (Nb, Ti) C particles. It is highly enriched with Nb and Ti at the grain boundary. The tensile strength has shown significant improvements in STA1 and STA2 conditions as compared to others. The precipitated coherent principal strengthening phase (i.e., γ"), minor strengthening phase (i.e., γ') in the matrix along with the δ phase in the grain boundary contributes to the strength of the Inconel 718 weld (Cormier et al., 2020). The XRD analysis of STA1 and STA2 confirms the presence of these phases and the SEM micrographs reveals the morphology of these phases in Fig 6.7. The coarsening of strengthening precipitates (i.e., γ' and γ") is observed in STA2 condition as compared to the STA1 condition due to higher aging time. The diameter of spheroidal precipitates in STA2 is calculated as 120-140 nm against 60-80 nm disc shape precipitates of STA1 condition. Hence the marginal improvement in tensile strength of STA2 weld against STA1 is mainly attributed to the coarsening of γ' and γ" strengthening precipitates inside the grains and refinement of δ phase in the grain boundary (Jouiad et al., 2016). Significant reduction in ductility is primarily due to the precipitation of needle-shaped δ phase in the grain boundary. Due to the dislocation pinning caused by γ' and γ" phases and obstruction of dislocation movement by needle-shaped δ phase in the grain boundary, the ductility of heat-treated samples is limited and often initiate transgranular fracture during the testing.

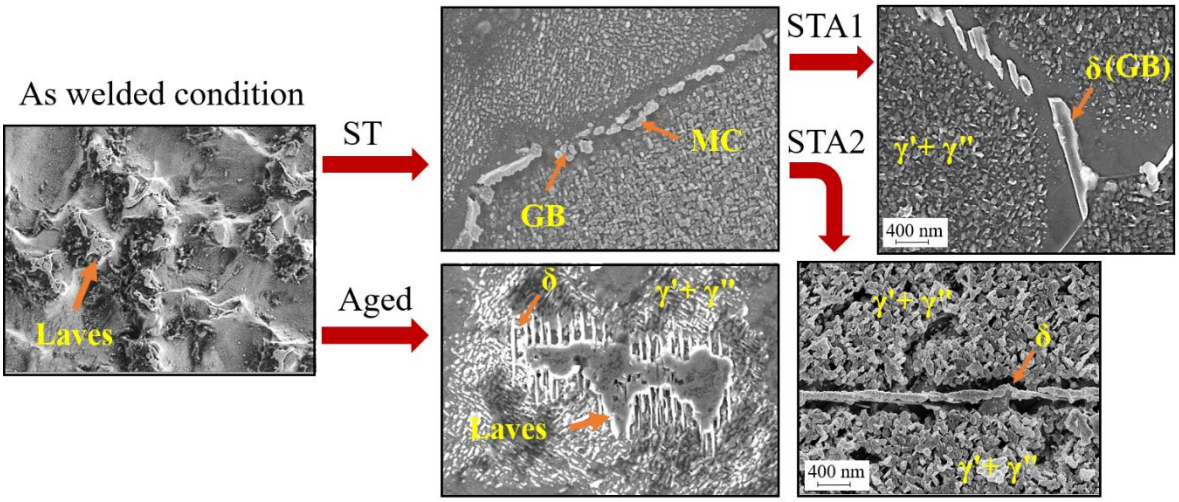

Fig. 5.20 Microstructural evolution from as-welded condition to various post weld solution and/or aging treatments.

The improvement in micro-hardness reflects the response of the weld zone to different post-weld heat treatment scheduled and the volume of Nb accessible for precipitation of γ' and γ" strengthening phases. The fusion zone hardness has seen significant improvement with the aging effect due to the precipitation of γ' and γ" strengthening phase in the austenitic matrix. With increase in the aging time, the weld zone hardness also increases and as a result, the STA2 condition weld bead is witnessed the maximum hardness of 448 HV. The fine γ' and γ" precipitates nucleates and grows into coarse γ'-γ" precipitates in duplet and triplet morphology with the aging time (Detor et al., 2018; Theska et al., 2020a). As a result, the volume fraction of γ'-γ" precipitates in the γ matrix increases with respect to the aging time and improves the hardness profile of the welded component. The hardness variation across the weld and base metal has reduced significantly by subjecting the welded component into aging treatments, and as a result, it reduces the effect of heterogeneity in the welded component.

5.3.6 Summary

An investigation on post-weld heat treatment of pulse micro-plasma arc welded structure is carried out with different double aging temperature and holding times. The outcomes obtained from the present assessment are

- The as-welded fusion zone contains various intermetallic phases like Laves (Fe_2Nb), NbC, and TiC in the interdendritic region.

- The double aging of the as-welded sample at 760 ºC/8 h and 680 ºC/6 h resulted in the partial dissolution of intermetallic phases and precipitation of the needle-shaped δ phase, γ" and γ' strengthening phase around the intermetallic phase.
- Improvement in tensile strength (7%) and fusion zone hardness (104%) is a witness for the aged condition weld in contrast to the as-welded sample.
- The high-temperature solution treatment at 1165 ºC/1h completely dissolves the intermetallic phases from the matrix but precipitated some intergranular MC carbides that are responsible for the formation of liquation cracking in the grain boundary.
- The solution treatment followed by double aging at 960 ºC/1 h and 760 ºC/5 h (STA1) responds in precipitation of platelet δ phase uniformly in the grain boundary and coherent γ" and γ' phases in the matrix. The tensile strength has improved by 16.3%, whereas the micro-hardness of the fusion zone was 115% compared to the as-welded sample.
- The solution treatment followed by duplex aging at 760 ºC/8 h and 680 ºC/6 h (STA2) resulted in the precipitation of needle-shaped δ phase in the grain boundary and γ" and γ' strengthening phases in the austenite matrix. The tensile strength is improved by 21% and the maximum fusion zone hardness by 121% compared to the untreated welded sample.
- The tensile failure of STA1 and STA2 condition occurs at a distant from the fusion zone, whereas other samples fail in the fusion zone.
- The post-weld heat treatment holding time is reduced by 53% without affecting the mechanical properties, by performing aging at 960 ºC (i.e., STA1) as compared to aging at 760 ºC (i.e., STA2) of the standard heat treatment procedure.

5.4 Micro plasma arc welding of Inconel 718 and AISI 316L

The present chapter addresses the weldability of Inconel 718 with AISI 316L stainless steel through metallurgical and mechanical characterization. The three dimensional (3D) heat transfer model analyzes the solidification behavior for a pulsed arc energy source. However, intermetallic formation deteriorates the welded joint properties and promotes solidification cracking in the weld zone. We attempt to join these dissimilar materials with the use of pulse current without any filler materials. The use of a pulse current during micro-plasma arc welding assists in the formation of a beneficial microstructure that produces strong welds. Since the solidification parameters (G·R and G/R) largely define the weld microstructure, their effect on

the weld joint properties is investigated herein. With an increase in the pulse current, the (G/R) decreases and enables, the formation of an equiaxed solidified structure in the weld zone. A reduction in the amount of various intermetallic phases is observed in the equiaxed regions compared to amount present in areas with a columnar structure. The tensile strength of the joint is superior to that of AISI 316L stainless steel, and failure is observed in the heat-affected zone of this material. The best joint efficiency is achieved for the welding condition having the lowest (G/R) value. An improvement in the elongation is achieved for the weld joint with a reduction in the (G/R) value.

5.4.1 General background

Welding of dissimilar materials significantly reduces the component costs by reducing the volume of expensive materials without compromising on their service condition. In gas power stations, the high-pressure and low-pressure stages of compressor rotor are made of Inconel 718 and AISI 316L austenitic stainless steel, respectively (Henderson et al., 2004). Dissimilar welding is always a challenging job due to the variation in composition and thermo-physical properties, which may result in metallurgical incompatibility between the metals to be joined. This issue is also associated with the Inconel 718 and AISI 316L bimetallic combination. The incompatibility between these materials is reflected by the formation of various intermetallic phases during fusion welding process which leads to the formation of micro fissuring and cracks in heat affected zone (HAZ) and fusion zone (FZ) (Lippold and Savage, 1982; Radhakrishnan and Thompson, 1992). Hence, the dissimilar welding of Ni-based super alloy and austenitic stainless steel is not completely free from metallurgical issues, and may lead to early failure of the components. The welding of this bimetallic combination is mainly performed by using GTAW process with a filler material of intermediate composition. If the composition of filler wire is not properly chosen, then it may trigger segregation of various useful elements from the metal matrix and can increase the intermetallic formation in the FZ and can severely affect the mechanical properties of the component. When filler material is used to produce weld, its composition and deposition technique becomes mainly responsible for the micro-structural morphology, formation of intermetallic and corresponding mechanical properties of the welded component. Hence, selection of filler composition is a major challenge for the dissimilar welding, as a result the primary objective of the present study is to produce a successful weld without using any filler material. So it's

become necessary to understand the micro-structural evolution and mechanical strength of the welded components, when joints are produced with the autogenous mode. Hence, micro-plasma arc welding (μ-PAW) process is used to obtain sound weld joints between Inconel 718 and AISI 316L material without using any filler material. First, the feasible domain of pulse parameters is established to produce good quality of weld. Then the effect of pulse parameter on weld microstructural morphology is established through solidification parameters and its impact on mechanical properties is analyzed, which has not been addressed by any researcher so far. In the current study, heat transfer model has been developed using Gaussian distributed quadruple-ellipsoidal heat source model for the dissimilar welding. The heat source parameters are defined from the measurement of weld dimensions. For over-penetrated weld, the parameter in the thickness direction is decided from the analogy of an extended weld profile that accomplishes the energy balance up to full thickness. The moving heat source and current pulsation effect is incorporated in the heat transfer model. The temperature distribution obtained from the model is utilized to calculate the solidification parameters and are correlated with the microstructural morphology and mechanical properties of the weld joint. Welds with butt joint configuration are produced herein by using the μ-PAW process with a pulse current mode for solution-treated Inconel 718 (1020°C for 1 hr.) and AISI 316L stainless steel. During welding the frequency of pulse current is maintained at 4.3 Hz. The other process parameters employed for the present experiment are shown in Table 3.4 of Chapter 3.

5.4.2 Characteristics of temperature distribution

The validation of numerical model is performed by comparing with experimentally measured weld bead dimensions. Fig. 5.21 shows the temperature isotherms that define the FZ, HAZ and unaffected base material zone. The FZ is confined between the liquidus temperature of both base materials and is shown for PD1 and PD5 weld. The solidus (T_S) and liquidus temperature (T_L) of AISI 316L are considered as 1649 K and 1673 K respectively (Wu et al., 2016) whereas for Inconel 718 corresponding temperatures are 1593 K and 1635 K respectively (Knorovsky et al., 1989). The mushy zone, where the solid and liquid phases coexist, lies between the T_S and T_L. The HAZ is defined by the 1593 K and 1273 K isotherms, below which no solid-state phase transformation occurs. The asymmetry in fusion zone is observed in both computed and experimental macrographs, which is mainly due to the

variation in thermo-physical properties. The shape and size between the computed and experimentally obtained fusion zone are found in well agreement with a maximum error of 4.4% for the PD1 weld. With an increase in the peak current, the width (w) to depth (d) ratio of the weld bead increases. For PD1, the (w/d) ratio is calculated to be 2.5, whereas it is 3.5 for PD5. This is attributed to the fact that a high heat input into the system causes a high heat flux density at almost a similar effective arc radius. However, the welds are found to be free from any type of micro-fissures or cracks in the fusion zone and HAZ.

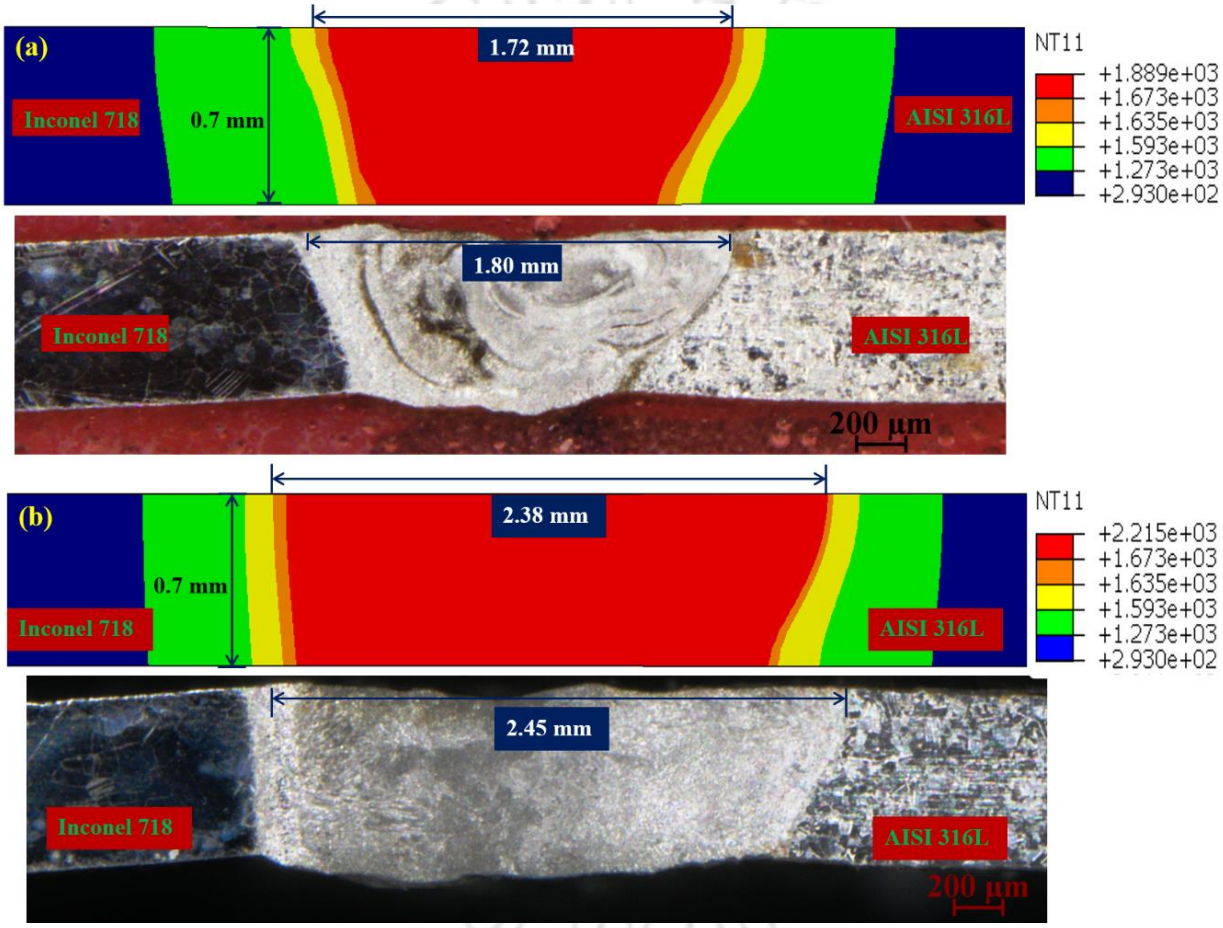

Fig. 5.21 Simulated and experimental weld bead profile of the (a) PD1 and (b) PD5 welding conditions

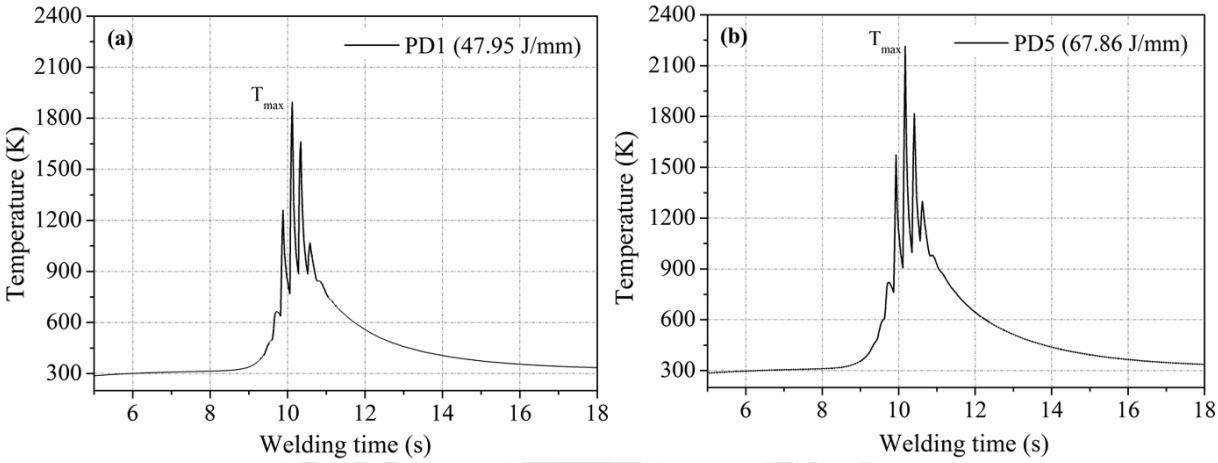

Fig. 5.22 Weld bead temperature distribution for the (a) PD1 and (b) PD5 welding conditions

The nodal time-temperature distribution for the PD1 and PD5 conditions at the weld center is shown in Fig. 5.22. Peak temperatures of 1889 K and 2215 K is achieved for the PD1 and PD5 welding condition, respectively. The width of the fusion zone for PD5 is higher than that for the other welding conditions. For high heat inputs, the peak temperature reaches a very high value and increases melting of the base materials, which results in formation of a large weld pool. The transient variation of the temperature caused by the current pulses is obvious from the computed results. During the pulse-on period, the temperature rises sharply and reaches the maximum value (i.e., 1889 K for PD1), which results in the complete melting of the base materials. At the base current of the same cycle, the temperature drops to a minimum value (i.e., 900 K for PD1), resulting in complete solidification of the weld pool. During the next cycle, the weld pool temperature rises to 1681 K (for the PD1 case), which is more than the liquidus temperatures of the base materials. Hence, this cyclic variation of the temperature inside the weld pool creates heterogeneous nucleation sites by remelting and breaking of the existing dendritic arms. As 1681 K is just 8 K and 46 K more than the liquidus temperature of AISI 316L stainless steel and Inconel 718, respectively, it is not enough to completely remelt the entire weld-pool or existing dendritic arms. So, partially melted and detached dendritic arms move inside the weld pool due to convection current. During the pulse off-period, these particles, instead of the existing base material grains, act as a substrate for heterogeneous nucleation. The transient nodal temperature changes corresponding to PD1 and PD5 are depicted in Fig. 5.23. At a pulse frequency of 4.3 Hz, total of four pulses are passed through a fixed nodal point, and the corresponding temperature differences during the pulse-on (i.e.,

heating) and pulse-off (i.e., cooling) periods are described in Fig. 5.23. The percentage overlap of two successive pulses in the welding direction (X-axis) is calculated as 80% and 72% for PD5 and PD1, respectively (Tzeng, 2000). The high peak current and greater pulse overlap for PD5 enable a peak temperature of 2215 K during the second pulse to the lowest temperature during the first pulse (~ 905 K). Therefore, the temperature difference during the heating period is the maximum herein (~ 1310 K) for PD5 compared to 1127 K for PD1. Similarly, during the cooling period of the second pulse, the temperature drops to 995 K from 2215 K for PD5 and to 884 K from 1889 K for PD1. The maximum temperature drop herein of 1220 K for PD5 is achieved compared to 1005 K for PD1. In effect, the enhancement of the pulse overlap increases the weld peak temperature for successive pulses. The overlapping of the first pulse helps to achieve the maximum temperature difference during the heating and cooling cycles of the second pulse. The temperature difference increases as the heat source approaches the node, and it reaches a maximum during the second pulse. However, the temperature difference decreases gradually when the heat source moves away (Fig. 5.23). It is noteworthy that the temperature difference between the cooling phase is less (~ 1220 K for PD5) than that of the heating phase (~ 1310 K for PD5) for a particular welding condition. This dynamic temperature variation during the heating and cooling periods induces microstructural changes during pulse welding in contrast to the changes that occur during a continuous mode of welding. During constant-current welding, the weld microstructure depends only on the peak temperature achieved during the process. The periodic temperature variation during pulse welding that causes remelting and resolidification of the weld zone results in grain refinement, the ability to control grain growth, and a reduction in the segregation of useful alloying elements. The magnitude of the maximum and minimum temperatures of successive pulses determines the percentage of remelting or resolidification of the weld pool.

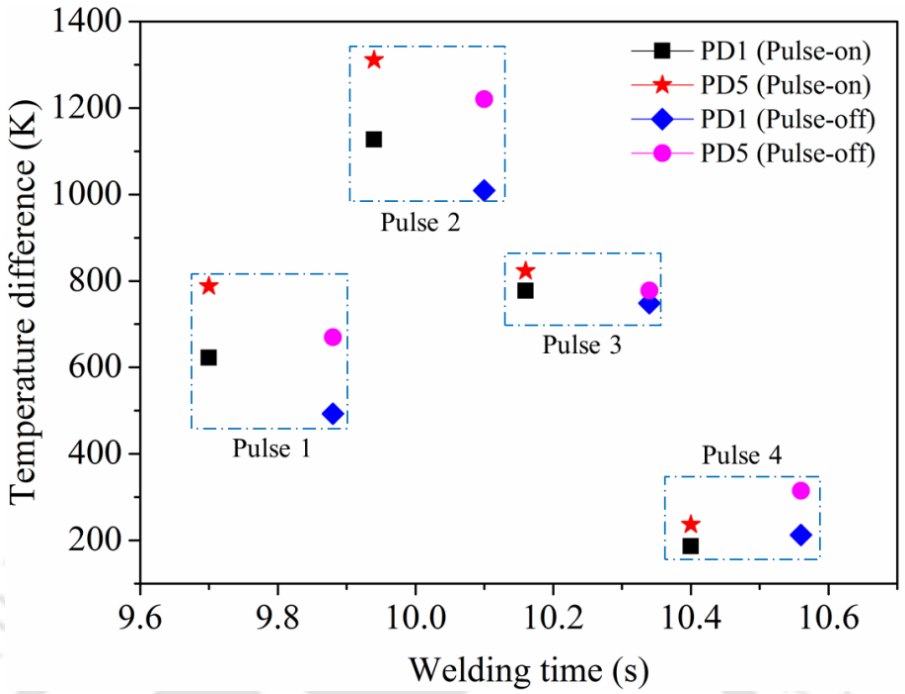

Fig. 5.23 Transient temperature change during pulse on and off time

5.4.3 Solidification parameters and the microstructure

Fig. 5.24 shows the microstructure of the weld zone, HAZ, and weld interface for PD1 and PD5. The unmixed/mushy zone is observed in both the Inconel 718 and AISI 316L stainless steel sides. The unmixed zone on the Inconel 718 side is wider for PD5 than for PD1, whereas it is narrow on the AISI 316L stainless steel side. A high input for PD5 and high thermal diffusivity for stainless steel characterize the variation of the unmixed zones. The existence of a steep temperature gradient towards the weld center promotes the growth of columnar dendrites along this direction for both welding conditions (the direction is shown with the arrow). The columnar structure of PD5 is coarser than that of PD1, which is mainly due to the variation in the heat input or cooling rate during the welding process. A high peak temperature corresponding to a high heat input allows the molten pool to last for an extended period of time, which decreases the cooling rate and produces a coarse microstructure.

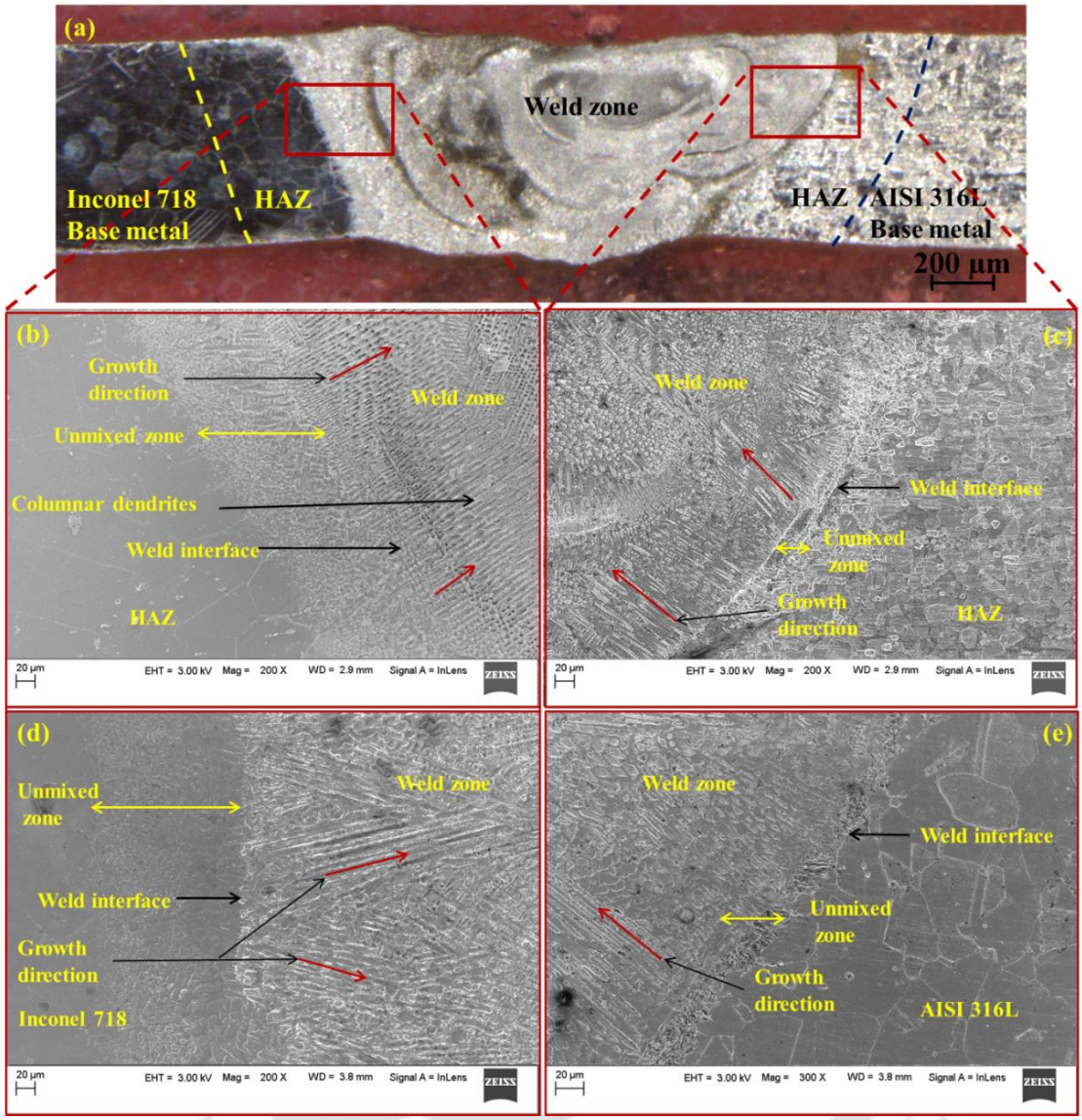

Fig. 5.24 Weld interface and weld zone of (a, b, c) PD1 and (d, e) PD5 weld

The effect of the temperature gradient *(G)* and solidification growth rate *(R)* on the microstructure is significant. The maximum variability of these parameters occurs along the weld velocity vector. Therefore, the longitudinal temperature gradient (along the velocity vector) concerning the weld center point is estimated for all welding conditions. As the heat source approaches the center point, the temperature gradient becomes positive (assumed to be the heating phase), and when it moves away, the temperature gradient becomes negative (assumed to be the cooling phase). Fig. 5.25 depicts the variation of the temperature gradients during pulse welding, considering the effect of the linear weld velocity. It is well known that

both the *G* and *R* values dominate the final microstructure. The ratio of *G* and *R* mainly determines the mode of solidification. A low value of *(G/R)* promotes an equiaxed structure, whereas a high value promotes a cellular or columnar dendritic structure (Kou, 2003). The product of *G* and *R* indicates the size of the weld microstructure, which is equivalent to the cooling rate. The estimation of the solidification parameters for all welding conditions is shown in Table 5.7. The longitudinal temperature gradient *(G)* at the weld center during the cooling cycle is calculated from the temperature distribution of the numerical model. The solidification growth rate *(R)* at the weld centerline is equal to the welding velocity, which is the maximum value along the longitudinal direction (Manikandan et al., 2014). The corresponding cooling rate *(G·R)* for each welding condition is given in Table 5.7.

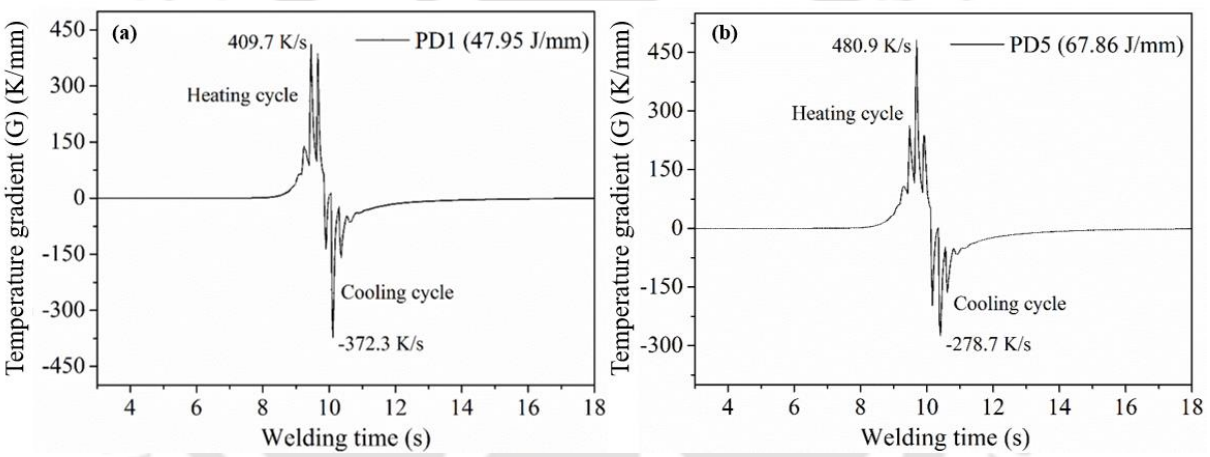

Fig. 5.25 Variation of temperature gradient at (a) PD1 and (b) PD5 welding conditions

Table 5.7 Estimation of solidification parameters

Welding condition	Temperature gradient - G (K/mm)	$(G/R)_{min}$	$(G \cdot R)_{max}$
PD1	372.3	114.2	1213.8
PD2	341.4	106.0	1099.3
PD3	350.0	102.9	1190.2
PD4	317.5	99.9	1041.7
PD5	278.7	92.0	844.5

The SEM images of the weld region for various welding conditions are shown in Fig. 5.26(a)-(e). It can be seen that the solidification mode changes from the fusion boundary to the weld interior. Multidirectional columnar grains and equiaxed dendrites are observed in the solidified zone. Columnar dendrites are mainly observed near the fusion boundary. Fine cellular and equiaxed dendrites are found at the weld center in the relatively low-temperature gradient zone (Kou, 2003). Fig. 5.27 shows the formation of various secondary phases in the interdendritic region during solidification. The high-magnification micrograph (Fig. 5.27c and d) reveals the formation of coarse continuous intermetallic phases in the columnar interdendritic region, which is in contrast to the equiaxed structure. With a decrease in the value of *(G/R)*, the weld microstructure has changed from columnar dendrites to equiaxed dendrites at the weld interior. PD5 has the lowest value of *(G/R)* among all the welding conditions, and equiaxed dendrites are observed all around the weld interior, in contrast to the appearance of the other welding conditions, which resulted in a decreased amount of segregation (Fig. 5.26e). However, PD1 has the maximum value of *(G/R)* herein, and as a result, the solidified zone solely consists of columnar dendrites throughout the weld. This structure promotes the formation of additional intermetallic phases. In PD2, equiaxed grains are only observed in the central region. The nucleation and growth of equiaxed grains obviously increase in PD3, PD4, and PD5 with a corresponding reduction in the *(G/R)* value. The PD1 weld has a maximum cooling rate herein of 1213.8 K/s, which is responsible for producing a very fine microstructure compared to that of the other welding conditions. Fig. 5.26 indicates that the coarseness of the weld microstructure increases with a decrease in the cooling rate. Solidification grain boundaries (SGBs) are also observed in the weld zone. The SGBs are mainly formed by the intersection of groups of sub-grains due to competitive growth in the trailing edge of the weld pool during solidification. The concentration of various alloying elements is very high in these grain boundaries, which are prone to form solidification cracks in the austenitic weldment.

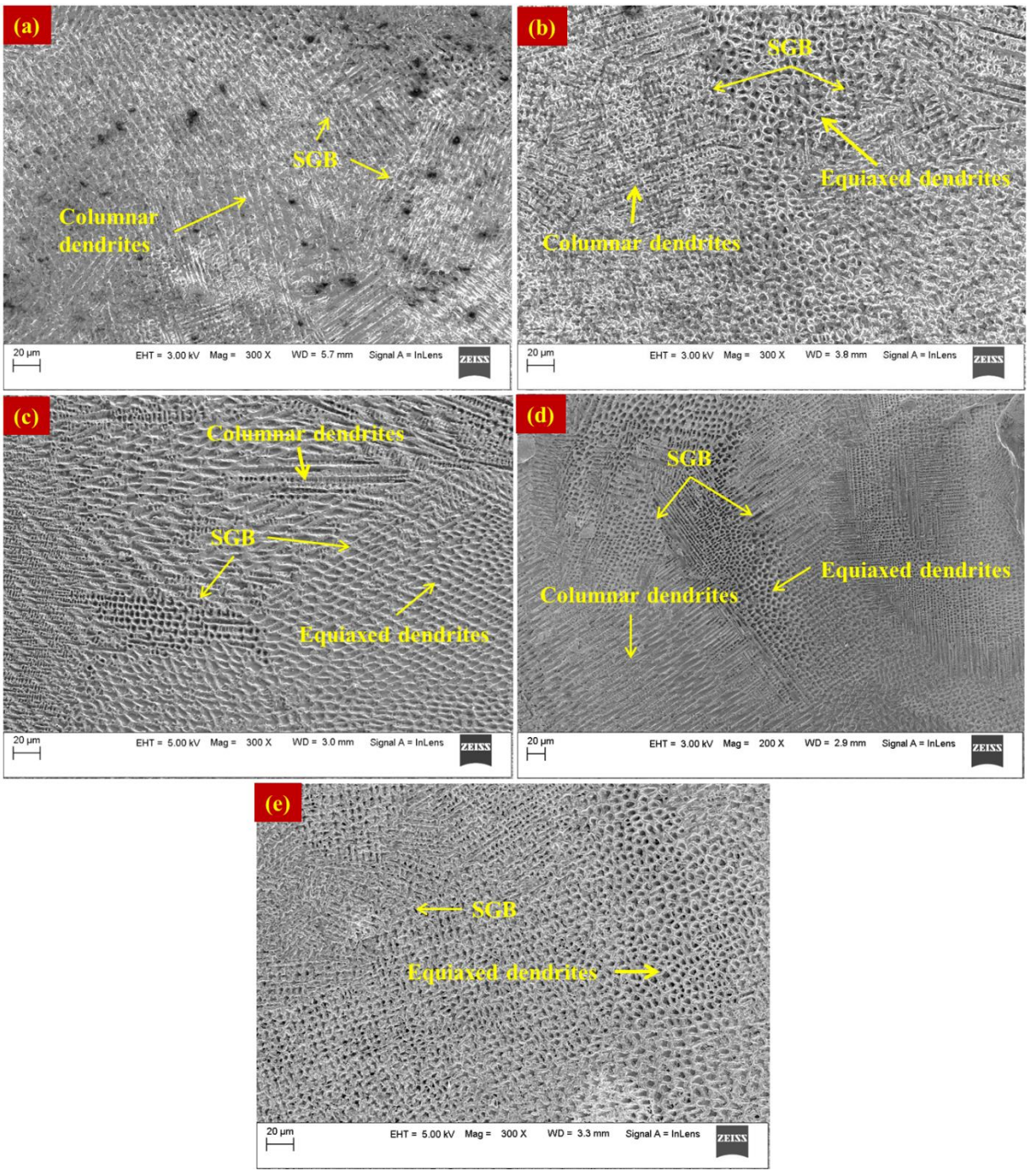

Fig. 5.26 Weld centre microstructure of (a) PD1 (b) PD2 (c) PD3 (d) PD4 and (e) PD5 welding conditions

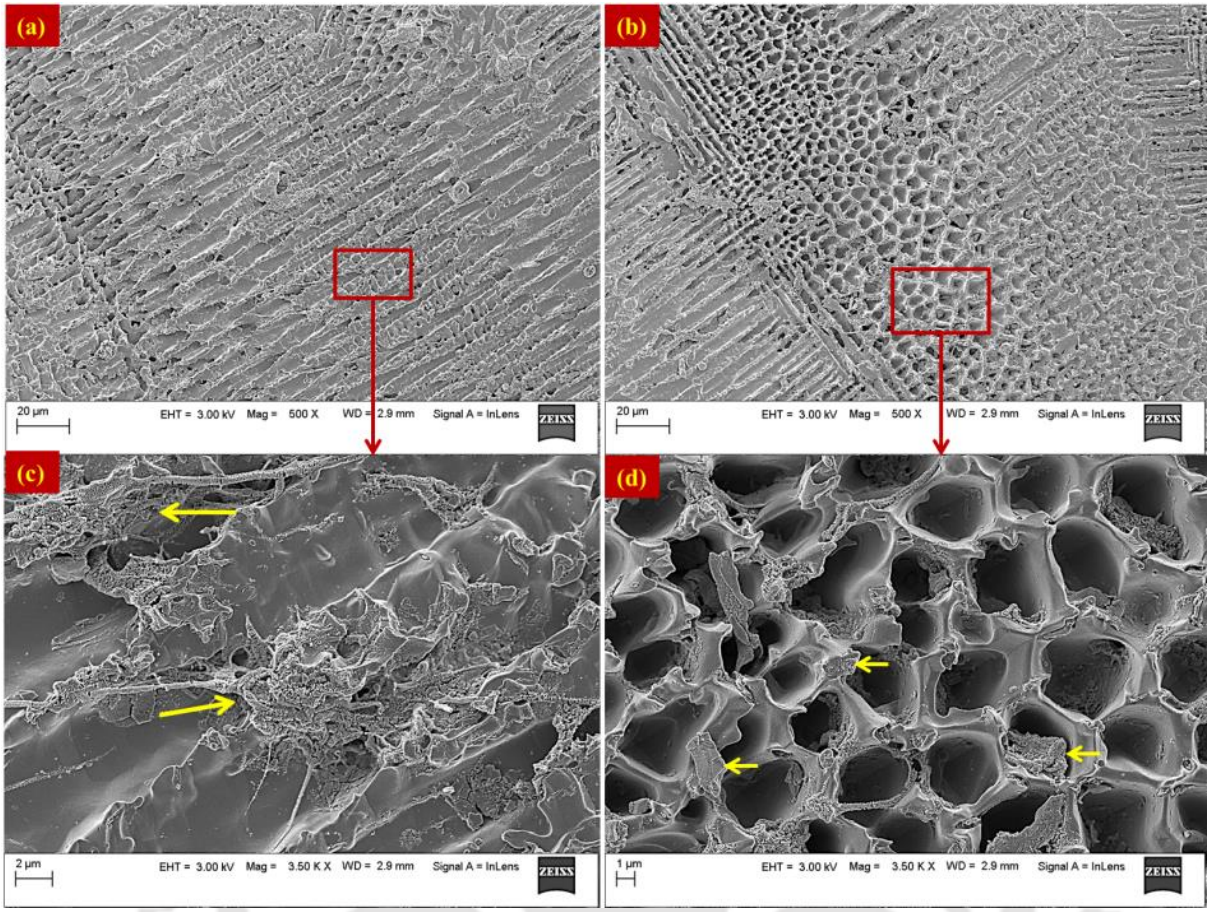

Fig. 5.27 Higher magnification microstructure of (a, c) columnar dendrites and (b, d) equiaxed dendrites

5.4.4 Characterization of intermetallics

Fig. 5.28 shows the X-ray diffraction (XRD) intensity patterns for Inconel 718 and AISI 316L stainless steel base materials and the solidified zone to confirm presence of various phases and structure. The acquired XRD pattern of AISI 316L base material has shown numbers of sharp peaks which reveals the presence of face centered cubic austenite (γ_{Fe}) matrix along various planes labelled in Fig. 5.28 (a). The pattern for the Inconel 718 base material indicates an austenite solid solution of nickel (γ_{Ni}) with an FCC structure that has a (111) preferred orientation and a primary hardening phase of γ"-Ni3Nb with a body-centered tetragonal (BCT) structure. During high temperature welding process, elements from both base materials reacts, get diffused and form the fusion zone along with various intermetallic. Fig. 5.28(b) shows the XRD spectrum of PD5 weld zone. Sharp peaks in the spectrum reveals

presence of austenite (γ_{Ni}, γ_{Fe}) FCC matrix, dominant in the (111) plane. The small peaks reveal the presence of various secondary phases such as niobium carbide (NbC), Laves phase (Fe_2Nb) and titanium carbide (TiC) in (111), (112) and (222) planes respectively along with the primary austenite matrix. The formation of various Nb rich intermetallic in fusion zone is mainly due to its higher segregation tendency. The low distribution coefficient (k<1) of Nb makes the redistribution of intermetallic easy in the interdendritic region during solidification. The high affinity of titanium towards carbon at high temperatures is the main cause of the formation of titanium carbide. Similar XRD patterns for the base materials and fusion zone are reported by researchers (Bansal et al., 2016; Kumar et al., 2015).

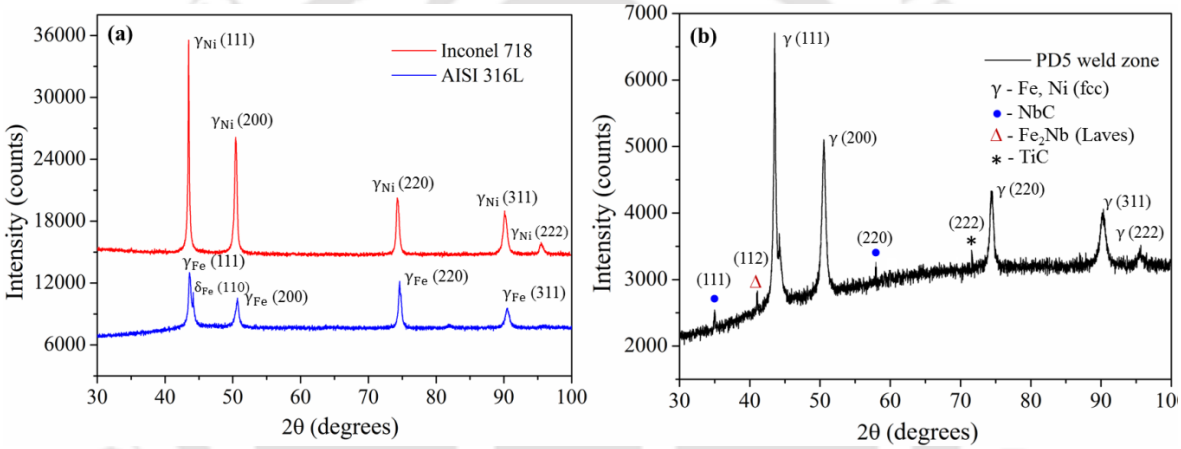

Fig. 5.28 XRD pattern of (a) base material and (b) PD5 weld zone

The elemental line mapping across the weld interface is carried out to confirm the elemental distribution across the base material, HAZ and weld zone (Fig. 5.29). The transport of elements from base metal to the FZ during welding is evident from the analysis. The tracing line from Inconel 718 base material to fusion zone (Fig. 5.29a) shows a sharp rise in iron (Fe) percentage with a significant drop in nickel (Ni) percentage. These variation in the disrtibution signifies migration and proper mixing of the elements from the base materials. AISI 316L has higher percenatge of iron (nealry 68%) and lower nickel (10.1%) containt as compared to Inconel 718 base material. Hence the FZ is found to have higher percentage of iron and lower percentage of nickel as compared to Inconel 718 due to migration of the respected elements from AISI 316L base material. Along the fusion bounday of AISI 316L side, further the concentraion of iron increases and nickel decreases in the tracing line towards the base

material. The concentration of chromium (Cr) is found almost constant throughout the base material and weld zone because of same weight percentage of Cr in both the base materials. However, the concentration of other alloying elements like niobium (Nb), molybdenum (Mo) and titanium (Ti) are reduced across the weld zone. Hence the EDX analysis confirms elemental distribution gradient along the welded joint due to transport phenomena caused by convection in the weldpool. The application of pulse current causes a periodic change in the convection inside the weld pool due to the periodic variation in the energy supplied by the arc. The magnitude of convection in the weld-pool depends upon the weld temperature, and it increases with increases in peak temperature (Kou, 2003). The convection causes the liquid metal to flow inside the molten zone, resulting in reduction of elemental segregation in the interdendritic region during solidification. The unmixed zone near the fusion boundary is evident because the elemental concentration is nearly similar to that of the base material.

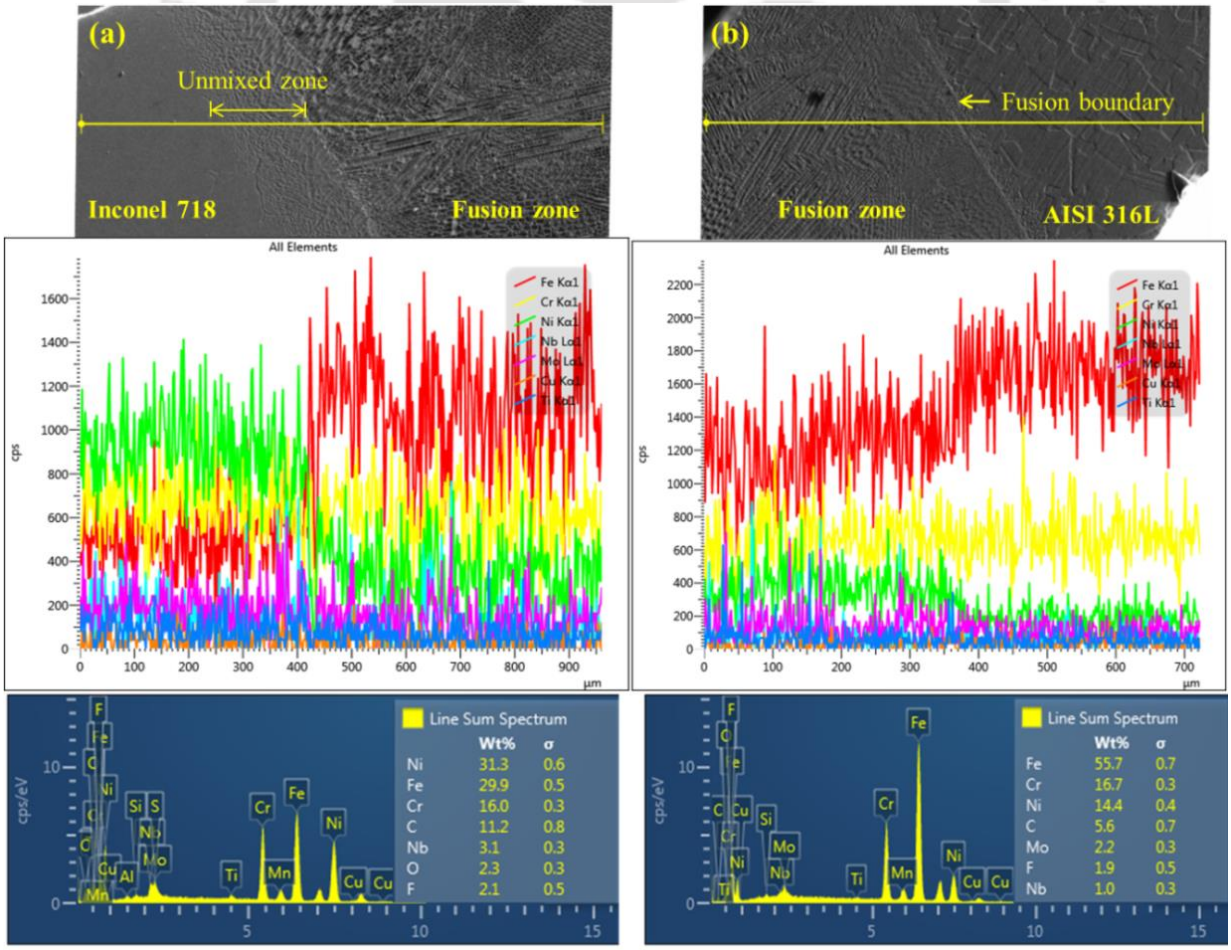

Fig. 5.29 Elemental line mapping across different zones for PD5 welding condition

The EDX elemental mapping for PD1 is described in Fig. 5.30. The enrichment of the columnar structure with several elements is presented with a color code (Nb: green, Mo: pink, and Ti: blue). It is concluded that the segregation of Nb and Mo may occur from the dendritic core as it is enriched with these elements. However, these Nb-, Mo-, and Ti-rich phases in the weld zone are primarily the Laves phase (Devendranath et al., 2014; Ning et al., 2018). EDX spot analysis of PD1 (columnar structure) and PD5 (equiaxed structure) is performed at different zones, which are depicted in Fig. 5.31(a). In PD1 weld, the presence of various secondary phases (appeared as white) are observed in the interdendritic regions and found to be highly enriched with Nb, Mo and Ti (spectrum 3) compared to that of the dendritic core (spectrum 2). In PD5, the equiaxed structures are enriched with Ni, Nb, Mo, and Ti in the boundaries. However, these phases are refined, in contrast to the columnar structure of PD1, which is mainly due to the formation of a fine equiaxed microstructure. The weight percentages of Mo and Nb in the interdendritic region of the equiaxed structure are reduced by 72% and 66%, respectively, compared to those in the columnar structure. Hence, the segregation of the useful alloying elements from the austenitic matrix is reduced significantly in the equiaxed structure. However, the formation of various secondary and intermetallic phases in the solidified structure cannot be avoided completely. They consume a significant amount of alloying elements from the metal matrix and are mainly responsible for crack initiation and growth.

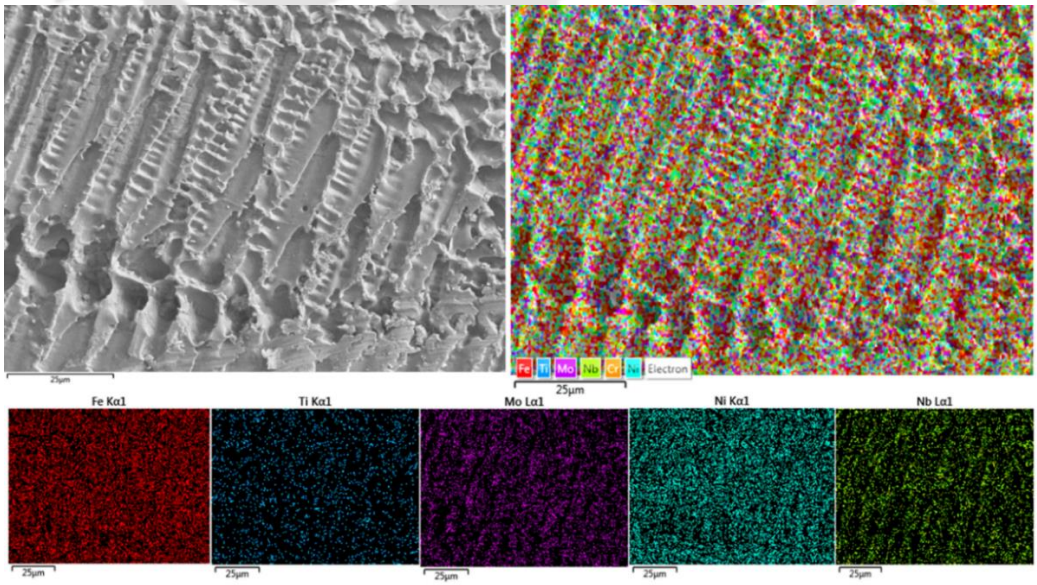

Fig. 5.30 EDX elemental mapping of the PD1 columnar structure

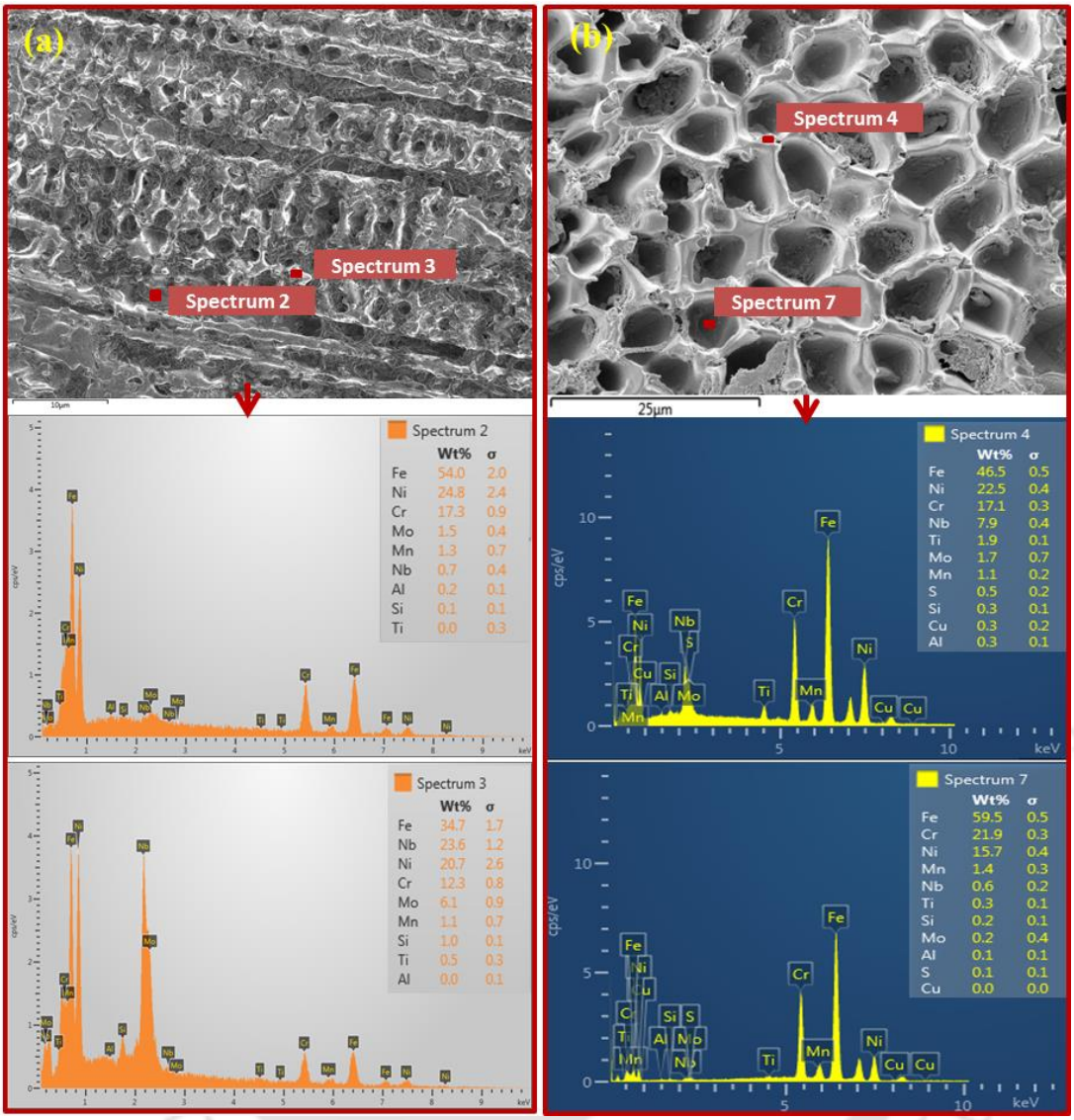

Fig. 5.31 EDX analysis of (a) PD1 and (b) PD5 weld zone

5.4.5 Impact on mechanical properties

The tensile test results for all welded samples are presented in Table 5.8. Two samples from each condition are tested, and the average value is reported. The Inconel 718 and AISI 316L stainless steel base material tensile strengths are 759.8 MPa and 610.9 MPa along with an elongation of 51.3% and 30.5% respectively. Except for PD1, all other samples fail in the HAZ on the AISI 316L stainless steel side (Fig. 5.32). Therefore, the fusion zone of PD1 is determined to be the weakest fusion zone herein, which could be mainly due to the presence of higher amount of intermetallic phases in the columnar interdendritic structure. For the other

welding conditions, the HAZ on the AISI 316L stainless steel side is determined to be the weakest zone herein, which could be due to the grain coarsening and formation of δ-ferrite during the welding process. Among all the welded samples, PD5 produces the maximum tensile strength of 660.1 MPa, which is 108% that of the AISI 316L stainless steel (610.9 MPa) and 88% that of the Inconel 718 (751.3 MPa). A reasonably good elongation of 35.3% is achieved for the PD5 condition. The excellent tensile strength of the PD5 weld is mainly attributed to the formation of an equiaxed weld microstructure that reduces the segregation of the principal alloying elements during solidification. The tensile strength of the all-welded samples is found to be superior to that of the weakest parent material (i.e., AISI 316L stainless steel). All welds except PD1 possess a high plastic deformation of more than 20% of the gauge length before fracture. The PD1 weld has been reported to have a minimum tensile strength and percent elongation of 611.5 MPa and 16.3%, respectively. The cross-sectional area of the fusion zone for all welding conditions is shown in Table 5.8. The PD5 weld has a maximum cross-sectional area of 1.59 mm^2 because of the highest heat input compared to that of the other welding conditions. Combining the effect of a large weld area and high heat input reduces the magnitude of the temperature gradient along the weld centerline during the cooling cycle, which reduces the solidification parameter *(G/R)* (Mortezaie and Shamanian, 2014). The decreased value of G intensifies the constitutional supercooling during solidification and leads to the formation of an equiaxed structure, which reduces the intermetallic formation and improves the mechanical properties.

Table 5.8 Tensile test results of the welded samples

Condition	Fusion zone area (mm^2)	UTS (MPa)	Elongation (%)	Joint efficiency (%)
Inconel 718	-	751.3 ± 9.5	51.3 ± 2.1	-
AISI 316L	-	610.9 ± 7.2	30.5 ± 2.5	-
PD1	0.97	611.5 ± 6.7	16.3 ± 2.0	100.1
PD2	1.01	630.6 ± 7.6	23.1 ± 1.8	103.2
PD3	1.21	618.5 ± 8.1	21.4 ± 2.1	101.4
PD4	1.41	641.8 ± 3.1	25.1 ± 3.1	105.0
PD5	1.59	660.1 ± 7.4	35.3 ± 1.6	108.0

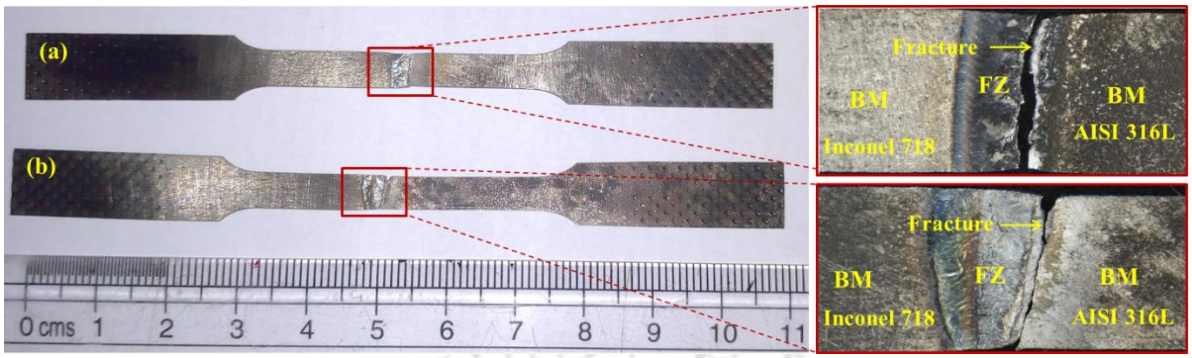

Fig. 5.32 Tensile fracture images of the (a) PD1 and (b) PD5 welding conditions

The tensile fracture surfaces of all weld conditions are shown in Fig. 5.33. All fracture surfaces are found to have macro/microvoids along with various secondary phases inside the voids and dimples. The PD1 fracture surface exhibits a very fine dimple structure, whereas ductile tearing ridges along with shallow and large dimples are observed on the PD4 and PD5 fracture surfaces; these structures indicate a ductile mode of failure. In the PD5 fracture surface, a decreased number of macro/micro voids are observed compared to that for the other welding conditions, which could be due to the formation of a decreased amount of secondary phases in the interdendritic regions.

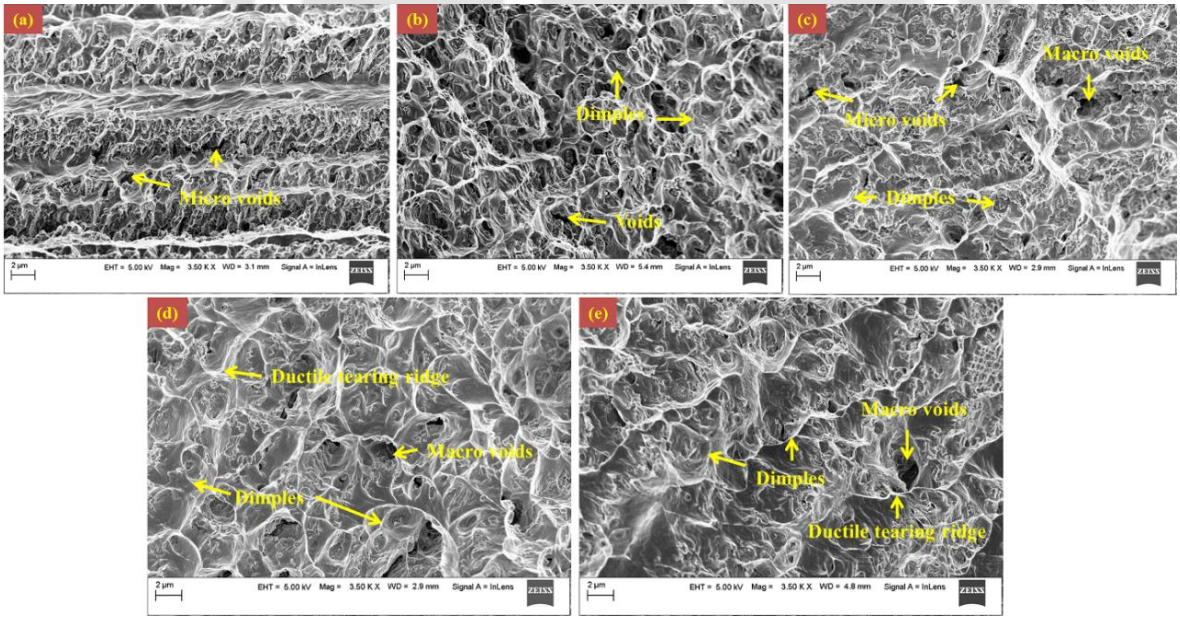

Fig. 5.33 Tensile fractography of the (a) PD1, (b) PD2, (c) PD3, (d) PD4 and (e) PD5 welding conditions

The microhardness distribution for all welding conditions is shown in Fig. 5.34. The average hardness values of the parent materials are 213 ± 4 HV and 194 ± 5 HV for the Inconel 718 and AISI 316L stainless steel, respectively. The hardness in the fusion zone slightly decreases from the Inconel 718 to the AISI 316L stainless steel side, which is mainly attributed to the migration of the principal strengthening alloying elements, like Ni, Nb, and Mo, from the Inconel 718 side to the AISI 316L stainless steel side. The AISI 316L stainless steel contains a marginal percentage of these strengthening elements compared to the that in the Inconel 718, and hence, the hardness mainly decreases towards the AISI 316L stainless steel side. The peak hardness of the weld joint is almost similar (~ 223 HV) for all cases except PD2. The maximum hardness herein of 227 HV is obtained for PD2 near the Inconel 718 fusion boundary. The fusion boundary is mainly enriched with alloying elements Ni, Mo, and Nb from the Inconel 718 metal matrix, as reported by Devendranath et al., (2014). The minimum hardness in the joint is observed herein in the fusion boundary and HAZ on the AISI 316L stainless steel side, which could be due to the presence of the δ-ferrite phase along with various carbides and intermetallic phases that are formed during the welding process.

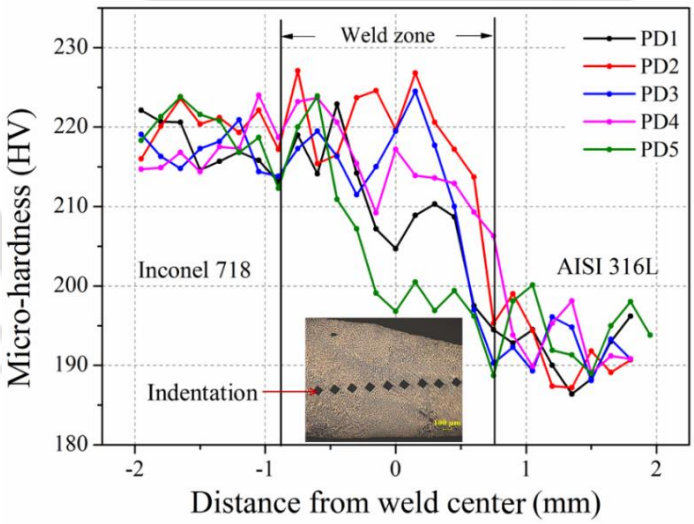

Fig. 5.34 Micro-hardness distribution across the weld joint

5.4.6 Summary

The present chapter addresses the welding of Inconel 718 and AISI 316L stainless steel without using any filler material under different pulse conditions in μ-PAW process. A relatively good weld joint strength is achieved for all welding conditions (~ 100%). However, an excellent joint efficiency (~ 108%) along with excellent elongation (~ 35.3%) is achieved

for PD5 when compared to those for the other welding cases. An improvement in the tensile property of PD5 is mainly due to the dominant equiaxed structure in the weld zone. An elevated heat input during the welding process assures a decreased value of the solidification parameter *(G/R)*. The decreased magnitude of *(G/R)* enhances the formation of the equiaxed structure and reduces the formation of the intermetallic phase by segregating useful alloying elements in the interdendritic regions. Overall, for this dissimilar combination of materials, an elevated heat input during the welding process has been found to have a beneficial effect on the mechanical properties. The following conclusions are derived from the present chapter

- A sufficient joint strength is achieved at a pulse current of 19 A to 25 A with a base current equal to 35% of the peak current, welding velocity of 3.3 mm/s, and constant duty cycle of 26%. The numerical model predicts the weld width with a maximum error of 4.4%.
- The solidification parameter *(G/R)* decreases with an increase in the pulse current. At increased values of *(G/R)*, the solidified weld is found to be mainly dominated by a columnar dendritic structure, whereas equiaxed dendrites prevail at decreased values of *(G/R)*.
- In the fusion zone, the presence of the Laves phase (Fe_2Nb) and various Nb- and Ti-rich secondary phases, such as NbC and TiC, along with the main γ matrix is observed.
- The formation of intermetallic phases is found to be greater in the columnar structure than in the equiaxed structure. However, the segregation of the Nb-, Mo-, and Ti-rich phases is more prone in the interdendritic regions than in the dendritic cores.
- An improvement in the elongation of 216% is achieved for the lowest value of *(G/R)* obtained herein at a similar range of joint efficiency (100% ~ 108%).
- The average hardness value of the weld zone is found to be less than that of the Inconel 718 (213 HV) but higher than that of the AISI 316L stainless steel (194 HV).

5.5 Micro-crack analysis in Inconel 718 and AISI 316L dissimilar weld

It is obvious that the intermetallic formation due to solute segregation during dissimilar welding of Inconel 718 and stainless steel poses a serious challenge as it promotes solidification cracking in the fusion zone. So minimization of these intermetallic phases and eventually the solidification cracks through variation in welding speed is undertaken in the

current study. With a decrease in the welding speed, morphology of weld zone microstructure is found to be of equiaxed dendrites types as compared to columnar dendrites at higher welding speed. The solute segregation is observed to be reduced in equiaxed structure as compared to the columnar dendrites. The investigation found enrichment of Nb, Mo, and Ti at the micro-crack sites that produced with the highest welding speed. The X-ray diffraction (XRD) analysis confirms the presence of various intermetallic phases and found to decrease with a reduction in the welding speed. The tensile strength has improved marginally, whereas remarkable improvement in tensile ductility is witnessed with the reduction of welding speed.

5.5.1 General background

The application of dissimilar welded material is immense and widely accepted by various industries to reduce the component cost without affecting service condition and quality of the product. The combination of Ni-Cr based superalloy with austenitic stainless steel has specific applications in gas power stations and aerospace industries due to their exceptional mechanical and corrosion resistance properties over a wide range of temperatures (Ramkumar et al., 2014). In gas compressor rotors, high pressure stages (final stages) are made of Inconel 718 discs, and other low pressure stages are made of stainless steel (Henderson et al., 2004). Inconel exhibits excellent weldability due to the presence of principal strengthening phase (γ") that obstruct strain age cracking during the fusion welding process (Brooks and Bridges, 1988). However, defects during dissimilar welding are promoted by the formation of intermetallic phases, which leads to solidification cracking and/or liquation crack during the fusion welding process (Cao et al., 2009). These welding defects are not entirely avoidable irrespective of the welding techniques but can be reduced significantly. Solidification cracks generally occur during the terminal stage of solidification (i.e., solid fraction (f_s) close to 1), when the thin film of liquid between two coherent solid-phases ruptures due to tensile stresses caused by thermal contraction (Davies and Garland, 1975). The range of solidification temperature along with the volume of solute concentration in the liquid phase mainly affects weld cracking susceptibility (Kou, 2003). The cracking can be reduced significantly by controlling the micro-segregation of useful alloying elements that trigger the formation of low melting point secondary phases during solidification (DuPont et al., 1999). During solidification of Ni-Cr-Nb based superalloy, in addition to primary γ-dendrites, eutectic phases like NbC and Laves [$(Ni, Cr, Fe)_2$ (Nb, Mo, Ti)] are also formed (Zhao et al., 2018). The eutectic reaction, L→ γ + Laves, occurs

predominantly at a lower temperature (1198℃) compared to the solidus temperature (1363℃) of Inconel 718. Hence it increases the solidification range of the weld zone and the probability of crack formation (Knorovsky et al., 1989). A reduction in these secondary phases generally diminishes the solidification cracking susceptibility in the welded zone and also in heat-affected zone (HAZ). Several investigators have considered typical parameters for controlling the Laves phase, and other intermetallic phases include heat input by the welding process, rate of cooling, thermal gradient developed, effect of pulsation, and beam or arc oscillation. Current pulsation during welding restricts the grain growth, refines the solidified structure, and as a result, hinders the formation of thick continuous intermetallic phases. In effect, it reduces the segregation and formation of Nb, Mo, and Ti-rich secondary phases (Devendranath et al., 2014). The reduction of secondary phases significantly enhances the weld joint properties, as these consumes a significant amount of useful strengthening elements from the metal matrix. In the current study, an attempt is made to produce sound quality dissimilar welds free from solidification cracks by using the pulse micro-plasma arc welding (μ-PAW) process. The welding was performed without using any filler material, unlike already published literature, to analyze the welding compatibility and dilution level between Inconel 718 and AISI 316L stainless steel. The effect of welding velocity on weld dilution level and intermetallic formation with consequence on solidification crack formation are investigated. The mechanical properties are correlated with the weld microstructure and solidification behavior of the welded joints. Thin sheets (0.7 mm thickness) of AISI 316L and Inconel 718 (solution treated at 1020ºC/1hr) are welded using the pulse μ-PAW process. The process parameters to obtain full penetration weld beads are depicted in Table 5.9. These parameters are obtained after several trials with varying the welding velocity over a wide range. The pulse frequency is taken as 4.3 Hz and the base current is set as 35% of peak current for all the welding conditions.

Table 5.9 Selected process parameters for the welding process

Sample	Peak Current (A)	Average heat input (J/mm)	Welding speed (mm/min)
PD1	19	48	196
PD2	19	52	180
PD3	19	56	167
PD4	19	65	145

5.5.2 Macro and micro structural characterization

The transverse cross-section of weld beads obtained with maximum (i.e., PD1) and minimum (i.e., PD4) welding speed conditions along with fusion boundary are shown in Fig. 5.35. The weld cap width of PD4 (~ 2.2 mm) is found more than the PD1 weld (~ 1.8 mm) because of low heat input to the system at higher welding speed. In PD1 weld, micro-fissures near the fusion boundary of Inconel 718 side (Fig. 5.35b) and macro-cracks in AISI 316L side near the fusion boundary (Fig. 5.35c) are clearly evident from the SEM images. Whereas PD4 and other welds are found free from any such types of solidification defects. The SEM images indicate that the columnar dendritic mode of solidification exists near the fusion boundary for both the welding conditions. The weld interior microstructure is found as of equiaxed type for PD4 weld (Fig. 5.35g) whereas columnar structure prevails in the case of PD1 (Fig. 5.35c). Equiaxed type of microstructure results in improvement of the mechanical properties as it reduces the segregational effect of useful alloying elements in the interdendritic region hence reducing the formation of intermetallic phases. Thavamani et al., (2018) indicated that the generation of micro-fissures and cracks in the weld zone is mainly due to the formation of low melting point intermetallic phases during the solidification.

The EDX elemental mapping over the micro-fissure region reveals enrichment with elements like Nb and Ti, compared to the weld zone, and can be clearly observed from Fig. 5.36(a). The EDX area analysis of micro-crack (Fig. 5.36b) edges also confirms very high enrichment of Nb, Mo, and Ti (spectrum 4 and 6) compared to dendritic core region of the metal matrix (spectrum 5). The weight percentage of Nb in the interdendritic region is found to be more than 50 times that of the dendritic core. Whereas for Mo and Ti it is around 14 and 7 times to that of the dendritic core. A similar variation in elemental concentration can also be observed in the line-scan analysis across the crack zone (Fig. 5.36c). The line scan results show a significant reduction of the elemental concentration over the crack region that seems to be the presence of void space. The segregation of these elements from the metal matrix to the interdendritic region during solidification is mainly due to the lower magnitude of the partition coefficient (k) (Vishwakarma et al., 2015). The magnitude of k is less than one for the alloying elements Nb, Mo, Ti, and Al. It infers that these elements generally tend to segregate into the interdendritic regions (i.e., solidifying liquid) during the solidification. Enrichment of these elements further triggers the precipitation of various low melting point brittle intermetallic

phases in the interdendritic region (as shown with arrow in Fig. 5.36b), which are mainly responsible for the formation of micro-fissure and solidification cracks. Enrichment of these elements near the micro-fissure and crack zone confirms the presence of MC type carbides and Laves intermetallic phases, as Nb, Mo, Ti, and Al are the principal constituent of these intermetallic phases.

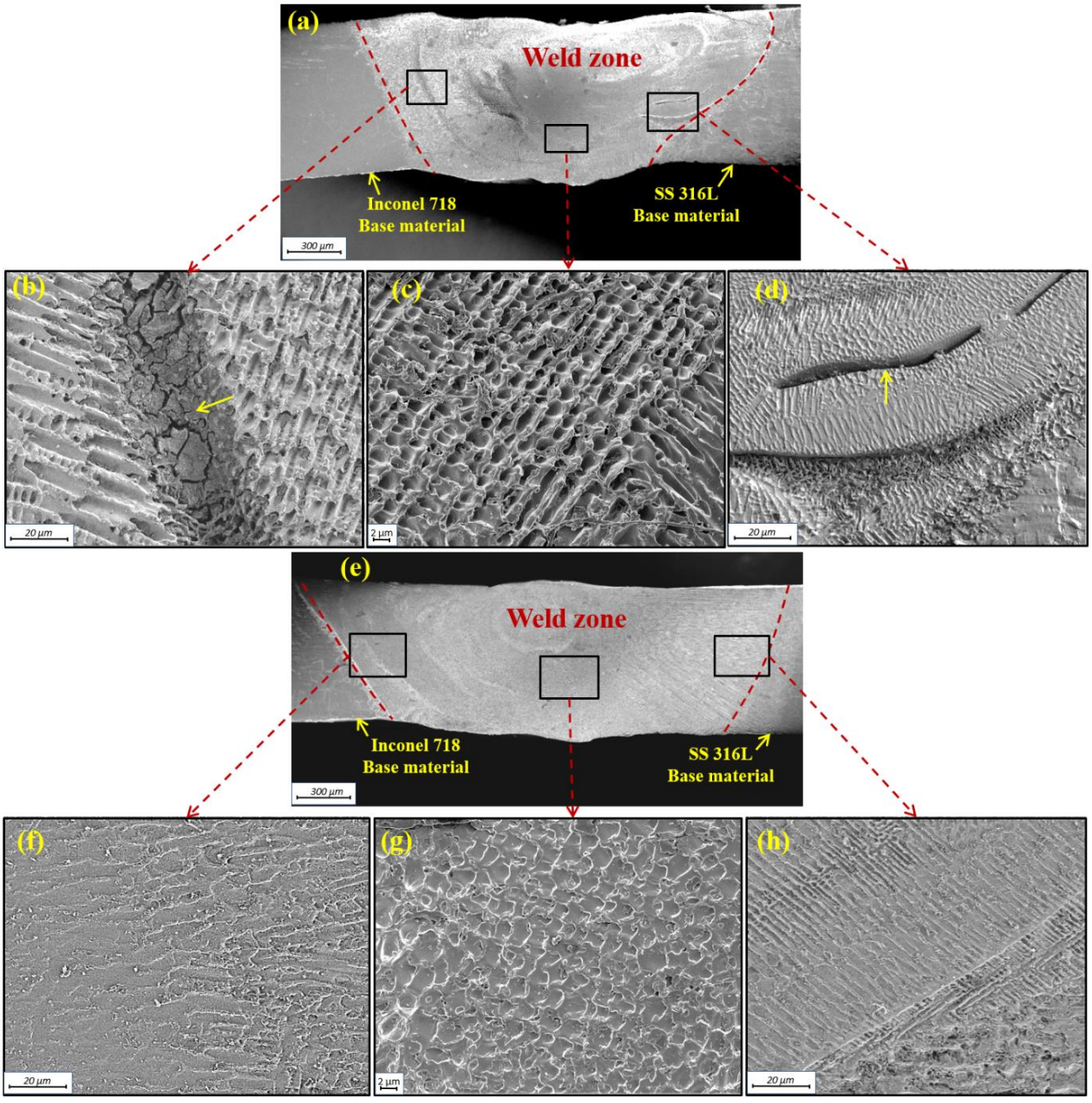

Fig. 5.35 SEM micrographs of PD1 (a, b, c, d) and PD4 (e, f, g, h) weld zone

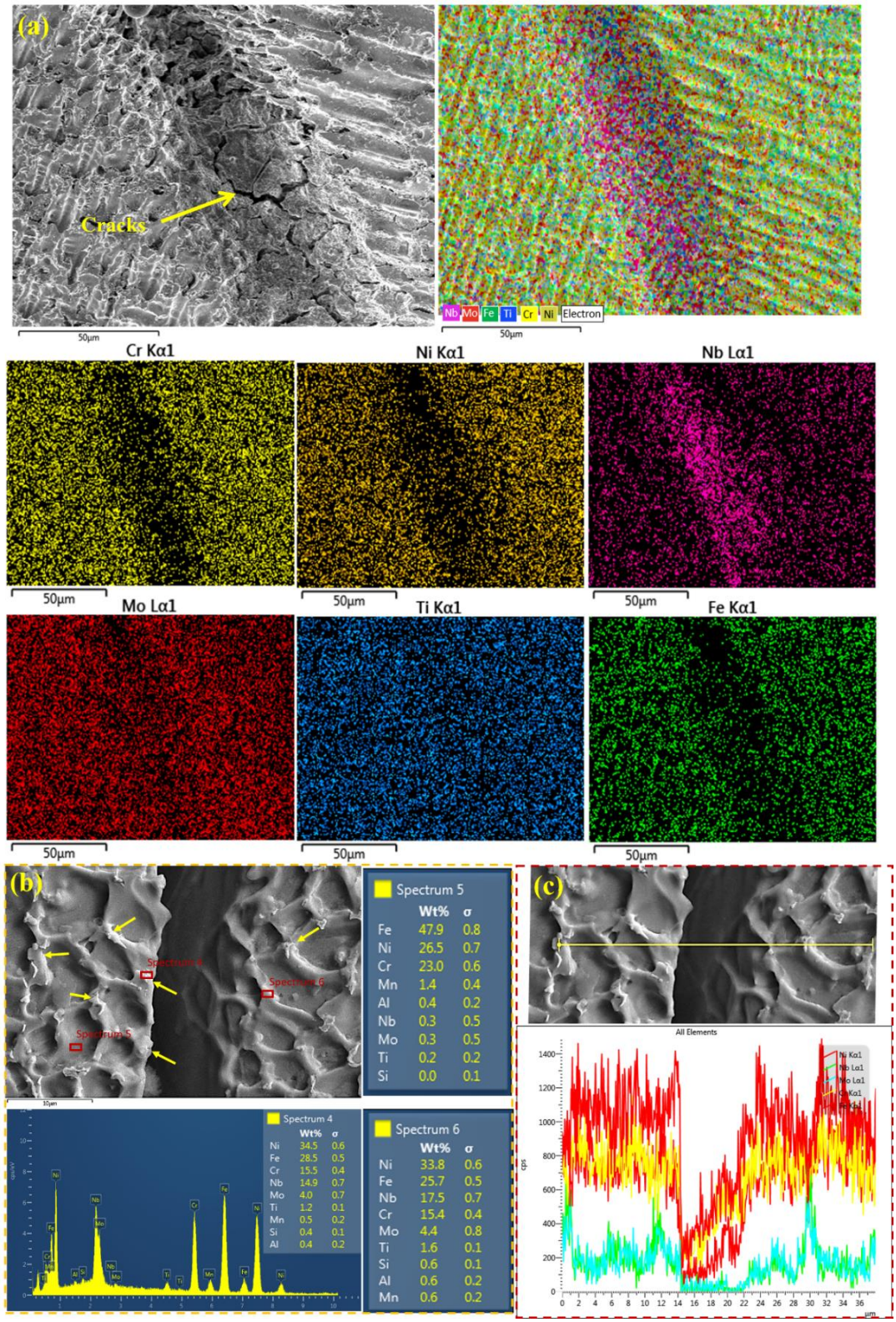

Fig. 5.36 (a) EDS elemental mapping (b) area analysis and (c) line scanning across the crack surface

5.5.3 XRD characterization

Fig. 5.37 shows the X-ray diffraction (XRD) patterns for PD1 and PD4 weld zone to confirm the presence of various secondary phases after solidification. The XRD spectrum reveals the intermetallic phases as NbC, TiC and Fe_2Nb (Laves phase) along (111), (220), (222), (110) and (112) direction respectively, with the main austenitic (γ_{Ni}, γ_{Fe}) matrix. Sharp and strong XRD peaks are observed in PD1 weld whereas weak and small peaks were clearly visible in PD4 weld.

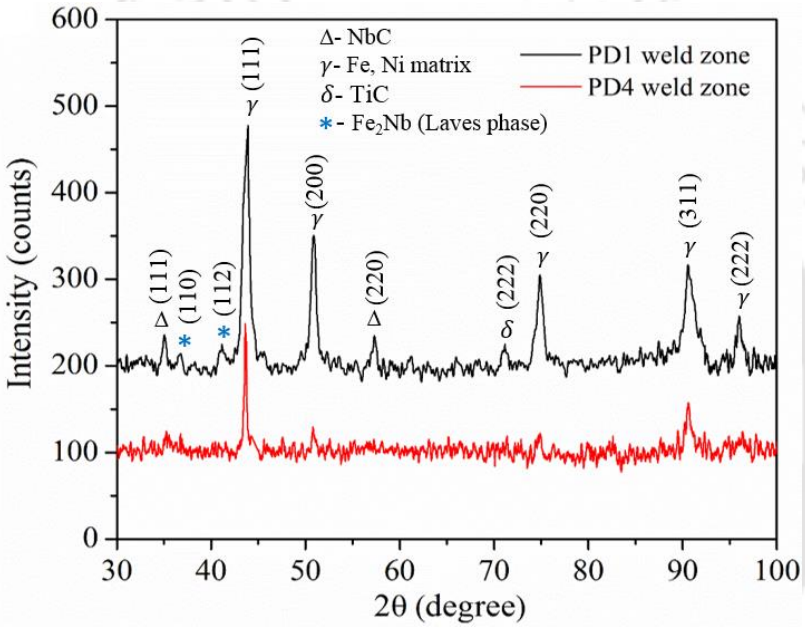

Fig. 5.37 XRD analysis of PD1 and PD4 weld

The relative amount of various phases present in the weld zone is calculated by the normalized intensity ratio (NIR). The peak intensities corresponding to various phases are given in Table 5.10. NIR for a particular phase *A*, is estimated by using the following relation as suggested by Peelamedu et al., (2002)

$$NIR_A = \frac{I_A - I_Z}{I_A + I_B + I_C + I_D - 4I_Z} \quad (5.2)$$

where I_A, I_B, I_C, and I_D are corresponding intensities of *A*, *B*, *C* and *D* phases, and I_Z is known as background intensity. The equation 8.1 is used to evaluate NIR (%) value for all other intermetallic phases present in the weld zone and given in Table 5.10. The estimated amount

of NbC, Fe_2Nb and TiC intermetallic phases for PD1 weld is found to be 8.83%, 5.1%, and 5.08% respectively, whereas these phases reduced to 7.83%, 3.94%, and 4.92% respectively in PD4 weld. Hence the deleterious NbC and Laves phases that are responsible for the formation of micro-fissure and micro-cracks have reduced by 11.3% and 22.7% respectively with decreasing the welding speed. The foremost reason for the reduction of these phases could be due to the high weld dilution level, and formation of equiaxed microstructure (Fig. 5.35g) compared to the continuous columnar dendritic structure of PD1 weld (Fig. 5.35c) (Manikandan et al., 2014).

Table 5.10 Relative XRD phase intensities for PD1 and PD4 weld

Welding condition	Phase	I_A	I_B	I_C	I_D	I_Z	**NIR,%**
PD1	A (NbC)	235.4				210	**8.83**
	B (Fe_2Nb)		224.7			210	**5.1**
	C (γ- matrix)			443.2		210	**80.9**
	D (TiC)				224.6	210	**5.08**
PD4	A (NbC)	123.1				110	**7.83**
	B (Fe_2Nb)		116.6			110	**3.94**
	C (γ- matrix)			249.3		110	**83.31**
	D (TiC)				118.2	110	**4.92**

In dissimilar welding, the mixing of parent materials is quantified by chemical dilution level (in percentage). The dilution level indicates the final composition and segregation potential of various alloying elements in the fusion zone. Hence, elemental dilution of principal alloying elements of Inconel 718 and AISI 316L during fusion welding is estimated by using equation 8.2 (Banovic et al., 2002), and the corresponding results are depicted in Table 5.11. The equation is

$$D = \frac{C_{BM1} - C_{FZ}}{C_{BM2} - C_{FZ}} \times 100 \quad (5.3)$$

where C_{BM1} and C_{BM2} are elemental compositions (wt.%) of Inconel 718 and AISI 316L, respectively; C_{FZ} is the average fusion zone composition. The magnitude of C_{FZ} is measured by EDS area analysis technique over a scanning area of approximately 9000 μm^2 in weld central region. The value of C_{FZ} for principal alloying elements is depicted in Table 5.11. The elemental dilution of major matrix elements (i.e., Ni and Fe) are observed to be changing inversely with the weight percentage of these elements. This trend is mainly due to the mixing of base materials, one enriched with Ni (Inconel 718: ~51.1%) and other with Fe (AISI 316L: ~68%). Whereas for minor matrix elements (i.e., Nb, Mo, and Ti), with increase in dilution level, the weight percentage reduces in the FZ. Further, the dilution level of weld zone is obtained by averaging the elemental dilution level of major alloying elements and is depicted in Table 5.11. The weld dilution level (D) in PD4 increases sharply by 98% to that of PD1 weld. The improvement is due to lower welding speed and higher heat input during the welding process that allows sufficient melting and mixing of the base materials. The magnitude of dilution level controls weld nominal composition and the segregational tendency of alloying elements. Banovic et al., (2002) reported, a higher dilution level significantly reduces secondary phases like Laves and NbC in the dissimilar weld zones of Ni-based superalloy and austenitic stainless steels. Hence, in the current investigation, both the dilution level and XRD analysis confirm a reduction in intermetallic phases with reduction in welding velocity. Therefore, the formation of weld micro-cracks in FZ could be mainly due to the formation of a higher amount of intermetallic phases.

Table 5.11 Effect of welding conditions on dilution level of principal alloying elements

Welding conditions/ Elemental dilution level (D_E)	C_{FZ} (wt. %)					**Weld dilution level (D) (%)**
	Ni	Fe	Nb	Mo	Ti	
PD1	36.4	33.8	5.2	3.2	0.9	
D_E (%)	55.9	42.1	1.9	18	22.2	**28.0**
PD4	37.1	30.6	4.0	2.6	0.6	
D_E (%)	51.8	29.9	32.5	80	83	**55.4**

5.5.4 Influence on mechanical properties

To further understand the effect of intermetallic phases on mechanical properties, micro-hardness distribution across base material and weld zone for each welding condition is depicted in Fig. 5.38(a). Solution treated Inconel 718 base material has an average hardness of 212±9 HV against 195±7 HV of AISI 316L. A variation in weld zone hardness is observed among the welding cases with a maximum hardness of 224.2 HV for PD1 against 198 HV of PD4. The maximum hardness of PD1 weld near Inconel 718 side could be mainly due to the formation of a higher amount of Nb, Mo rich brittle intermetallic phases as compared to the PD4 weld (Devendranath et al., 2014). Further tensile strength of each welded joints along with joint efficiency (compared to the base material strength) and elongation percentage is shown in Fig. 5.38(b). All the welded samples have failed near AISI 316L side fusion boundary but shown excellent joint strength (more than 99%). The tensile elongation (%) of PD1 weld is found to be almost half (i.e. 29%) to that of PD4 weld (55%). Early failure without much deformation of the PD1 weld could be mainly due to the presence of micro-fissure and/or cracks in the welded zone. The tensile fractograph (Fig. 5.38c) of PD1 weld further confirms the presence of micro-cracks inside the dimples as compared to the PD4 fracture surface.

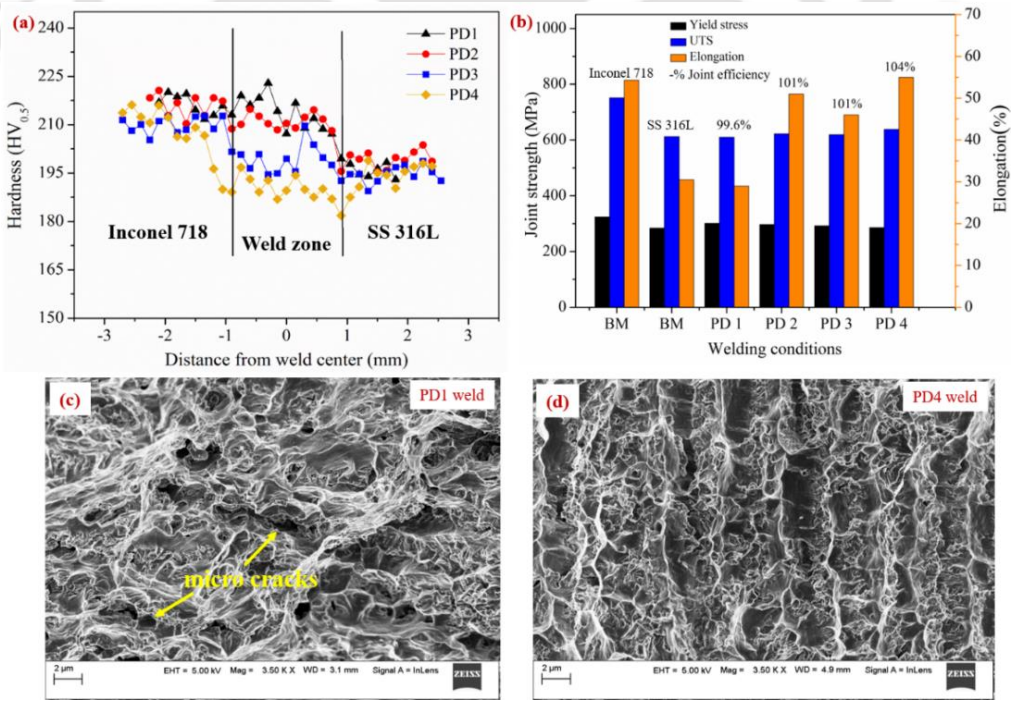

Fig. 5.38 (a) Hardness distribution (b) tensile properties of the welds and (c, d) fractographs of tensile specimens

5.5.5 Summary

The impact of welding velocity on weld bead morphology and mechanical properties are studied herein. A reasonably good joint strength and ductility are obtained at low welding speed of pulse μ-PAW between Inconel 718 and AISI 316L without using any filler material. Based on the results, following conclusions are drawn

- The columnar dendritic structure is observed in the entire weld-bead at high welding speed (196 mm/min) whereas equiaxed structure prevails in the weld interior at low welding speed (145 mm/min).
- The zone where micro-fissures and solidification micro-cracks are observed is enriched with Nb, Mo, and Ti that forms intermetallic.
- The XRD analysis confirms the presence of NbC, Laves (Fe_2Nb) and TiC intermetallic phases in the weld zone. These phases are found decreasing with the reduction in welding speed and continuous columnar dendritic structure.
- The weld zone micro-hardness has marginally decreased with the decrease in welding speed. The weld tensile strength has improved marginally, whereas the elongation has improved substantially (89%) with decreasing the welding speed.

5.6 Studies on microstructure of CO_2 laser welding of Inconel 718 and AISI 316L stainless steel

Intermetallic formation in dissimilar welding is always a hindrance to produce acceptable quality of weld joint. In the present work, a high power CO_2 laser welding system is employed to join Inconel 718 and AISI 316L stainless steel. The macro and microstructural characterization along with mechanical properties are evaluated in the light of intermetallic formation. The micro-segregation and intermetallic formation during the solidification are correlated with solidification parameters. With increasing the laser beam power, the mode of solidification changes from columnar to equiaxed dendrites. EDX and XRD analysis confirms the presence of various secondary intermetallic phases at the fusion zone. The presence of these low melting point secondary phases are primarily responsible for providing micro-crack sites in the fusion zone. In equiaxed dendrites, the segregation and formation of these secondary particles are reduced significantly (> 40%) that results in excellent tensile strength and

elongation of the welded joint. A 3D finite element based heat transfer model is employed to evaluate the solidification parameters for different welding conditions.

5.6.1 General background

Welding of dissimilar material using a laser source is always advantageous in terms of precise control on heat input, size of fusion zone (FZ) and heat affected zone (HAZ) along with high production rate compared to conventional arc welding processes. Joining of dissimilar material extensively reduces the component cost and provide flexibility in the product designing. The Inconel 718 and AISI 316L material combination is widely used for making pressure tubes in nuclear reactors, that are implemented over a wide range of temperature, pressure and stress level (Hinojos et al., 2016). The successful welding of these dissimilar materials is always a challenging task due to the metallurgical incompatibility between them. The failure in weld zone under loading condition possess restrictions for direct application in the industries, hence complete metallurgical analysis of the dissimilar welded component is essential before putting into the service. The traditional arc welding processes escalate the formation of secondary intermetallic compounds in the weld zone and affect the joint properties (Devendranath et al., 2014). The intermetallic precipitation due to solute segregation in the interdendritic region often triggers the initiation of micro crack sites in the fusion zone and causing early failure of the component (Kar et al., 2017). Most of the available literature are confined to the arc welding process and selection of suitable filler material (during TIG welding) to weld Inconel 718 with AISI 316L stainless steel. The main aim was to reduce the influence of segregation of various useful alloying elements through proper selection of filler material as a result the weld properties can be enhanced. But implication of high energy beam source to weld these material combination is not addressed so far. The laser beam welding is one of the most preferred joining technique in aerospace and power generation industries. The solidification mechanism in laser welding is completely different from the conventional arc welding techniques due to the higher cooling rate (Ramkumar. et al., 2019). The variation in solidification mechanism of CO_2 laser welding compared to arc welding and the corresponding impact on microstructure and mechanical strength is need to be analyzed. Hence, proper optimization of the CO_2 laser welding process parameters for successful joining of Inconel 718 and AISI 316L stainless steel is inevitable.

The solidification behavior of the Inconel 718 and AISI 316L fusion zone are characterized by the solidification parameters. Experimental estimation of solidification parameters is not feasible due to the application of high temperature laser beam during the welding process (Kumar et al., 2020). Hence, 3D finite element based thermal model is developed to predict the thermal history of the weld pool during the welding process (Rahman et al., 2015). It is essential to establish a credible heat transfer model that properly represents the heat source and material interaction during the welding process. Several researchers employed heat source of different geometry, based on the mapping of weld pool size and shape (Baruah and Bag, 2016; Kumar and Bag, 2019). For thin sheets, conduction based transient heat transfer models are extensively used to obtain the time-temperature history of the small fusion zone by neglecting convective fluid flow (Bag and De, 2008; Wu et al., 2006). The CO_2 laser source is represented by a Gaussian distributed double ellipsoidal volumetric heat source to facilitate the flux distribution in thickness direction (Ebrahimi et al., 2016). After validation of the numerical model with the experimentally obtained weld bead, simulated time-temperature profiles are used for estimation of the weld solidification parameter. The CO_2 laser process parameters used for producing sound quality welds in the present analysis are shown in Table 3.5 of Chapter 3.

5.6.2 Characteristics of temperature distribution

The developed numerical model is need to be validated before utilizing the simulated thermal data for the evaluation of solidification parameters. The validation is done by comparing the simulated weld bead extent with the experimentally produced weld bead and corresponding comparison in LD1 and LD5 conditions is shown in Fig. 5.39. The fusion zone is confined between the liquidus temperature isotherms of the respective base material (i.e., 1673 K for AISI 316L and 1635 K for Inconel 718) (Knorovsky et al., 1989; Wu et al., 2016). The maximum error in the size of computed and experimental weld bead is estimated to be 6% for the LD1 condition. With increase in laser beam power the error percentage is observed to be reducing and for LD5 it is estimated as less than 2%. Hence, a good agreement between the numerical and experimental data signifies the robustness of the developed thermal model for the CO_2 laser welding process.

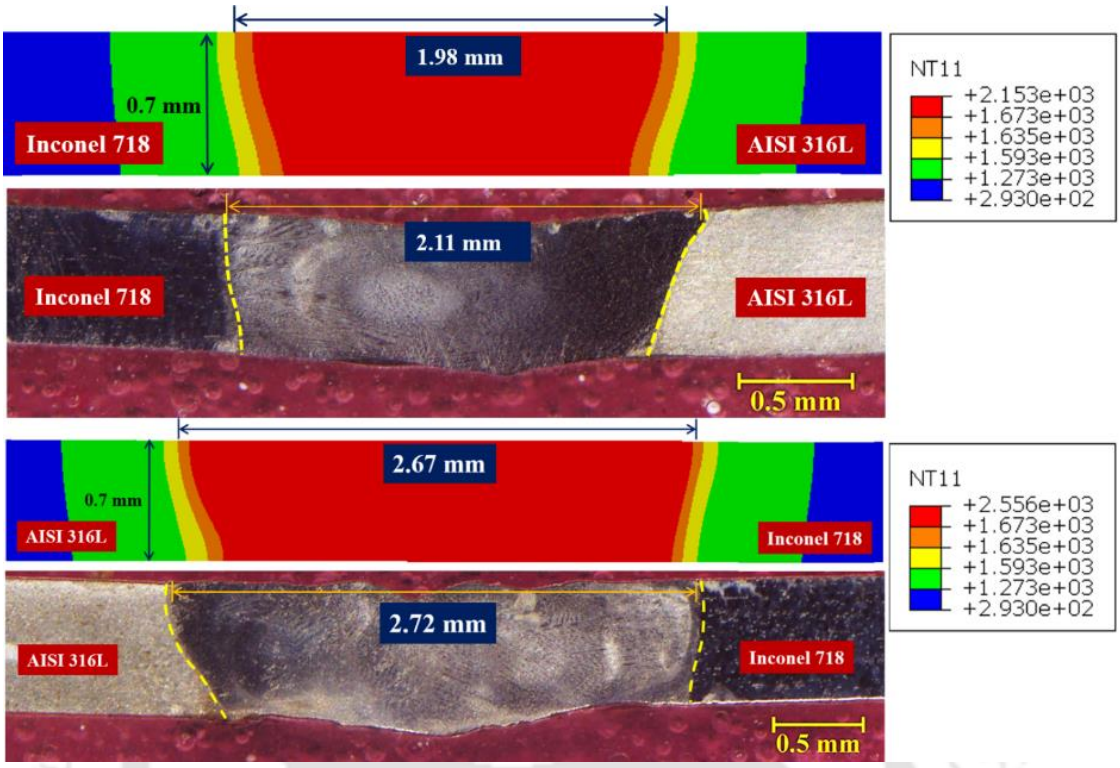

Fig. 5.39 Comparison of experimental and numerically obtained weld bead

The nodal time-temperature profile at the weld center for LD1, LD3 and LD5 weld conditions is depicted in Fig. 5.40(a). The temperature profile witnessed a sharp rise in magnitude as the heat source approaches the node and attain a maximum value. Afterwards, the temperature decreases gradually to room temperature as the heat source moves away from the node. The LD5 condition attained a peak temperature of 2556 K during the welding process, which is much less than the boiling temperature of both the base material. As a result, the vaporization in weld pool is avoided by proper selection of the welding process parameter. The weld pool time-temperature data are further employed to estimate the longitudinal temperature gradient (G) (i.e., along the welding direction) for each welding condition. The temperature gradient distribution corresponding to LD1, LD3 and LD5 condition is presented in Fig. 5.40(b). At the beginning, temperature gradient increases due to the heating action that result in melting of the substrate material. However, at the end of heating cycle, the slope of temperature gradient turns into negative as a result a sharp fall in (G) is witnessed. The change in temperature gradient sign from positive to negative signifies the cooling cycle. The corresponding lowest value of temperature gradient during the cooling cycle is used for the calculation of solidification parameters. The combine form of temperature gradient (G) with

solidification growth rate (*R*) is known as the solidification parameter and it influences the final weld microstructure (Kou, 2003). The product of (*G*) and (*R*) (i.e., cooling rate) dominates the scale of final weld microstructure whereas the ratio of (*G*) and (*R*) controls the mode of solidification. A higher magnitude of (*G/R*) always promotes planar and cellular mode whereas a lower magnitude facilitates columnar and equiaxed mode of solidification (Kou, 2003). The solidification growth rate (*R*) at weld center in longitudinal direction is equivalent to the welding scanning speed (i.e., maximum value) (Manikandan et al., 2014). Hence, the laser scanning speed (i.e., 6.67 mm/sec) is used for the estimation of solidification parameters for each welding condition and the corresponding values are given in Table 5.12. Inconel 718 is a heavily alloyed material hence; it solidifies in dendritic mode (i.e., combination of columnar and equiaxed dendrites).

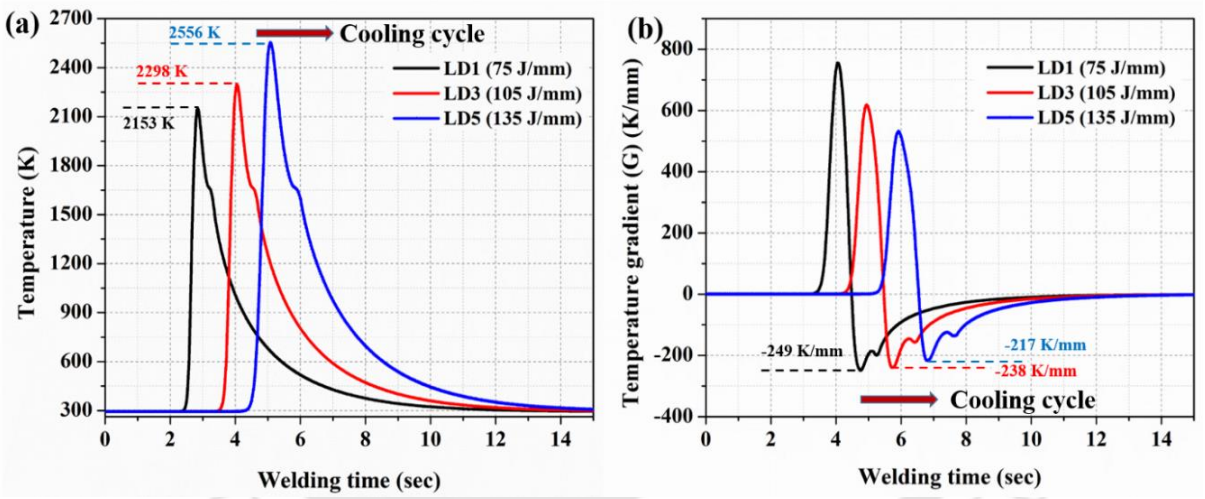

Fig. 5.40 Showing (a) nodal time - temperature distribution and (b) weld temperature gradient variation during the welding

Table 5.12 Thermal characteristics of the welding conditions

Sample no.	Peak temperature (*K*)	Temperature gradient (*G*)	*G.R* (*K/s*)	*G/R* (*K-s/m²*)
LD1	2153	249	1660	37.3
LD2	2220	242	1614	36.2
LD3	2298	238	1587	35.6
LD4	2461	230	1534	34.4
LD5	2556	217	1447	32.5

5.6.3 Impact of solidification parameters on microstructure

The variation in fusion zone morphology with respect to the solidification parameters is the potential outcome of this section. The fusion zone SEM micrographs for each welding condition is depicted in Fig. 5.41. The presence of intermetallic phase is evident in the micrographs. The morphology of final microstructure is witnessed to be different with respect to different process parameters. The presence of continuous long columnar dendrites (primary dendrites) is witnessed in LD1 weld, highlighted, and shown with the arrow in Fig. 5.41(a). The columnar dendritic solidification morphology is mainly due to the higher magnitude of (*G/R*) for LD1 weld (i.e., 37.3 K-s/m^2) as compared to other welding conditions. However, the higher cooling rate in LD1 (i.e., 1660 K/s) leads to a relatively finer intermetallic structure compared to LD2 and LD3 condition. The length of intermetallic phases in LD1 weld are varied between 0.5 µm to µm and a width between 0.5 µm to 4 µm. The variation in weld morphology is evident with decrease in (G/R) ratio and (*G.R*) in LD2 and LD3 weld. The growth of secondary dendritic arms (SDA) are witnessed in LD2 and LD3 weld instead of only primary dendrites (as in LD1) with the reduction in (*G/R*) (Fig. 5.41b and c). The secondary arms in LD2 weld are found to be interconnected continuous chain of dendrites whereas in LD3 fragmentation of secondary dendrites are witnessed. With further reduction in solidification parameters, the final microstructure has completely transformed into discrete and equiaxed type of morphology in LD4 and LD5 condition respectively. The size of intermetallic particles is reduced significantly as compared to the LD1, LD2 and LD3 weld. The average length of intermetallic particles is in the range of 0.5 to 5 µm with a maximum width of 1.5 µm in LD2 weld. In LD5 the length is further reduced and estimated to be in the range of 0.2 µm to 2.5 µm maximum. The significant diminution (~ 90%) in interdendritic particle size in LD5 weld compared to LD1 considerably reduces the volume of intermetallic phases in the produced weld bead. Hence, reduction in the magnitude of solidification parameters is witnessed to be beneficial in controlling the intermetallic formation for the CO_2 laser dissimilar welding of Inconel 718 and AISI 316L steel.

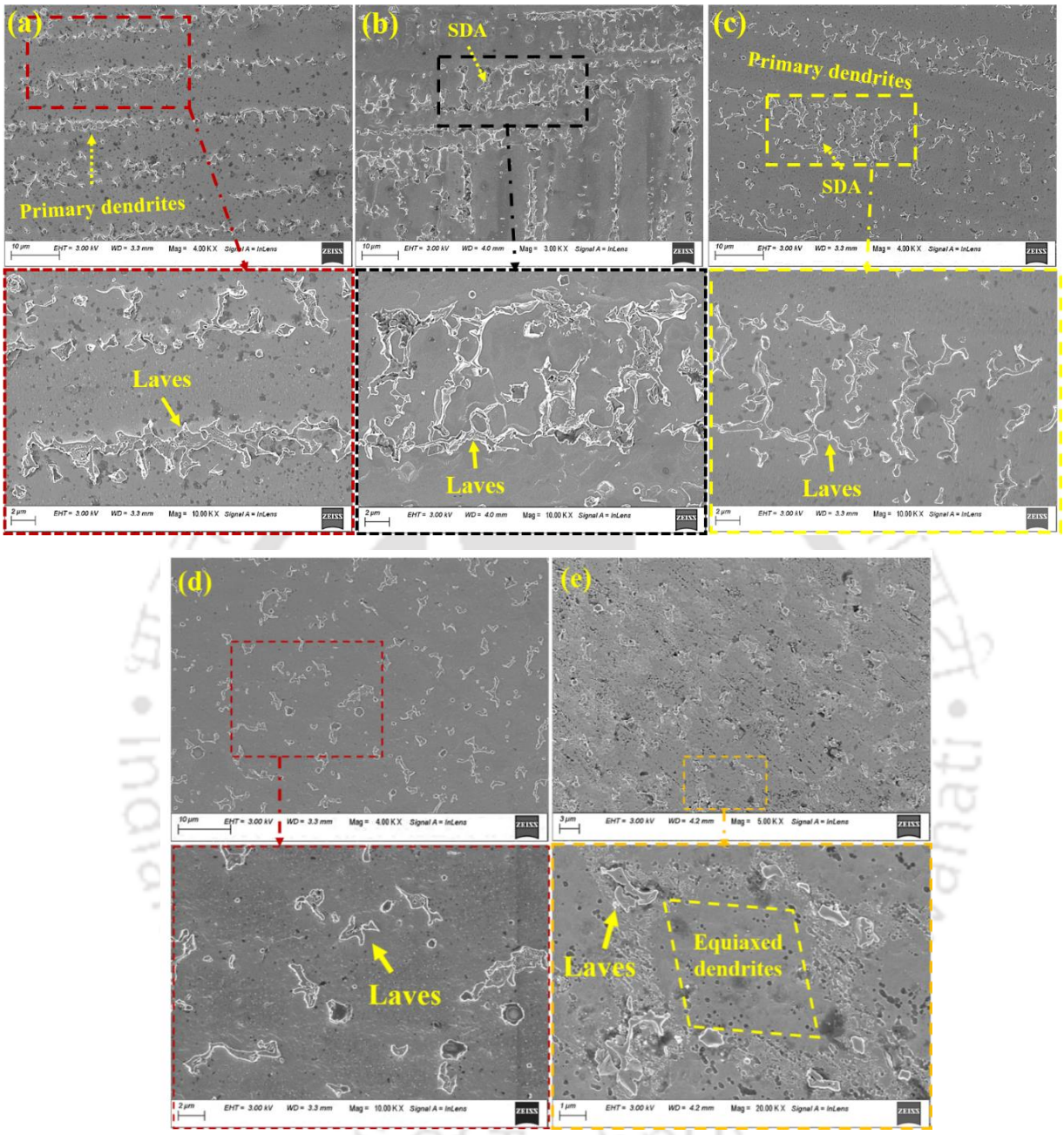

Fig. 5.41 SEM micrographs of (a) LD1 (b) LD2 (c) LD3 (d) LD4 and (e) LD5 weld

The characterization of various intermetallic particles through elemental distribution is performed by EDX characterization of the fusion zone. The elemental mapping on the intermetallic of LD3 fusion zone is shown in Fig. 5.42(a). The precipitated intermetallic during the solidification are observed to be enriched with Nb (pink), Mo (teal) and Ti (blue) elements by the segregation from nearby region. Whereas Cr, Fe and Ni are distributed equally throughout the scanning fusion zone area. For quantitative analysis of elemental distribution

and composition, the EDX spot analysis is performed on intermetallic particles (spectrum 9 and 12) and core area (spectrum 8) and the obtained results are shown in Fig. 5.42(b). The weight percentage of Nb, Ti and Mo in the secondary phase is almost increased by 500%, 400% and 150% (spectrum 9) as compared to the core (spectrum 8). These phases enriched with crucial alloying elements in the weld zone are primarily the Laves phase (Devendranath Ramkumar et al., 2014; Ning et al., 2018). The presence of MC carbides (i.e., TiC and NbC) are also witnessed through spectrum 12, as the enrichment of Ti is witnessed to be 42.5 times to that of the core weight percentage. Hence, the precipitation of intermetallic like Laves and other carbide particles during the fusion welding is not possible to eliminate completely. However, the formation of these secondary phases can be widely restrained through the solidification parameters. The formation of equiaxed micro-structure in the FZ were witnessed to be reducing the volume of these secondary phases.

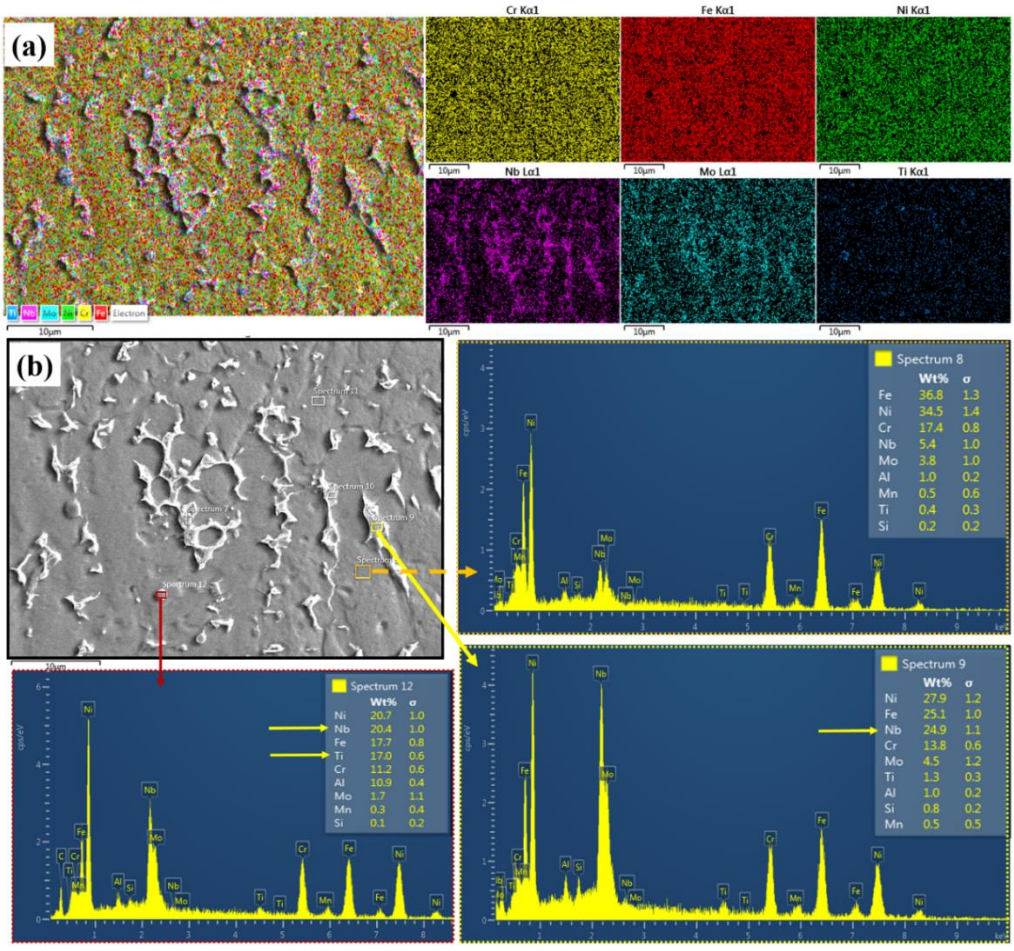

Fig. 5.42 (a) EDX elemental mapping and (b) EDX spot analysis on weld microstructure

5.6.4 XRD characterization of the fusion zone

The precipitation of various secondary intermetallic phases is reaffirmed through the XRD analysis of weld zone. The diffraction peaks corresponding to NbC (2θ: 35.45, 58.45), TiC (2θ: 71.13) and Laves (Fe_2Nb) (2θ: 37.19, 42.54) secondary phases are witnessed and index for LD1, LD3 and LD5 welding condition (Fig. 5.43). The sharp peaks corresponding to Fe-Ni austenite (γ) matrix [dominating in the (200) direction] are witnessed due to use of the bulk sample. The peaks corresponding to different secondary phases are witnessed to be sharp and strong in the LD1 condition whereas weak and relatively small peaks are witnessed for LD5 weld.

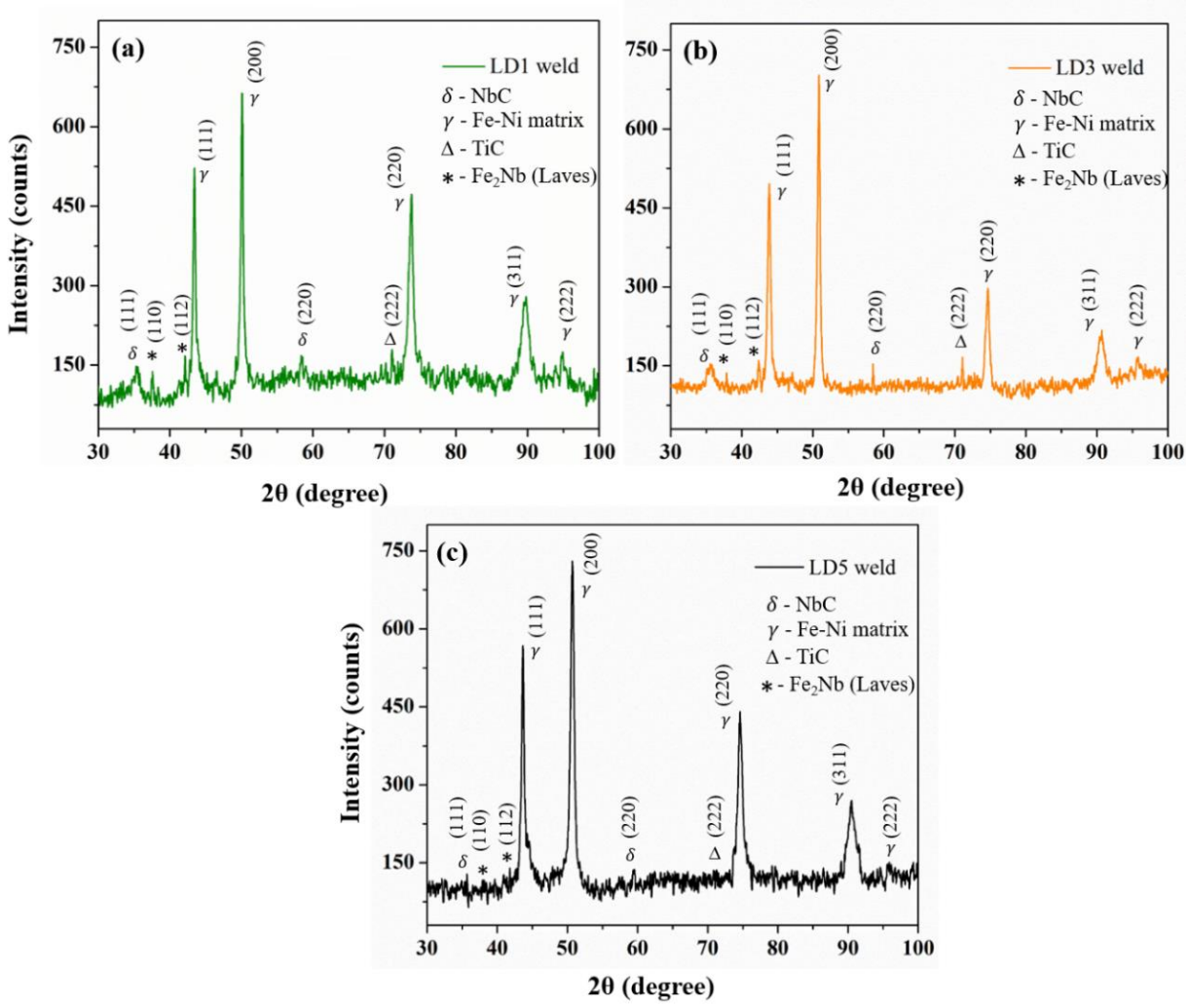

Fig. 5.43 X-ray diffraction analysis of (a) LD1 (b) LD3, and (c) LD5 weld

Normalized intensity ratio (NIR) technique is employed to evaluate the presence of (i.e., relative proportion) each intermetallic phases in the fusion zone by using the XRD peaks. The magnitude of NIR (%) for a specific phase 1 is estimated through the following equation (Peelamedu et al., 2002)

$$NIR_1 = \frac{(I_1 - I_B)}{I_1 + I_2 + I_3 + I_4 - 4I_B} \tag{5.4}$$

where I_1, I_2, I_3 and I_4 are the XRD intensities corresponding to NbC, Laves, austenite (γ) and TiC phase respectively, and I_B is the base intensity. The corresponding NIR for each phase corresponding to LD1, LD2 and LD3 weld is given in Table 5.13. For LD1 condition the estimated amount of NbC, Fe_2Nb and TiC are 7.94%, 7.84% and 9.32%, respectively. Whereas these intermetallic are reduced significantly by 51%, 45% and 40% in the LD5 condition. The reduction in intermetallic phases is mainly due the high dilution level and development of equiaxed microstructure (Fig. 5.41e) compared to columnar dendrites in LD1 weld (Fig. 5.41a) (Manikandan et al., 2014). In dissimilar welding, the segregational tendency is influenced by the dilution level. A higher dilution level hinders the segregation and formation of intermetallic phases, and can be achieved by applying higher heat input during the course of welding (Banovic et al., 2002). A higher heat input provides time for sufficient melting action and mixing of the base material and results in reduction of the secondary phase formation. In the current analysis, LD5 weld is produced with the maximum laser beam power, therefore reducing the segregation of principal alloying element and formation of intermetallic phases. The SEM micrograph and XRD peaks corresponding to LD5 weld is confirming the lower segregation and secondary phase formation.

Table 5.13 Relative XRD peak intensities for LD1, LD3 and LD5 weld

Welding condition	Phase No.	I_1	I_2	I_3	I_4	I_B	NIR,%
LD1	1 (NbC)	168.3				110	**7.94**
	2 (Fe_2Nb)		167.4			110	**7.84**
	3 (TiC)			178.5		110	**9.32**
	4 (γ- matrix)				660.8	110	**74.9**
LD3	1 (NbC)	153.8				110	**6.03**
	2 (Fe_2Nb)		158.4			110	**6.67**
	3 (TiC)			151		110	**5.65**
	4 (γ- matrix)				702	110	**81.63**
LD5	1 (NbC)	137				110	**3.88**
	2 (Fe_2Nb)		139.8			110	**4.28**
	3 (TiC)			134.8		110	**3.56**
	4 (γ- matrix)				724	110	**89.7**

5.6.5 Mechanical analysis

The correlation of final weld morphology through tensile and hardness distribution is an important aspect to understand the influence of welding process parameters on strength of the produced weld. For each condition, two tensile samples are tested at room temperature, the average value is reported in Table 5.14, and the corresponding stress-strain curves are depicted in Fig. 5.44(a). All the welded samples are failed in the weld zone area. The LD1, LD2 and LD3 welded samples are failed at the center of the fusion zone, whereas for LD4 and LD5 the fracture location is in the AISI 316L side fusion boundary. Hence, based on the failure location, fusion zone is weakest in LD1, LD2 and LD3 weld compared to the LD4 and LD5 condition. All the welded samples achieved a joint efficiency of more than 90% (compared to AISI 316L base material). The further improvement in tensile strength of LD4 and LD5 (more than 95%) weld is mostly due to lower segregation and formation of Laves and carbide phases during the solidification. The brittle intermetallic phases deplete a substantial volume of strengthening alloying elements from the matrix therefore deteriorating the mechanical properties. Further, these low melting point intermetallic phases are also responsible for providing micro-crack

initiation sites as shown in Fig. 5.44(c). These micro-crack sites eventually propagate and cause rapid failure of the component, under tensile loading. As a result, it affects the ductility of the welded samples. The tensile elongation corresponding to welded samples are found to be inferior to that of parent materials. The tensile fracture surfaces corresponding to LD1 and LD5 weld are shown in Fig. 5.44(d) and (e) respectively. The LD5 fracture surface reveals presence of tearing ridges along with shallow and coarse dimple structure whereas small dimples are observed in the LD1 weld. Number of micro-void sites are also clearly evident in the LD1 fracture surface, whereas LD5 surface is witnessed to be free from such defects. As a result, in LD1 condition, the elongation has reduced significantly by 70% (w.r.t. Inconel 718) and 83% (w.r.t. AISI 316L). However, the elongation has considerably improved in LD4 and LD5 weld (w.r.t. LD1) due to the formation of discrete and equiaxed dendrite morphology. The lower magnitude of (G/R) in LD5 weld is the driving parameter for the formation of equiaxed morphology. At constant solidification rate (R), reduction in temperature gradient (G) escalates the constitutional supercooling in the solidification front, that lead to the nucleation and growth of equiaxed dendrites. The equiaxed dendrites restricts the growth of continuous columnar structure as a result segregation of strengthening elements reduces significantly (Kou, 2003). Hence, reduction in segregation, consequently improves the tensile properties of the welded component.

Table 5.14 Tensile test results

Sample no.	UTS (MPa)	Elongation (%)	Joint efficiency (η)
Inconel 718	801 ± 13	27 ± 4	-
AISI 316L	668 ± 11	48 ± 2	-
LD1	606 ± 8	8 ± 1.5	90.7
LD2	627 ± 5	14.6 ± 1.2	93.8
LD3	631 ± 7	10.1 ± 1.4	94.4
LD4	640 ± 9	19 ± 1.5	95.8
LD5	661 ± 7	14.2 ± 2	99.9

The characteristic of micro-hardness variation across the weld bead for each welding condition is shown in Fig. 5.44(b). The hot rolled Inconel 718 base material has an average

hardness of 233 ± 12 HV, whereas it is 202 ± 6 HV for AISI 316L. The variation in fusion zone hardness characteristic is predominantly due to the variation in mode of solidification in each welding condition. The utmost fusion zone hardness of 276 HV is witnessed in the LD1 whereas lowest hardness of 171 HV is observed for LD5 weld. Migration of Nb, Mo and Ni from the matrix to the interdendritic sites, enriches it with intermetallic and various carbide phases (i.e., NbC, TiC, Laves and δ-ferrite) and influence the hardness characteristic of the fusion zone (Prabaharan et al., 2014). As already explain in the earlier section various intermetallic phases present in LD1 weld are almost twice to that of the LD5 weld. Hence, increase in the formation of these brittle intermetallic secondary phases in LD1 and LD2 weld is the primary cause of higher hardness compared to the LD5 weld (Devendranath et al., 2014). Bansal et al. (Bansal et al., 2016) measured the hardness on a carbide particle and witnessed it to be double compared to the matrix. Hence, the hardness distribution across the weld bead is a function of intermetallic and carbide phases produced during the welding process.

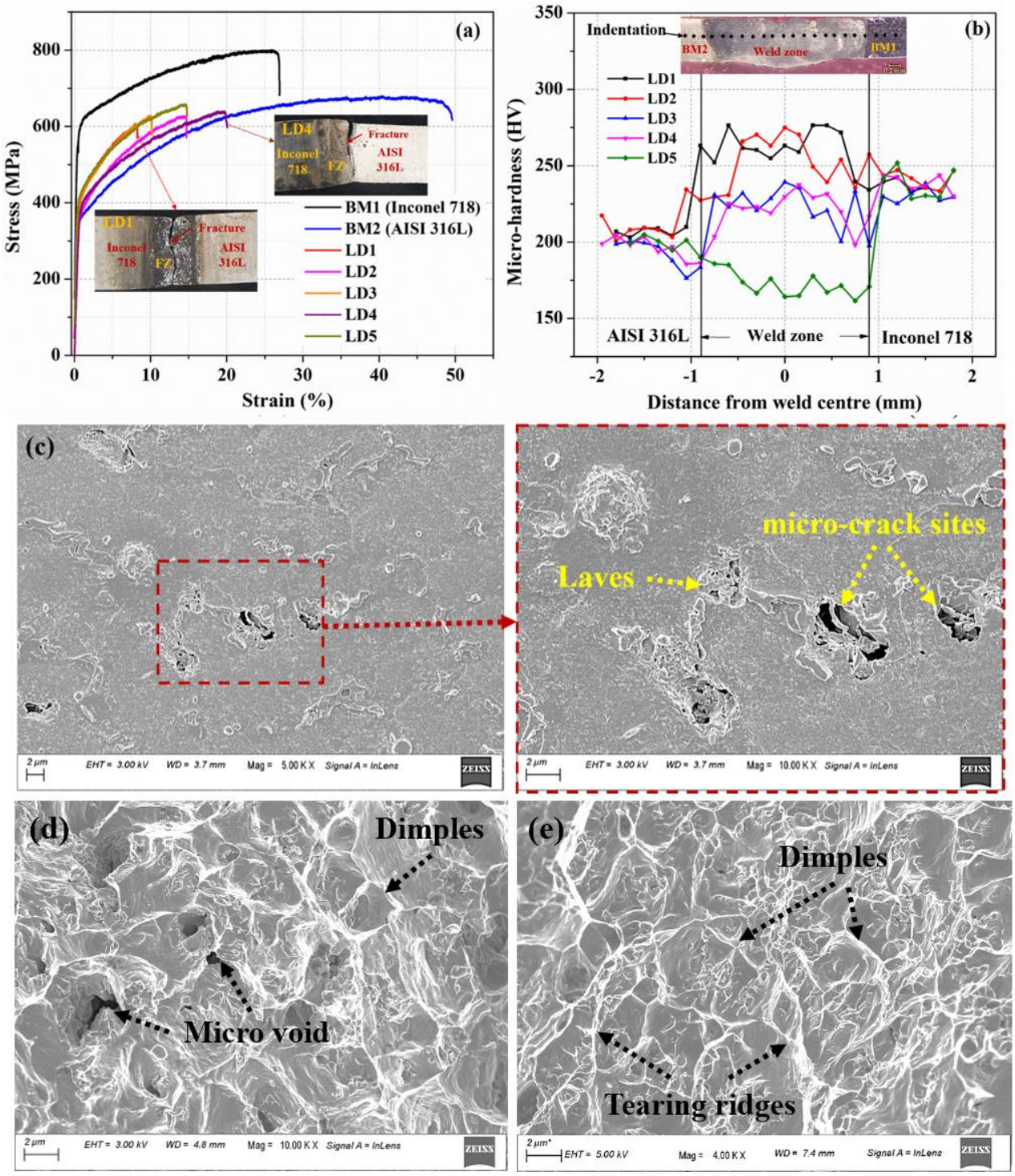

Fig. 5.44 Tensile stress-strain curves along with fracture location for welded samples; (b) hardness distribution of welded samples (c) location of crack sites in final solidified structure and (d, e) tensile fracture surfaces of LD1 and LD5 weld respectively

5.6.6 Summary

In this study, weldability of Inconel 718 with AISI 316L steel using CO_2 laser welding is addressed and based on the outcome outlined above, the following conclusions are derived.

- Successful weld beads with joint efficiency more than 90% are obtained by using beam power between 500 to 900 W with a scanning speed of 400 mm/min. The numerical model accurately predicted the weld bead geometry with a highest error of 6%.
- The solidification mode in fusion zone is varying from columnar dendrites to equiaxed dendrites with increase in the laser beam power. The increase in the beam power reduces the solidification parameter (G/R).
- The fusion zone XRD analysis confirms the formation of Laves and other metal carbides (NbC and TiC) during the solidification. The formation of intermetallic phases is witnessed to be reduced significantly (~40%) in equiaxed dendrites compared to the columnar dendrites.
- The highest tensile strength (~100%) with good elongation (14.2%) is achieved for the joint having lowest magnitude of (G/R) against the weld produced with highest (G/R).
- The fusion zone hardness is witnessed decreasing with the increase in laser beam power. Hence, fusion zone with columnar dendrites attain a maximum hardness of 276 HV, whereas minimum hardness of 171 HV is witnessed for the equiaxed structure.

Chapter 6

Conclusions and Future Scope

6.1 Introduction

The overall aim behind the presented work is to produce successful welds of Inconel 718 in similar and dissimilar combination with AISI 316L stainless steel by implementing fusion welding techniques like micro plasma and laser welding processes. The reduction of various intermetallic phases or micro crack formation through welding techniques and proper choice of process parameters to improve the weld quality is undertaken in this work. With this aim, a reliable data base for Inconel 718 welding and Inconel 718 - AISI 316L welding is obtained, which can be utilized further to predict the life of the fabricated structure and the components operating at high temperature and extreme environments. The present work aims to encounter commonly occurring problems of interdendritic segregation and formation of different intermetallic phases in fusion welding of Inconel 718 and Inconel 718-AISI 316L. The formation of these intermetallic phases consumes significant alloying elements from the matrix and deteriorates the tensile and hardness properties. Apart from that, it also provides preferable sites for crack initiation and propagation, causing early failure of the weld component. The solidification parameters mainly govern the microstructural morphology in a welded structure. In Inconel 718, the cooling rate is more deterministic parameter as compared to the solidification mode. By applying current pulsation, full penetration weld beads were obtained at a lower heat input and high cooling rate compared to constant current mode of plasma welding. Moreover, the variability in the solidification parameters (i.e. $G.R$ and G/R) due to continuous melting and re-melting by the pulsation effect is also a deterministic factor for obtaining sound quality Inconel 718 weld joints. An investigation on post-weld heat treatment of pulse micro-plasma Inconel 718 welded structure is carried out with different

aging techniques (i.e., different temperature and holding time). It is understood that the microstructural evolution in Inconel 718 is complex in nature due to the coexistence of different phases (i.e., γ', γ'', δ and MC) along with the main austenite (γ) matrix. The precipitation of strengthening phases is hindered due to the formation of the intermetallic phases enriched with principal strengthening alloying elements (i.e., Nb, Mo, Al and Ti). Hence, dissolution of these phases makes ample amount of these elements available for the precipitation of strengthening phases during the aging treatments. The variation in aging temperature and holding time adversely influence the morphology of this strengthening phase and finally improves mechanical properties the welded joint.

Welding of dissimilar materials significantly reduces the product cost by reducing the volume of expensive material without sacrificing its mechanical properties required to meet the operating condition. But, welding of dissimilar materials (i.e., Inconel 718 with AISI 316L) is a challenging task due to complicated metallurgical characteristics of the different base materials, which is often encountered by formation of various secondary phases in the weld zone. These intermetallic phases are mostly accountable for the formation of hot cracking in the weld during solidification process. However, these defects can be reduced significantly by proper selection of welding technique and welding process parameters. Hence, micro-plasma arc welding (μ-PAW) and laser welding process is utilized to produce sound weld joints of this bimetallic combination. The effect of plasma pulse current and welding velocity on solidification mode and intermetallic formation with consequence effect on solidification crack formation are also investigated. The solidification mechanism in laser welding is completely different from the arc welding techniques in terms of transient and gradients. The variation in solidification mechanism of CO_2 laser welding compared to arc welding and the corresponding impact on microstructure and mechanical strength is analysed. The accurate measurement of time-temperature profile to estimate solidification parameters of the fusion zone through experimental analysis is unfeasible due to the formation of small weld pool and involvement of high temperature gradients and transients. Hence, 3D conduction based heat transfer models are developed for the prediction of weld geometry and cooling rate at the fusion zone and HAZ.

6.2 Conclusions

The following conclusions are drawn in the course of conducting micro plasma arc welding (μ-PAW), CO_2 laser welding and developing 3D computational modelling for Inconel 718 and AISI 316L in similar and dissimilar configuration. The present methodology adopted for welding this material combination in autogenous mode is a good alternative for the thin sheets.

- The autogenous welding of Inconel 718 was mainly confined to high energy beam source welding techniques like EBW and LBW. The economical micro-plasma arc welding is implemented to successfully produce autogenous welds of Inconel 718 sheets. The full penetration in welding is achieved with 22% less heat input (J/mm) during the pulse mode of welding compared to constant current mode of μ-PAW. As a result, the maximum weld cooling rate is witnessed for the pulse mode of welding. The pulse mode reduces the intermetallic formation significantly and 96% of joint efficiency is achieved.
- The conduction based heat transfer models are well suited for small scale welding, and the influence of convective heat transport can be approximated by using a volumetric heat source. The effect of current pulsation is often suppressed by averaging the heat input to perform the numerical simulation. A double ellipsoidal heat source model is found suitable to represent the pulse plasma arc during similar welding of Inconel 718. The shape and size of the simulated weld profiles are in good agreement with the experimental results with a maximum error of 7.3%, which signifies soundness of the developed numerical model.
- The final weld microstructure is governed by the solidification parameters. In Inconel 718 weld, the mode of solidification changes from columnar to equiaxed structure with the reduction in *(G/R)* magnitude. And the scale of solidified microstructure is reducing with increase in (*G.R*). The lowest variability in *G.R* and *G/R* between heating and cooling phase in pulse mode produces the highest quality of weld joint.
- The segregation and formation of secondary phases are inevitable during fusion welding of Inconel 718. Precipitation of secondary phases enriched with Nb, Mo and Ti are observed in the interdendritic region of Inconel 718 and found increasing with reduction in cooling rate (*G.R*). The secondary dendritic arm spacing is reduced by 44% and average Laves particle size by 51% with the lowest heat input welding compared to high heat input pulse welding process.

- It is experienced that an inappropriate pulse characteristic can triggers the segregation tendency of intermetallic phases and may produce micro-cracks in the fusion zone. The implemented pulse characteristics i.e., high welding cycle time and pulse frequency are witnessed to have detrimental effect on the mechanical properties of the weld. With increase in pulse welding heat input, the average hardness of the fusion zone decreases. Overall, the current pulsation with low average heat input (less than 52 J/mm) results in significant improvement in weld microstructure and mechanical strength of the Inconel 718 weld.
- Through microstructural characterization, presence of intermetallic phases like Laves (Fe_2Nb), NbC, and TiC are confirmed in the interdendritic region of Inconel 718. The formation of these intermetallic phases is unavoidable during solidification but post weld heat treatment is widely implemented to dissolve these phases to improve the weld quality. The double aging heat treatments of the as-welded sample at 760 ºC/8 h and 680 ºC/6 h resulted in the partial dissolution of intermetallic phases and precipitation of the needle-shaped δ phase, γ" and γ' strengthening phases around the intermetallic phase are experienced resulting in nominal improvement in weld mechanical properties.
- The high-temperature solution treatment (at 1165 ºC/1h) completely dissolves the intermetallic phases from the matrix but precipitated some intergranular MC carbides that are responsible for the formation of micro-crack in the grain boundary. The solution treatment followed by double aging at 960 ºC/1 h and 760 ºC/5 h responds in precipitation of platelet δ phase uniformly in the grain boundary and coherent γ" and γ' phases in the matrix. As a result, the tensile strength has improved by 16.3%, whereas the micro-hardness of the fusion zone by 115% compared to the as-welded Inconel 718 samples.
- Whereas the solution treatment followed by duplex aging at 760 ºC/8 h and 680 ºC/6 h resulted in the precipitation of needle-shaped δ phase in the grain boundary and γ" and γ' strengthening phases in the austenite matrix. The tensile strength is improved by 21% and the maximum fusion zone hardness by 121% compared to the untreated welded samples. The post-weld heat treatment holding time is reduced by 53% without affecting the mechanical properties, by performing aging at 960ºC as compared to aging at 760ºC of the standard heat treatment procedure.

- The dissimilar welding of Inconel 718 and AISI 316L is largely restricted to conventional arc welding techniques (mainly GTAW) with different filler materials of intermediate composition. So, it is important to understand the microstructural evolution and corresponding impact on mechanical properties of the joints produced in autogenous mode. So, defect free successful autogenous dissimilar welds are produced through pulse μ-PAW process for this material combination.
- The double-ellipsoidal heat source accounts for the nonsymmetric temperature distribution in the front and rear quadrants due to the weld velocity. However, it cannot accommodate the nonsymmetric weld profile due to the difference in thermo-physical properties of the dissimilar materials. Hence, the heat transfer model is developed using the Gaussian-distributed quadruple-ellipsoidal heat source model for the μ-PAW process of Inconel 718 and AISI 316L stainless steel. The developed numerical model for the dissimilar weld has a maximum error of 4.4% compared to the experimental results.
- The estimated solidification parameters *(G/R)* are observed to vary inversely with the applied pulse current. Lower magnitude of *(G/R)* in the weld results in formation of equiaxed dendrites and consequently improves the joint efficiency. In fusion zone, presence of Laves phase (Fe_2Nb) and various Nb and Ti rich secondary phases like NbC and TiC along with the main austenite (γ) matrix is observed.
- The micro-fissures and solidification crack zones are enriched with Nb, Mo, and Ti alloying elements, that eventually indicates the formation of intermetallic phases. The segregation (wt.%) are observed to be more in the columnar structure as compared to the equiaxed structure. The reduction in secondary phases caused a significant improvement in elongation for the lowest value of *(G/R)*, compared to welds with highest magnitude. For Inconel 718- AISI 316L material combination, a higher heat input during μ-PAW welding process has found to have beneficial effect on the mechanical properties.
- The solidification mechanism in laser welding is completely different from the arc welding techniques due to presence of high cooling rate. Full penetration sound quality dissimilar welds are produced by using CO_2 laser welding technique with a 53% less heat input (J/mm) to that of μ-PAW technique. The solidification mode in fusion zone is varying from columnar dendrites to equiaxed dendrites with increase in the laser beam power.

- The numerical model for laser welding is also developed by using Gaussian distributed quadruple-ellipsoidal volumetric heat source, which predicted the weld bead geometry with a highest error of 6%. The increase in the beam power also witnessed to reduce the solidification parameter *(G/R)* during the laser welding process.
- The formation of intermetallic phases is witnessed to be reduced significantly (~40%) in equiaxed dendrites compared to the columnar dendrites. The highest tensile strength (~100%) with good elongation (14.2%) is achieved for the joint having lowest magnitude of *(G/R)* against the weld produced with highest *(G/R)*. The fusion zone hardness distribution is witnessed to be decreasing with the increase in laser beam power. Hence, fusion zone with columnar dendrites attain a maximum hardness compared to the equiaxed structure.

6.3 Scope for future work

In the present work, an effort has been put forward to develop the process window for producing successful butt joint by implementing micro-plasma arc and CO_2 laser welding techniques for similar (Inconel 718) and dissimilar (Inconel 718-AISI 316L) combinations of materials. However, the experimental processes and the analysis techniques can be improved in several ways. Due to process limitation, thickness of the base materials used in the investigation is kept below 1 mm, whereas similar process can be employed to weld this material combination in autogenous mode for higher thickness according to the requirements. Inconel 718 is the workhorse material of aerospace industry, approximately 51% (i.e., more than 1500 individual parts) of the space shuttle main engine components of different thickness and size are made of Inconel 718 superalloy. The parts were fabricated mainly using GTA, LBW and EB welding technique and no failure were reported under testing and flight condition. The thin sheets of Inconel 718 are widely used for making casing that are used for fan containment applications around parts of the compressor and the turbine region. For producing casing, first it need to be welded into cylindrical part then will follow different deformation process to produce the final product. Similarly, AISI 316L is used with Inconel 718 in the region where operating condition is around 600°C. Hence, this material combination is widely used in chemical processing, oil industries and gas power stations for the fabrication of various hot section components. This bimetallic welds are implemented for construction of

hoses (AISI 316L) and quick disconnects coupling (Inconel 718), and employed in the international space station for carrying ammonia. This material combination is also widely used in nuclear reactors for making pressure tubes. The application of Inconel 718 alone and with AISI 316L is immense, hence a further study based on these material is worthwhile. The current work is limited to only the microstructural characterization of the similar and dissimilar weld produced in autogenous mode. The other aspect of welding like, the influence of welding techniques and solidification parameters on residual stress development in the welded structure is worthy to investigate. The effect of pulse shaping on weld morphology and corresponding effect on segregation and secondary phase formation can be a future direction of investigation. The post weld heat treatment of this dissimilar material combination could be another important domain of future investigation. The conduction based heat transfer model can be improved further to enhance the effectiveness of the model by incorporating convective mode of heat transfer for the similar and dissimilar combination of weld.

References

Ahmadi, M.R., Rath, M., Povoden-Karadeniz, E., Primig, S., Wojcik, T., Danninger, A., Stockinger, M., Kozeschnik, E., 2017. Modeling of precipitation strengthening in Inconel 718 including non-spherical$\upgamma$$\dprime$ precipitates. Modelling Simul. Mater. Sci. Eng. 25, 055005. https://doi.org/10.1088/1361-651X/aa6f54

Antonsson, T., Fredriksson, H., 2005. The effect of cooling rate on the solidification of INCONEL 718. Metall and Materi Trans B 36, 85–96. https://doi.org/10.1007/s11663-005-0009-0

Arnberg, L., Chai, G., Backerud, L., 1993. Determination of dendritic coherency in solidifying melts by rheological measurements. Materials Science and Engineering: A 173, 101–103. https://doi.org/10.1016/0921-5093(93)90195-K

ASTM Int, ASTM E384: Standard Test Method for Knoop and Vickers Hardness of Materials. ASTM Stand, 2012, 1–43.

ASTM Standard E 407, Standard Practice for Microetching Metals and Alloys. ASTM International, 1999, 1–21.

ASTM Standard E8/E8m, Standard Test Methods for Tension Testing of Metallic Materials. ASTM International, 2008, 743–746.

Bag, S., Amin, M.R., 2020. Investigation on Ultrashort Pulse Laser Welding of Dissimilar Metallic Materials Expending Phase-Lag Influence. J. Therm. Sci. Eng. Appl. 12. https://doi.org/10.1115/1.4046360

Bag, S., De, A., 2008. Development of a Three-Dimensional Heat-Transfer Model for the Gas Tungsten Arc Welding Process Using the Finite Element Method Coupled with a Genetic Algorithm–Based Identification of Uncertain Input Parameters. Metall. Mater. Trans. A 39, 2698–2710. https://doi.org/10.1007/s11661-008-9607-1

Bag, S., De, A., 2010. Computational modelling of conduction mode laser welding process. Laser welding. Engineering Electrical and Electronic Engineering Sciyo 133–160.

Banerjee, K., Richards, N.L., Chaturvedi, M.C., 2005. Effect of filler alloys on heat-affected zone cracking in preweld heat-treated IN-738 LC gas-tungsten-arc welds. Metall and Mat Trans A 36, 1881–1890. https://doi.org/10.1007/s11661-005-0051-1

Banovic, S.W., Dupont, J.N., Marder, A.R., 2002. Dilution and microsegregation in dissimilar metal welds between super austenitic stainless steel and nickel base alloys. Sci. Technol. Weld. Join. 7, 374–383. https://doi.org/10.1179/136217102225006804

Bansal, A., Sharma, A.K., Das, S., Kumar, P., 2016. On microstructure and strength properties of microwave welded Inconel 718/ stainless steel (SS-316L). Proc. Inst. Mech. Eng. Part J. Mater. Des. Appl. 230, 939–948. https://doi.org/10.1177/1464420715589206

Baruah, M., Bag, S., 2016. Influence of heat input in microwelding of titanium alloy by micro plasma arc. J. Mater. Process. Technol. 231, 100–112. https://doi.org/10.1016/j.jmatprotec.2015.12.014

Baruah, M., Bag, S., 2017. Influence of pulsation in thermo-mechanical analysis on laser micro-welding of Ti6Al4V alloy. Optics & Laser Technology 90, 40–51. https://doi.org/10.1016/j.optlastec.2016.11.006

Brooks, J.W., Bridges, P.J., 1988. Metallurgical stability of Inconel alloy 718. Superalloys 88, 33–42.

Cao, X., Rivaux, B., Jahazi, M., Cuddy, J., Birur, A., 2009. Effect of pre- and post-weld heat treatment on metallurgical and tensile properties of Inconel 718 alloy butt joints welded using 4 kW Nd:YAG laser. J Mater Sci 44, 4557–4571. https://doi.org/10.1007/s10853-009-3691-5

Chen, H.C., Pinkerton, A.J., Li, L., 2011. Fibre laser welding of dissimilar alloys of Ti-6Al-4V and Inconel 718 for aerospace applications. The International Journal of Advanced Manufacturing Technology 52, 977–987.

Chen, W., Chaturvedi, M.C., Richards, N.L., 2001. Effect of boron segregation at grain boundaries on heat-affected zone cracking in wrought INCONEL 718. Metallurgical and Materials Transactions A 32, 931–939.

Cieslak, M.J., Headley, T.J., Knorovsky, G.A., Romig, A.D., Kollie, T., 1990. A comparison of the solidification behavior of INCOLOY 909 and INCONEL 718. Metall Mater Trans A 21, 479–488. https://doi.org/10.1007/BF02782428

Clark, D., Bache, M.R., Whittaker, M.T., 2010. Microstructural Characterization of a Polycrystalline Nickel-Based Superalloy Processed via Tungsten-Intert-Gas-Shaped Metal Deposition. Metall and Materi Trans B 41, 1346–1353. https://doi.org/10.1007/s11663-010-9410-4

Cormier, J., Gadaud, P., Czaplicki, M., Zhang, R.Y., Dong, H.B., Smith, T.M., Zhang, F., Tiley, J.S., Semiatin, S.L., 2020. In-Situ Determination of Precipitation Kinetics During Heat Treatment of Superalloy 718. Metall Mater Trans A. https://doi.org/10.1007/s11661-020-06078-4

Davies, G.J., Garland, J.G., 1975. Solidification Structures and Properties of Fusion Welds. International Metallurgical Reviews 20, 83–108. https://doi.org/10.1179/imtlr.1975.20.1.83

De, A., Maiti, S.K., Walsh, C.A., Bhadeshia, H., 2003. Finite element simulation of laser spot welding. Science and Technology of Welding and joining 8, 377–384.

Detor, A.J., DiDomizio, R., Sharghi-Moshtaghin, R., Zhou, N., Shi, R., Wang, Y., McAllister, D.P., Mills, M.J., 2018. Enabling Large Superalloy Parts Using Compact Coprecipitation of γ′ and γ″. Metall Mater Trans A 49, 708–717. https://doi.org/10.1007/s11661-017-4356-7

Devendranath Ramkumar, K., Patel, S.D., Sri Praveen, S., Choudhury, D.J., Prabaharan, P., Arivazhagan, N., Xavior, M.A., 2014. Influence of filler metals and welding techniques on the structure–property relationships of Inconel 718 and AISI 316L dissimilar weldments. Mater. Des. 1980-2015 62, 175–188. https://doi.org/10.1016/j.matdes.2014.05.019

Draxler, J., Edberg, J., Andersson, J., -E. Lindgren, L., 2019. Modeling and simulation of weld solidification cracking part III. Weld World 63, 1883–1901. https://doi.org/10.1007/s40194-019-00784-3

Drexler, A., Oberwinkler, B., Primig, S., Turk, C., Povoden-Karadeniz, E., Heinemann, A., Ecker, W., Stockinger, M., 2018. Experimental and numerical investigations of the γ″ and γ′ precipitation kinetics in Alloy 718. Materials Science and Engineering: A 723, 314–323. https://doi.org/10.1016/j.msea.2018.03.013

Du, H., Hu, L., Liu, J., Hu, X., 2004. A study on the metal flow in full penetration laser beam welding for titanium alloy. Computational Materials Science 29, 419–427. https://doi.org/10.1016/j.commatsci.2003.11.002

DuPont, J.N., Notis, M.R., Marder, A.R., Robino, C.V., Michael, J.R., 1998. Solidification of Nb-bearing superalloys: Part I. Reaction sequences. Metall Mater Trans A 29, 2785–2796. https://doi.org/10.1007/s11661-998-0319-3

DuPont, J.N., Robino, C.V., Marder, A.R., 1999. Modelling mushy zones in welds of multicomponent alloys: implications for solidification cracking. Science and Technology of Welding and Joining 4, 1–14. https://doi.org/10.1179/stw.1999.4.1.1

Dvornak, M.J., Frost, R.H., Olson, D.L., 1991. Influence of solidification kinetics on aluminum weld grain refinement. Welding Journal 70, 271s–276s.

Dye, D., Hunziker, O., Roberts, S.M., Reed, R.C., 2001. Modeling of the mechanical effects induced by the tungsten inert-gas welding of the IN718 superalloy. Metall. Mater. Trans. A 32, 1713–1725.

Ebrahimi, A.N., Arab, N.B.M., Gollo, M.H., 2016. Thermal analysis of laser beam welding of nickel-based super alloy Inconel 625 to AISI 316L, using Gaussian optics theory in keyhole. J. Braz. Soc. Mech. Sci. Eng. 38, 1199–1206. https://doi.org/10.1007/s40430-015-0422-5

Frewin, M.R., Scott, D.A., 1999. Finite element model of pulsed laser welding. WELDING JOURNAL-NEW YORK-78, 15-s.

Friedman, E., 1975. Thermomechanical analysis of the welding process using the finite element method.

Gobbi, S., Zhang, L., Norris, J., Richter, K.H., Loreau, J.H., 1996. High powder CO2 and Nd□YAG laser welding of wrought Inconel 718. Journal of Materials Processing Technology, International Conference on Advances in Material and Processing Technologies 56, 333–345. https://doi.org/10.1016/0924-0136(95)01847-6

Goldak, J., Chakravarti, A., Bibby, M., 1984. A new finite element model for welding heat sources. Metall. Trans. B 15, 299–305. https://doi.org/10.1007/BF02667333

Goldak, J.A., Akhlaghi, M., 2005. Computational welding mechanics. Springer Science & Business Media.

Henderson, M.B., Arrell, D., Larsson, R., Heobel, M., Marchant, G., 2004. Nickel based superalloy welding practices for industrial gas turbine applications. Sci. Technol. Weld. Join. 9, 13–21. https://doi.org/10.1179/136217104225017099

Hinojos, A., Mireles, J., Reichardt, A., Frigola, P., Hosemann, P., Murr, L.E., Wicker, R.B., 2016. Joining of Inconel 718 and 316 Stainless Steel using electron beam melting additive manufacturing technology. Mater. Des. 94, 17–27. https://doi.org/10.1016/j.matdes.2016.01.041

Hong, J.K., Park, J.H., Park, N.K., Eom, I.S., Kim, M.B., Kang, C.Y., 2008. Microstructures and mechanical properties of Inconel 718 welds by CO2 laser welding. Journal of Materials Processing Technology, 10th International Conference on Advances in Materials and Processing Technologies 201, 515–520. https://doi.org/10.1016/j.jmatprotec.2007.11.224

Huang, C.A., Wang, T.H., Lee, C.H., Han, W.C., 2005. A study of the heat-affected zone (HAZ) of an Inconel 718 sheet welded with electron-beam welding (EBW). Mater. Sci. Eng. A 398, 275–281. https://doi.org/10.1016/j.msea.2005.03.029

Janaki Ram, G.D., Venugopal Reddy, A., Prasad Rao, K., Madhusudhan Reddy, G., 2004. Control of Laves phase in Inconel 718 GTA welds with current pulsing. Science and technology of welding and joining 9, 390–398.

Janaki Ram, G.D., Venugopal Reddy, A., Prasad Rao, K., Reddy, G.M., Sarin Sundar, J.K., 2005. Microstructure and tensile properties of Inconel 718 pulsed Nd-YAG laser welds. Journal of Materials Processing Technology 167, 73–82. https://doi.org/10.1016/j.jmatprotec.2004.09.081

Jiang, P., Wang, C., Zhou, Q., Shao, X., Shu, L., Li, X., 2016. Optimization of laser welding process parameters of stainless steel 316L using FEM, Kriging and NSGA-II. Advances in Engineering Software 99, 147–160. https://doi.org/10.1016/j.advengsoft.2016.06.006

Jiang, W., Yahiaoui, K., 2010. Influence of Cooling Rate on Predicted Weld Residual Stress Buildup in a Thick-Walled Piping Intersection. J. Press. Vessel Technol. 132, 021205-021205–8. https://doi.org/10.1115/1.4000634

Jou, M., 2003. Experimental Study and Modeling of GTA Welding Process. Journal of Manufacturing Science and Engineering 125, 801–808. https://doi.org/10.1115/1.1537740

Jouiad, M., Marin, E., Devarapalli, R.S., Cormier, J., Ravaux, F., Le Gall, C., Franchet, J.-M., 2016. Microstructure and mechanical properties evolutions of alloy 718 during isothermal and thermal cycling over-aging. Materials & Design 102, 284–296. https://doi.org/10.1016/j.matdes.2016.04.048

Kar, J., Roy, S.K., Roy, G.G., 2017. Effect of Beam Oscillation on Microstructure and Mechanical Properties of AISI 316L Electron Beam Welds. Metall and Mat Trans A 48, 1759–1770. https://doi.org/10.1007/s11661-017-3976-2

Knorovsky, G.A., Cieslak, M.J., Headley, T.J., Romig, A.D., Hammetter, W.F., 1989. INCONEL 718: A solidification diagram. Metall. Trans. A 20, 2149–2158. https://doi.org/10.1007/BF02650300

Kou, S., 2003. Welding metallurgy,New Jersey, USA. A JOHN WILEY & SONS,INC., PUBLICATION 2, 431–446. https://doi.org/10.1557/mrs2003.197

Kumar, B., Bag, S., 2019. Phase transformation effect in distortion and residual stress of thin-sheet laser welded Ti-alloy. Opt. Lasers Eng. 122, 209–224. https://doi.org/10.1016/j.optlaseng.2019.06.008

Kumar, B., Bag, S., Paul, C.P., Das, C.R., Ravikumar, R., Bindra, K.S., 2020. Influence of the mode of laser welding parameters on microstructural morphology in thin sheet Ti6Al4V alloy. Opt. Laser Technol. 131, 106456. https://doi.org/10.1016/j.optlastec.2020.106456

Kumar, K.G., Ramkumar, K.D., Arivazhagan, N., 2015. Characterization of metallurgical and mechanical properties on the multi-pass welding of Inconel 625 and AISI 316L. Journal of Mechanical Science and Technology 29, 1039–1047.

Kuo, C. M., Yang, Y.-T., Bor, H.-Y., Wei, C.-N., Tai, C.-C., 2009. Aging effects on the microstructure and creep behavior of Inconel 718 superalloy. Materials Science and Engineering: A, 11th International Conference of Creep and Fracture of Engineering Materials and Structures, CREEP 2008 510–511, 289–294. https://doi.org/10.1016/j.msea.2008.04.097

Kuo, C.M., Yang, Y.T., Bor, H.Y., Wei, C.N., Tai, C.C., 2009. Aging effects on the microstructure and creep behavior of Inconel 718 superalloy. Materials Science and Engineering: A 510, 289–294.

Lee, C.-H., Chang, K.-H., 2012. Temperature fields and residual stress distributions in dissimilar steel butt welds between carbon and stainless steels. Appl. Therm. Eng. 45–46, 33–41. https://doi.org/10.1016/j.applthermaleng.2012.04.007

Liao, X., Zhai, Q., Luo, J., Chen, W., Gong, Y., 2007. Refining mechanism of the electric current pulse on the solidification structure of pure aluminum. Acta Materialia 55, 3103–3109. https://doi.org/10.1016/j.actamat.2007.01.014

Lippold, J.C., Savage, W.F., 1982. Solidification of austenitic stainless steel weldments: Part III–the effect of solidification behavior on hot cracking susceptibility. WELDING J. 61, 388.

Ma, D., 2004. Response of primary dendrite spacing to varying temperature gradient during directional solidification. Metallurgical and Materials Transactions B 35, 735–742.

Madhusudhana Reddy, G., Srinivasa Murthy, C.V., Srinivasa Rao, K., Prasad Rao, K., 2009. Improvement of mechanical properties of Inconel 718 electron beam welds—influence of welding techniques and postweld heat treatment. Int J Adv Manuf Technol 43, 671–680. https://doi.org/10.1007/s00170-008-1751-7

Manikandan, S.G.K., Sivakumar, D., Rao, K.P., Kamaraj, M., 2014. Effect of weld cooling rate on Laves phase formation in Inconel 718 fusion zone. J. Mater. Process. Technol. 214, 358–364. https://doi.org/10.1016/j.jmatprotec.2013.09.006

Manikandan, S. G. K., Sivakumar, D., Rao, K. P., & Kamaraj, M., 2015. Laves phase in alloy 718 fusion zone—microscopic and calorimetric studies. Mater. Charact., 100, 192-206. https://doi.org/10.1016/j.matchar.2014.11.035

McAllister, D., Lv, D., Peterson, B., Deutchman, H., Wang, Y., Mills, M.J., 2016. Lower temperature deformation mechanisms in a γ″-strengthened Ni-base superalloy. Scripta Materialia 115, 108–112. https://doi.org/10.1016/j.scriptamat.2015.11.026

Mei, Y., Liu, Y., Liu, C., Li, C., Yu, L., Guo, Q., Li, H., 2016. Effect of base metal and welding speed on fusion zone microstructure and HAZ hot-cracking of electron-beam welded Inconel 718. Materials & Design 89, 964–977. https://doi.org/10.1016/j.matdes.2015.10.082

Mills, W.J., 1984. Effect of heat treatment on the tensile and fracture toughness behaviour of alloy 718 weldments. Welding journal 63, 237s–245s.

Mortezaie, A., Shamanian, M., 2014. An assessment of microstructure, mechanical properties and corrosion resistance of dissimilar welds between Inconel 718 and 310S austenitic stainless steel. International Journal of Pressure Vessels and Piping 116, 37–46. https://doi.org/10.1016/j.ijpvp.2014.01.002

Nastac, L., Stefanescu, D.M., 1996. Macrotransport-solidification kinetics modeling of equiaxed dendritic growth: Part II. Computation problems and validation on INCONEL 718 superalloy castings. MMTA 27, 4075–4083. https://doi.org/10.1007/BF02595656

Niang, A., Viguier, B., Lacaze, J., 2010. Some features of anisothermal solid-state transformations in alloy 718. Materials Characterization 61, 525–534. https://doi.org/10.1016/j.matchar.2010.02.011

Ning, F., Hu, Y., Liu, Z., Wang, X., Li, Y., Cong, W., 2018. Ultrasonic Vibration-Assisted Laser Engineered Net Shaping of Inconel 718 Parts: Microstructural and Mechanical Characterization. J. Manuf. Sci. Eng. 140, 061012-061012–11. https://doi.org/10.1115/1.4039441

Odabaşı, A., Ünlü, N., Göller, G., Eruslu, M.Ni., 2010. A Study on Laser Beam Welding (LBW) Technique: Effect of Heat Input on the Microstructural Evolution of Superalloy Inconel 718. Metall and Mat Trans A 41, 2357–2365. https://doi.org/10.1007/s11661-010-0319-y

Oreper, G.M., Szekely, J., Eagar, T.W., 1986. The role of transient convection in the melting and solidification in arc weldpools. Metallurgical Transactions B 17, 735–744.

Pavelic, V., 1969. Experimental and computed temperature histories in gas tungsten arc welding of thin plates. Welding Journal Research Supplement 48, 296–305.

Peelamedu, R.D., Roy, R., Agrawal, D.K., 2002. Microwave-induced reaction sintering of NiAl2O4. Mater. Lett. 55, 234–240. https://doi.org/10.1016/S0167-577X(01)00653-X

Pereira, J.M., Lerch, B.A., 2001. Effects of heat treatment on the ballistic impact properties of Inconel 718 for jet engine fan containment applications. Int. J. Impact Eng. 25, 715–733. https://doi.org/10.1016/S0734-743X(01)00018-5

Phillips, P.J., McAllister, D., Gao, Y., Lv, D., Williams, R.E.A., Peterson, B., Wang, Y., Mills, M.J., 2012. Nano γ′/γ″ composite precipitates in Alloy 718. Appl. Phys. Lett. 100, 211913. https://doi.org/10.1063/1.4721456

Prabaharan, P., Devendranath Ramkumar, K., Arivazhagan, N., 2014. Characterization of microstructure and mechanical properties of Super Ni 718 alloy and AISI 316L dissimilar weldments. J. Mater. Res. 29, 3011–3023. https://doi.org/10.1557/jmr.2014.329

Qi, H., Azer, M., Ritter, A., 2009. Studies of Standard Heat Treatment Effects on Microstructure and Mechanical Properties of Laser Net Shape Manufactured INCONEL 718. Metall Mater Trans A 40, 2410–2422. https://doi.org/10.1007/s11661-009-9949-3

Qian, M., Lippold, J.C., 2003. The effect of rejuvenation heat treatments on the repair weldability of wrought Alloy 718. Materials Science and Engineering: A 340, 225–231. https://doi.org/10.1016/S0921-5093(02)00187-9

Radavich, J.F., 1989. The Physical Metallurgy of Cast and Wrought Alloy 718, in: Superalloys 718 Metallurgy and Applications (1989). Presented at the Superalloys, TMS, pp. 229–240. https://doi.org/10.7449/1989/Superalloys_1989_229_240

Radhakrishna, C., Rao, K.P., 1994. Studies on creep/stress rupture behaviour of superalloy 718 weldments used in gas turbine applications. Materials at high temperatures 12, 323–327.

Radhakrishna, C.H., Rao, K.P., 1997. The formation and control of Laves phase in superalloy 718 welds. Journal of Materials Science 32, 1977–1984.

Radhakrishna, Ch., Rao, K.P., Srinivas, S., 1995. Laves phase in superalloy 718 weld metals. J Mater Sci Lett 14, 1810–1812. https://doi.org/10.1007/BF00271015

Radhakrishnan, B., Thompson, R.G., 1992. A model for the formation and solidification of grain boundary liquid in the heat-affected zone (HAZ) of welds. Metall and Mat Trans A 23, 1783–1799. https://doi.org/10.1007/BF02804371

Rahman Chukkan, J., Vasudevan, M., Muthukumaran, S., Ravi Kumar, R., Chandrasekhar, N., 2015. Simulation of laser butt welding of AISI 316L stainless steel sheet using various heat sources and experimental validation. J. Mater. Process. Technol. 219, 48–59. https://doi.org/10.1016/j.jmatprotec.2014.12.008

Ram, G.D.J., Reddy, A.V., Rao, K.P., Reddy, G.M., 2004. Control of Laves phase in Inconel 718 GTA welds with current pulsing. Science and Technology of Welding and Joining 9, 390–398. https://doi.org/10.1179/136217104225021788

Ram, G.D.J., Reddy, A.V., Rao, K.P., Reddy, G.M., 2005. Microstructure and mechanical properties of Inconel 718 electron beam welds. Materials Science and Technology 21, 1132–1138. https://doi.org/10.1179/174328405X62260

Ramkumar, D.K., Sidharth, D., K.V., Phani Prabhakar., R., Rajendran., K., Giri Mugudan, S., Narayan, 2019. Microstructure and properties of inconel 718 and AISI 416 laser welded joints. J. Mater. Process. Technol. 266, 52–62. https://doi.org/10.1016/j.jmatprotec.2018.10.039

Ramkumar, T., Selvakumar, M., Narayanasamy, P., Begam, A.A., Mathavan, P., Raj, A.A., 2017. Studies on the structural property, mechanical relationships and corrosion behaviour of Inconel 718 and SS 316L dissimilar joints by TIG welding without using activated flux. Journal of Manufacturing Processes 30, 290–298. https://doi.org/10.1016/j.jmapro.2017.09.028

Ranjbarnodeh, E., Serajzadeh, S., Kokabi, A.H., Fischer, A., 2012. Prediction of temperature distribution in dissimilar arc welding of stainless steel to carbon steel. Proceedings of the Institution of Mechanical Engineers, Part B: Journal of Engineering Manufacture 226, 117–125. https://doi.org/10.1177/0954405411403551

Reddy, G.M., Murthy, C.V.S., Rao, K.S., Rao, K.P., 2009. Improvement of mechanical properties of Inconel 718 electron beam welds—influence of welding techniques and postweld heat treatment. Int. J. Adv. Manuf. Technol. 43, 671–680. https://doi.org/10.1007/s00170-008-1751-7

Richards, N.L., Huang, X., Chaturvedi, M.C., 1992. Heat affected zone cracking in cast inconel 718. Materials Characterization, 1988 IMS Symposium Metallography and Corrosion 28, 179–187. https://doi.org/10.1016/1044-5803(92)90080-2

Rocha, O.L., Siqueira, C.A., Garcia, A., 2003. Heat flow parameters affecting dendrite spacings during unsteady-state solidification of Sn-Pb and Al-Cu alloys. Metall and Mat Trans A 34, 995–1006. https://doi.org/10.1007/s11661-003-0229-3

Rosenthal, D., 1946. The Theory of Moving Sources of Heat and Its Application to Metal Treatments. Trans American Soc. Mech. Engr. 68, 849–866.

Savage, W.F., Lundin, C.D., Hrubec, R.J., 1968. Segregation and hot cracking in low-alloy quench and tempered steels. Welding Journal 47, S420.

Schirra, J.J., Caless, R.H., Hatala, R.W., 1991. The effect of Laves phase on the mechanical properties of wrought and cast+ HIP Inconel 718. Superalloys 718, 375–388.

Shi, R., McAllister, D.P., Zhou, N., Detor, A.J., DiDomizio, R., Mills, M.J., Wang, Y., 2019. Growth behavior of γ'/γ'' coprecipitates in Ni-Base superalloys. Acta Mater. 164, 220–236. https://doi.org/10.1016/j.actamat.2018.10.028

Sivaprasad, K., Raman, S.G.S., 2007. Influence of magnetic arc oscillation and current pulsing on fatigue behavior of alloy 718 TIG weldments. Materials Science and Engineering: A 448, 120–127.

Sun, W., Mohammed, M.B., Xu, L., Hyde, T.H., McCartney, D.G., Leen, S.B., 2014. Process modelling and optimization of keyhole plasma arc welding of thin Ti-6Al-4V. The Journal of Strain Analysis for Engineering Design 49, 410–420.

Sundararaman, M., Mukhopadhyay, P., 1993. Carbide precipitation in Inconel 718. High Temperature Materials and Processes 11, 351–368.

Texier, D., Gómez, A.C., Pierret, S., Franchet, J.-M., Pollock, T.M., Villechaise, P., Cormier, J., 2016. Microstructural Features Controlling the Variability in Low-Cycle Fatigue Properties of Alloy Inconel 718DA at Intermediate Temperature. Metall Mater Trans A 47, 1096–1109. https://doi.org/10.1007/s11661-015-3291-8

Thavamani, R., Balusamy, V., Nampoothiri, J., Subramanian, R., Ravi, K.R., 2018. Mitigation of hot cracking in Inconel 718 superalloy by ultrasonic vibration during gas tungsten arc welding. Journal of Alloys and Compounds 740, 870–878. https://doi.org/10.1016/j.jallcom.2017.12.295

Theska, F., Nomoto, K., Godor, F., Oberwinkler, B., Stanojevic, A., Ringer, S.P., Primig, S., 2020a. On the early stages of precipitation during direct ageing of Alloy 718. Acta Materialia 188, 492–503. https://doi.org/10.1016/j.actamat.2020.02.034

Theska, F., Stanojevic, A., Oberwinkler, B., Primig, S., 2020b. Microstructure-property relationships in directly aged Alloy 718 turbine disks. Materials Science and Engineering: A 776, 138967. https://doi.org/10.1016/j.msea.2020.138967

Theska, F., Stanojevic, A., Oberwinkler, B., Ringer, S.P., Primig, S., 2018. On conventional versus direct ageing of Alloy 718. Acta Materialia 156, 116–124. https://doi.org/10.1016/j.actamat.2018.06.034

Thompson, R.G., 1988. Microfissuring of Alloy 718 in the Weld Heat-Affected Zone. JOM 40, 44–48. https://doi.org/10.1007/BF03258151

Thompson, R.G., Dobbs, J.R., Mayo, D.E., 1986. The Effect of Heat Treatment on Microfissuring in Alloy 718. Weld. J. 65, 299.

Thompson, R.G., Mayo, D.E., Radhakrishnan, B., 1991. The relationship between carbon content, microstructure, and intergranular liquation cracking in cast nickel alloy 718. MTA 22, 557–567. https://doi.org/10.1007/BF02656823

Trivedi, A., Bag, S., De, A., 2007. Three-dimensional transient heat conduction and thermomechanical analysis for laser spot welding using adaptive heat source.

Tucho, W.M., Cuvillier, P., Sjolyst-Kverneland, A., Hansen, V., 2017. Microstructure and hardness studies of Inconel 718 manufactured by selective laser melting before and after solution heat treatment. Materials Science and Engineering: A 689, 220–232. https://doi.org/10.1016/j.msea.2017.02.062

Tzeng, Y.-F., 2000. Process Characterisation of Pulsed Nd:YAG Laser Seam Welding. Int J Adv Manuf Technol 16, 10–18. https://doi.org/10.1007/PL00013126

Vincent, R., 1985. Precipitation around welds in the nickel-base superalloy, Inconel 718. Acta Metallurgica 33, 1205–1216.

Vishwakarma, K.R., Ojo, O.A., Richards, N.L., 2015. Nano-size solidification microconstituents in electro-spark deposited Ni-base superalloy. Philosophical Magazine Letters 95, 30–36. https://doi.org/10.1080/09500839.2014.995740

Wang, L., Li, C., Dong, J., Zhang, M., 2009. An Investigation of Microsegregation and Liquid Density Redistribution During Solidification of Inconel 718. Chemical Engineering Communications 196, 754–765. https://doi.org/10.1080/00986440802557518

Watanabe, T., Nakamura, H., Ei, K., 1990. Solidification Control of Austenitic Stainless Steel Weld Metal by Electromagnetic Stirring : Transactions of the Japan Welding Society 21, 109–115.

Whitesell, H.S., Li, L., Overfelt, R.A., 2000. Influence of solidification variables on the dendrite arm spacings of Ni-based superalloys. Metall Mater Trans B 31, 546–551. https://doi.org/10.1007/s11663-000-0162-4

Wu, C., Li, S., Zhang, C., Wang, X., 2016. Microstructural evolution in 316LN austenitic stainless steel during solidification process under different cooling rates. Journal of Materials Science 51, 2529–2539. https://doi.org/10.1007/s10853-015-9565-0

Wu, C.S., Wang, H.G., Zhang, Y.M., 2006. A New Heat Source Model for Keyhole Plasma Arc Welding in FEM Analysis of the Temperature Profile 8.

Wu, C.S., Wang, L., Ren, W.J., Zhang, X.Y., 2014. Plasma arc welding: Process, sensing, control and modeling. Journal of Manufacturing Processes, Recent Developments in Welding Processes 16, 74–85. https://doi.org/10.1016/j.jmapro.2013.06.004

Yadaiah, N., Bag, S., 2012. Effect of Heat Source Parameters in Thermal and Mechanical Analysis of Linear GTA Welding Process. ISIJ International 52, 2069–2075. https://doi.org/10.2355/isijinternational.52.2069

Yadaiah, N., Bag, S., 2014. Development of egg-configuration heat source model in numerical simulation of autogenous fusion welding process. International Journal of Thermal Sciences 86, 125–138. https://doi.org/10.1016/j.ijthermalsci.2014.06.032

Ye, X., Hua, X., Wang, M., Lou, S., 2015. Controlling hot cracking in Ni-based Inconel-718 superalloy cast sheets during tungsten inert gas welding. Journal of Materials Processing Technology 222, 381–390. https://doi.org/10.1016/j.jmatprotec.2015.03.031

Yuan, H., Liu, W.C., 2005. Effect of the δ phase on the hot deformation behavior of Inconel 718. Mater. Sci. Eng. A 408, 281–289. https://doi.org/10.1016/j.msea.2005.08.126

Zacharia, T., David, S.A., Vitek, J.M., Debroy, T., 1989. Heat transfer during Nd: YAG pulsed laser welding and its effect on solidification structure of austenitic stainless steels. Metallurgical Transactions A 20, 957–967.

Zhang, Y. N., Cao, X., & Wanjara, P., 2013. Microstructure and hardness of fiber laser deposited Inconel 718 using filler wire. The International Journal of Advanced Manufacturing Technology, 69(9-12), 2569-2581.

Zhao, X., Chen, J., Lin, X., Huang, W., 2008. Study on microstructure and mechanical properties of laser rapid forming Inconel 718. Materials Science and Engineering: A 478, 119–124.

Zhao, Z., Qu, H., Bai, P., Li, J., Wu, L., Huo, P., 2018. Friction and wear behaviour of Inconel 718 alloy fabricated by selective laser melting after heat treatments. Philosophical Magazine Letters 98, 547–555. https://doi.org/10.1080/09500839.2019.1597991

Zhou, N., Lv, D.C., Zhang, H.L., McAllister, D., Zhang, F., Mills, M.J., Wang, Y., 2014. Computer simulation of phase transformation and plastic deformation in IN718 superalloy: Microstructural evolution during precipitation. Acta Materialia 65, 270–286. https://doi.org/10.1016/j.actamat.2013.10.069

Bibliography

Kou, S., 2003. Welding Metallurgy, second ed. ed. John Wiley & Sons, New Jersey, USA.

Manikandan, S.G.K., Sivakumar, D., Kamaraj, M., 2019. Welding the Inconel 718 Superalloy: Reduction of Micro-segregation and Laves Phases. Elsevier.

List of publications

International journals

1. **Sahu, A. K.,** and S. Bag. **"**Design of a double aging treatment for the improvement of mechanical and microstructural properties of pulse micro-plasma arc welded Alloy 718". ***Journal of Materials Science*** (2021): 56(23), 13400–13415.
2. **Sahu, A. K.,** and S. Bag. "Probe pulse conditions and solidification parameters for the dissimilar welding of Inconel 718 and AISI 316L stainless steel." ***Metallurgical and Materials Transactions A*** (2020): 51(5), 2192-2208.
3. **Sahu, A. K.,** S. Bag, and Ke Huang. "Mitigation of micro-cracks in dissimilar welding of Inconel 718 and austenitic stainless steel." ***Philosophical Magazine Letters*** (2020): 100(8), 365-374.
4. **Sahu, A. K.,** and S. Bag, (2020). **"**Influence of current pulsation on solidification parameters during micro plasma arc welding of Inconel 718", **(Under Review).**
5. **Sahu, A. K.,** S. Bag and V. Kumar (2020). **"**Role of intermetallic formation on microstructural and mechanical properties in dissimilar laser welding of Inconel 718 and AISI 316L**", (Under Review).**

Book chapters

1. **Sahu, Ajit Kumar** and Swarup Bag**.** "Effect of current pulsation on weld microstructure during micro-plasma arc welding of Inconel 718". ***Next Generation Materials and Processing Technologies, Springer; Singapore:*** (2021), 159-169. https://doi.org/10.1007/978-981-16-0182-8_13
2. **Sahu, Ajit Kumar** and Swarup Bag. "Effect of pre-weld solution treatment on mechanical properties and microstructure of micro-plasma arc welded Inconel 718". In: Shunmugam MS, Kanthababu M, editors. ***Advances in Additive Manufacturing and Joining, Springer; Singapore:*** (2020), 373–383. https://doi.org/10.1007/978-981-32-9433-2_33
3. **Sahu, Ajit Kumar** and Swarup Bag. "Finite element modelling and experimental verification of dissimilar joining between Inconel 718 and SS 316L by micro-plasma arc welding." ***Advances in Computational Methods in Manufacturing, Springer; Singapore:*** (2019), 231-243. https://doi.org/10.1007/978-981-32-9072-3_20

Conferences

1. **Sahu, Ajit Kumar** and Swarup Bag. “Micro-plasma arc welding of Inconel 718 thin sheets, ***5th International Congress of the International Institute of Welding (IIW)***”, 7-9 December, 2017, Chennai, India.
2. **Sahu, Ajit Kumar** and Swarup Bag. “Effect of pre-weld solution treatment on mechanical properties and microstructure of micro-plasma arc welded Inconel 718”. ***7th International and 28th All India Manufacturing Technology Design and Research (AIMTDR) Conference***, 13-15 December, 2018, Anna University, Chennai, India.
3. **Sahu, Ajit Kumar** and Swarup Bag. "Finite element modelling and experimental verification of dissimilar joining between Inconel 718 and SS 316L by micro-plasma arc welding." ***2nd International Conference on Computational Methods in Manufacturing (ICCMM),*** 8-9 March, 2019, Indian Institute of Technology, Guwahati, India.
4. **Sahu, Ajit Kumar** and Swarup Bag**.** “Effect of current pulsation on weld microstructure during micro-plasma arc welding of Inconel 718”. ***National Conference on Research and Developments in Material Processing, Modelling and Characterization (RDMPMC-2020),*** 26-27 August 2020, National Institute of Technology, Jamshedpur, India.